

**Photophysics, electronic structure and
picosecond excited-state dynamics
of boron-nitrogen-bridged
ferrocene-donor organic-acceptor
charge-transfer compounds**

Dissertation zur Erlangung des Doktorgrades der Naturwissenschaften

Vorgelegt beim Fachbereich Physik
der Johann Wolfgang Goethe-Universität
in Frankfurt am Main

von Mark David Thomson
aus Palmerston North, Neuseeland

Frankfurt am Main 2004
(D F 1)

vom Fachbereich Physik der

Johann Wolfgang Goethe-Universität als Dissertation angenommen.

Dekan: Prof. Dr. W. Aßmus

Gutachter: Prof. Dr. H. G. Roskos, Prof. Dr. R. Valenti

Datum der Disputation: 14 Dezember 2004

Contents

Abbreviations and notation	III
Molecular structures and nomenclature	V
1. Introduction	1
1.1. Outline	6
1.2. Publications	7
1.3. Zusammenfassung	11
2. Background molecular theory and results	17
2.1. Basic electronic and photophysics theory of polyatomic molecules .	17
2.1.1. Molecular wavefunctions and radiative transitions	17
2.1.2. Non-radiative transitions and motion on potential energy surfaces	20
2.1.3. Intramolecular charge transfer	21
2.1.4. Solvatochromism of CT absorption band	27
2.2. UV-vis spectroscopic properties of ferrocene and ferrocene derivatives	30
2.2.1. Electronic structure and optical transitions of ferrocene . .	31
2.2.2. Electronic description and spectroscopic properties of established Fc-donor MLCT compounds	37
2.3. Electronic and spectroscopic properties of relevant organic acceptor compounds	43
3. Ultrafast spectroscopy: system design and characterisation	49
3.1. Femtosecond optical pulse sources	49
3.1.1. Regenerative amplifier laser	49
3.1.2. White-light continuum pulse generation	49
3.1.3. Second harmonic generation (SHG)	51
3.1.4. Prism compression and autocorrelation	52
3.1.5. Non-collinear optical parametric amplifier (NOPA)	54
3.2. Pump-probe methodology and system design	56
3.3. Coherent artifacts and time resolution with white-light continuum probing	62
4. CW spectroscopy, electrochemical and quantum chemistry results	67
4.1. Introduction	67
4.2. UV-vis absorption in solution	70
4.2.1. Extraction of UV-vis absorption bands	70
4.2.2. Solvation effects on the UV-vis absorption spectra	72
4.2.3. Comparison of electronic spectra for $[\mathbf{nA}]\mathbf{X}_n$	78
4.3. UV-vis absorption in solid state	84
4.3.1. $[\mathbf{2N}](\mathbf{PF}_6)_2$ -doped polymer film absorption vs temperature	84
4.3.2. Single-crystal absorption of $[\mathbf{2A}](\mathbf{PF}_6)_2$	87
4.4. UV-vis absorption spectra of other Fc-B-bpy derivatives	90
4.5. Electrochemistry measurements	98
4.5.1. Cyclovoltammetry data and redox potentials	99

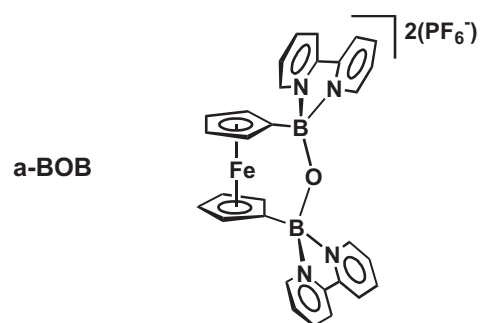
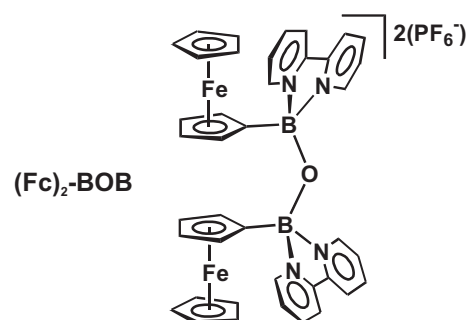
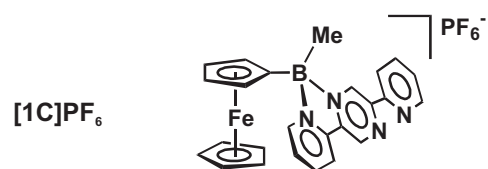
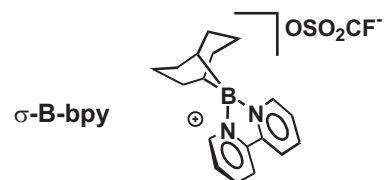
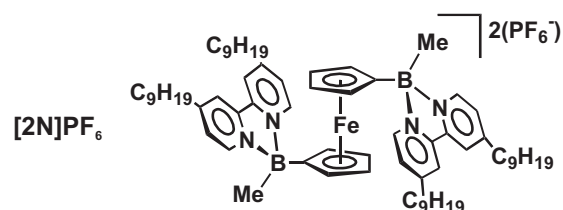
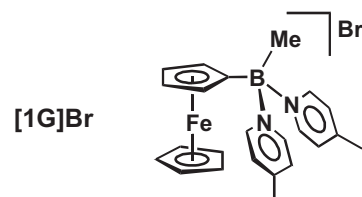
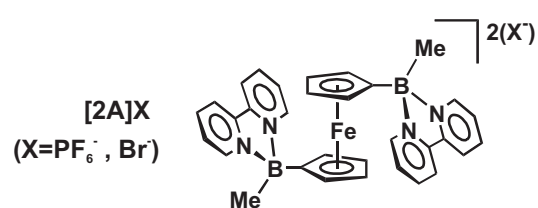
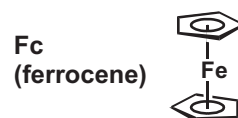
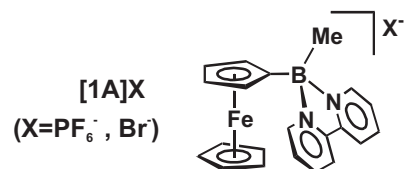
4.5.2. Correlation between MLCT transition energies and redox potentials	104
4.5.3. UV-vis spectroelectrochemistry results	108
4.6. Quantum chemistry results	111
5. Time-resolved transient-absorption spectroscopy of Fc-B-bpy compounds in solution	125
5.1. Additional experimental details	127
5.2. Transient absorption spectra	129
5.3. Transient absorption kinetics	133
5.4. Interpretation of time-resolved data and proposed relaxation models	139
6. Conclusions	151
A. Auxiliary spectroscopic data and results	155
A.1. Solvent data for solvatochromism analysis	155
A.2. Fc-B-bpy UV-vis absorption data and fitted band parameters . . .	155
A.3. Fc-B-bpy UV-vis spectroelectrochemical time-series	157
A.4. Expressions for the initial degenerate transient-absorption signal of a two-component sample	159
A.5. Spectroscopic comparison of contaminated/purified samples of a-BOB	160
A.6. Additional materials	162
B. Derivation of theoretical results	163
B.1. Perturbation theory results for D- A^n complexes	163
B.1.1. Donor–single-acceptor complex, D-A	163
B.1.2. Symmetric double-acceptor complex, A-D-A	165
B.2. One-electron wavefunctions and charge transfer transitions of D- A^n complexes	166
B.2.1. Donor–single-acceptor complex, D-A	166
B.2.2. Symmetric donor–double-acceptor complex, A-D-A	168
B.3. Solvatochromic shift and broadening of a symmetric charge-transfer electronic transition for a charged-solute	171
C. Auxiliary results from theoretical (TD-)DFT calculations	181
Bibliography	183
Curriculum Vitae	201
Acknowledgments	203

Abbreviations and notation

AC	autocorrelation
b-ET	back-electron transfer
bpy	2,2'-bipyridine
B-bpy	bipyridylboronium cation
CA	coherent artifact
Cp	cyclopentadiene
CPA	chirped-pulse amplification
CT	charge transfer
CW	continuous-wave
DFG	difference-frequency generation
dpp	2,5-bis(2-pyridyl)pyrazine
ESA	excited-state absorption
ESR	electron spin resonance
Fc	ferrocene
FWHM	full-width at half-maximum
GDD	group dispersion delay
GVD	group velocity dispersion
HOMO	highest occupied molecular orbital
IR	infra-red
LMCT	ligand-to-metal charge transfer
LUMO	lowest unoccupied molecular orbital
MA	magic angle
MCD	magnetic circular dichroism
MLCT	metal-to-ligand charge transfer
MO	molecular orbital
NOPA	non-collinear optical parametric amplifier
OD	optical density
PMMA	poly(methylmethacrylate)
PS	polystyrene
RT	room temperature
SFG	sum-frequency generation
SHG	second-harmonic generation
(TD)-DFT	(time-dependent) density functional theory
TOD	third-order dispersion
UV	ultra-violet (range)
vis	visible (range)
WL	white light (continuum)

Symbol		Units
χ_e	solvation reorganisation energy	J, eV
ΔE_{solv}	solvatochromic band shift energy	J, eV
$\Delta\nu_{\text{FWHM}}$	wavenumber bandwidth (FWHM)	m^{-1} , cm^{-1}
$\Delta\nu_{\text{solv}}$	solvatochromic band shift wavenumber	m^{-1} , cm^{-1}
$E'_{(\text{ox,red})}$	formal oxidation/reduction potentials	V
$\varepsilon_{(\text{max})}$	extinction coefficient	$\text{M}^{-1}\text{cm}^{-1}$ ($\text{M}\equiv\text{mol L}^{-1}$)
ϵ_s	solvent static dielectric constant	-
f	oscillator strength	
λ_{max}	peak absorption wavelength	m, nm
ν	photon wavenumber	m^{-1} , cm^{-1}

Molecular structures and nomenclature



1. Introduction

The aim of this study is to investigate the photophysics and electronic structure of a class of novel donor-acceptor charge-transfer complexes, which are composed of a ferrocene-donor (Fc^1) attached to organic acceptors via an intervening B-N network (as per the prototype compound shown in Figure 1.1(a), with a specific example for a single bipyridine-based acceptor (B-bpy) in Figure 1.1(b)) [1, 2, 3, 4, 5, 6, 7].

The central goal was to confirm the proposed assignment [7] of the observed visible absorption band in these compounds (which we refer to hereafter as Fc-B-bpy compounds) as a metal-to-ligand charge transfer (MLCT) electronic transition, i.e. a direct optically induced transfer of an electron localised on the Fc unit into vacant orbitals on the acceptor group.

Due to the fact that the bridge between the Fc-donor and acceptor group(s) involves a saturated tetracoordinated B-atom, it could be expected that negligible

¹Ferrocene, i.e. dicyclopentadienyl-iron(II), is composed of a central Fe(II) atom between two cyclopentadienyl rings (Cp^- , C_5H_5^-).

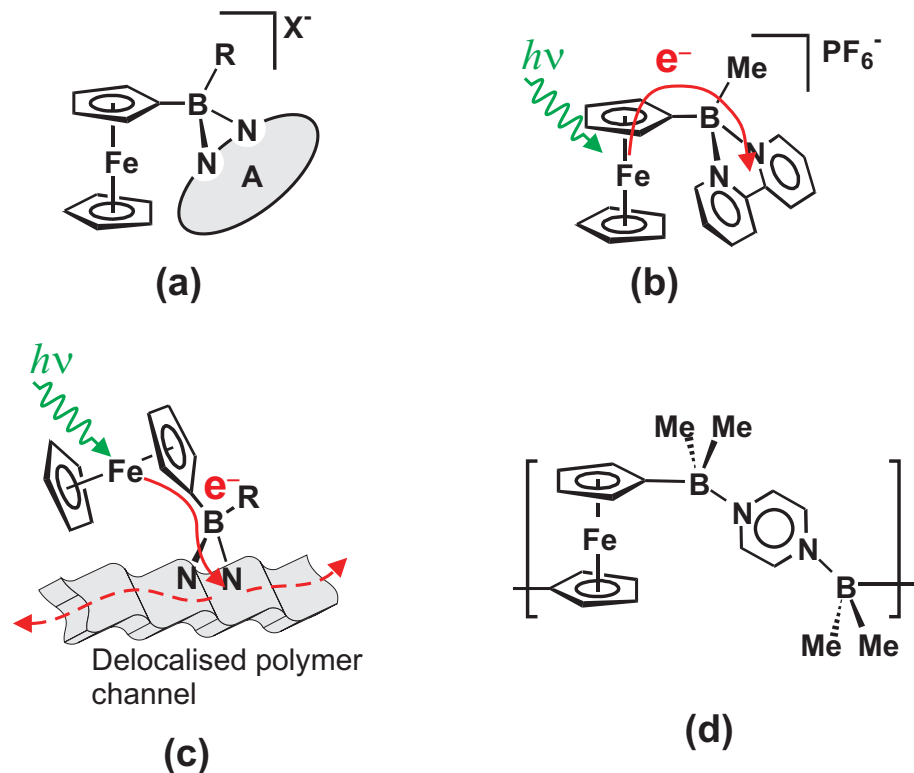


Figure 1.1.: Related Fc-B-bpy derivatives. (a) Generic model for Fc-B-bpy charge-transfer compounds studied in this work. (b) Example compound $[\mathbf{1A}]\text{PF}_6$ indicating optically-induced charge-transfer. (c) Related target polymer systems where optically induced charge transfer (CT) is used to inject charge into delocalised electronic states in a polymer backbone. (d) Example of existing Fc-B-bpy polymers with the monomer units in the main chain (with possible applications for mixed-valence transport along the polymer).

delocalisation of molecular orbitals across the B-atom would result, with only a very weak through-bond electronic coupling between donor and acceptor. Hence it was unclear as to whether the observed visible absorption band (with a peak wavelength of $\lambda_{\max} \sim 500$ nm) was due to a MLCT transition, or simply an excitation predominantly localised on the Fc donor, with the transition energy shifted into the visible range due to inductive effects from the acceptor substituent, or only a small degree of delocalisation onto the acceptor. Whilst evidence supporting an electronic interaction between the Fc-donor and B-bpy-acceptor was provided in an initial study [7], based on the semi-quantitative spectroscopic comparison of certain derivatives and indirect ESR measurements of the electrochemically-reduced derivatives², the assignment of the MLCT band remained uncertain and no detailed description of the degree of charge transfer upon optical excitation was available.

In this study, we present and collectively analyse results from UV-vis absorption and (spectro-)electrochemistry measurements, quantum chemistry calculations and ultra-fast time-resolved spectroscopy on various Fc-B-bpy derivatives. A combined interpretation of these data confirm the assignment of the MLCT absorption band and provide a better understanding of the electronic structure of these compounds and the relaxation dynamics of the MLCT excited state.

The compelling evidence that emerges in support of the assignment of the visible absorption band in the Fc-B-bpy compounds as a direct MLCT transition that involves an almost complete excited-state transfer of an electron from the Fc-donor to the B-bpy acceptors is based on (i) an analysis of the effect of the solvent environment on the MLCT transition energy, (ii) the correlation between the MLCT transition energy and the corresponding redox potentials of the Fc-donor and organic-acceptor for a range of derivatives, (iii) the molecular orbitals from theoretical DFT calculations on a prototype Fc-B-bpy compound, and (iv) the correlation between the UV-vis absorption changes that result upon electrochemical oxidation/reduction of the Fc-B-bpy compounds and the transient absorption spectra of the MLCT excited state.

A critical comparison with other Fc-donor-based compounds and auxiliary spectroscopic measurements provide further details of the electronic and photophysical properties of these compounds to aid in the future design of monomers with improved properties (e.g. greater absorption strength and extended excited-state lifetime) and macromolecular systems incorporating these monomers. An important result from the time-resolved spectroscopy measurements is that for the Fc-B-bpy derivatives with flexible linkage between donor and acceptor, a significant fraction of the CT excited-state relaxation (non-radiative back-electron-transfer, (b-ET)) occurs on a $\sim 18 - 45$ ps time scale (i.e. exponential time constant), whereas for compounds where the donor and acceptor geometry is constrained by additional bridging bonds, the b-ET occurs only on a much longer time scale of ~ 780 ps.

The investigation of these prototype Fc-B-bpy monomers is part of a larger project³ aiming at incorporating these molecular units into low-dimensional solid-state macromolecular assemblies (e.g. polymers), where the optically-induced charge transfer acts as the first step in injecting charge into a delocalised system (Figure 1.1(c)) where the injected excess charge will have a strong effect on the ex-

²Note that a detailed description of the evidence existing at the beginning of this study in support of the assignment of the MLCT band is given in the introduction to Chapter 4.

³The work on optical control of the charge and spin correlations in low-dimensional metal-organic systems is a key theme for the work of AG Roskos, Physikalisches Institut, J. W. Goethe-Universität, as part of a larger multi-disciplinary Deutsche Forschungsgemeinschaft (DFG) *Forscherguppe* project (412), ‘Spin- und Ladungskorrelationen in niedrigdimensionalen metal-organischen Festkörpern’. The Fc-B-bpy compounds studied in this work were synthesised and initially characterised within AG Wagner, Anorganische Chemie, J. W. Goethe-Universität.

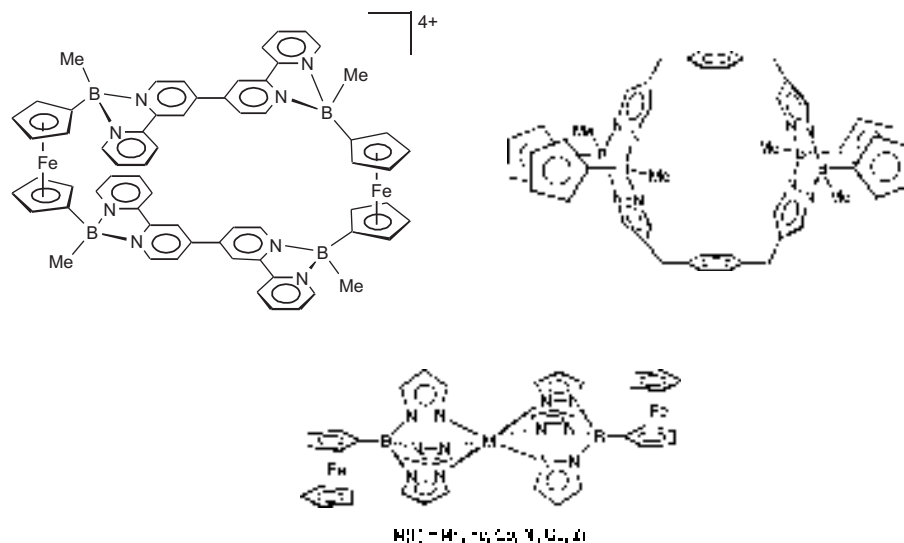


Figure 1.2.: Examples of existing macrocyclic and oligomeric derivatives related to the Fc-B-bpy compounds.

isting electronic charge- and spin-correlation phenomena of the electrons already in the delocalised system [8]. An important part of the characterisation of the MLCT excited-state for the Fc-B-bpy monomers involves determining the excited-state lifetime, i.e. the time scale for b-ET to the Fc-unit. This is a critical parameter for their performance when incorporated into larger molecular systems, as it determines (i) the steady-state concentration of CT states that can be maintained for a given irradiation level of a sample, and (ii) the net efficiency of secondary charge-transport mechanisms following the initial CT which will compete with the b-ET. Moreover, a comprehensive investigation of the differences in electronic structure for different derivatives provides an important key to improving the strength of the initiating MLCT absorption.

Whilst existing MLCT compounds involving a Fc-donor connected to an organic acceptor via a conjugated carbon bridge have been well established (for use as non-linear optical chromophores), the use of a B-N architecture can provide significant synthetic advantages in achieving sophisticated target systems, due to the spontaneous formation of B-N bonds [9, 10, 11, 12, 13, 14]. Examples of the kinds of macromolecular systems incorporating B-N linkage achieved to date are shown in Figure 1.2. An important additional property of the Fc-B-bpy compounds is that they can exist in a number of stable oxidation states, allowing the additional control of their properties through electrochemical electron removal/addition.

In addition to the use of these monomeric units as functional pendant groups attached to macromolecular systems, due to the excited-state delocalisation between the Fc-donor and organic-acceptor groups, they are interesting candidates for in-chain polymer building blocks (e.g. Figure 1.1(d)). As an example, in the case of a mixed-valence polymer [15, 16] where adjacent Fc-units are present as Fc and oxidised Fc⁺ (i.e. with the valence electron involved in the MLCT removed from the latter), the optical MLCT excitation of the Fc groups will place an electron on an acceptor which may then relax into either of the resultant oxidised Fc⁺ groups, hence providing a means for optically-induced electron transport (i.e. photoconductivity).

In order to place the Fc-B-bpy compounds in perspective, we briefly identify related systems and some relevant applications in the following.

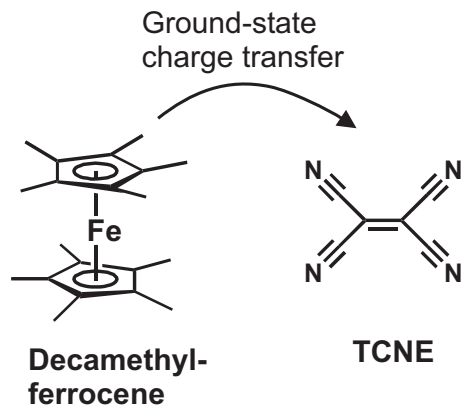


Figure 1.3.: Decamethylferrocene-donor/TCNE-acceptor charge transfer complexes ('Miller compounds'). Ground state electron transfer generates a cation/anion radical pair with ferromagnetic interaction between the two spins.

The use of ferrocene as a donor in *ground-state* charge-transfer complexes demonstrating interesting magnetic phenomena is well-established in the so-called 'Miller compounds' [17, 18, 19, 20], which are composed of an array of decamethylferrocene-donors (DMFc, where the -H atoms of the Cp⁻-rings are replaced with CH₃ groups) and organic electron acceptors, such as TCNE (Figure 1.3). In these compounds the relative energy of the DMFc-HOMO is actually lower than that of the TCNE-LUMO, such that in the solid state, through-space electron transfer occurs in the ground state to create a cationic radical DMFc⁺ and anionic TCNE⁻ pair. The interaction between these two radical spins is ferromagnetic, which, based on a McConnell model for the spin-interaction, occurs due to the fact that a small admixture of the lowest-lying excited states (involving further electron transfer from DMFc⁺ → TCNE⁻) is stabilised when the two spins are parallel [18]. In related systems where the lowest excited-states involve charge transfer back to the DMFc donor, antiferromagnetic interaction between the two spins results.

Whilst no ground-state CT is observed for the Fc-B-bpy compounds due to the fact that the donor-HOMO/acceptor-LUMO energy separation is large (and the CT must be induced by optical excitation), this example DMFc-TCNE system demonstrates that if a metastable charge-transfer state resulting from electron transfer from Fc to an attached organic unit can be prepared, there could be appreciable spin coupling between the two radicals. The ultrafast time-resolved measurements presented in this work indicate that the lifetime of the (optically-excited) MLCT state in the Fc-B-bpy monomers is < 1 ns (and depends critically on the flexibility of the derivative), indicating that no metastable CT state can be prepared by optical means with their existing design. Nevertheless, it is envisaged that the results presented here will aid in the design of modified Fc-B-bpy compounds with stronger MLCT absorption strength and longer lifetimes for the CT state following optical excitation.

Several applications of *excited-state* CT compounds incorporating Fc as a donor have been demonstrated. One active area of research involves Fc-donor organic-acceptor compounds where the two are bridged by a conjugated carbon bridge (such as the representative compound in Figure 1.4(a)) [21, 22, 23, 24, 25, 26, 27, 28, 29, 30], and an intense direct MLCT absorption band in the visible/near-infrared (vis-NIR) range is observed (we review these compounds in Section 2.2.2). The fact that the MLCT band occurs in the vis-NIR region is a highly desirable

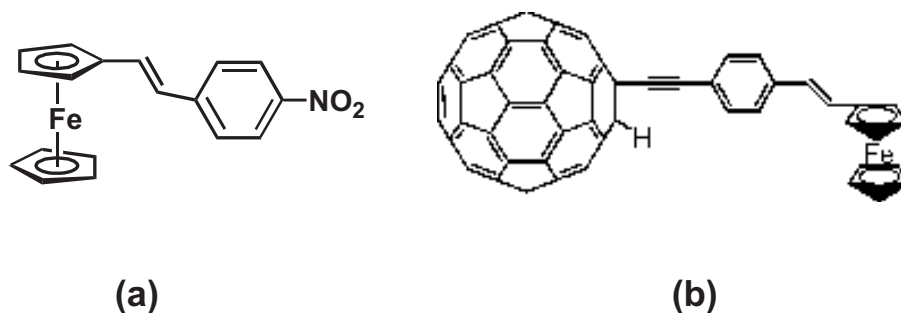


Figure 1.4.: Examples of established Fc-donor excited-state CT compounds. (a) Prototype MLCT compound with conjugated carbon bridge between Fc-donor and organic acceptor, for use as non-linear optical chromophore. (b) Fc-donor fullerene-acceptor compound where (UV) optical excitation of the fullerene results in long-lived CT from Fc to fullerene (following intersystem crossing)

attribute for the design of pendant groups for optically-driven CT into macromolecular systems, where excitation in the UV range is less desirable due to the likely presence of overlapping bands from the macromolecular system (which one would prefer not to perturb directly with the optical pumping of the CT groups). However, in accord with the intense absorption strength of these MLCT bands (which is in itself also highly desirable), the strong donor-acceptor coupling should also be accompanied by a relatively short-lived excited-state (although this is still an open question for these particular derivatives, with one of the only measurements of the MLCT excited-state lifetime being for a ferrocene derivative which showed complete ground state recovery on a time scale of <50 ps [31]).

An alternative mechanism for optically-induced CT is demonstrated by the Fc-donor fullerene-acceptor compounds [32, 33], such as that shown in Figure 1.4(b). In this case, the fullerene-*acceptor* is optically excited (in the UV), and following an intersystem crossing (i.e. a singlet-triplet transition), electron transfer from Fc to the fullerene occurs in the excited state to form a relatively long-lived excited state (with lifetimes approaching 40 ns [32]).

Despite the number of various Fc-donor CT systems reported, no such system appears to possess the required attributes for an ideal pendant group for charge injection into a polymer system, i.e. (i) strong MLCT absorption strength in the visible and (ii) a long-lived CT state (which must be achieved by the presence of an excited-state relaxation mechanism which inhibits the back-ET relaxation). Given the synthetic advantages of employing a B-N architecture, the possibility to achieve these targets with a design based on the Fc-B-bpy compounds is a particularly promising direction for study.

In conclusion, as an example of the possible application of optically-induced charge-injection in macromolecular systems, we mention the ‘polaronic ferromagnetic’ systems [17, 34, 35, 36]. These polymers are composed of spin-containing units connected by ferromagnetic-coupling bridges, such as the example poly(*m*-phenylenefuchson) (PMPF) shown in Figure 1.5. This system employs a simple meta-phenylene group as an efficient ferromagnetic coupler between fuchson radicals, which is based on the favourable alternation of transmitted spin-density between neighbouring C-atoms in the phenyl rings. We note that in the existing reports on these systems, the unpaired spins are generated *after* synthesis, either by chemical or electrochemical oxidation/reduction. However, by appropriate attach-

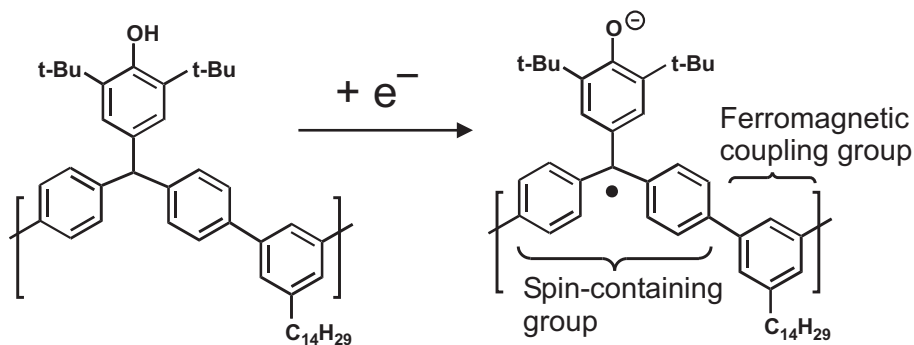


Figure 1.5.: Example of polaronic-ferromagnetic polymer, PMPF [36], with *m*-phenylene ferromagnetic coupling groups linking fuchsonone spin radicals. The radicals are prepared after synthesis by electrochemical reduction.

ment of an optical-CT chromophore to the fuchsonone group one could in principle optically control the presence of these spins, and the delocalised ferromagnetic interaction.

1.1. Outline

The structure of this dissertation is as follows:

Chapter 2. A short background theory of electronic structure in polyatomic molecules, radiative and non-radiative electronic transitions and intramolecular charge-transfer phenomena is presented. We also review the electronic structure and photophysical properties of Fc, and established Fc-donor compounds which exhibit strong MLCT transitions in the vis-NIR range, to lay down a benchmark for the MLCT absorption properties that can be achieved in Fc-donor compounds. The UV-vis absorption and electrochemical properties of the relevant organic acceptor groups are also presented, for comparison with the results of the Fc-B-bpy compounds in Chapter 4.

Chapter 3. Here we present the background theory and experimental details pertaining to the femtosecond time-resolved measurements. This includes a discussion of the optical pulse sources used in the transient absorption measurements, i.e. white-light continuum pulses and non-collinear optical parametric amplifiers (NOPA), and the design and instrumentation of the measurement system that was built up as part of the research work. A brief discussion of the time resolution and coherent artifacts that arise in the time-resolved signals is given.

Chapter 4. This chapter summarises all the non-time-resolved results for the Fc-B-bpy compounds. We present the UV-vis spectra of the Fc-B-bpy compounds in solution and the quantitative extraction and comparison of the absorption bands for a range of Fc-B-bpy derivatives. An analysis of the solvatochromic shift of the MLCT band using a modified model developed for cationic solutes is applied to the data for the single-B-bpy-acceptor compound (**[1A]Br**), which supports a MLCT transition involving almost complete displacement of a unit electronic charge from the Fc-donor to the B-bpy-acceptor. Measurements of certain derivatives in doped polymer films (including low-temperature measurements) and as a single crystal are presented, which demonstrate the effect of a solid-state environment on the MLCT absorption band.

The electrochemical data for a selected set of derivatives is given, including a correlation analysis of the Fc-donor-oxidation and B-bpy-acceptor-reduction poten-

tials vs the MLCT transition energy, which supports the MLCT assignment and provides an estimate for the Stokes shift associated with the MLCT transition. We also present the relevant UV-vis spectroelectrochemistry data which is compared to the excited-state transient spectra in Chapter 5.

The final section of this chapter presents the calculated density-functional theory (DFT) results for a representative prototype Fc-B-bpy compound, $[1]^+(\text{H})$, including (i) the molecular orbitals and energies for both cationic and dicationic oxidation states, (ii) a preliminary time-dependent-DFT (TD-DFT) calculation for the lowest optical excitation energies, (iii) the ground-state potential and molecular orbitals for an active reaction coordinate describing the relative conformation of the Fc-donor and B-bpy-acceptor for $[1]^+(\text{H})$, and (iv) the electrostatic potential of the cationic oxidation state. These results provide support for the MLCT band assignment, and are used wherever applicable in comparison with the experimental results.

Chapter 5. Here the time-resolved transient-absorption results in the visible range following direct MLCT excitation for three related Fc-B-bpy derivatives in solution are presented. The three derivatives are chosen to compare the effects of (i) a relatively unhindered rotation about the B-C bridging bonds connecting Fc-donor and B-bpy-acceptor, and (ii) the presence of an -O- bridging bond between multiple acceptors. The excited-state transient-absorption spectra are compared to analogous spectral changes observed upon electrochemical donor-oxidation and acceptor-reduction which aids in the assignment of the various bands in the excited-state spectra and provides further support for the MLCT band assignment. A comparative analysis of the decay of the transient absorption kinetics for the three derivatives is performed, which suggests that for the two derivatives where large-scale excited-states conformational changes can occur, a significant fraction of the MLCT excited state can relax on a time scale of 10s of picoseconds, whilst in the presence of a constraining bridge between acceptors where this motion is suppressed, all ground-state recovery proceeds on a far longer time scale \rightarrow 1000 ps. Schematic models involving multiple reaction coordinates are proposed to account for the observed dynamics for each derivative, with the conclusion that for the two derivatives with flexible donor-acceptor conformation, an efficient non-radiative coupling to the ground state is encountered during excited-state relaxation, which, considering the number of degrees of freedom in these medium-sized polyatomics, is tentatively assigned to the involvement of a conical intersection in each case.

Chapter 6. We conclude with a summary of the key results and suggestions for future work on related Fc-B-bpy systems.

1.2. Publications

The publications directly related to the research work presented in this dissertation are as follows:

1. M. Thomson, H. G. Roskos and M. Wagner, *On the way to ‘optical doping’ of electronically low-dimensional polymer systems with strong charge and spin correlations*, Appl. Phys. A **78** 477-481 (2004)
2. M. Thomson, M. Novosel, H. G. Roskos, T. Müller, M. Scheibitz, M. Wagner, F. Fabrizi de Biani and P. Zanello, *Electronic structure, photophysics, and relaxation dynamics of charge transfer excited states in boron-nitrogen bridged ferrocene-donor organic-acceptor compounds*, J. Phys. Chem. A **78** 3281-3291 (2004)

As part of the broader research work on opto-electronics, significant contributions were made to the following publications:

1. R. Leonhardt, K. J. Siebert, H. Quast, T. Löffler, M. Thomson, and H. G. Roskos, *Continuous-Wave THz Imaging with Photoconductive LT-GaAs Antennae* Proceedings of the 3rd Symposium On Non-Stoichiometric III-V Compounds pp. 25-30, (2001).
2. M. Weckenbrock, M. Hattass, A. Czasch, O. Jagutzki, L. Schmidt, T. Weber, H. Roskos, T. Löffler, M. Thomson, and R. Dörner *Experimental evidence for electron repulsion in multiphoton double ionization* Journal of Physics B **34**, L449-55 (2001).
3. T. Löffler, S. Eden, M. Thomson, and H. G. Roskos, *THz generation by third-order non-linearities in air and air-plasmas* Ultrafast Phenomena XIII, Springer Series in Chemical Physics, Vol. 71, pp. 274, Springer Verlag, Berlin (2002).
4. K. J. Siebert, H. Quast, R. Leonhardt, T. Löffler, M. Thomson, T. Bauer, H. G. Roskos, and S. Czasch, *All-optoelectronic CW THz-imaging* OSA Trends in Optics and Photonics (TOPS), CLEO 2002, Postconference Edition, CFD1 p. 633 (2002).
5. S. Eden, T. Löffler, M. Thomson, and H. G. Roskos, *Optoelectronic THz Generation by Third-order Non-linearities in Air and Air Plasmas* OSA Trends in Optics and Photonics (TOPS), QELS 2002, Postconference Edition, QWA23 p. 144 (2002).
6. K. J. Siebert, H. Quast, R. Leonhardt, T. Löffler, M. Thomson, T. Bauer, H. G. Roskos, and S. Czasch, *Continuous-wave all-optoelectronic terahertz imaging* Appl. Phys. Lett. **80**, 3003 (2002).
7. K. Siebert, T. Löffler, H. Quast, M. Thomson, T. Bauer, R. Leonhardt, S. Czasch, and H. G. Roskos, *All-optoelectronic CW THz imaging for biomedical applications* Phys. Med. Bio. **47**(21), 3743 (2002).
8. K. J. Siebert, T. Löffler, H. Quast, R. Leonhardt, M. Thomson, T. Bauer, H. G. Roskos, and S. Czasch, *All-optoelectronic CW THz imaging for tumor recognition* Ultrafast Phenomena XIII, Springer Series in Chemical Physics, Vol. 71, pp. 280, Springer Verlag, Berlin (2002).
9. N. Hasegawa, T. Löffler, M. Thomson, and H. G. Roskos, *Remote Identification of Protrusions and Dents on Surfaces by Terahertz Reflectometry with Spatial Beam Filtering and Out-of-Focus Detection* Appl. Phys. Lett. **83**, 3996 (2003).
10. T. Löffler, T. Hahn, M. Thomson, F. Jacob, and H. G. Roskos, *Large-Area Electro-optic ZnTe Terahertz Emitters*, to be submitted to Optics Express.
11. T. Löffler, M. Krefß, T. Hahn, M. Thomson, and H. G. Roskos, *Terahertz emitters for amplifier laser systems*, to be submitted to Semiconductor Science and Technology.
12. T. Löffler, M. Krefß, M. Thomson and H. G. Roskos, *Efficient Terahertz Pulse Generation in Laser-Induced Gas Plasmas*, accepted for publication in Acta Physica Polonica (A).

-
13. M. Kreß, T. Löffler, S. Eden, M. Thomson and H. G. Roskos, *Terahertz-pulse generation by photoionisation of air with laser pulses composed of both fundamental and second-harmonic wave*, Optics Letters, **29** 1120 (2004).

1.3. Zusammenfassung

Im Rahmen dieser Dissertation wurden die Photophysik und die elektronische Struktur einer Klasse neuartiger Donator-Akzeptor-Ladungstransfer-Komplexe untersucht. Im Wesentlichen bestehen diese Verbindungen aus einem Ferrocen-Donator (Fc) und organischen Akzeptoren, die über B-N-Bindungen verbrückt sind. Abbildung 1.6(a) zeigt einen Prototyp dieser Art von Komplexverbindungen. Eine spezielle Verbindung mit einem einzelnen auf Bipyridin basierenden Akzeptor (2,2'-bipyridylboroniumkation, B-bpy) ist in Abbildung 1.6(b) dargestellt⁴.

Zentrales Ziel der Untersuchungen war es, die Annahme zu bestätigen, dass die beobachtete Absorptionsbande dieser kationischen Komplexverbindungen, die im Weiteren als Fc-B-bpy-Verbindungen bezeichnet werden, einem Ladungstransfer von Metall zu Ligand (engl. Abkürzung: MLCT) zugeordnet werden kann, gleich bedeutend mit einem optisch induzierten Übergang eines in der Fc-Einheit lokalisierten Elektrons in ein unbesetztes Orbital der Akzeptor-Gruppe.

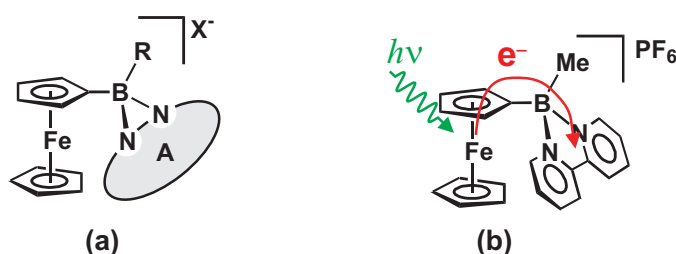


Abbildung 1.6.: (a) Schema einer metallorganischen Verbindung mit B-N-Brücke zwischen Donator und Akzeptor. (b) Spezifisches Beispiel **[1A]PF₆** mit einem einfachen B-bpy-Akzeptor und dem schematisch dargestellten optisch induzierten Ladungstransfer.

Die vorliegende Arbeit wurde im Rahmen eines größeren Projektes⁵ durchgeführt, dessen Ziel es unter anderem ist, niedrigdimensionale makromolekulare metallorganische Verbindungen, z.B. Polymere, herzustellen und zu untersuchen. Der hier untersuchte optisch induzierte Ladungstransfer soll dabei den Ladungsüberschuss regeln, der in delokalisierten elektronischen Kanälen auftritt, in denen starke Spin- und Ladungs-Korrelationen existieren. Dabei würden die Fc-B-bpy-Monomere entweder (a) an das Polymerrückgrat angehängt, um dort Ladungsträger zu injizieren, oder (b) direkt in das Polymerrückgrat integriert. Eine B-N-Architektur erscheint dabei besonders vielversprechend, da sich B-N-Bindungen bei dieser Art makromolekularer Systeme spontan ausbilden.

Die Brücke zwischen Fc-Donator und B-bpy-Akzeptor enthält ein gesättigtes vierfach-koordiniertes B-Atom. Daher könnte man annehmen, dass nur eine vernachlässigbare elektronische Delokalisierung über diese Brücke erfolgt und deshalb nur eine schwache elektronische Kopplung zwischen Donator und Akzeptor existiert. Aus diesem Grund war es unklar, ob die beobachtete Absorptionsbande, die z.B. für **[1A]PF₆** ihr Maximum bei 500 nm hat, von einem MLCT-Übergang oder von einer im Fc-Donator lokalisierten Anregung herrührt. Im zweiten Fall kommen

⁴Die Fc-B-bpy-Verbindungen wurden von unseren Hauptkollaborateuren, AG Wagner, Anorganische Chemie, J. W. Goethe-Universität, Frankfurt am Main, hergestellt.

⁵Die Untersuchung von optisch kontrollierbaren Spin- und Ladungs-Korrelationen in niedrigdimensionalen metallorganischen Systemen ist eines der Hauptarbeitsgebiete der Arbeitsgruppe Roskos, J.W. Goethe Universität, Frankfurt am Main, als Teilprojekt eines größeren interdisziplinären Forschergruppe-Projekts (412) 'Spin- und Ladungskorrelationen in niedrigdimensionalen metallorganischen Festkörpern' der Deutschen Forschungsgemeinschaft (DFG).

eine durch den B-bpy-Akzeptor induzierte Verschiebung in Richtung des sichtbaren Spektralbereichs oder nur eine schwache Delokalisierung in Richtung des Akzeptors als Ursachen in Frage.

Während eine frühere Arbeit Hinweise auf eine elektronische Wechselwirkung zwischen Fc-Donator und B-bpy-Akzeptor gab, blieb die Zuordnung der MLCT-Bande unsicher. Des Weiteren war eine detaillierte Beschreibung des optischen Übergangs, speziell des Grades des Ladungstransfers, nicht verfügbar.

Die vorliegende Arbeit analysiert eine Vielzahl verschiedener verwandter Fc-B-bpy-Derivate. Gegliedert ist die Arbeit in (i) Untersuchungen der Absorptionsspektren vom UV bis zum nahen Infraroten Spektralbereich (250-1000 nm) an Lösungen, dotierten Polymer-Dünnschichten und Einkristallen, (ii) elektrochemische Messungen an Lösungen⁶, (iii) quantenchemische Berechnungen⁷ und (iv) zeitaufgelöste optische Spektroskopie des angeregten Zustands auf der Pikosekunden-Zeitskala.

Den Großteil der experimentellen Arbeiten im Rahmen dieser Dissertation stellen (i) die Präparation und Charakterisierung der verschiedenen molekularen Proben für die spektroskopischen Messungen und (ii) die Entwicklung des optischen Spektroskopie-Systems mit breitbandigen Femtosekunden-Pulsen sowie den entsprechenden Detektionsmethoden dar.

Die Ergebnisse dieser Arbeit deuten sehr stark auf die Existenz des MLCT-Übergangs, entsprechend eines fast vollständigen Übergangs eines Fc-Donator-Elektrons zum B-bpy-Akzeptor in den angeregten Zustand hin. Zu diesem Schluss führen die folgenden zentralen Resultate:

(a) Im Rahmen dieser Arbeit wurde die Abhängigkeit der MLCT-Übergangsenergie von der Dipolarität der Lösung experimentell bestimmt und mit einem Modell, das für diese Art von kationischen Verbindungen weiterentwickelt wurde, verglichen. Diese Analyse beinhaltet eine Abschätzung der Änderung des effektiven Dipolmoments der Verbindung bei optischer Anregung des MLCT-Übergangs, woraus auf die effektive Verschiebung der Elektronendichte geschlossen werden kann. Im Fall einer typischen Fc-B-bpy-Verbindung mit einfachem Akzeptor beträgt die effektive Verschiebung $\sim 70\%$ des Donator-Akzeptor-Abstandes.

(b) Die Redox-Potentiale für die elektrochemische Oxidation des Fc-Donators und für die Reduktion des B-bpy-Akzeptors werden mit den entsprechenden Maxima der MLCT-Bande für verschiedene Fc-B-bpy-Derivate in Lösung verglichen. Die Differenz beider Redoxpotentiale korreliert mit der beobachteten MLCT-Übergangsenergie, wobei die Korrelationsfunktion eine lineare Steigung von 0.99 aufweist, entsprechend des erwarteten fast kompletten Ladungsübergangs zwischen Donator und Akzeptor, die nur schwach gekoppelt sind. Mit anderen Worten korreliert die Photonenenergie, die zur Präparation des angeregten Zustands benötigt wird, mit der Energiedifferenz, die durch das Entfernen eines Elektrons vom Donator und Hinzufügen des entsprechenden Elektrons zum Akzeptor hervorgerufen wird.

(c) Es werden die Ergebnisse theoretischer Grundzustandsberechnungen für eine typische Fc-B-bpy-Verbindung in der Gasphase vorgestellt. Dabei werden Methoden aus der Dichte-Funktionaltheorie (DFT) angewendet. Daraus folgend befinden sich die höchsten besetzten Molekülorbitale (engl. Abkürzung: HOMOs) im Fc-Donator, während die tiefsten unbesetzten Zustände (engl. Abkürzung: LUMOs) im B-bpy-Akzeptor lokalisiert sind.

⁶Die elektrochemischen Messungen wurden im Rahmen einer Kollaboration in der AG Zanello (Department of Chemistry, University of Siena, Siena, Italien) durchgeführt.

⁷Die quantenchemischen Ergebnisse wurden von Dr. Thomas Müller, Anorganische Chemie, J. W. Goethe-Universität, Frankfurt am Main, berechnet.

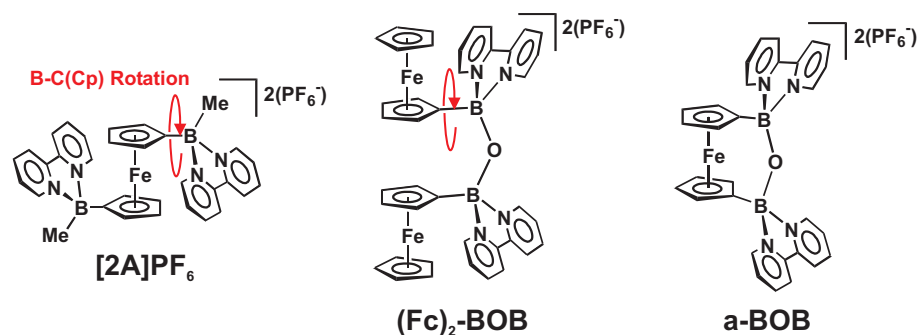


Abbildung 1.7.: Fc-B-bpy-Verbindungen, an denen zeitaufgelöste optische Absorptionsmessungen auf der pikosekunden Zeitskala durchgeführt wurden.

(d) Es wurden transiente Absorptionsspektren bestimmter Fc-B-bpy-Derivate in Lösung nach gepulster Anregung der MLCT-Bande (bei 500 nm) über einen Zeitbereich von 0,1-1000 ps und einen Wellenlängenbereich von 460-760 nm aufgenommen. Diese differentiellen Spektren besitzen Absorptionsbanden des angeregten Zustands (engl. Abkürzung: ESA), die qualitativ mit der Gleichgewichts-Absorptionsänderung nach elektrochemischer Oxidation des Fc-Donators und Reduktion des B-bpy-Akzeptors übereinstimmen. Dieses Ergebnis unterstützt die Aussage, dass der MLCT-angeregte Zustand eine ähnliche elektronische Natur hat wie ein oxidiertes Fc-Donator und ein reduzierter B-bpy-Akzeptor.

Zusätzlich wurden zahlreiche vergleichende Untersuchungen durchgeführt, die weitere wichtige Details der elektronischen Struktur der Fc-B-bpy-Verbindungen zeigen. Ein wesentliches Ergebnis ergibt sich aus zeitaufgelösten Absorptionsmessungen auf der Pikosekunden-Zeitskala, aus denen Lebensdauern von angeregten MLCT-Zuständen für verschiedene Fc-B-bpy-Derivate bestimmt werden. Dabei werden drei Derivate ($[2A](PF_6)_2$, $(Fc)_2BOB$ und $a-BOB$, Abbildung 1.7) verglichen. Alle diese Verbindungen besitzen zwei B-bpy Akzeptoren, wobei $[2A](PF_6)_2$ und $a-BOB$ einen einzelnen Fc-Donator besitzen und $(Fc)_2BOB$ zwei Fc-Donatoren besitzt.

Bei den beiden Derivaten $a-BOB$ und $(Fc)_2BOB$ existiert eine Sauerstoffbrückenbindung zwischen den B-bpy-Akzeptoren, welche die elektronische Kopplung zwischen den Akzeptoren im Vergleich zu $[2A](PF_6)_2$ erhöht. Ferner kann für $[2A](PF_6)_2$ und $(Fc)_2BOB$ durch flexible Bindungen die relative Konstellation von Donatoren und Akzeptoren relativ großen Änderungen unterliegen. Eine flexible Bindung erfolgt beispielsweise über B-C(Cp)-Bindungen (siehe Abbildung 1.7), bei denen Bindungsrotationen mit einer relativ kleinen Energiebarriere erzeugt werden können, wie man aus den Grundzustandseigenschaften folgern kann. Bei $a-BOB$ erzeugt die B-O-B-Brücke eine deutlichere Einschränkung der möglichen Geometrien. Dies ermöglicht bei einem Vergleich der drei Derivate die Untersuchung der beiden folgenden Effekte: (1) der elektronischen Kopplung der Sauerstoffbrücke der B-bpy-Akzeptoren und (2) den Einfluss ungehinderter Änderungen der Konstellation im angeregten Zustand. Beide Effekte könnten prinzipiell auf die Relaxations-Eigenschaften des angeregten MLCT-Zustands Einfluss haben, wie z.B. auf die Relaxation in den Grundzustand, bei der ein Elektronenrücktransfer (engl. Abkürzung: b-ET) vom B-bpy-Akzeptor zum Fc-Donator stattfindet.

Aus den zeitaufgelösten Absorptionsmessungen ergibt sich für $(Fc)_2BOB$, unter der Annahme einer einfachexponentiellen vollständigen Relaxation in den Grundzustand eine Zeitkonstante von $\tau \sim 45$ ps, ohne einen Hinweis auf die Existenz eines

Zwischenzustands. Für **a-BOB** findet diese Relaxation auf einer Zeitskala von $\tau \sim 780$ ps statt. Nach unserer Interpretation der Daten des **[2A](PF₆)₂**-Derivats, findet bei diesem die Relaxation auf zwei bestimmten Wegen statt, mit Zeitkonstanten von $\tau \sim 18$ ps und $\tau \sim 910$ ps und nahezu gleicher Häufigkeit. Diese Unterschiede deuten darauf hin, dass die für die b-ET-Relaxation geltenden Zeitskalen hauptsächlich in der Flexibilität der Konformation der Derivate begründet sind; im Gegensatz zum Einfluss der Kopplung über die B-O-B-Brücke auf die angeregten elektronischen Zustände.

Die schnellen Relaxationsprozesse für **[2A](PF₆)₂** und **(Fc)₂BOB** suggerieren, dass für das Wellenpaket des angeregten Zustands ein strahlungsfreier Relaxationskanal in den Grundzustand wahrscheinlich ist. Aufgrund der Komplexität der Moleküle und der großen Anzahl an möglichen Freiheitsgraden gibt es bislang keine eindeutige Erklärung für diesen Relaxationskanal. Ein vorläufiger Ansatz führt diesen Relaxationskanal auf eine konische Schnittfläche zwischen den Potentialflächen des Grund- und des angeregten Zustands mit mehreren aktiven „Reaktionskoordinaten“ zurück. Ein sehr wahrscheinlicher Kandidat für einen dieser Reaktionskoordinaten ist die B-C(Cp)-Bindungsrotation, da diese Bewegung im Fall von **a-BOB** stark unterdrückt ist. Dieser Erklärungsversuch hat erheblichen Einfluss auf das zukünftige Design derartiger Derivate mit verlängerten Lebensdauern der angeregten MLCT-Zustände. Das heißt, um strahlungsfreie Übergänge in den Grundzustand zu verhindern, muss eine starre Architektur zwischen den Fc-Donatoren und den B-bpy-Akzeptoren erreicht werden.

Absorptionsmessung im UV und im sichtbaren Spektralbereich an Dünnschichten (bei $T=20$ K und $T=300$ K) und Einkristallen zeigen nur eine geringe Beeinflussung der MLCT-Bande durch die Festkörperumgebung und die Temperatur. In beiden Fällen tritt eine Blauverschiebung und eine leichte zusätzliche Bandenverbreiterung auf. Dies bedeutet, dass die Fc-B-bpy-Verbindungen ihre potenzielle Fähigkeit zum optisch induzierten Ladungstransfer in Festkörperumgebung aufrecht erhalten, was für mögliche zukünftige Anwendungen von entscheidender Bedeutung ist.

Ein Vergleich der MLCT-Banden verschiedener verwandter Fc-B-bpy-Verbindungen in Lösung mit mehrfachen B-bpy-Akzeptoren (mit der zusätzlichen Option zwischen den Akzeptoren B-O-B- und B-N-B-Brücken einzufügen) zeigt ein kompliziertes Verhalten der Position und Breite der MLCT-Bande. Durch die Annahme eines einfachen Eielektronenmodells für die Ladungstransferzustände, die für verschiedene Molekülsymmetrien und Akzeptor-Kopplungen erwartet werden, und bei Berücksichtigung des Einflusses der Lösung und der Ergebnisse der elektrochemischen Messungen, wurden die Rahmenbedingungen für ein besseres Verständnis des Verhaltens der MLCT-Bande geschaffen. Die Ergebnisse untermauern die Annahme, dass zwei nahezu entartete MLCT-Übergänge für Derivate nichtlinearer Geometrie mit akzeptor-kopplungsabhängiger Energieaufspaltung existieren, die sich jedoch unter der großen Bandenbreite, infolge der Franck-Condon-Verteilung und der Konformationsverbreiterung der flexiblen Verbindungen, verbirgt.

Die MLCT-Bande eines Derivats, bei dem der B-bpy-Akzeptor durch ein delokalisiertes Drei-Ring-System (‘B-dpp’, basierend auf der organischen Verbindung 2,5-bis(2-pyridyl)pyrazin) ersetzt wurde, zeigt eine deutliche Rotverschiebung, mit einem Bandenmaximum bei 600 nm. Dies unterstützt die Zuordnung der MLCT-Banden, da man aus elektrochemischen Messungen auf eine niedrigere LUMO-Energie dieses B-dpp-Akzeptors schließen kann, und zeigt die Möglichkeit auf, die Bandenenergie durch verschiedene Akzeptoren zu variieren.

Die Ergebnisse der DFT und zeitabhängigen-DFT (engl. Abkürzung: TD-DFT) in der Gasphase für eine repräsentative Fc-B-bpy-Verbindung mit einem einzelnen B-bpy-Akzeptor sind unterteilt in, (i) die Grenzorbitale und Energien sowohl

der kationischen als auch der oxidierten dikationischen Form, (ii) eine vorläufige TD-DFT-Berechnung der Anregungsenergien und Oszillatorenstärken, (iii) einen Vergleich des Grundzustandspotentialverlaufs in Abhängigkeit eines Parameters, der die B-C(Cp)- Bindungsrotation repräsentiert, und (iv) das elektrostatische Potential des kationischen Grundzustands.

Wie bereits erwähnt, legen die berechneten Molekülorbitale des kationischen Oxidationszustands für den MLCT-Übergang HOMOs und LUMOs nahe, die hauptsächlich im Fc-Donator bzw. hauptsächlich im Akzeptor lokalisiert sind. Für den dikationischen Oxidationszustand existieren HOMOs und LUMOs, die sowohl über den Fc-Donator als auch über den B-bpy-Akzeptor delokalisiert sind. In diesem Fall kann eine deutlich größere elektronische Donator-Akzeptor-Kopplung für den oxidierten Zustand angenommen werden. Dies hat Einfluss auf zukünftige makromolekulare Systeme, die mehrfache Fc-B-bpy-Einheiten enthalten und mit gemischten Valenzsystemen, d.h. einer Kombination neutraler und oxidierter Fc-Zentren, hergestellt werden.

Ein wichtiges Ergebnis in Bezug auf die Anwendung von TD-DFT-Berechnungsmethoden zur Vorhersage der Übergangsenergien und -intensitäten konnte durch den Vergleich mit dem Experiment erzielt werden. Es zeigt sich, dass TD-DFT-Methoden angewandt auf derartige Ladungstransferverbindungen nur qualitative Ergebnisse liefern können, da diese systematisch zu niedrige Übergangsenergien (Fehler bis zu ~ 1 eV) und -intensitäten liefern.

Die Berechnung der Grundzustandspotentialkurve für die Rotation um die B-C(Cp)-Bindung zwischen Donator und Akzeptor besitzt in der Gasphase bei Raumtemperatur zwei symmetrische Minima. Auf einem dieser Minima ist eine quasiklassische Schwingung mit einer relativ großen Amplitude ($\sim 30^\circ$) und einer charakteristischen Frequenz von ~ 320 GHz zentriert. Aus diesem Ergebnis kann die Größenordnung der MLCT-Banden-Verbreiterung abgeschätzt werden, die sich unter Verwendung der HOMO-LUMO-Energiedifferenz aus Orientierungsschwankungen der B-C(Cp)-Bindung ergibt. Abschließend sei noch erwähnt, dass die elektrostatischen Potentialflächen darauf hindeuten, dass die positive Ladung des Kations im B-bpy-Akzeptor delokalisiert und damit das Grundzustandsdipolmodell für Lösungen anwendbar ist.

Wir gehen davon aus, dass diese ausführliche quantitative Untersuchung der elektronischen und spektroskopischen Eigenschaften der Fc-B-bpy-Verbindungen bedeutenden Einfluss auf das zukünftige Design verwandter makromolekularer Systeme hat. In derzeitigen Arbeiten werden bereits oligomere Derivate dieser Monomere untersucht. Des Weiteren wird an neuen Systemen mit dreifach koordinierten B-Atomen zwischen Fc-Donatoren und Polymerrückgrat geforscht. Erste Untersuchungen an verwandten Polymeren ohne Fc-donatoren suggerieren, dass bei stärkerer Delokalisierung eine stärkere elektronische Kopplung zwischen Fc-Donator und organischen Akzeptor-Zuständen im Polymerrückgrat bestehen könnte.

2. Background molecular theory and results

2.1. Basic electronic and photophysics theory of polyatomic molecules

2.1.1. Molecular wavefunctions and radiative transitions

The description of the electronic states $\Psi_n(\mathbf{r}, \mathbf{Q})$ in polyatomic molecules with nuclear coordinates \mathbf{Q} ¹ and electronic coordinates \mathbf{r} can be described within the Born-Oppenheimer approximation (i.e. neglecting coupling between electronic states) by the adiabatic product wavefunctions,

$$\Psi_{n,M}(\mathbf{r}, \mathbf{Q}) = \chi_{n,M}(\mathbf{Q}) \psi_n(\mathbf{r}; \mathbf{Q}),$$

where $\chi_{n,M}(\mathbf{Q})$ and $\psi_n(\mathbf{r}; \mathbf{Q})$ describe the nuclear and electronic wavefunctions, respectively² [37, 38]. With this factorisation, the electronic wavefunctions $\psi_n(\mathbf{r}; \mathbf{Q})$ are eigenfunctions of the molecular electronic Hamiltonian H_{el} (i.e. the total molecular Hamiltonian excluding the kinetic and potential energy terms involving only nuclei) for fixed nuclear positions \mathbf{Q} , with a resulting energy $E_n^{\text{el}}(\mathbf{Q})$. In turn, the nuclear (vibrational) wavefunctions $\chi_{n,M}(\mathbf{Q})$ are then taken as eigenfunctions of a Hamiltonian composed of the nuclear kinetic energy, and an effective nuclear potential energy,

$$U_n(\mathbf{Q}) = E_n^{\text{el}}(\mathbf{Q}) + V_{\text{nuc-nuc}}(\mathbf{Q}), \quad (2.1)$$

where $V_{\text{nuc-nuc}}(\mathbf{Q})$ is the electrostatic potential between the nuclei. Examples of the potential energy curves and vibrational wavefunctions are shown in Figure 2.1(a).

The transition dipole moment for the radiative transition from the ground electronic-vibrational state $\Psi_0 = \chi_{0,0}\psi_0$ to the excited electronic-vibrational state $\Psi_{n,M} = \chi_{n,M}\psi_n$ is given by [37],

$$\boldsymbol{\mu}_{0,0 \rightarrow n,M} = \langle \psi_n | \sum \mathbf{r} | \psi_0 \rangle \langle \chi_{n,M} | \chi_{0,0} \rangle, \quad (2.2)$$

where $\mathbf{M}_{n \rightarrow 0} = \langle \psi_n | \sum \mathbf{r} | \psi_0 \rangle$ is the electronic transition dipole moment and $\langle \chi_{n,M} | \chi_{0,0} \rangle$ is the Franck-Condon factor.

Given that the absorption strength for each transition is given by $f \propto |\boldsymbol{\mu}_{0,0 \rightarrow n,M}|^2$, for a finite absorption strength we require that both the electronic transition dipole moment and Franck-Condon factor are finite. For molecules possessing well-defined symmetry, a finite electronic dipole moment requires that the two electronic states are of opposite parity, whilst in general, (and more important for the charge-transfer electronic transitions under study here) the two electronic wavefunctions must also possess *extensive* spatial overlap for an appreciable absorption strength (i.e. they must extend into a common spatial region). Moreover, the Franck-Condon factor will only be appreciable for transitions between vibrational wavefunctions which possess finite amplitude in the same region of nuclear coordinate space – a requirement which leads to the Franck-Condon principle of a vertical transition, which is analogous to requiring no displacement of the nuclei

¹Note that the nuclear coordinates \mathbf{Q} are taken as any linear basis of the nuclear positions (weighted by the appropriate inertia), which are often taken as the normal modes of vibration for the molecule.

²Note that here a non-relativistic Hamiltonian is assumed, and the spin-dependence of the wavefunctions is neglected.

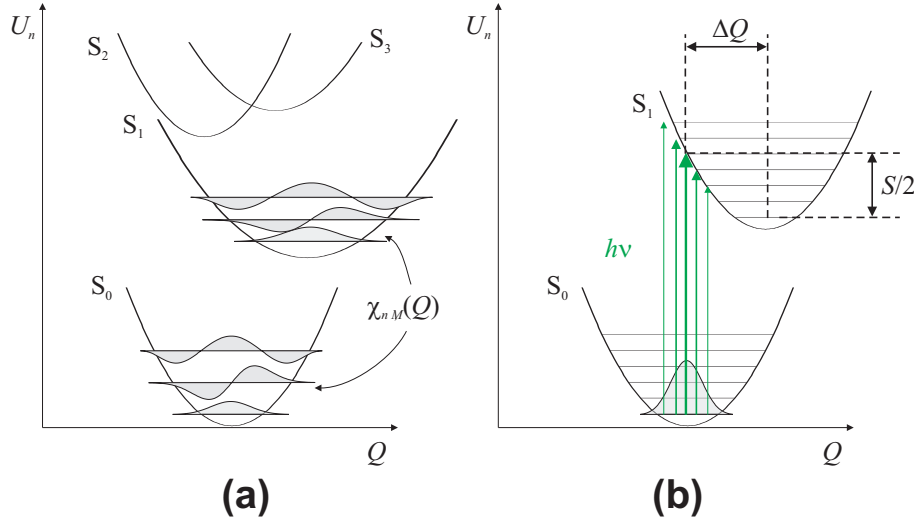


Figure 2.1.: (a) Schematic of the lowest energy singlet electronic states, S_n and corresponding vibrational energy levels vs a single reaction coordinate. (b) Franck-Condon radiative transition between two electronic states, indicating the Stokes shift energy S and displacement of the nuclear coordinate ΔQ .

during the absorption process (see Figure 2.1(b)). This implies that as the equilibrium positions of the two potential energy surfaces are displaced, the transition strength will be maximal for transitions to higher excited vibrational states in the excited electronic state, and consequently the required photon energy for the transition increases, and the transition results in an initial excited state with increasing excess vibrational energy. As the Franck-Condon factor is appreciable for a range of vibrational states $|\chi_{n,M}\rangle$, we expect a finite absorption bandwidth composed of transitions to each vibrational state (i.e. the Franck-Condon bandwidth), as indicated in Figure 2.1(b). As the displacement between the two potential energy surfaces increases, the magnitude of any single Franck-Condon factor decreases due to the decreased overlap between the nuclear wavefunctions, but the bandwidth increases due to the weaker dependence of the Franck-Condon factor $\langle \chi_{n,M} | \chi_{0,0} \rangle$ on M . If we assume parabolic potentials $U_n(\mathbf{Q})$ in the ground- and excited-electronic states (with the same vibrational frequency ω_{vib}) then the absorption intensity for each vibrational transition can be written as (for zero temperature)³ [38],

$$|\langle \chi_M | \chi_0 \rangle|^2 = e^{-(\Delta g)^2} \frac{(\Delta g^2)^M}{M!},$$

where the dimensionless potential-energy-curve shift is given by $\Delta g = \left(\sqrt{\omega_{\text{vib}}/2\hbar} \right) \Delta Q$. Hence the envelope of the absorption band (neglecting other sources of broadening) conforms to a Poisson distribution with mean (Δg^2) . For large displacements, this band shape $|\langle \chi_M | \chi_0 \rangle|^2$ will tend to a Gaussian with a variance in photon energy $\sigma = \omega_{\text{vib}} \sqrt{\langle M^2 \rangle} = \omega_{\text{vib}} \Delta g = \left(\sqrt{\omega_{\text{vib}}^3/2\hbar} \right) \Delta Q$ and mean (maximum) band position $\hbar\omega_{\text{max}} = \hbar(\omega_0 + \omega_{\text{vib}}\Delta g^2)$, where $\hbar\omega_0$ is the energy

³Note that more general analytic expressions for the Franck-Condon factors between harmonic potential surfaces for finite temperature and multiple vibrational coordinates (not necessarily with the same frequency) can be derived, but this expression reflects the key qualitative aspects of the effect of displacement between the two potential energy curves.)

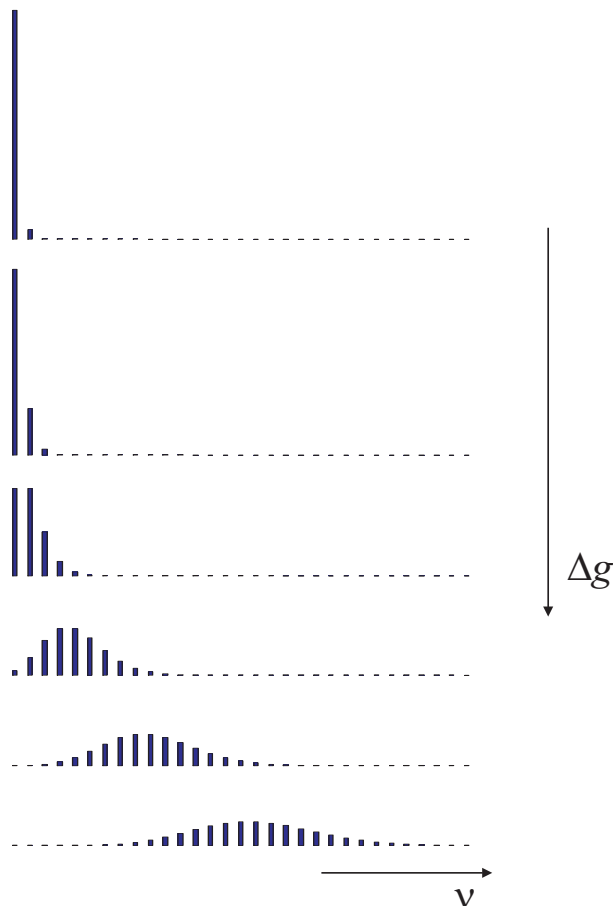


Figure 2.2.: Example of the absorption spectral envelope (Franck-Condon manifold) $|\langle\chi_M|\chi_0\rangle|^2$ vs displacement of two one-dimensional potential energy curves (with equal vibrational quanta in each electronic state.)

separation of the potential energy curve minima of the two electronic states (i.e. the spectroscopic origin of the electronic transition). An example of the expected absorption envelope vs increasing displacement Δg is shown in Figure 2.2. We note that the integral of the absorption band is independent of the displacement, i.e. the peak absorption strength falls away with increasing band broadening. In the case of several displaced vibrational coordinates, the resulting absorption band envelope is a convolution of the single-coordinate band envelopes. When the solute is placed in a condensed-phase environment, additional broadening mechanisms may wash out any detectable vibrational structure, resulting in a continuous Gaussian bandshape (for large displacements).

The expression for the transition dipole moment above (Eq. 2.2) made use of the Condon approximation (i.e. assuming that the electronic transition dipole moment $\mathbf{M}_{n\rightarrow 0} = \langle\psi_n|\sum \mathbf{r}|\psi_0\rangle$ is independent of the instantaneous nuclear coordinates [38]). However, given that molecular vibrations induce a finite distortion of the electronic wavefunctions, this expression should be generalised to include the resulting ‘vibronic mixing’ of the excited electronic wavefunctions. The effect of this mixing becomes important whenever $\mathbf{M}_{n\rightarrow 0}$ vanishes due to symmetry (parity) of the electronic states 0 and n . From perturbation theory, the next most significant term contributing to the radiative transition $\mu'_{0,0\rightarrow n,M}$ between the two electronic-vibrational states involves the vibronic-mixing with other excited electronic states,

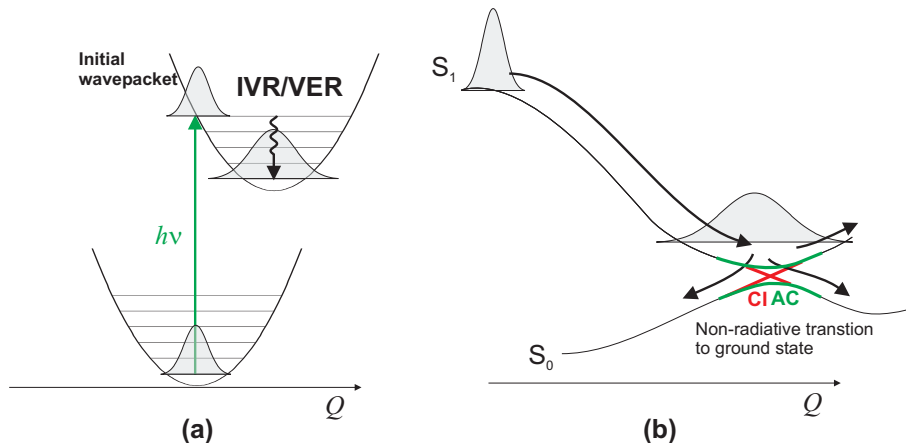


Figure 2.3.: (a) Schematic of initial optical excitation and vibrational relaxation (due to intramolecular vibrational redistribution (IVR) and vibrational energy relaxation (VER) through coupling with the external environment). (b) Propagation of wavepacket on a potential energy gradient. Also included is an encounter with the ground-state potential surface, where either an avoided crossing (AC) or conical intersection (CI) is present.

Ψ_j , and can be written,

$$\mu'_{0,0 \rightarrow n,M} = \sum_k \langle \chi_{n,M} | \left\{ \frac{\langle \Psi_j | \left(\frac{\partial H_{el}}{\partial Q_k} \right)_0 | \Psi_n \rangle}{E_j - E_n} Q_k \right\} | \chi_{0,0} \rangle \mathbf{M}_{0 \rightarrow j}, \quad (2.3)$$

where the sum is over all coordinates Q_k where $(\partial H_{el}/\partial Q_k)$ causes significant mixing between the excited states Ψ_j and Ψ_n . Hence even in the case where a transition is parity-forbidden, the transition can ‘borrow intensity’ from other allowed electronic transitions $\mathbf{M}_{0 \rightarrow j}$ involving other excited-states lying nearby in energy. This intensity-borrowing mechanism is responsible for the finite absorption strength of $d-d$ -transitions in ferrocene (Section 2.2.1) which are parity forbidden.

2.1.2. Non-radiative transitions and motion on potential energy surfaces

In this section, it is assumed that the excited-state has been prepared by a coherent broadband optical radiation (i.e. an optical pulse). In this case, the excited wavefunction is composed of a coherent superposition of excited vibrational states which form a coherent wavepacket $\chi = \sum_j c_j \chi_j$, as shown in Figure 2.3(a). Following excitation, excess vibrational energy will be lost through anharmonic coupling to other nuclear degrees of freedom in the polyatomic molecule (intramolecular vibrational redistribution, IVR) or the surrounding environment (vibrational energy relaxation, VER) [38], and the nuclear wavefunction decays towards the lowest-energy vibrational wavefunctions of the electronic state. These vibrational cooling processes typically occur on a time scale of 0.1-1 ps [37].

In addition, if along certain nuclear (reaction) coordinates the potential energy surface in this vicinity does not correspond to a stable minimum, due to a large change in the equilibrium conformation in the excited state, then the wavepacket will propagate (and broaden) along these directions on a time scale depending on the gradient of the potential energy surface, as shown in Figure 2.3(b) (note that excitation to only the first excited state is assumed here). This motion is

also accompanied by additional vibrational energy loss, and a new conformational distribution is established.

Moreover, in exploring regions of lower energy on this excited-state potential energy curve, the wavepacket may encounter a region where the potential energy approaches that of the ground state. In such regions two situations can result, depending on the interaction between the two molecular states, or more specifically the interaction with respect to more than one reaction coordinate⁴: (1) The adiabatic potential energy surfaces are repelled from one another due to the interaction between the molecular states near this intended intersection, i.e. an ‘avoided crossing’ results. A finite probability of transfer to the adiabatic ground-state potential is due to the mixing of the adiabatic electronic states by the nuclear motion (non-adiabatic coupling). (2) Due to the involvement of a second (or multiple) reaction coordinate(s), a certain coordinate in reaction coordinate point (or curve) exists where both the intended crossing occurs *and* the effective coupling between the two molecular states vanishes such that the adiabatic potential surfaces can touch, i.e. a ‘conical intersection’. In this region, a highly localised, singular, non-adiabatic coupling occurs between the two surfaces which results in a far more efficient coupling to the ground state. The occurrence of such conical intersections are quite plausible in complex polyatomic molecules [40].

2.1.3. Intramolecular charge transfer

In the case where a molecule is composed of two fragments containing (a) an electron-donor moiety which is easily oxidised (i.e. has a relatively low ionisation potential), and (b) an electron-acceptor moiety which is easily reduced (i.e. has a relatively high electron affinity), the lowest energy electronic excitations in the combined complex can involve transfer of an electron from an occupied orbital localised on the donor into unoccupied orbitals localised on the acceptor (assuming a small but finite overlap of their respective molecular orbitals). Two examples of how such an intramolecular charge-transfer (CT) can be optically induced are shown in Figure 2.4. In the first case (a) an optical excitation involving orbitals localised on the donor is followed by excited-state charge transfer (due to finite electronic coupling between the LUMOs of the donor and acceptor, and an intersection between the corresponding reaction coordinate potential surfaces) [38]. Due to the fact that the optical excitation corresponds to a localised electronic transition, the oscillator strength for such a transition can be very large, and efficient (rapid) excited-state charge transfer will be achieved if the electronic-vibrational coupling between the LUMOs of donor and acceptor is large. In certain systems, this process can occur on a time scale as short as $\lesssim 100$ fs [38, 41, 31].

Another form of optically-induced intramolecular CT (which is the case considered in this study of the Fc-B-bpy compounds) involves (b) the direct optical excitation from a predominantly donor-localised HOMO into a predominantly acceptor-localised LUMO, with the oscillator strength for the electronic transition afforded by a finite overlap of the donor and acceptor molecular orbitals. This type of direct CT electronic transition is referred to as a ‘Mulliken’ (or direct) charge-transfer transition [42], and was first studied in the context of *inter*-molecular CT. Due to the fact that these transitions involve excitation directly into the acceptor

⁴Note that a rigorous discussion of the physical basis for the occurrence of avoided crossings vs conical intersections would require a formal introduction of diabatic and adiabatic bases, and the dependence of the adiabatic potential energy surfaces on the diabatic coupling in the vicinity of the diabatic potential surface crossing along more than one reaction coordinate [38, 39]. Hence a more qualitative statement is given here.

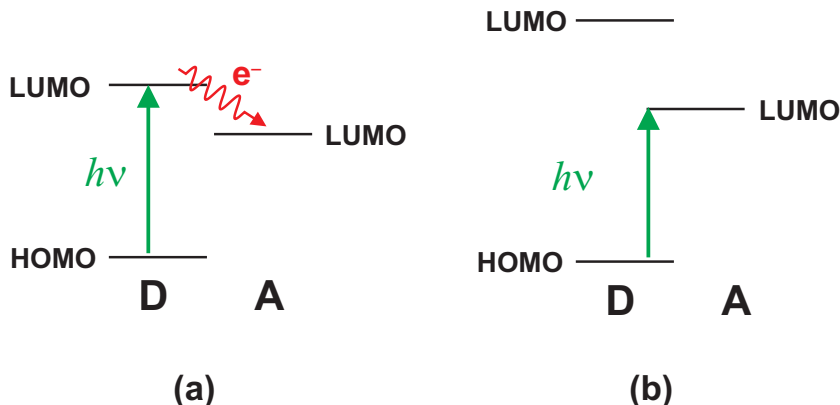


Figure 2.4.: Schematic for two forms of optically-induced intramolecular charge transfer (a) Excited-state charge-transfer following local excitation of the donor. (b) Mulliken (or direct) optical charge-transfer (as per the MLCT band studied here).

LUMO, the required photon energy is in general lower than that required for case (a).

Based on simplified theory for weakly-interacting donor and acceptor (see Appendix B.1 and Ref.s [43, 42, 37]), the interaction between a neutral-donor and neutral-acceptor (with isolated energies E_d and E_a , respectively) leads to the perturbation of the MO energies as shown in Figure 2.5. (Note that in this approximate one-electron model the neutral donor is represented as V^{D+} , i.e. the effective core potential seen by the valence electron involved in the CT.). The first-order donor-acceptor interaction leads to a weak stabilisation of the donor-HOMO (due to attractive van der Waals interaction) and a significant stabilisation of the acceptor-LUMO (due to the electrostatic interaction between D^+ and A^-). The second-order effects involve mixing of the donor-HOMO and acceptor-LUMO, which leads to an additional stabilisation (destabilisation) of the donor-HOMO (acceptor-LUMO), and increases both the strength and required photon energy for the CT transition (see Appendix B.1).

In the present study, the Fc-B-bpy compounds possess cationic acceptor groups (Chapter 4), which leads to a different interaction between the CT valence electron and the effective core potential of the donor and acceptor in the ground and CT states. This situation is represented schematically in Figure 2.6 (where for simplicity only the effects of first-order donor-acceptor interaction are shown). Here both the donor-HOMO and acceptor-LUMO are stabilised by a comparable degree due to ion-induced-dipole donor-acceptor interactions in the ground state (DA^+) and CT state (D^+A), as indicated by the potential terms in Figure 2.6 (see Appendix B.1 for the precise expressions).

In the spectroscopic study of the Fc-B-bpy compounds in Chapter 4, we compare the MLCT spectra of derivatives with a single cationic acceptor, or multiple cationic acceptors with different geometries and inter-acceptor coupling. The presence of two identical acceptors leads to near-degenerate (symmetric and anti-symmetric) LUMOs which are split by the inter-acceptor interaction and their different interaction with the donor, whilst the donor HOMO is now perturbed by the presence of two acceptors. Due to the fact that there should be significant electrostatic interaction between the donor and acceptors for these net-charged complexes, in the following, we neglect the second-order perturbations due to mixing (which will lead in general to a small blue-shift of the HOMO-LUMO energy separation)

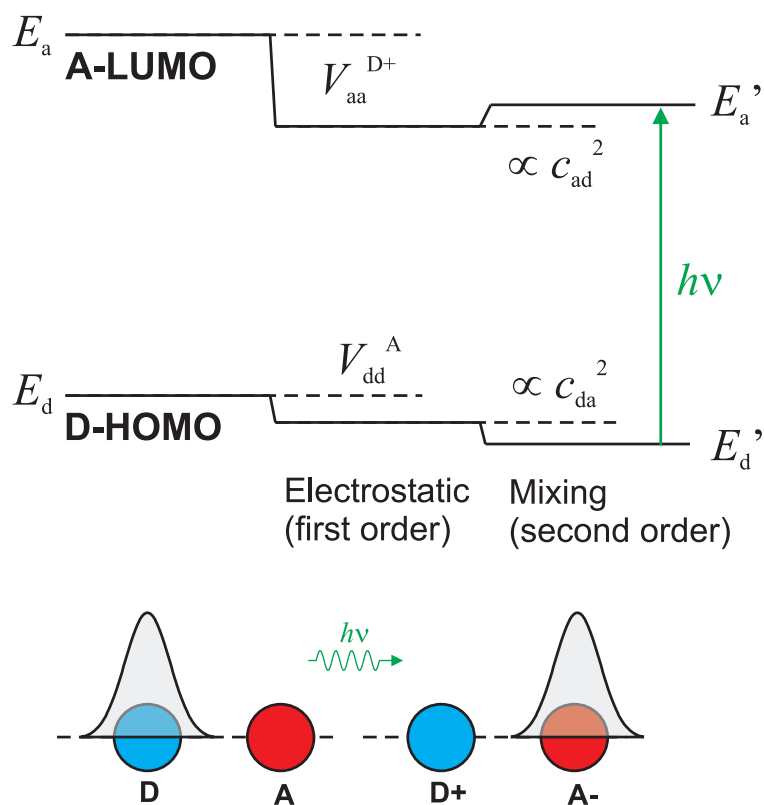


Figure 2.5.: Donor-HOMO and acceptor-LUMO energies resulting from first-order (electrostatic) and second-order (mixing) donor-acceptor interaction (assuming a simple one-electron model) and resulting CT transition energy, for a neutral-donor-neutral-acceptor complex.

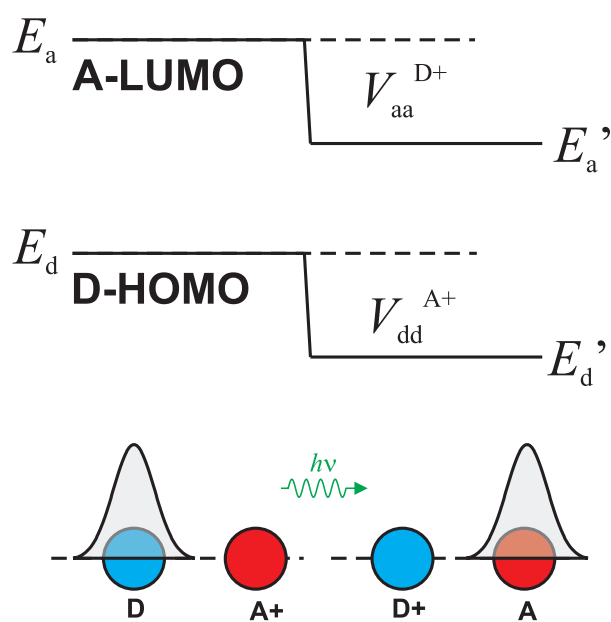


Figure 2.6.: Donor-HOMO and acceptor-LUMO energies due to first-order (electrostatic) donor-acceptor interaction for a neutral-donor-cationic-acceptor complex.

In Figure 2.7, a schematic of the situation for a linear-symmetric donor-acceptor complex with two cationic acceptors is shown. As the two acceptors are significantly displaced from each other (with the additional electrostatic shielding of the intervening polarisable donor), the interaction between the two acceptors is small, and a small average stabilisation and splitting between the symmetric (α) and antisymmetric (β) orbital energies results. The donor-HOMO, on the other hand, is now stabilised by the combined presence of two cationic acceptors, such that the net HOMO-LUMO separation will increase relative to the single-acceptor complex⁵. Due to the parity of the wavefunctions, only the electronic transition to the β -LUMO is allowed, which is analogous to the selection rules in molecular exciton theory for a dimer (where two identical chromophores, with distinct HOMO and LUMOs interact) [44, 45]. Moreover, as shown in Appendix B.2, the expected absorption strength for the CT transition to the β -LUMO in the case of two acceptors is expected to be twice that of the single-acceptor complex. We note that any symmetry-breaking between the two acceptors (i.e. due to fluctuations in relative conformation or surrounding environment) will lead to an increase in the localisation of the two wavefunctions on one of the acceptors (such that the α - and β -LUMOs no longer correspond to symmetric/antisymmetric combinations).

The situation is modified considerably in the case where the two cationic-acceptors are connected by a short chemical bridge (as is the case for certain Fc-B-bpy derivatives in Chapter 4). In this case (i) there will be a far larger inter-acceptor coupling (due to both through-space and through-bond interaction), and (ii) the linear symmetry is replaced by a mirror symmetry between the two acceptors. As shown in Figure 2.8, the inter-acceptor coupling should give rise to a larger stabilisation and splitting of the α - and β -LUMOs, such that the CT transition energy should be decreased relative to the unbridged linear A-D-A complex. Moreover, the transition dipole moment to both α - and β -LUMOs is finite (and directed parallel to the symmetry plane of the D-AB complex), with the CT absorption strength being shared between the two transitions (with a ratio depending on the angle θ between the bonds to each acceptor). Hence, one expects two non-degenerate CT transitions for the bridged-acceptor complex (although as presented in Section 4.4 for the relevant Fc-B-bpy derivatives, in the presence of significant band-broadening these two transitions may remain unresolvable).

It is clear that the energy separation between the donor-HOMO and acceptor-LUMO for a CT complex should show a correlation with the corresponding CT transition energy, and hence an experimental determination of these energies over a range of related derivatives would allow a test for the assignment of a CT band. Whilst photoelectron spectroscopy can determine the vertical ionisation potential of a compound (i.e. an estimate of the donor-HOMO energy), this technique cannot always be readily applied to organic complexes (which may not be stable in the gas phase). A practical method for determining estimates of the relative HOMO and LUMO energies for a complex in solution is with electrochemical techniques (e.g. cyclic voltammetry) [46], which are employed for the characterisation of the Fc-B-bpy compounds in Section 4.5, where the relative potentials can be determined for the processes: (i) electron-removal reaction (oxidation) at the donor (E_{ox}°), and (ii) electron-addition reaction (reduction) at the acceptor (E_{red}°). However, these electrochemical potentials represent different processes with respect to the optically-induced direct CT transition. Firstly, the electrochemical processes are assumed to proceed *adiabatically*, i.e. such that the molecular conformation

⁵As discussed further in Section 4.2.3, this blue-shift for the linear-symmetric double-acceptor complex relative to the single-acceptor complex can be physically rationalised by considering the rearrangement of formal positive charge in the complex.

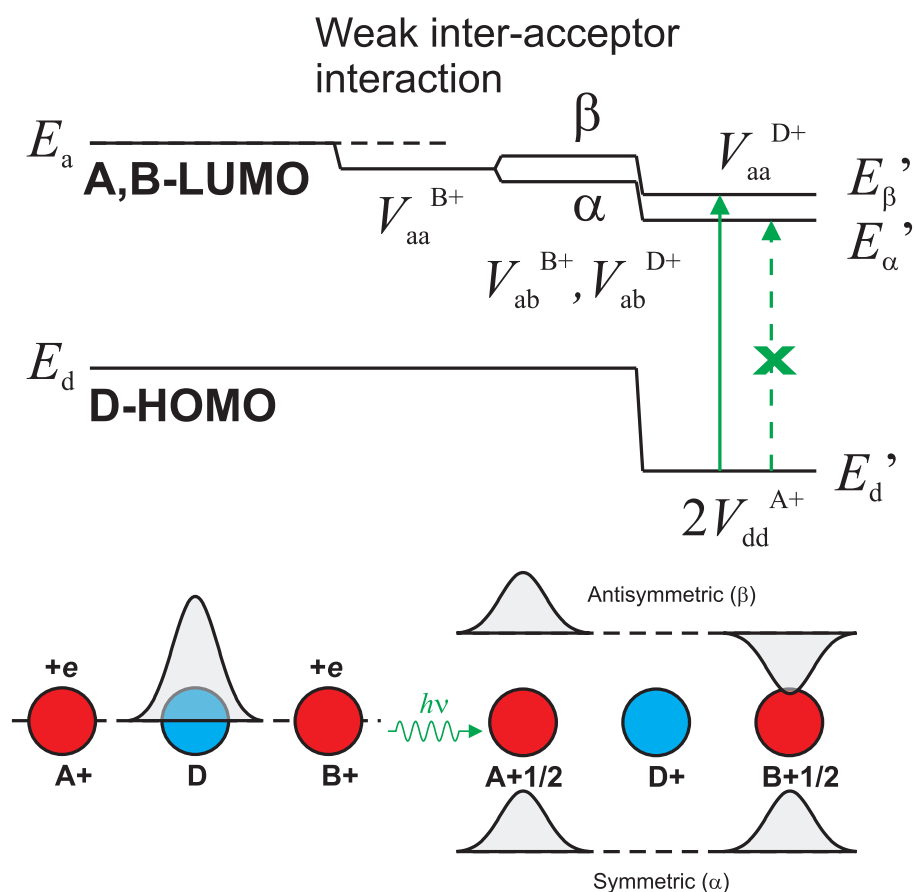


Figure 2.7.: Donor-HOMO and near-degenerate acceptor-LUMO energies due to first-order (electrostatic) donor-acceptor interaction for a *linear* neutral-donor-*double-cationic*-acceptor complex with weak inter-acceptor coupling. Only the transition to the antisymmetric delocalised acceptor wavefunction (β) is allowed.

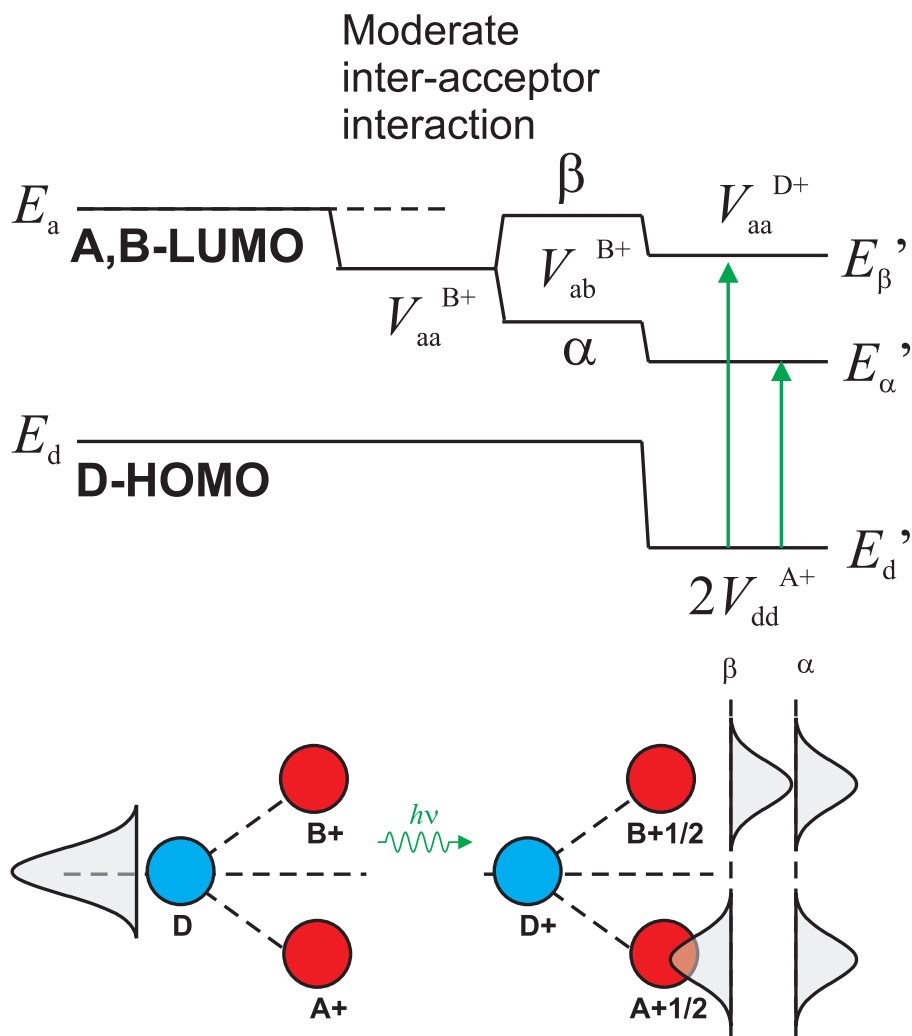


Figure 2.8.: Donor-HOMO and near-degenerate acceptor-LUMO energies due to first-order (electrostatic) donor-acceptor interaction a *bent* neutral-donor-*double-cationic*-acceptor complex with moderate inter-acceptor coupling. Both CT transitions to the symmetric and antisymmetric delocalised acceptor wavefunctions (α, β) are allowed. With increasing inter-acceptor interaction, both CT transitions will red-shift and split in energy.

and surrounding solvent environment can adjust to their new equilibrium positions (in the presence/absence of the added/removed electron) *during* the process. For an optical CT transition, the Franck-Condon principle dictates that these degrees of freedom remain fixed during the optical transition and the relevant MO energies all correspond to those in the ground-state equilibrium conformation of the nuclei and surrounding solvent molecules [47]. Secondly, the electrochemical processes involve different formal charges of the complex, whereas in the optical CT process, the total charge of the complex remains fixed. Taking these effects into consideration, the expected CT transition energy can be related to the difference in the electrochemical potentials $\Delta E'^o$ for oxidation and reduction by [47],

$$E_{\text{MLCT}} = e\Delta E'^o + \chi_e + \Delta E_{\text{FC}} - C, \quad (2.4)$$

where χ_e is the difference between the excited-state solvent interaction energies for the Franck-Condon (i.e. ground-state) and CT (excited-state) solvent equilibrium configurations, and ΔE_{FC} is one-half the Stokes shift for the transition (i.e. the relaxation energy in going from the ground-state equilibrium internal geometry to the CT state equilibrium geometry). The electrostatic interaction term $C > 0$ corresponds to the difference between the hypothetical reduction potential for the acceptor in the case where the donor is *oxidised* (a situation not realisable in practice) and that measured with a neutral donor. We employ this relation to analyse the experimental data for a range of Fc-B-bpy compounds in Section 4.5.2.

2.1.4. Solvatochromism of CT absorption band

In solution, electrostatic interaction with the charge distribution of the solute leads to dipole orientation and induced polarisation in the surrounding solvent molecules. This leads to an additional electric field ('reaction field') [48, 49] experienced by the solute molecule, which causes a shift in the molecular energy (relative to the gas-phase). Upon CT electronic excitation, the solute charge distribution will change dramatically, and this solvent interaction energy will be different for the excited-state, which results in a solvent-dependent shift (and broadening) of the CT absorption band energy – an effect referred to as solvatochromism. The case where an electronic transition shifts to lower energy with increasing solvent polarity/dipolarity is termed 'positive' solvatochromism (resulting in a 'bathochromic' shift) [49], whereas in the case where the transition shifts to higher energies, the effect is referred to as 'negative' solvatochromism (resulting in a 'hypsochromic' shift).

In the case of the cationic Fc-B-bpy compounds studied here (which are soluble only in polar solvents), the dominant solute-solvent interactions are ion-dipole and dipole-dipole interactions. However, as the net charge of the solute does not change upon optical excitation, the effect of the ion-dipole interaction affects the solvatochromic shift only through its influence on the orientation of the surrounding solvent molecules. This situation is depicted in Figure 2.9. In Figure 2.9(a), the typical situation for a neutral dipolar solute surrounded by dipolar solvent molecules is shown. The solvent molecules tend to align themselves to the dipole electric field created by the solute. In the case of a cationic solute (Figure 2.9(b)), the field component arising from the net ionic charge of the solute dominates, and the equilibrium orientation of the solvent molecules will tend to align with this field. Note that due to solvent-solvent interaction and thermal fluctuations, the actual instantaneous solvent configuration will deviate from the idealised situation shown in Figure 2.9.

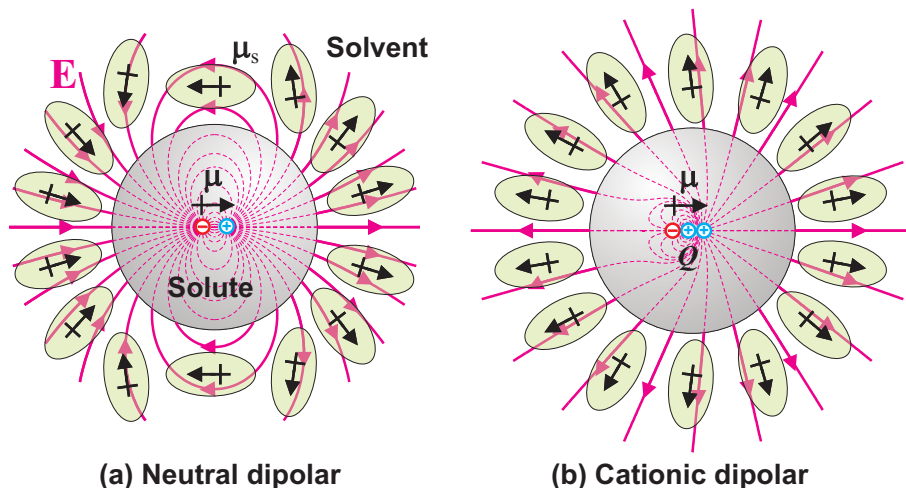


Figure 2.9.: Schematic representation of the dipole orientation (μ_s) of polar solvent molecules surrounding (a) a neutral solute molecule (with dipole μ), and (b) a cationic solute (represented as a superposition of a dipole μ and net charge Q). (Only the first solvent shell is shown. Induced dipole components omitted. Note that in this model, the internal dielectric constant of the solute “sphere” is taken as unity.)

Another difference between a neutral CT complex and a cationic CT complex is represented in Figure 2.10. In Figure 2.10(a) a neutral CT complex with negligible ground-state dipole is shown⁶. Upon CT excitation, an appreciable excited-state solute dipole is created. In this example, the ground-state orientation of the dipolar solvent molecules will be predominantly random (due to the absence of any strong dipole-dipole interaction in the ground state, although anisotropy in the polarisability of the solute and solvent will result in a weak residual preferential orientation of the solvent molecules). Upon optical excitation, the interaction between the excited-state solute dipole with the random arrangement of solvent dipoles (which cannot reorient on the time scale of the absorption process) will result in no net energetic dipole-dipole interaction energy. In this case, the dominant solvatochromic shift will arise from the solute-dipole–solvent-induced-dipole interaction, which will stabilise the excited-state and lead to a red-shift of the transition, as is commonly observed for such neutral CT compounds [49].

For the case of the cationic CT complex (Figure 2.10(b)) however, the ground- and excited-state dipole moments are not uniquely defined (due to the fact that now the calculated dipole moment depends on the choice of origin, which arises from the general principle that only the first non-vanishing term in a multipole expansion is independent of the chosen coordinate system [52]). However, as per the treatment in Ref. [51], we derive an effective dipole moment using the construction shown in Figure 2.10(b). If we assume that the donor and acceptor are of comparable dimensions (as is the case for the single-acceptor Fc-B-bpy compounds in Chapter 4), with the effective molecular centre at a position lying halfway between the donor and acceptor, then we can decompose the ground-state charge distribution into the sum of a centralised point charge and an effective dipole, μ_g

⁶Note that for the case of zwitterionic CT compounds, both the ground- and excited-state solute dipoles are large [50, 51], and a significant dipole-dipole solvent shift results, similar to the case considered for the cationic solute, i.e. with a reversal in the direction of the solute dipole upon excitation.

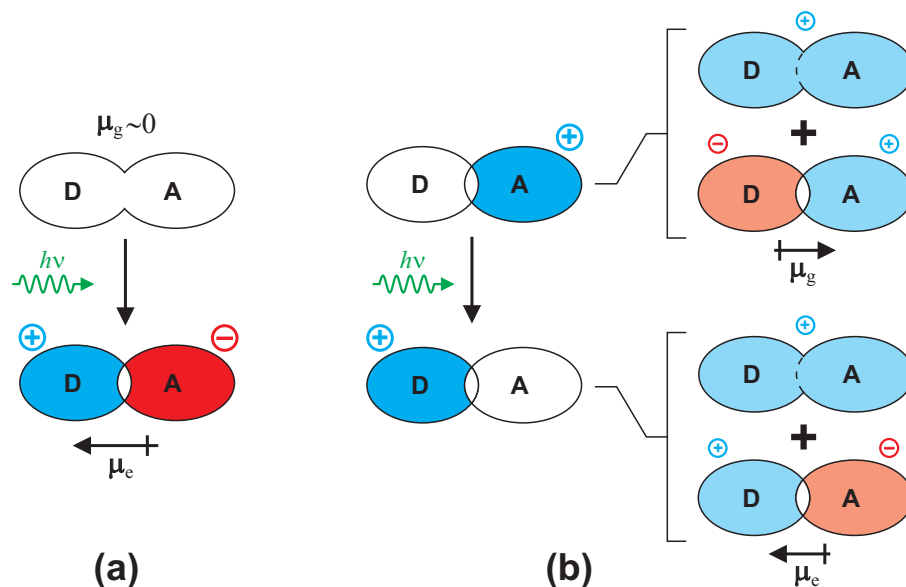


Figure 2.10.: Schematic representation of the charge density distribution in ground and excited states of donor-acceptor CT compounds for the case of (a) a neutral non-polar ground state, and (b) a cationic ground state acceptor (with a symmetrically-displaced CT in the excited state). In (b), the counteranion in solution is assumed to be sufficiently dissociated and is omitted).

(as shown in Figure 2.10(b))⁷. For the CT excited state, we displace the formal positive charge symmetrically about the molecular centre from the acceptor onto the donor, resulting in the same centralised point charge, but with an antiparallel excited-state dipole $\mu_e = -\mu_g = 1/2\Delta\mu$.

Employing the foregoing description of a CT transition in a cationic complex, i.e. an equilibrium solvent orientation dictated by the ion-dipole interaction with a symmetric change in dipole moment $\Delta\mu$, in Appendix B.3 we derive an approximate expression for the expected solvatochromic shift as,

$$\Delta E_{\text{solv}} = \frac{\gamma}{a^3} \Xi \left(\frac{a}{\sqrt{B}} \right) (\Delta\mu)^2 (\varphi(\epsilon_s) - \varphi(n^2)), \quad (2.5)$$

where $\gamma = 1/(4\pi\epsilon_0)$, a is the effective solute radius (i.e. the radius of the first solvent shell, assuming a spherical solute), $B \equiv \gamma Q\mu_g^s/kT$ is a measure of the ion-dipole orientation (in terms of the solute charge Q and solvent permanent dipole moment μ_g^s), $\Xi(x)$ is a special integral function (defined in Appendix B.3) which varies in the range (1, 2) for $x \in (0, \infty)$, and $\varphi(\epsilon_s)$ and $\varphi(n^2)$ are solvent polarity functions [48] (defined in Appendix B.3) in terms of the solvent static dielectric constant ϵ_s and optical refractive index n . We note that Eq. 2.5 predicts a solvatochromic shift of the CT transition to necessarily higher energies with increasing solvent dipolarity (i.e. increasing solvent static dielectric constant), as is observed for the Fc-B-bpy compounds (Section 4.2.2), and reported for other compounds where a cationic model was appropriate [51].

⁷Note that formally, the charge distribution should be regarded as a sum of a quadrupole term (i.e. two positive charges $e/2$ separated by the donor-acceptor separation) and the dipole term. However, at the radius of the first solvent shell, we can reduce the quadrupole contribution to an effective centralised charge of e [51].

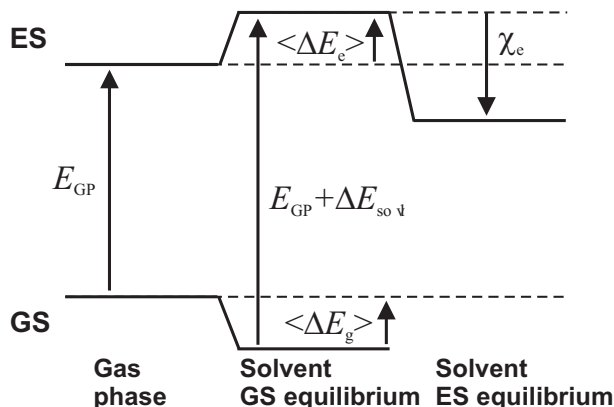


Figure 2.11.: Schematic demonstrating the hypsochromic (negative) solvent shift ΔE_{solv} for a CT transition within the symmetric charge displacement model employed for a cationic solute (see Figure 2.10) relative to the gas-phase transition energy (E_{GP}). Also shown is the excited-state solvent reorganisation energy, χ_e . Note that only the dipole-dipole interaction term is shown (i.e. the large constant ion-dipole contribution is omitted).

The resulting solvatochromic blue shift arises because the average orientation of the surrounding solvent is distorted from perfect alignment to the ionic field of the solute, in a way that reduces the dipole-dipole interaction energy in the ground state. Upon CT excitation, the solute dipole is inverted, and the excited-state is correspondingly destabilised by interaction with this ground-state equilibrium solvent conformation. The net shifts due to the dipole-dipole interaction are shown in Figure 2.11 (note that the significantly larger, constant solute-ion-solvent-dipole interaction shifts are excluded). Following excitation, the solvent dipoles will readjust to the excited-state solute dipole, resulting in an equal dipole-dipole stabilisation to that in the ground state. This results in a solvent reorganisation energy of $\chi_e = \Delta E_{\text{solv}}$. Moreover, due to thermal fluctuations, the solvatochromic interaction also results in a broadening of the CT absorption band. As derived in Appendix B.3, the dominant term for the broadening is characterised by a variance in photon energy of (Eq. B.109),

$$\sigma_{\text{solv}}^2 = 2kT\Delta E_{\text{solv}}. \quad (2.6)$$

We note that this implies a fixed relation between the solvatochromic blue-shift and the solvatochromic contribution to the absorption bandwidth. As presented in Section 4.2.2, this allows a relatively robust test of the solvatochromic model by a combined analysis of the CT band energy and width.

2.2. UV-vis spectroscopic properties of ferrocene and ferrocene derivatives

In this section, we present an overview of the electronic structure and spectroscopic properties of ferrocene and substituted Fc-derivatives. As mentioned in Section 2.1.3, in the case of a weakly coupled donor and acceptor, the electronic states of the donor-acceptor complex are expected to be related to those of the isolated donor and acceptor units through only a low-order perturbation of the original orbitals and energies. Hence the results presented here (and corresponding details of the acceptor groups in Section 2.3) provide a basis for interpreting the electronic and

spectroscopic results of the Fc-B-bpy compounds presented in Chapter 4. Moreover, this section presents a summary of established Fc-donor compounds with strongly-accepting substituents connected to the Fc via a conjugated bridge, which exhibit strong vis-NIR MLCT transitions from the Fc core into the acceptor-based unoccupied orbitals. These results provide a benchmark for Fc-based MLCT compounds for comparison with the Fc-B-bpy compounds, as well as demonstrating the electronic description developed to explain the observed spectroscopic behaviour.

2.2.1. Electronic structure and optical transitions of ferrocene

Since its discovery [53, 54, 55] the electronic structure of Fc has been studied intensively, incorporating results from UV-vis spectroscopy [56, 57, 58, 59, 60, 61, 62], and theoretical calculations based on ligand-field theory [63, 64, 65, 66], semi-empirical [67, 68], X- α - [69, 70], Hartree-Fock [71, 72, 73, 74, 75, 76, 77] and DFT [78, 79, 80, 81, 82, 83, 84, 85, 86, 87] methods. Valuable information has also been provided from additional experimental characterisation including gas- and crystal-structure determination [88, 89, 90], electrochemical [91, 92], photoelectron spectroscopy [93], resonance Raman [94], and magnetic circular dichroism [95, 96] measurements.

Figure 2.12 shows the correlation diagram which describes the formation of the molecular orbitals of Fc in terms of the contributing s , p and d -orbitals of Fe^{2+} and the π -orbitals of $2(\text{Cp}^-)$ [83, 85]. Note that both (i) the staggered relative conformation between the Cp^- (i.e. C_5H_5^-) rings presented here (with the corresponding group theoretical representation D_{5d}), and (ii) the eclipsed conformation (D_{5h}), are employed in the literature. Although the equilibrium conformation in the gas phase was determined to possess eclipsed Cp^- rings [88] (whilst the Fc-crystal [89] and many gas-/solution-phase substituted-ferrocenes possess a staggered equilibrium conformation), the choice of geometry does not lead to significantly different results for the molecular orbitals and their energies, as indicated by the almost free relative rotation of the Cp^- rings in the gas phase (which has an experimentally-determined barrier of only $\sim 0.9 \text{ kcal mol}^{-1}$ ($\cong 0.04 \text{ eV}$)) [88].

The corresponding frontier molecular orbitals (MOs)⁸ extracted from a modern DFT treatment [84] are shown in Figure 2.13, which demonstrate that the e_{2g} and a_{1g} HOMOs of ferrocene are predominantly of Fe- d character, whilst the e_{1g}^* LUMO is more delocalised over the whole Fc structure.

Figure 2.14 shows the UV-vis absorption spectra of Fc measured in room temperature (RT) solution (in CHCl_3 , CH_3CN and isopentane). The two main absorptive features in the near-UV/vis range are labelled ‘Fc-I’ ($\lambda_{\text{max}} = 440 \text{ nm}$, $\varepsilon = 110 \text{ M}^{-1}\text{cm}^{-1}$) and ‘Fc-II’ ($\lambda_{\text{max}} = 325 \text{ nm}$, $\varepsilon = 78 \text{ M}^{-1}\text{cm}^{-1}$) (although this band Fc-II is present only as a shoulder in CHCl_3). Also shown is a modified-Gaussian fit⁹ to the Fc-I band (for CH_3CN) which yields an oscillator strength of $f = 0.004$ - a value of this magnitude for a localised electronic transition generally corresponds to a perturbed symmetry-forbidden spin-allowed transition.

The appearance of such weak, broad and featureless bands in the visible range is predicted from simple ligand field theory [98], where the reduction in symmetry of the Fe^{2+} environment due to the electrostatic interaction with the Cp^- rings lifts the degeneracy of the Fe^{2+} d -orbitals, resulting in the existence of low-energy d - d electronic transitions. In most of the early investigations of these low-energy

⁸The highest-occupied molecular orbitals (HOMOs) and lowest-unoccupied molecular orbitals (LUMOs) are denoted in this work by H(OMO)[- n] and L(UMO)[- n], where $n = 0, 1, 2, \dots$, where $n=0$ corresponds to the highest energy HOMO and lowest energy LUMO.

⁹See Section 4.2.1, Eq. 4.2 for the definition of the model function.

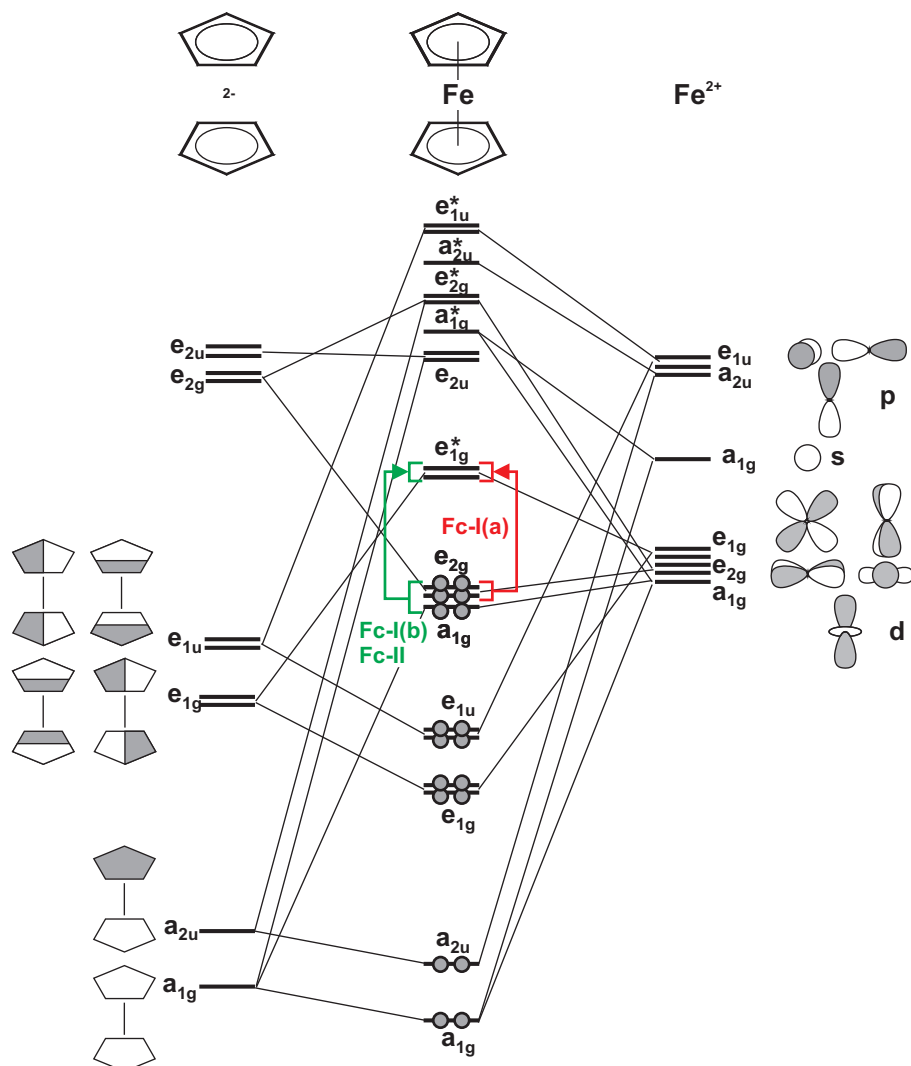


Figure 2.12.: Molecular orbital correlation diagram of ferrocene constructed from the molecular orbitals of isolated Fe^{2+} and dicyclopentadienyl. Also indicated are the dominant molecular orbitals associated with the lowest energy singlet optical transitions as presented in Figure 2.14. (Figure adapted from [83, 85].)

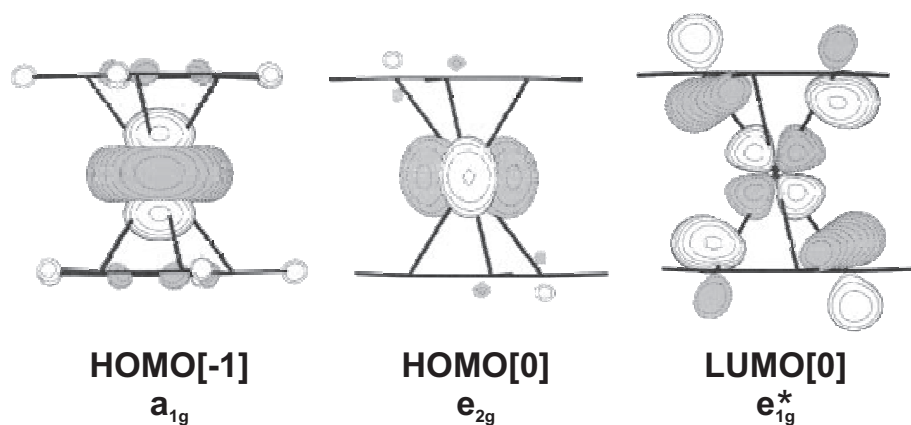


Figure 2.13.: Frontier Kohn-Sham molecular orbitals of ferrocene from Ref. [84].

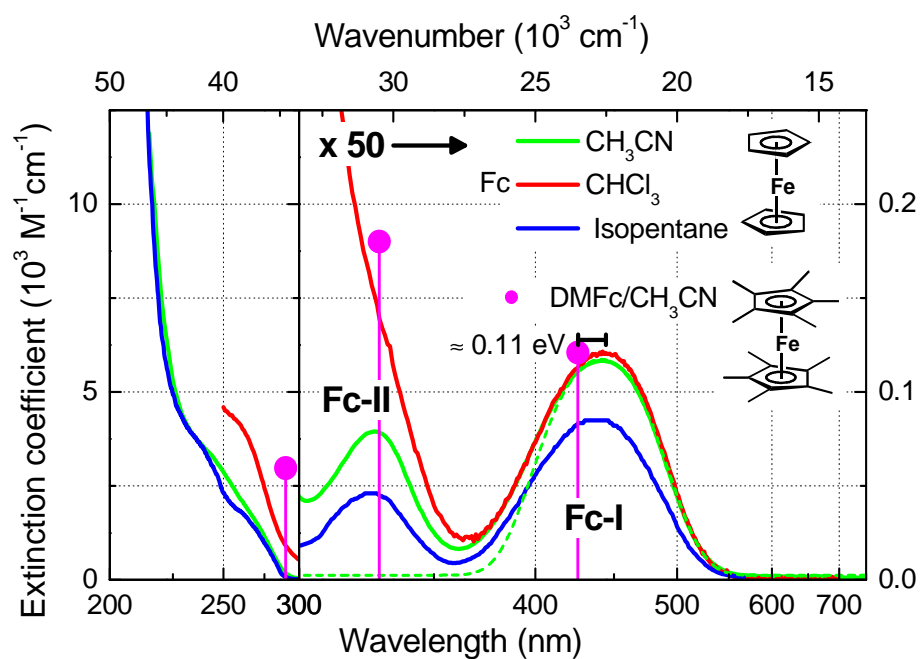


Figure 2.14.: UV-vis absorption spectra of unsubstituted Fc in CH₃CN, CHCl₃ and isopentane, indicating the two resolvable low-energy singlet-singlet absorption bands ‘Fc-I’ and ‘Fc-II’. A modified-Gaussian fit to the Fc-I band in CH₃CN is included for estimating the transition oscillator strength. Absorption peak data for decamethylferrocene (((CH₃)₅Cp)₂Fe, ‘DMFc’) in CH₃CN are shown as points. (Isopentane spectrum for Fc extracted from [57]. DMFc data from [97])

absorption bands of Fc [57, 59, 60], this simplified ligand-field-based treatment of the absorption spectra was employed with certain success to explain the strength and position of the Fc-I and Fc-II bands, with the conclusion that the Fc-I band (which is actually composed of two distinct electronic transitions, Fc-I(a) and Fc-I(b), see Figure 2.15) was associated with an almost pure $d-d$ transition. This was supported by absorption spectral measurements of a (limited) set of substituted Fc-derivatives (Ref. [59], see next section), as well as the first Hartree-Fock/semi-empirical calculations [69, 71, 68]¹⁰.

However, even certain early (perhaps, less-often-cited) reports at the time [62, 58, 67, 100] came to the conclusion that even the lowest Fc-I band system must involve appreciable contribution of delocalisation onto the Cp^- rings. This is consistent with the frontier molecular orbitals from more accurate modern quantum chemical calculations, as well as the relatively smaller number of reports on explicit calculations of the electronic excitations using SAC-CI¹¹ [77] and TD-DFT [86] methods. The lowest-energy transition, Fc-I(a), corresponds to a fairly pure orbital transition $e_{2g} \rightarrow e_{1g}^*$, whilst the slightly higher-energy Fc-I(b) and the Fc-II transitions correspond to mixed configurations have significant contributions from both $e_{2g} \rightarrow e_{1g}^*$ and $a_{1g} \rightarrow e_{1g}^*$ orbital transitions [77].

Despite the finite contribution of the Cp^- rings in the relevant MOs, these transitions are still symmetry-forbidden (i.e. Laporte-forbidden) [77]. Typical for predominantly $d-d$ transitions, the Fc-I/II bands acquire the moderate observed absorption strength due to vibronic coupling (or intensity borrowing) due to mixing with higher-energy allowed transitions [101, 67, 37, 102]. This mechanism is promoted by the many low-energy degrees of conformational freedom that Fc possesses, such as the unhindered rotation of the Cp^- rings, which also leads to the characteristic temperature-dependence (see below) and featureless nature of the bands [58]. In passing, we note that the poorly-resolved but significantly stronger absorption region further into the UV range (i.e. $\lesssim 300$ nm) is associated with several allowed ligand-to-metal charge transfer (LMCT) transitions, i.e. from predominantly Cp^- - π based orbitals into predominantly d -based orbitals [57, 77].

Also plotted in Figure 2.14 are the absorption band peak data for decamethylferrocene (DMFc, i.e. where the -H atoms of the Cp^- rings are replaced with CH_3 groups) [97], where one observes a set of corresponding bands only somewhat shifted in energy. As discussed further in Section 2.2.2, the substitution of (relatively) electron-rich methyl groups on the Cp^- -rings increases the electron density on both the Cp^- rings and the Fe^{2+} core, which destabilises the d -orbitals, as testified by the considerable reduction in the electrochemical oxidation potential of DMFc relative to Fc ($\Delta E_{\text{ox}}^{\circ} \sim -0.5$ eV) [103]. For the Fc-I band, one observes that the band peak of DMFc is blue-shifted relative to Fc ($hc\Delta\nu_{\text{max}} \approx 0.11$ eV), which implies that the e_{1g}^* orbital associated with the Fc-I excited state is actually slightly destabilised relative to the corresponding ground-state e_{2g} and a_{1g} orbitals. This observation is consistent with the assertion that the excited-state orbitals possess an appreciable contribution on the Cp^- rings, where the increased electron density of the CH_3 -groups is felt more strongly¹².

We will return to the comparison of Fc and DMFc again in comparing the MLCT

¹⁰Note that the somewhat erroneous conclusion that the Fc-I transitions are strongly localised $d-d$ transitions can still be found in certain modern reports, e.g. Ref. [99].

¹¹SAC-CI: Symmetry Adapted Cluster/Configuration Interaction.

¹²Whilst the implications of the destabilised Fe d -orbitals upon Cp-ring methylation has been well-appreciated in terms of the more facile oxidation and expected red-shift of charge-transfer transitions into acceptor orbitals in Fc-donor-acceptor compounds (where the acceptor orbitals are less affected by the increased electron density localised on Fc, see Section 2.2.2), a critical comparison of the Fc and DMFc UV-vis absorption spectra could not be found in the literature.

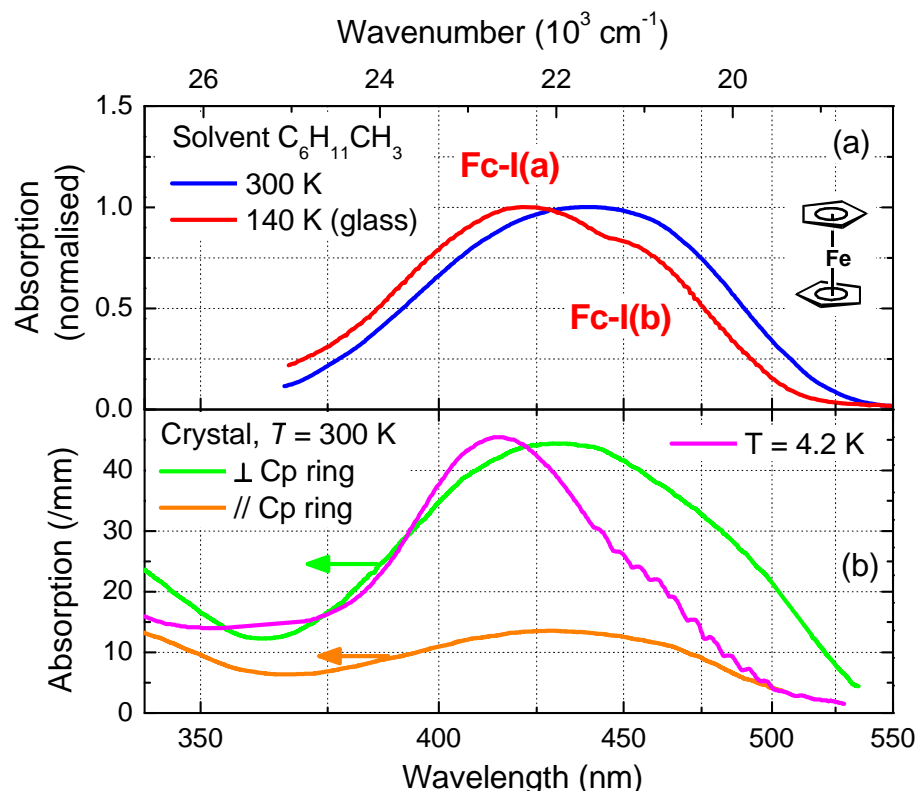


Figure 2.15.: (a) UV-vis absorption spectra of Fc in methylcyclohexane at two temperatures, 300 K and 140 K. At 140 K, the degeneracy of two d - d transitions is lifted and two bands can be partially resolved (Fc-I(a), Fc-I(b)). (Spectra extracted from [94]). (b) Fc crystal absorption spectra at RT with polarisation perpendicular (green curve) and parallel (orange curve) to the Cp⁻-ring plane, and for $T = 4.2$ K. (Spectra extracted from [61] and [57], respectively).

spectra of corresponding Fc- and DMFc-donor compounds (Section 2.2.2). We note that the Fc-II band is not significantly shifted by the presence of the CH₃-groups, although a significant increase in absorption strength occurs (which indicates that the mechanisms leading to symmetry-reduction (and hence allowing a finite transition dipole moment for this transition) are sensitive to the electronic/steric influence of the CH₃ groups, and that different d -based orbitals are affected to differing degrees. Moreover, in the UV range, a significant red-shift of at least one of the LMCT absorption bands occurs upon methylation (which from inspection of the spectra, must involve a red-shift of at least some 100s of meV), which is also consistent with the assignment of the higher energy bands as being of Cp→ d character.

We note that corresponding electrochemistry data of substituted 1,1'-dimethylferrocene [103, 56] and octamethylferrocene [104, 105] (i.e. Fc bearing 2 and 8 CH₃-groups, respectively) demonstrate that the trends of the less-positive oxidation potential and the weak blue-shift of the Fc-I band are approximately additive with the number of CH₃ groups (which is useful rule for designing Fc-derivatives where other substituent groups must replace some of the CH₃ groups).

Further information concerning these electronic transitions can be gained from measurements in the solid phase. As shown in Figure 2.15(a), the absorption spectrum in frozen solvent reduces the degree of broadening such that the band Fc-I can be resolved into two distinct electronic transitions, Fc-I(a) and Fc-I(b) [57, 94]

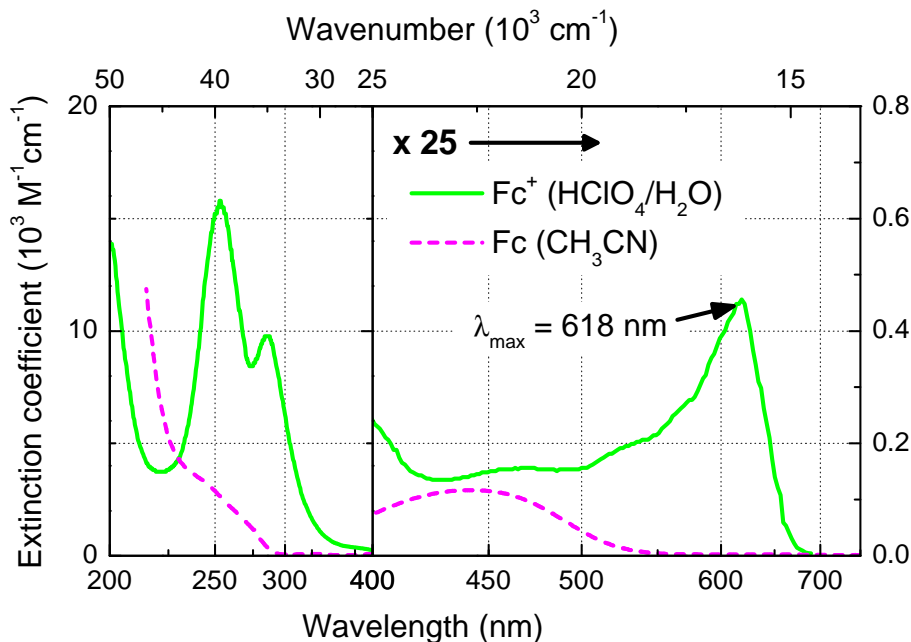


Figure 2.16.: UV-Vis absorption spectra of ferricinium (Fc^+ , in 1-mol-% $\text{HClO}_4/\text{H}_2\text{O}$). (Fc absorption spectrum in CH_3CN shown for comparison. Fc^+ spectrum extracted from [57].)

discussed above. (The existence of two distinct unresolved electronic transitions was also confirmed by MCD¹³ measurements of Fc and certain substituted derivatives [95, 96]). Moreover, the whole absorption band system is blue shifted by $\sim 500 \text{ cm}^{-1}$, which as stated in the literature is consistent with a hypothesis of a vibronically-coupled predominantly $d-d$ transition [65, 58].

This trend is also reflected in low-temperature crystal measurements (Figure 2.15(b)), where for $T = 4.2 \text{ K}$ one also observes vibrational structure and a relative suppression of the absorption strength on the red-side of the band (i.e. in the region of Fc-I(b)). The observed vibrational spacing is in the range $240 - 300 \text{ cm}^{-1}$, which corresponds to the totally-symmetric excited-state vibration of the Fe-Cp separation [57]. Concerning the emergence of the vibrational structure, we add that for the corresponding measurement of a crystal of a derivative with a single $-\text{C}_6\text{H}_5$ group attached to one of the Cp^- rings, this vibrational structure is not observed [57], although the blue-shift and clear band asymmetry are still evident.

Figure 2.15(b) also shows the polarisation dependence of the absorption (at room temperature) for a single crystal. A strong linear dichroism is observed, supporting that the transition dipole moment is aligned along the C_5 axis, although the fact that the polarisation contrast is only $\sim 3.3:1$ supports the fact that the transitions involve significant intensity borrowing [106].

An additional important spectroscopic result for Fc (which will emerge in the discussion concerning the charge-transfer in Fc-B-bpy compounds in Chapters 4 and 5) is the absorption spectrum of the ferricinium ion, Fc^+ i.e. Fc following oxidation (electron removal). Figure 2.16 shows the absorption spectrum of Fc^+ , which possesses several new partially resolvable transitions extending into the visible [57, 68]. The main absorptive features in this range have all been assigned to LMCT transitions from predominantly Cp^- -based orbitals into the electron hole

¹³MCD: Magnetic circular dichroism [37].

that is localised on the oxidised Fe^{3+} core (although the weak oscillatory structure apparent between $\sim 420 - 600$ nm is attributed to a superposition of weak predominantly $d-d$ transitions remaining available to the Fe^{3+} centre).

We conclude this section by mentioning briefly the general effects of addition of substituent groups to the Cp^- rings of the Fc unit. As reflected in the numerous reports on the UV-vis spectroscopic properties of Fc-derivatives with (neutral) substituents [95, 94, 56, 57, 62, 107, 108, 59, 109, 110, 111, 112, 113, 100, 114, 115] the addition of even simple (i.e. electronically ‘innocent’) substituents generally leads to a symmetry-lowering of the Fc-based orbitals, such that the (predominantly $d-d$) Fc-I band can gain significant intensity (i.e. with $\epsilon_{\text{max}} \rightarrow 500 \text{ M}^{-1}\text{cm}^{-1}$). Moreover, with increasingly electron-withdrawing substituents, the Fc-band undergoes a significant red-shift (with $\lambda_{\text{max}} \rightarrow 500$ nm) and gains additional strength due to the mixing of the π -orbitals of the Cp^- ring with those of the substituent (which implies a certain degree of charge transfer to the substituent in the excited state). In the limiting case of a strong acceptor substituent with a low-lying LUMO, the excited-state orbital is predominantly localised on the substituent itself, constituting a true MLCT charge-transfer transition, such as the Fc-donor compounds presented in the next section.

2.2.2. Electronic description and spectroscopic properties of established Fc-donor MLCT compounds

In this section, we present a summary of the electronic and spectroscopic properties of established Fc-donor/organic-acceptor MLCT compounds, which have been studied intensively over the last decade due to their promise as non-linear optical chromophores [21, 22, 23, 24, 25, 26, 27, 28, 29, 30]. The general structure of these compounds is shown in Figure 2.17(a), where the Fc-donor and organic acceptor (‘A’) are covalently attached via a conjugated carbon bridge, although several other synthetic strategies have been investigated to a lesser degree, e.g. using Schiff base- [116, 117], ethylene- [118] and single- σ -bonding [119, 120, 121] schemes (Figure 2.17(b-d), respectively). A review of these compounds (hereafter referred to as ‘Fc- π -A’) is important for the consideration of any new Fc-donor MLCT compounds, due to the fact that their electronic structure and spectroscopic properties have been extremely well characterised, both experimentally and theoretically. They also provide a benchmark for the performance of other Fc-based donor-acceptor compounds (at least in terms of the strength and wavelength range of their MLCT absorption bands).

The absorption spectra of a selected set of these Fc- π -A compounds is shown in Figure 2.18 [25, 24]. For all compounds, two main bands (referred to hereafter as ‘low-energy’ (LE) and ‘high-energy’ (HE)) can be identified in the range 300-900 nm, which both undergo a progressive red-shift and increase in strength for the sequence of compounds shown (with an additional band entering in the near-UV for the compounds with the most red-shifted spectra). The absorption peak of the LE band progresses from $\lambda_{\text{max}} = 513$ nm ($\epsilon_{\text{max}} = 4600 \text{ M}^{-1}\text{cm}^{-1}$) for the nitrophenyl acceptor (bottom curve) to $\lambda_{\text{max}} = 854$ nm ($\epsilon_{\text{max}} = 19700 \text{ M}^{-1}\text{cm}^{-1}$) for the thioflavyliumyl acceptor, with a similar red-shift (although somewhat less pronounced absorption increase) for the HE band. One notes that this sequence includes both neutral and mono-cationic species, the charge of the acceptor *per se* is not a critical factor for achieving a strong MLCT transition. We note that for the neutral derivatives shown, the LE band is reported to undergo a bathochromic shift with increasing solvent polarity, whereas for the cationic derivatives a hypsochromic shift is observed [24] (consistent with the discussion in Section 2.1.4). However, no

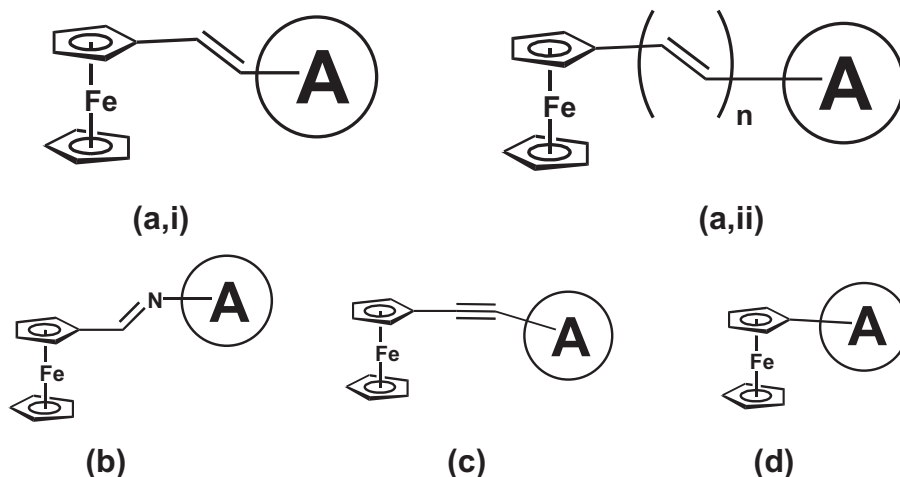


Figure 2.17.: General structure of established Fe-donor/organic-acceptor intramolecular MLCT compounds, with various bridges: (a) conjugated carbon, (b) Schiff base, (c) ethynyl and (d) single- σ bonding.

quantitative analysis of the solvatochromic shifts in a series of different solvents appears to have been reported in the literature.

Several theoretical models of the electronic structure were presented to explain the origin and spectroscopic trends of these absorption bands using extended Hückel [29], ZINDO¹⁴ [122, 123, 124] and DFT [24] methods with the aim of identifying which electronic transitions might possess significant charge transfer character, and hence be a useful indicator of strong molecular hyperpolarisability (i.e. the higher-order polarisability tensors which give rise to nonlinear optical effects). As further derivatives were synthesised, especially those incorporating stronger acceptor groups (as shown in Figure 2.18), the earlier proposed models [25, 29] were found to be inconsistent with experiment¹⁵, with the interpretation based on the frontier molecular orbitals from the more recent (ground-state) DFT calculations being the only picture consistent with the observed solvatochromism, electrochemistry, photoelectron and Stark spectral results [24].

Details of the theoretical model are depicted in Figure 2.19(a,b). The LE band is assigned to a transition from predominantly d -based orbitals¹⁶ of the Fc-core into the LUMO (Figure 2.19(b)) which is predominantly localised on the acceptor, such that the transition possesses a strong CT character. In contrast, the HE band is assigned to a transition from a lower-lying π -bridge-based occupied orbital (HOMO[-3], Figure 2.19(b)) into the acceptor LUMO. (Ironically, the previous interpretations, which included theoretical models of ZINDO-based transition energies [123] predicted that the LE transition was a localised d - d transition, whilst the HE band was assigned as the MLCT transition responsible for the large hyperpolarisability of this class of compounds). By inspection of the spatial distributions of the HOMO[-3] and LUMO orbitals, it is clear that this transition could possess significant wavefunction overlap and hence the appreciable observed oscil-

¹⁴ZINDO: Zerner's Intermediate Neglect of Differential Overlap.

¹⁵It is instructive to note that even after several years of concentrated experimental and theoretical research on this class of compounds, which reached a fair level of maturity, the provision of experimental data from additional measurement techniques and on a wider range of derivatives can lead to drastic changes in the qualitative interpretations of results.

¹⁶Note that no graphical representations for the calculated Fe-based HOMO[0,1,2] were found in the literature, although they are described as being similar to the unperturbed d -orbitals of Fc (see Figure 2.13).

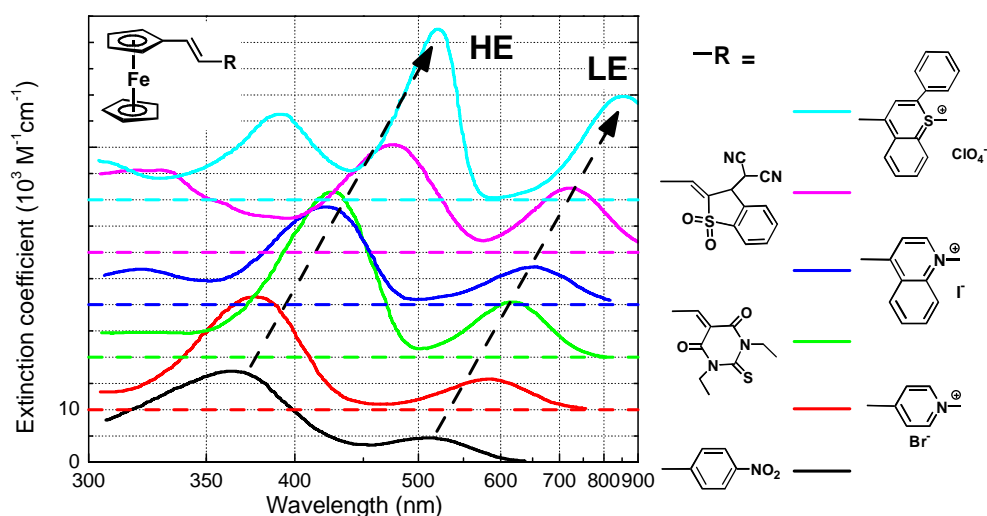


Figure 2.18.: UV-vis-NIR absorption spectra of a set of Fc- π -A compounds (in CH_2Cl_2), demonstrating the progression of the low-energy (LE) MLCT, and high-energy (HE) absorption bands. Note that each curve is vertically shifted (with the zero-level indicated by the corresponding dashed lines). (Data extracted from [25].)

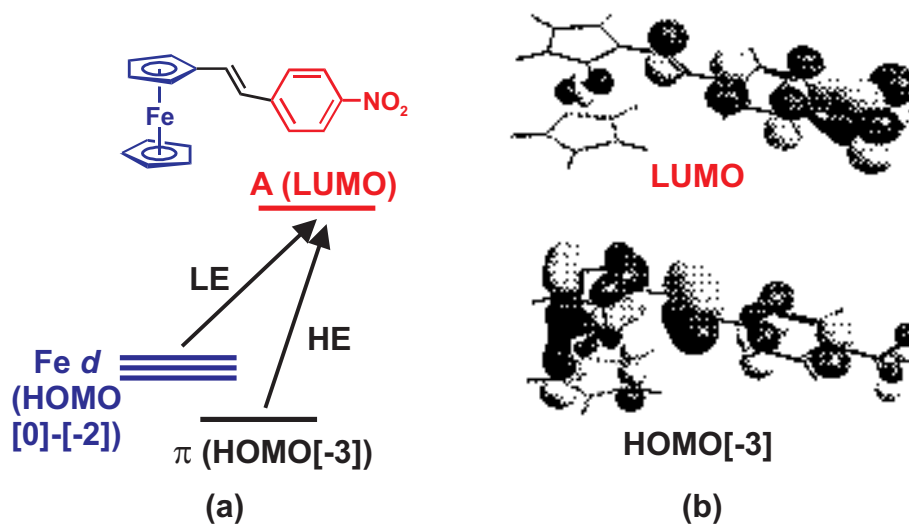


Figure 2.19.: Model of electronic transitions in Fc-donor conjugated-bridge MLCT compounds with strong acceptor groups, illustrated for the nitrophenyl acceptor. (a) Schematic Jablonski diagram depicting the origin of the LE ($d \rightarrow$ acceptor MLCT) and HE (π -bridge \rightarrow acceptor) transitions. (b) Molecular orbitals extracted from the DFT calculation results: π -bridge-based HOMO[-3] (responsible for both the HE transition and intensity borrowing enhancement of the LE band) and acceptor-based LUMO. (Molecular orbital surfaces from Ref. [24].)

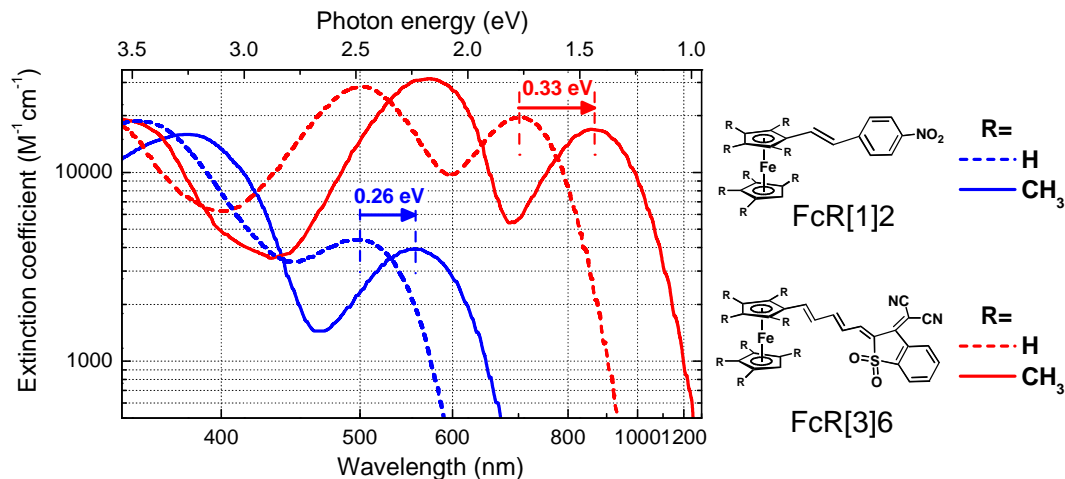


Figure 2.20.: Comparative UV-vis absorption spectra of MLCT compounds with ferrocene and octamethylated-ferrocene donors ($R=H$ and $R=CH_3$, respectively). (Data extracted from [24].)

lator strength. However, the direct wavefunction overlap of the essentially d -based HOMO[0,-1,-2] with the acceptor LUMO is predicted to be far too small to account for the observed absorption strength of the LE band.

This apparent disparity was explained [24] by considering the fact that the LE band can gain significant absorption strength through ‘intensity borrowing’ (Section 2.1.1) from the strongly-allowed HE transition (which increases in strength with increasingly stronger acceptor groups). In support of this, a closer analysis of the exact peak positions of the LE and HE bands in Figure 2.18 shows that the absorption strength of the LE band relative to the HE band increases with decreasing energetic separation between the two bands (i.e. with decreasing separation of the corresponding excited-state energies, such that the denominator in Eq. 2.3 is reduced)¹⁷. The fact that the LE band possesses an appreciable oscillator strength through this mechanism (which is the basis of their practical value as CT materials) demonstrates the important role of auxiliary electronic states and transitions in enhancing the usefulness of direct CT transitions, which are otherwise limited in their absorption strength by the inherently low degree of HOMO-LUMO spatial overlap.

We mention two final pertinent results for these Fc-donor MLCT compounds. Figure 2.20 shows the UV-vis spectra for two representative Fc-MLCT compounds and the corresponding octa-methylated derivatives where the Cp^- -rings bear CH_3 groups (labelled ‘FcR[1]2’ and ‘FcR[3]6’, $R=H, CH_3$, as per Ref. [24]). As mentioned in Section 2.2.1, it is well-established from electrochemical and theoretical studies of decamethylferrocene [125, 97, 103] that replacement of the $-H$ atoms with $-CH_3$ groups on the Cp rings leads to a destabilisation of the d -based HOMOs by ≈ 0.5 eV, due to the relative increase in electron density at the Fe^{2+} core induced by the CH_3 groups (which leads to an increase in Coulomb repulsion in the Fc core and renders an energetically more facile oxidation of $Fe^{2+} \rightarrow Fe^{3+}$).

As seen in Figure 2.20, this modification does indeed lead to a significant red-shift (in the range 0.22-0.33 eV) of both the LE and HE bands for the octa-methylated derivatives, with the values extracted from the literature spectra listed in Table

¹⁷Note this trend was identified from personal analysis of the published data, which supports the statements in Ref. [24].

Compound	λ_{\max} (nm) (ϵ_{\max} ($\text{M}^{-1}\text{cm}^{-1}$))				Changes upon methylation $\Delta(h\nu_{\max})$ (eV) ($\Delta\epsilon_{\max}/\epsilon_{\max, \text{R=H}}$ (%))	
	LE		HE		LE	HE
	R=H	R=CH ₃	R=H	R=CH ₃		
FcR[1]2	496.8 (4401)	554.5 (3936)	356.6 (18700)	380.8 (15920)	-0.26 (-10.6)	-0.22 (-14.9)
FcR[3]6	701.5 (19600)	864.9 (16980)	501.2 (28470)	569.4 (31430)	-0.33 (-13.4)	-0.30 (+10.4)

Table 2.1.: Analysis of the absorption band peak positions for LE and HE transitions for two compounds **FcR[1]2** and **FcR[3]6**, demonstrating red-shift and absorption strength change upon octamethylation of the Fc-Cp⁻ rings (see Figure 2.20 for structures). (Raw data extracted from [24].)

2.1. This supports the fact that both transitions involve a LUMO which is not localised on the Fc-unit, where one would expect a corresponding destabilisation of the *d*-based LUMO (as discussed in Section 2.2.1), and a resulting small blue-shift for the absorption band. One useful conclusion arising from these considerations is that the comparison of the spectral band position of a certain proposed Fc-donor-acceptor compound with its corresponding methylated derivative could provide a reliable test of the degree of charge-transfer in the optical excitation: if the excited state orbitals remain predominantly localised on the Fc-unit, then a significant red-shift of the band will most probably not result. However, also evident is that the absorption *strength* of the LE (MLCT) transition is in both cases slightly *decreased* by methylation, due to the distortion of the donor and bridge electronic states. This is an important point in considering design modifications to the Fc-B-bpy compounds under study in this work, which suggests that methylation of the Cp⁻ rings will not necessarily yield any increase in the MLCT absorption strength, despite the predicted red-shift of the transition¹⁸.

To conclude this section, in Figure 2.21 the results of a Stark (i.e. electroabsorption) measurement are shown for compound **Fc(CH₃)3]6** in frozen solution [24]. The net Stark spectrum (i.e. the changes in UV-vis absorption induced by an applied quasi-DC electric field, [126, 127, 128, 129, 130]) of a rigid¹⁹, isotropic molecular ensemble reflects contributions from the change in polarisability ($\Delta\alpha$) and dipole moment ($|\Delta\mu|$) that result upon optical excitation (ideally manifested as spectral contributions proportional to the (frequency-weighted) first- and second-derivatives, respectively, of the original absorption band(s)). The second derivative term is ideally proportional to $|\Delta\mu|^2$. From a comparison of Figure 2.21(b) and (c), one sees that the Stark spectrum bears a strong resemblance to the numerically-generated second-derivative function of the zero-field frequency-weighted absorption spectrum (in Figure 2.21(a)), which indicates a dominant contribution from

¹⁸It should be noted that this comparison for the Fc-B-bpy compounds remains untested due to the synthetic challenges of producing the methylated derivatives, although this discussion should motivate continued efforts to synthesise methylated derivatives for spectroscopic comparison.

¹⁹Note that a rigid environment, such as a frozen glass matrix, is required in order to prevent molecular reorientation (and, in the case of ionic salts, ion motion) of the molecular ensemble in the applied electric field.

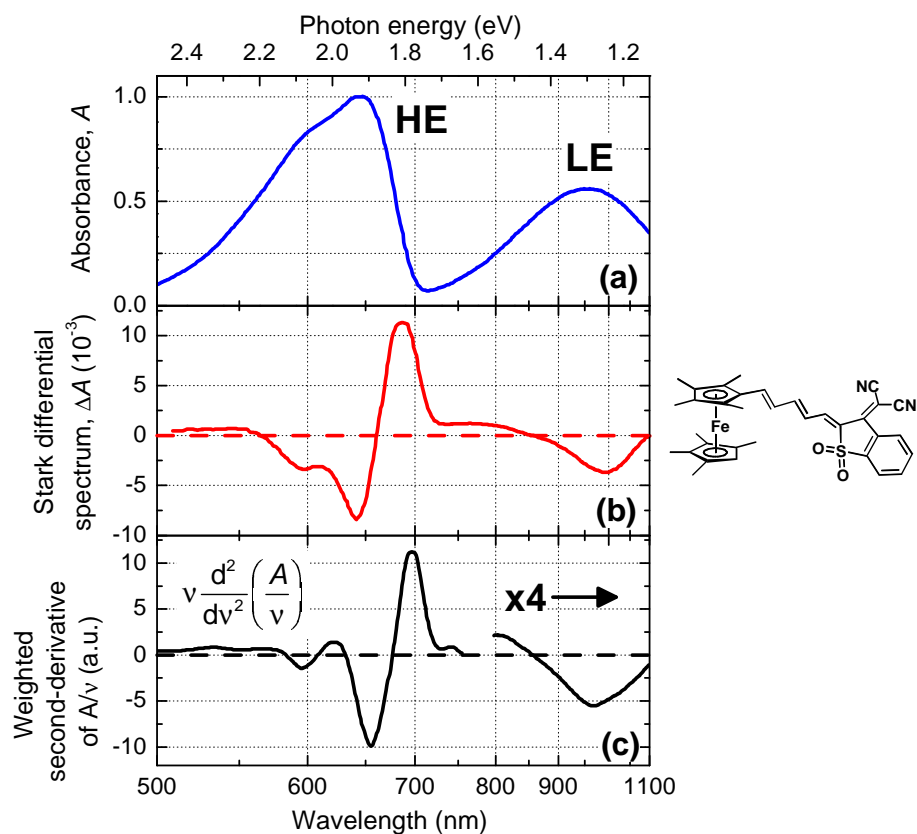


Figure 2.21.: UV-vis spectra of compound **Fc[3]6** (in frozen 2-methyl-THF) (a) absorption spectrum, (b) (differential) Stark spectrum and (c) weighted second-derivative of absorption spectrum. (Data extracted from [24].)

the electronic dipole moment change upon excitation.

Note that the LE band region of the numerically-generated second-derivative of the spectrum in Figure 2.21(c) was scaled up by a factor 4 relative to the HE band region, in order to maintain the relative proportion to the Stark spectrum in this region. This implies that the Stark spectrum is enhanced by a factor of ~ 4 in the LE band region relative to the HE band region, and hence that the LE transition represents a larger degree of CT (i.e. a larger value of $|\Delta\mu|$ by a factor of ~ 2) than the HE transition, which provides additional support for the theoretical model. Quantitative analysis of the spectra in Figure 2.21 [24] yielded the values $|\Delta\mu| \simeq 18$ D (LE) and $|\Delta\mu| \sim 9$ D (HE) (D=debye), which corresponds to the displacement of a single electronic charge e by ~ 3.8 Å and ~ 1.9 Å, respectively, which is in agreement with the displacement of charge suggested by the MOs in Figure 2.19.

It is clear that Stark spectral measurements can provide extremely useful information for quantifying the degree of charge transfer involved in an electronic transition. Moreover, it should be noted that the results derived are generally more applicable to straightforward interpretation than those obtained from other condensed phase techniques, such as the solvatochromism analysis presented for a Fc-B-bpy compound in Chapter 4. Nevertheless, one needs to invest considerable effort and care in the experimental implementation involving optical-quality frozen solutions with high applied electric fields (i.e. of some 100s of kV/cm), especially to obtain artifact-free results with weakly-absorbing species. In any case, it is clear that spectroscopic studies on CT compounds can benefit greatly from this type of spectroscopy, and this would be an important direction for future study of the Fc-B-bpy compounds studied in this work.

We note that although these Fc-based MLCT compounds with conjugated-carbon bridges have been studied intensively for over a decade, no information in the literature could be found concerning their excited-state relaxation dynamics²⁰. A study of the luminescence properties and ultrafast relaxation dynamics of the MLCT states for the π -bridged Fc-donor organic-acceptor derivatives presented in this section poses a very interesting direction for future study, especially to complement parallel studies on the Fc-B-bpy compounds.

2.3. Electronic and spectroscopic properties of relevant organic acceptor compounds

In this section, we provide a brief description of the electronic and spectroscopic properties of the organic acceptor groups (Figure 2.22) which are present in the Fc-B-bpy compounds. The key acceptor group for the Fc-B-bpy compounds studied in this work is the 2,2'-bipyridylboronium cation (as indicated by the generic structure '(R,R')B-bpy', Figure 2.22(c)), whilst another important related derivative studied in Chapter 4 incorporates the acceptor group 'B-dpp' (Figure 2.22(d)), which possesses an even more delocalised π -system than the B-bpy acceptor.

These two acceptors are related to the parent organic groups 2,2'-bipyridine ('bpy', Figure 2.22(a)) and 2,5-bis(2-pyridyl)pyrazine ('2,5-dpp', Figure 2.22(b)), which have been incorporated as acceptors in a wide range of charge transfer complexes (e.g. [131, 102]). In the case of 'B-bpy' and 'B-dpp' a tetracoordinated-B-atom is bonded to the N-atoms of two pyridine rings to form a cationic acceptor group where the positive charge is delocalised over the whole B-bpy system [7] with

²⁰The fact that no time-resolved excited-state study on these π -bridged Fc-donor compounds has been performed was supported by personal communication with one of the key researchers of these compounds, S. R. Marder, Department of Chemistry, University of Arizona.

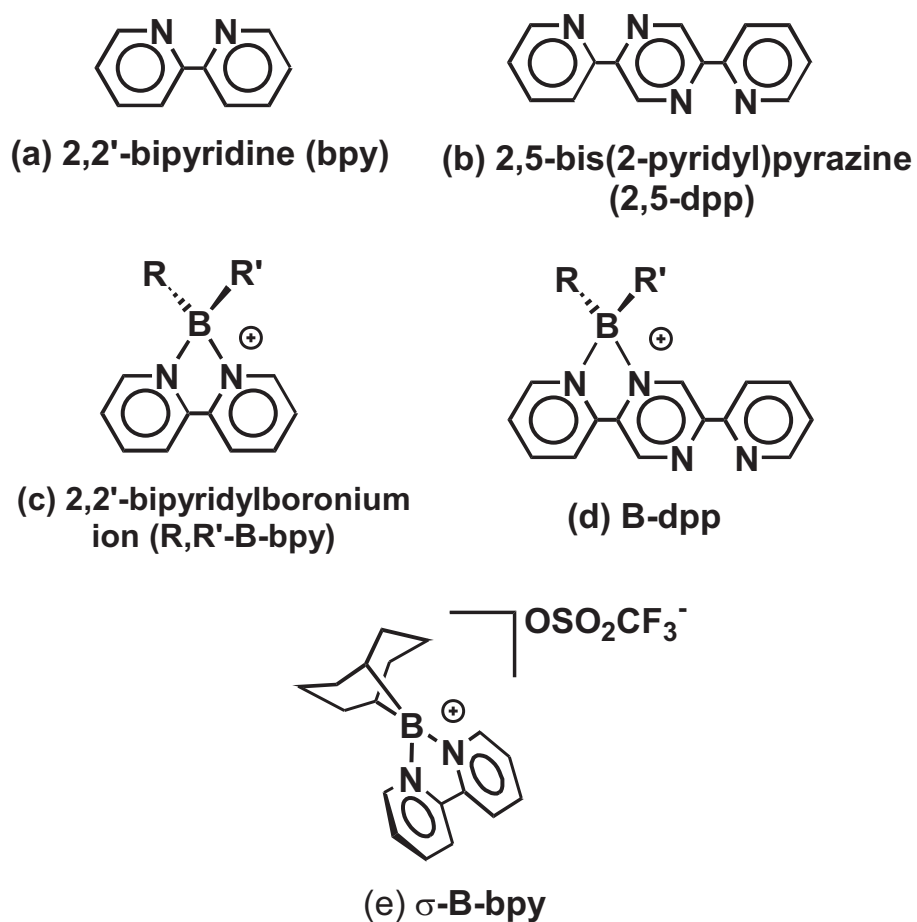


Figure 2.22.: Relevant isolated organic acceptor compounds employed in the Fc-B-bpy compounds.

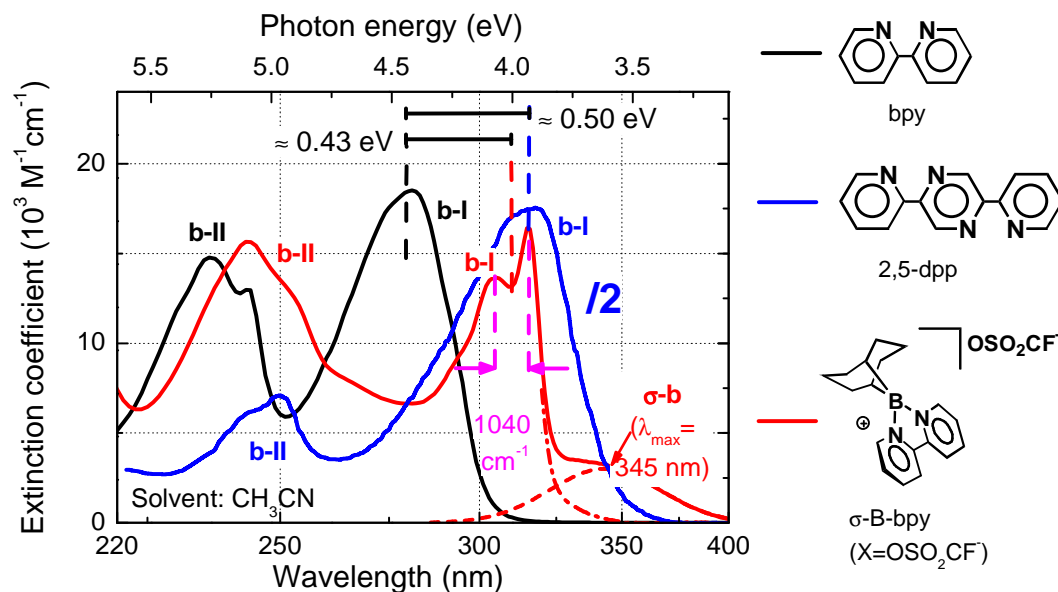


Figure 2.23.: UV absorption spectra of relevant bpy-derivative acceptor groups, including a comparison of the neutral bpy and prototype cationic acceptor σ -B-bpy. For σ -B-bpy a Gaussian band fit to the lowest-energy absorption region (labelled ' σ -b') and residual is shown. (Note that vertical scale for 2,5-dpp has been reduced by a factor of 2. Data for 2,5-dpp extracted from [132]).

ductive bonding from the N-atoms to the B-atom. These acceptors are incorporated into the Fc-B-bpy compounds via attachment to a Cp ring of the Fc group using one of the two additional substituent sites (R). In order to obtain the spectroscopic properties of the isolated B-bpy acceptor groups, the compound ' σ -B-bpy' (Figure 2.22(c)) was synthesised, where the fully-saturated carbon structure is expected to have only a weak effect on the spectroscopic properties of the B-bpy unit. Further details were available from existing studies on the bpy and 2,5-dpp acceptors [132, 133] as well as a report on the (spectro-)electrochemical properties of various derivatives of R,R'-B-bpy [134].

A comparison of relevant UV absorption spectra is provided in Figure 2.23. The lowest-energy absorption band of bpy (labelled 'b-I') occurs at $\lambda_{\max} = 280$ nm ($\epsilon_{\max} = 18400$ M⁻¹cm⁻¹), with a second absorption band ('b-II') in the range 220-250 nm, both of which are assigned to $\pi - \pi^*$ transitions involving orbitals that are delocalised over both pyridine rings [131]. Analogous bands are present for both 2,5-dpp and the cationic σ -B-bpy, which shows that the delocalised positive charge in σ -B-bpy still results in similar HOMO-LUMO orbitals for the system. Considering 2,5-dpp, the b-I band peak is red-shifted some 0.5 eV relative to bpy, with an increase in oscillator strength by a factor of ~ 2 , which results from the greater delocalisation of the π -orbitals over the three aromatic rings and a correspondingly larger transition dipole moment. Comparing the bands for σ -B-bpy relative to bpy, one observes a red-shifting of both bands b-I and b-II relative to bpy (with a red-shift of ~ 0.43 eV for the b-I band), although only small changes in relative absorption strength are observed. Note also that a resolvable vibrational structure (with a spacing of $\Delta\nu \sim 1040$ cm⁻¹) can be observed in the b-I band of σ -B-bpy in contrast to bpy, which can be attributed to the increased rigidity of the bpy conformation enforced by the presence of the N-B-N substructure (similar vibrational structure is observed for other bipyridines upon addition of a common

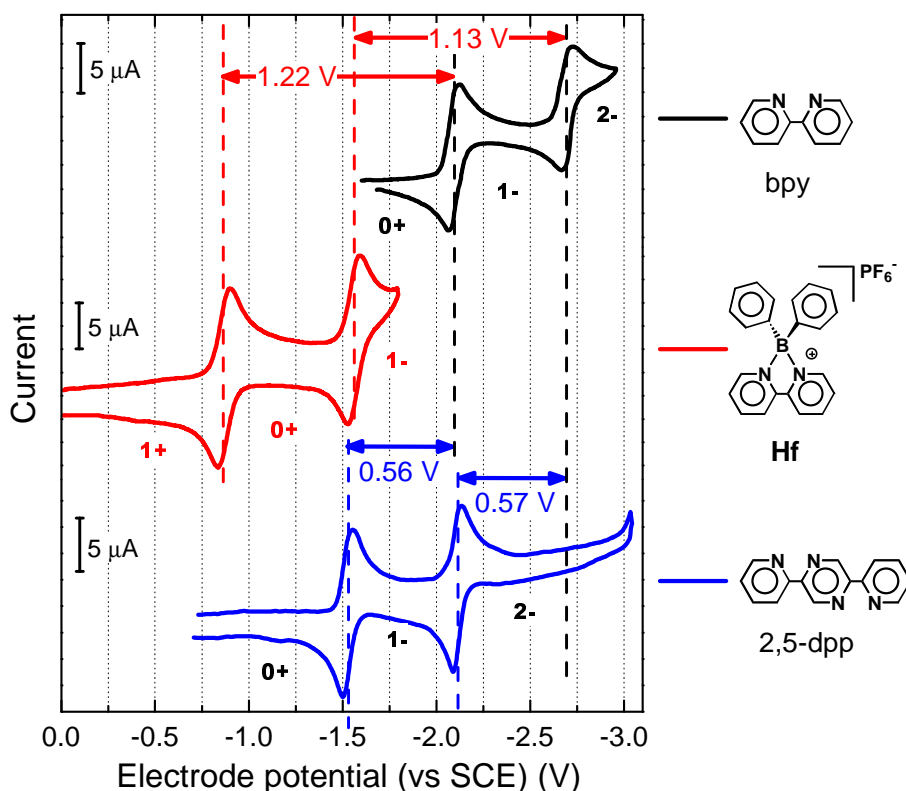


Figure 2.24.: Cyclic voltammograms for bpy, **Hf** and 2,5-dpp. (Data for bpy and 2,5-dpp extracted from Ref.s [133] and [131], respectively).

atom bonded to both N-atoms [132]). The weaker band (σ -b) on the red-edge of the spectrum for σ -B-bpy was not reported for other related B-bpy derivatives and may be due to a residual impurity in the sample. A Gaussian fit to this band (and the residual absorption after subtracting this fitted band) is included in Figure 2.23 to aid in comparison with the other spectra.

The corresponding electrochemical data for bpy, 2,5-dpp and a (Ph)₂-B-bpy derivative (**Hf**)²¹ are shown in Figure 2.24. In comparing bpy and 2,5-dpp, we note that the first reduction potential for 2,5-dpp is shifted to less negative potential by 0.56 V relative to bpy, indicating a corresponding stabilisation of the LUMO energy in 2,5-dpp relative to that of bpy. Hence the red-shift of the b-I band for 2,5-dpp relative to bpy (Figure 2.23) is due predominantly to a stabilisation of the corresponding LUMO, with only a small shift between the HOMO energies of bpy and 2,5-dpp.

Most striking is a comparison of the reduction potentials between bpy and the B-bpy cation **Hf** (Figure 2.24), which shows that the first electron addition for **Hf** occurs at 1.22 V less negative potential than for bpy, indicating that the LUMO energy is significantly stabilised for the cationic acceptor (consistent with its positive charge). A comparison of the literature data [134] allows an estimate of the expected shift of the reduction potential for σ -B-bpy relative to bpy, i.e. also strongly shifted to less negative potential by a similar magnitude (i.e. ~ 1.14 V). This significantly lower LUMO energy for the B-bpy derivatives is an important property for their use as acceptor groups in CT compounds, where a lower energy CT band will result (e.g. see Figure 2.5).

²¹Note that data for the compound **Hf** was reported in [134] as well as being measured by a collaborating group (Professor Zanella, University of Siena).

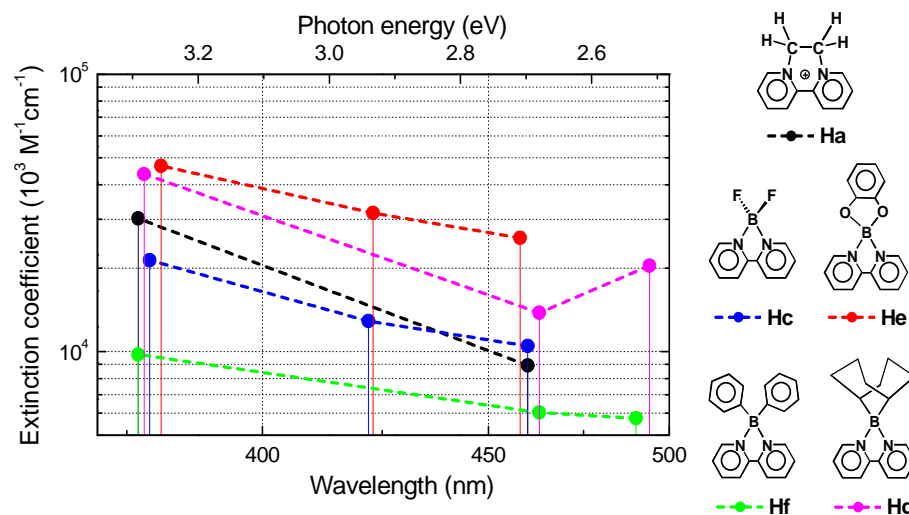


Figure 2.25.: UV-vis absorption peak positions for various B-bpy derivatives (in CH_3CN) following electrochemical reduction (i.e. in their neutral state). Counteranions (PF_6^-) not shown. (Data extracted from [134]). Note that the two lowest energy bands are blue-shifted for the electron-withdrawing compounds (**Hc** and **He**) relative to compounds **Hf**/**Hg**. Compound **Hg** is identical to σ -B-bpy except for the different counteranion.

A final important result that we will refer to in Chapter 4 and 5 is the position of the absorption bands that occur in the B-bpy acceptors upon the first electrochemical reduction. The peak wavelengths of the absorption bands for a range of these (neutral) B-bpy derivatives were tabulated in Ref. [134] and are shown in Figure 2.25. As can be seen by the band energies, the electron addition leads to new absorption peaks which are red-shifted relative to the b-I and b-II bands of the cationic form (Figure 2.23). However, the lowest-energy absorption peak position depends critically on the nature of the substituents attached to B. For the case of electron-withdrawing substituents (**Hc** and **He**) the lowest energy absorption peaks are strongly blue-shifted to 460 nm and 458 nm, respectively, relative to the case of aromatic/alicyclic substituents in **Hf** and **Hg**, where the lowest energy transitions are at 490 nm and 494 nm, respectively.

In Section 4.5.3 we will present the corresponding spectra for the Fc-B-bpy complexes following electrochemical reduction of the B-bpy groups, which leads to absorption bands with positions very similar to those of **Hf** and **Hg**. In contrast, in considering the MLCT excited-state of the Fc-B-bpy compounds in Chapter 5, we treat the excited-state as a combination of a simultaneously oxidised-Fc-donor attached to a reduced-B-bpy acceptor. In this case, the oxidised Fc connected to the reduced B-bpy should resemble more closely the situation of an electron-withdrawing substituent as per the case of **Hc** and **He**, and any excited-state absorption due to localised transitions on the B-bpy acceptors should be blue-shifted to higher energy (i.e. ~ 460 nm), which will be shown to be consistent with the excited-state spectra in Chapter 5.

3. Ultrafast spectroscopy: system design and characterisation

In this chapter the elements of the femtosecond broadband spectroscopy system used for the measurements in Chapter 5 are presented, including an overview of the pulse sources used (i.e. white-light continuum and non-collinear optical parametric amplifier (NOPA)) and the measurement system, with a brief discussion of the time-resolution and coherent artifacts for the measured transient absorption signals.

3.1. Femtosecond optical pulse sources

3.1.1. Regenerative amplifier laser

The femtosecond broadband optical pulse sources used for the measurements presented here all employ the output of a 1-kHz-repetition-rate regenerative amplifier laser (Clark-MXR CPA-2001) as the pump-pulse source. A schematic for this laser system is given in Figure 3.1. As shown, an Er-doped fibre laser followed by a high-efficiency second-harmonic-generation (SHG) stage (frequency doubler) produces a high-repetition (~ 25 MHz) pulse train of 150-fs-duration seed pulses with a centre wavelength of 775 nm. A frequency-divider produces a 1-kHz signal frequency-locked to this pulse-train. This 1-kHz signal triggers an intracavity-doubled Q-switched YAG laser which produces 8-mJ pulses (of some 100s of ns pulse length) at 532 nm, which pump a Ti:sapphire crystal in the regenerative-amplifier cavity. The 1-kHz signal also triggers a Pockels cell which couples a single seed pulse from the 25-MHz pulse train into the cavity, where it experiences amplification from the inversion created in the Ti:sapphire crystal. After the cavity amplification saturates, the pulse is coupled out by a second switching of the Pockels cell, with an output pulse energy of typically $\sim 800 \mu\text{J}$ (centre wavelength: 775 nm, pulse duration: ~ 150 fs (FWHM)). Note that due to the high instantaneous intensity of the amplified pulse in the cavity, the seed pulse passes through a grating pulse-stretcher before entering the cavity (which greatly reduces the peak intensity, and avoids damage to the intra-cavity optics) and is subsequently re-compressed after leaving the cavity. Due to the use of such a temporally-dispersed (or ‘chirped’) pulse in the amplifier cavity, this technique is referred to as ‘chirped-pulse amplification’. The two main issues for the CPA performance that required careful attention for its use as a pump source for the subsequent nonlinear pulse generation (i.e. NOPA and white-light-continuum generation) were (i) the beam profile, and (ii) the presence of slow drifts in output power (on a time scale of hours) – both of these had a critical influence on the stability of the subsequent pulse generation mechanisms.

3.1.2. White-light continuum pulse generation

In general, all media demonstrate a third-order non-linear response in the polarisation (characterised by the non-linear susceptibility, $\chi^{(3)}$ [135]) for sufficiently intense optical radiation. When an ultrashort pulse is focussed into such a medium, one of the resulting effects is an intensity-dependent (spatiotemporal) refractive index change, which (for most materials) leads to an increased refractive index on the beam axis. This leads to a distortion of the wavefronts corresponding to a stronger focussing of the beam, i.e. self-focussing [135, 136], which causes a rapid

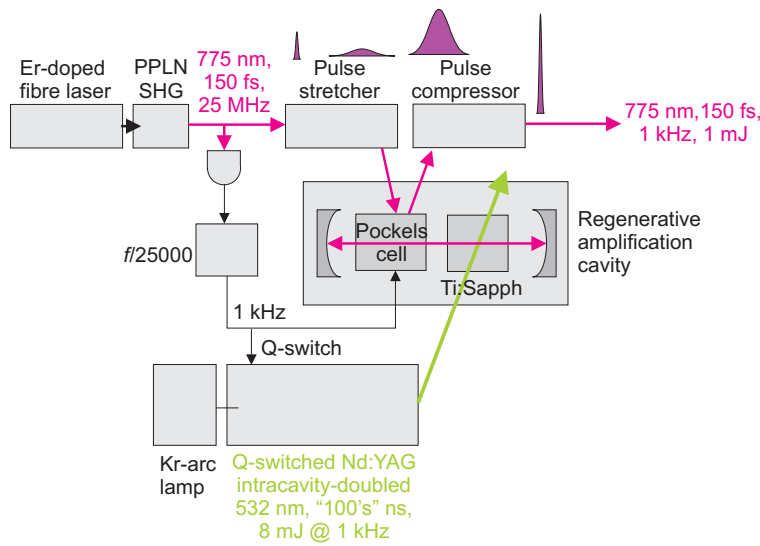


Figure 3.1.: Schematic for the commercial regenerative amplifier laser system (Clark-MXR CPA-2001) based on chirped-pulse amplification.

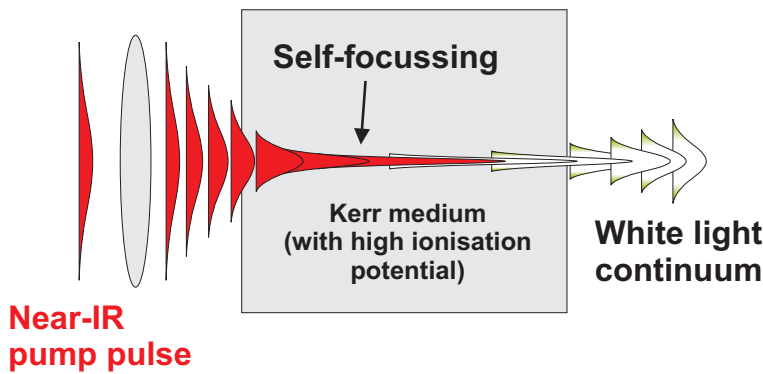


Figure 3.2.: Generation of white-light continuum by self-focussing of femtosecond near-IR pulses in a large-band-gap dielectric medium (e.g. sapphire), followed by higher-order non-linear processes resulting in the generation of a broad white-light pulse.

collapse of the beam profile to a thin filament with an extreme peak intensity ($\sim 10^{13} \text{ W cm}^{-2}$), as depicted in Figure 3.2. Due to an interplay of self-phase modulation (SPM), dispersion and higher-order nonlinear effects, these high intensities lead to the generation of a white-light (WL) continuum pulse [135, 136, 137, 138], which for near-IR femtosecond pump pulses has a spectrum predominantly on the blue-side of the pump wavelength [136].

A typical spectrum of these WL pulses is shown in Figure 3.3, which was generated by focussing $\sim 2 \mu\text{J}$ of each pulse from the CPA (as described above) into a 3-mm-thick sapphire disk (using a lens with a focal length of 30 mm, diameter 22.4 mm). As can be seen, the spectrum extends down to $\lesssim 450 \text{ nm}$ and the total conversion efficiency in the range 450-750 nm is $\lesssim 1\%$. These WL pulses are employed directly as the probe pulses in the pump-probe system described in this chapter, as well as the seed light for the NOPA. We note the photon spectral density (per pulse) is rather low ($\sim 10^8 \text{ photons/nm}$), which needs to be considered when using the WL pulses for optical measurements, where the fluctuations due

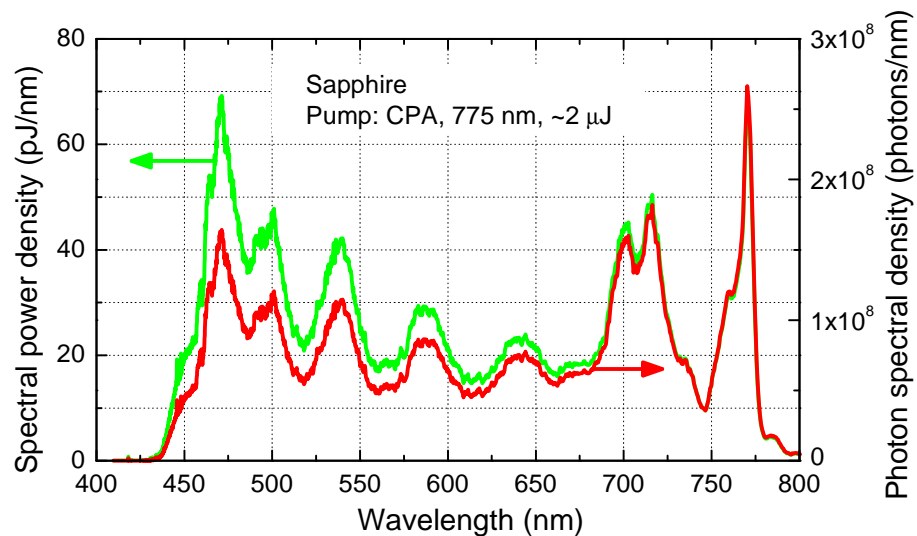


Figure 3.3.: Calibrated spectrum of white-light continuum pulses generated in a 3-mm sapphire disk (with extraordinary axis normal to the surface) using a near-IR regenerative amplifier pump-pulse (CPA 2001, 775 nm, ~ 150 -fs pulse duration, $\sim 2 - \mu\text{J}$ pulse energy). Calibration involved absolute-power measurements through a range of interference filters with known spectral transmission. Residual 775-nm pump light suppressed with short-pass optical filter.

to single-shot photon noise can become significant [139]. Moreover, from measurements of the spectrally-resolved beam profile, the divergence and beam diameter of the white-light were determined to be wavelength-dependent, such that subsequent collimation and refocussing of these beams should involve fairly long focal lengths to avoid significant chromatic aberrations (or ‘spatial chirp’). Specifically, for a 30-mm NIR-pump focus, a collimating optic with a focal length of 70-100 mm is preferable ¹.

3.1.3. Second harmonic generation (SHG)

In non-centrosymmetric crystals, there is a second-order non-linear response in the polarisation to incident electric fields, i.e. $P^{(2)}(t) = \varepsilon_0 \chi^{(2)} E(t) \cdot E(t)$ (assuming an instantaneous response), which for an incident optical field leads to a mixing of each frequency component pair (ω_1, ω_2) in the spectrum of $E(t)$ to produce new waves at $\omega_1 - \omega_2$ (difference-frequency generation, DFG) and $\omega_1 + \omega_2$ (sum-frequency generation, SFG) [135, 139, 138]. For a single incident optical pulse (with a centre frequency ω_0), this SFG corresponds to the generation of a second pulse with a centre frequency $(2\omega_0)$ (and hence photon energy) twice that of the incident pulse. As mentioned above, this effect is referred to as second harmonic generation (SHG). The SHG process is used in the NOPA (described in Section 3.1.5) to convert the incoming near-IR (775-nm) pulses into near-UV pump pulses required for the OPA process.

Moreover, the SHG effect can be exploited in the measurement of pulse durations [138, 139]. If an optical pulse (described by $E(t)$) and a delayed replica ($E(t - \tau)$)

¹For the measurements presented in Chapter 5, a collimating off-axis paraboloidal mirror with an effective focal length of 25.4 mm was used, although test measurements with dye samples were performed to confirm that the chromatic aberrations of the white light did not lead to a significant distortion of the measured signals.

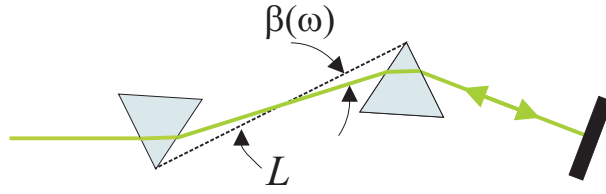


Figure 3.4.: Double-pass prism-pair compressor, with an inter-apex distance L between the two prisms, with the intermediate ray at frequency ω crossing the inter-apex line at an angle $\beta(\omega)$.

overlap at a small angle (i.e. in the absence of temporal interference) in a (thin) SHG crystal, then a component of the SHG signal is given by $E_{AC} \propto E(t)E(t - \tau)$ [139]. This signal has a corresponding time-integrated intensity,

$$I_{AC} \propto \int_{-\infty}^{\infty} dt I(t) I(t - \tau), \quad (3.1)$$

which is the intensity autocorrelation of the pulse $E(t)$.

3.1.4. Prism compression and autocorrelation

Given an optical pulse (centre frequency ω_0) with spectral intensity $I(\Omega)$ and a spectral phase $\varphi(\Omega)$ (where $\Omega = \omega - \omega_0$), the corresponding variance of the temporal intensity (i.e. pulse width) is minimised for $\varphi(\Omega) = A + B\Omega$ (for any $A, B \in \mathbb{R}$), i.e. for a constant (or linear) spectral phase (A and B only dictate the absolute carrier phase and temporal position of the optical pulse, respectively) [138]. Such a pulse is said to be ‘transform-limited’.

When the optical pulse propagates through a transparent medium with thickness L and refractive index $n(\omega)$, an additional spectral phase is acquired, $\varphi(\Omega) = k(\omega_0 + \Omega)L$ where $k(\omega) = n(\omega)\omega/c$ is the wavevector (magnitude). Expanding this phase about the centre frequency gives,

$$\varphi(\Omega) = \left[k(\omega_0) + k'(\omega_0)\Omega + \frac{1}{2}k''(\omega_0)\Omega^2 + \frac{1}{6}k'''(\omega_0)\Omega^3 + \dots \right] L \quad (3.2)$$

such that the first terms which lead to temporal broadening of the optical pulse are the group dispersion delay (GDD), $\varphi''(\Omega) = \frac{1}{2}k''(\omega_0)\Omega^2 L$ (where $k''(\omega_0)$ is referred to as group velocity dispersion (GVD)), and the third-order delay $\varphi'''(\Omega) = \frac{1}{6}k'''(\omega_0)\Omega^3$ (where $k'''(\omega_0)$ is referred to as the third-order dispersion (TOD)). For most dielectric materials in the near-UV/vis range, $k''(\omega_0) > 0$ (positive GVD), so that in order to compensate for the dispersion of optics between the pulse source and the sample in an experiment, an optical system which possesses a variable negative GVD is required.

The simplest construction to achieve this is a prism-pair compressor [140, 141], shown in Figure 3.4. For any given frequency component of the incident optical pulse, the net phase shift through this system (assuming a double pass) is $\varphi(\omega) = (2\omega L/c) \cos(\beta(\omega))$ [141], where $\beta(\omega)$ is the wavelength-dependent angle formed between the intermediate ray between the two prisms and the line connecting the apex of each prism. Taking the second derivative of this phase shift results in,

$$\frac{d^2\varphi}{d\omega^2} = \left(\frac{2L}{c} \right) \left[- \left(2 \frac{d\beta}{d\omega} + \omega \frac{d^2\beta}{d\omega^2} \right) \sin(\beta) - \omega \left(\frac{d\beta}{d\omega} \right)^2 \cos(\beta) \right]. \quad (3.3)$$

The second term in the square brackets is necessarily negative and for small β will dominate, resulting in a net negative-GDD contribution which can be used to eliminate the positive-GDD introduced by other optics in the system. Note that a given target negative-GDD can be achieved over a continuous range of configurations of the two prisms (due to the dependence on both L and β), i.e. by varying the distance between the two prisms and the amount of prism glass the beam passes through. In this case, we consider the contribution to the TOD from the prism-pair. For a simple prism-pair and materials such as SF10 (used in the experiments in this work) for the typical prism configuration needed to compensate the GDD from the other optics, the TOD of the prism compressor is generally more *negative* than the corresponding positive-TOD from the dispersive optics in the system [141]. Given that the negative-TOD of the prism-pair increases with the inter-apex distance, L , the optimal experimental configuration is to reduce L as far as possible (until the practical limit for the minimum amount of prism glass traversed is reached). We note that for other prism materials, such as fused-silica, the residual negative-TOD is smaller than for SF10, allowing superior pulse compression. However, the required inter-apex distance for a fused-silica prism-pair (to eliminate the typical levels of GDD, i.e. $L \sim 1 - 2$ m) is far larger than that for SF10 (10s of cm), such that SF10 is a more practical choice if reaching the absolute minimum pulse duration is not essential. In the case of more complex pulse compression constructions (involving a combination of multiple prisms/gratings), even more control of the dispersion compensation (including over a wider bandwidth) is possible at the expense of more involved optimisation procedure.

The prism compression is used to achieve the shortest possible pulse duration at the sample position (i.e. including pre-compensation of the positive-GDD between compressor and sample). Many experimental techniques exist in order to measure the duration of femtosecond optical pulses (for obtaining optimal compression and determining the corresponding time-resolution of the experiment) [142, 143, 144], with the simplest being methods of ‘intensity autocorrelation’ (AC) [139] (c.f. Eq. 3.1).

The two implementations for measuring the pulse AC used in this work are shown in Figure 3.5. A Mach-Zehnder-type interferometer assembly is used to produce two beams composed of the input optical pulse $E(t)$ and a variably-delayed replica ($E(t-\tau)$) with the relative delay τ controlled by a rapid-scanning computer-controlled delay stage. The use of two (1-mm-thick ultra-broadband metallic) beam-splitters in this way incurs the same small degree of material dispersion for the two pulse replicas, with a paraboloidal mirror used for focusing to avoid incurring any further dispersion².

For generating the AC signal, the first method involves the use of SHG in a β -barium-borate (BBO) crystal to generate an AC optical signal (Section 3.1.3) which is detected by a UV-sensitive detector and sent to a (12-bit) boxcar-integrator for recording the signal. We note that for optical pulses with centre wavelengths in the range 500-550 nm and bandwidths of ~ 15 nm (corresponding to a transform-limited (FWHM) pulse width of 20-30 fs), the material dispersion between the input and generated SHG pulse requires the use of a BBO crystal no thicker than 100 μm .

The second method for generating the AC signal involves the use of two-photon-absorption (TPA) directly in the detection element of a photodiode [144], where the detection element is a material with a band-gap larger than the photon energy

²Note that the autocorrelator is used at a position in the pump-probe measurement system (Section 3.2) such that the material dispersion from the beamsplitters is approximately matched to the material dispersion incurred in reaching the sample.

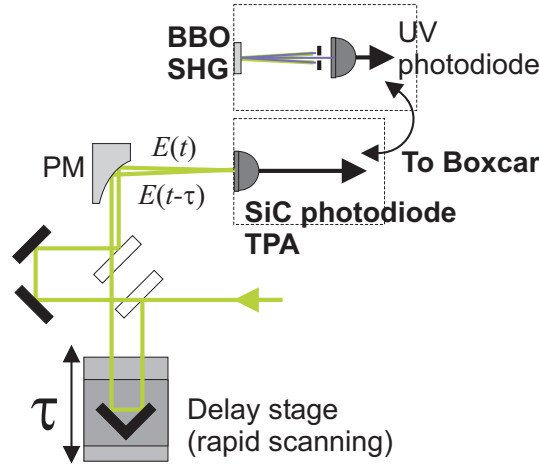


Figure 3.5.: Schematic of real-time non-collinear intensity autocorrelator (with balanced dispersion employing either (i) two-photon absorption (TPA) directly in a SiC photodiode, or (ii) measurement of the SHG cross-signal from a thin BBO crystal).

of the fundamental pulse (such that the linear absorption signal is negligible). In this case, the instantaneous generation of photocarriers in the photodiode is given by $i_{\text{TPA}} \propto (I(t) + I(t - \tau))^2$, which contains the cross-term $i_{\text{AC}} \propto I(t)I(t - \tau)$. Hence a measurement of the time-integrated photodiode signal vs delay τ also yields the intensity AC (Eq. 3.1) of the optical pulses. For pulses with centre wavelengths in the range 460-600 nm, a suitable choice of detector material is SiC [144]. Three practical advantages of the use of a TPA photodiode (over SHG in a BBO crystal) are (i) the low cost and simplicity of implementation, (ii) the wide bandwidth over which a single device can be used, and (iii) the fact that if a TPA photodiode with an active area slightly smaller than the focussed input beams is used, then spatial overlap of the two beams is achieved very simply by maximising the TPA signal from each beam alone. However, it should be noted that due to saturation of the TPA signal for large signals, only a very weak input pulse energy should be used, to avoid distortion of the measured AC signal (which will result in a significantly broadened width of the measured AC trace). This limits the maximum signal-to-noise (in a given measurement time) for TPA-based autocorrelations.

The measurement of the intensity-AC signal does not provide a unique determination of the optical pulse shape (or spectral phase). However, if a certain temporal pulse profile is assumed, then there is a well-defined relation between the width of the measured AC signal ($T_{\text{FWHM}}^{\text{AC}}$) and the temporal intensity profile of the optical pulse (T_{FWHM}). For transform-limited pulses, the ratio $T_{\text{FWHM}}^{\text{AC}}/T_{\text{FWHM}}$ for several common pulse shapes can be derived analytically [139]. For a Gaussian intensity profile ($I(t) \propto \exp(-4 \ln(2) t^2/T_{\text{FWHM}}^2)$) we have $T_{\text{FWHM}}^{\text{AC}}/T_{\text{FWHM}} = \sqrt{2}$, whereas for a hyperbolic-secant pulse ($I(t) \propto \text{sech}^2(-2 \ln(1 + \sqrt{2}) t/T_{\text{FWHM}})$), $T_{\text{FWHM}}^{\text{AC}}/T_{\text{FWHM}} \approx 1.55$.

3.1.5. Non-collinear optical parametric amplifier (NOPA)

For pump-probe measurements, an ultrashort pump pulse tuned to the absorption wavelength of the sample under study is required. Such tunable pump pulses in the visible and near-IR (460-1600 nm) can be obtained using a non-collinear optical parametric amplifier (NOPA) [145, 146]. For the research work, we employed both

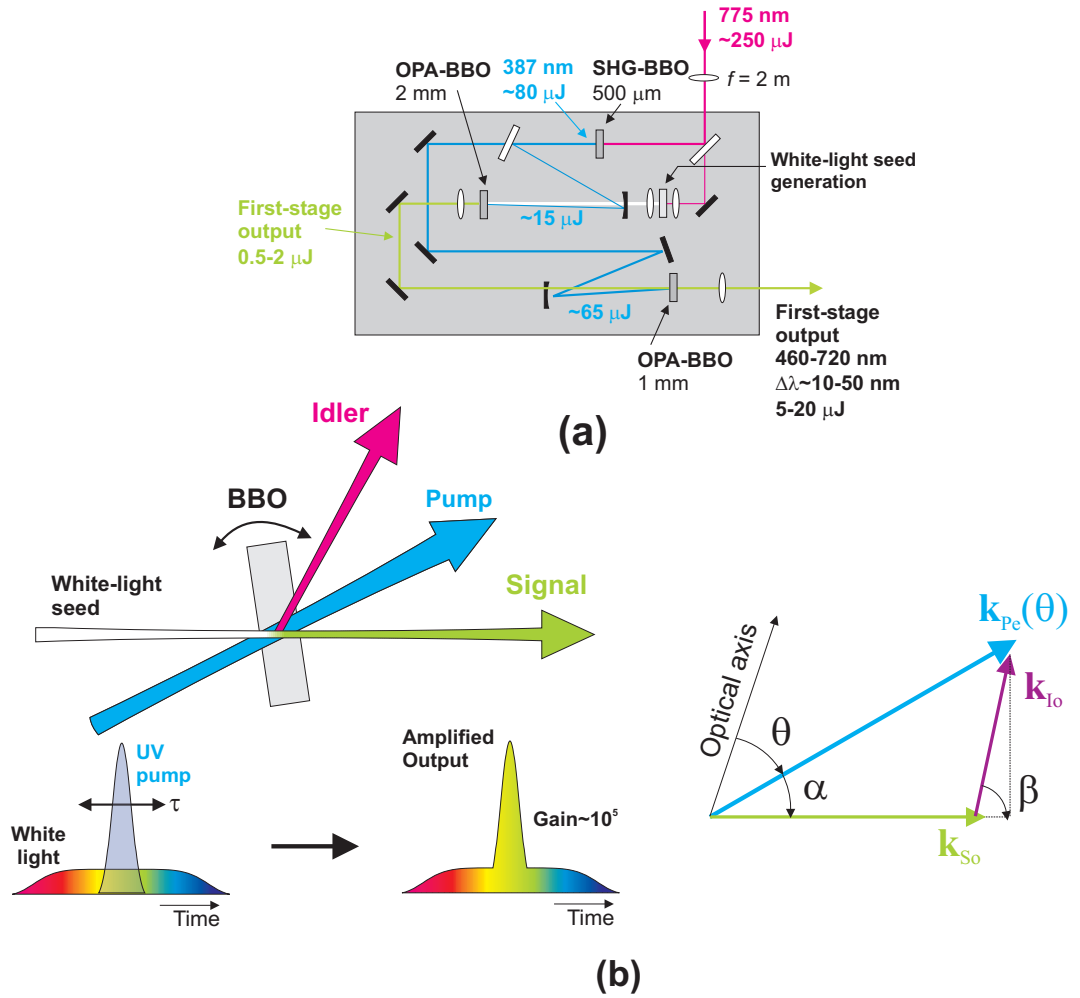


Figure 3.6.: (a) Schematic of a non-collinear optical parametric amplifier with two cascaded amplification stages. (b) Beam geometry for non-collinear parametric process with near-UV pump pulse (387.5 nm) and white-light-continuum seed, showing amplified bandwidth of white light.

a commercially-obtained NOPA as well as a home-built version of similar design. The layout of these NOPAs is shown in Figure 3.6(a), with the relevant schematic of the optical parametric amplification process in Figure 3.6(b).

The optical parametric amplification (OPA) process involves the down-conversion of photons in a near-UV pump pulse (with centre frequency ω_p) into a signal (ω_s) and idler (ω_i) pulse in a second-order nonlinear medium (in this case a BBO crystal), with conservation of photon energy dictating that $\omega_p = \omega_s + \omega_i$ [146]. The near-UV femtosecond pump pulses (in this case, at 387 nm) are generated by frequency-doubling of the near-IR pulses (775 nm) from the regenerative amplifier laser in an SHG crystal (in this case, using a 10-mm-aperture, 0.5-mm-thick BBO). In order to provide a significant gain for the process, a seed-light source is required, which is provided by a white-light continuum pulse (Section 3.1.2) covering the wavelength range of the required signal pulse. Due to residual dispersion in the WL generation process, the WL components are temporally dispersed (i.e. ‘chirped’). Both UV-pump and WL seed pulses are spatially overlapped into a BBO crystal, with the relative delay tuned to achieve temporal overlap of the UV pump pulse with the target signal wavelength range.

Besides the conservation of photon energy, the OPA process must also conserve photon momentum (or, equivalently, the vectorial sum of the photon wavevectors must satisfy $\mathbf{k}_p = \mathbf{k}_s + \mathbf{k}_i$, as represented graphically in Figure 3.6(b)), which is referred to as ‘phase-matching’. The signal amplification of the OPA process includes a phase-matching factor $L^2 \text{sinc}^2(\Delta k L/2)$ where L is the interaction length in the mixing crystal and $\Delta \mathbf{k} = \mathbf{k}_p - \mathbf{k}_s - \mathbf{k}_i$ is the wavevector mismatch [139].

In order to satisfy this phase-matching condition, one needs to utilise a birefringent crystal (due to the fact that for a common polarisation one has $k_p > k_s + k_i$ for the wavelengths considered). For a negative-birefringent crystal [139] (such as BBO, where the extraordinary and ordinary refractive indices satisfy $n_e < n_o$) the UV-pump pulse is linearly polarised along the extraordinary axis, such that the magnitude of the wavevector k_p can be controlled by the angle of propagation θ to the optical axis of the crystal [139].

An important degree of freedom is introduced by employing non-collinear beam geometries, i.e. with an angle between the propagation direction of the pump and signal beams (α). This allows the phase-matching condition to be met for a continuous range of beam geometries/crystal rotations (for a signal in the visible range). This added degree of freedom can be exploited to satisfy not only the phase-matching condition $\Delta k = 0$, but also to achieve the broadband phase-matching condition $\partial(\Delta k)/\partial\omega_s = 0$ [146], such that a far greater phase-matched signal bandwidth can be achieved than for a collinear beam geometry. Depending on the BBO crystal used and temporal dispersion of the white-light seed, this bandwidth is sufficient to achieve pulses (after passing through a pulse compression setup) with a duration of 10-25 fs (in the range 460-720 nm).

Due to the energy fluctuations in the WL seed pulse, a single OPA amplification stage can result in considerable signal pulse fluctuations (i.e. 3-5 %). In order to improve the stability of the output, an OPA setup with two amplification stages is used (Figure 3.6(a)) (resulting in reduced relative pulse fluctuations of 1-2%), each using a fraction of the pulse energy of the UV-pump pulses, with the signal output of the first OPA stage forming the ‘seed’ for the second OPA stage.

The spectrum and autocorrelation for the typical NOPA output pulses used in the experiments here is shown in Figure 3.7, which following the optimised prism-pair compressor (SF10 prisms) results in a pulse duration of $T_{\text{FWHM}} \sim 35$ fs. We note that based on the spectral intensity bandwidth of $\Delta\lambda = 15.5$ nm, a Gaussian model predicts a transform-limited pulse duration of $T_{\text{FWHM}} \approx (2 \ln 2/\pi c) \lambda^2/\Delta\lambda_{\text{FWHM}} \approx 24$ fs [138]. The resultant longer pulse width implied by the autocorrelation is a result of the residual uncompensated higher-order phase distortion of the NOPA output (as evidenced by the wings of the autocorrelation trace). Careful tuning of the NOPA and the use of fused-silica prisms allows one to achieve a pulse duration closer to the transform-limit, although for the measurements presented here the resulting experimental time resolution is determined by dispersion of the WL probe pulses, such that further optimisation of the NOPA pump pulse was not beneficial.

3.2. Pump-probe methodology and system design

In order to measure the excited-state transient UV-vis absorption spectra of a molecular sample and obtain a signature for the relaxation dynamics, one can employ a pump-probe scheme, as shown in Figure 3.8(a), where the time resolution of the measurement is limited only by the duration of the optical pulses (with < 50 fs being readily achievable with modern pulse generation techniques). In the pump-probe technique, a fraction of the sample is excited by a pump pulse (tuned to the appropriate excitation wavelength, λ_{ex}), and the differential absorption of a

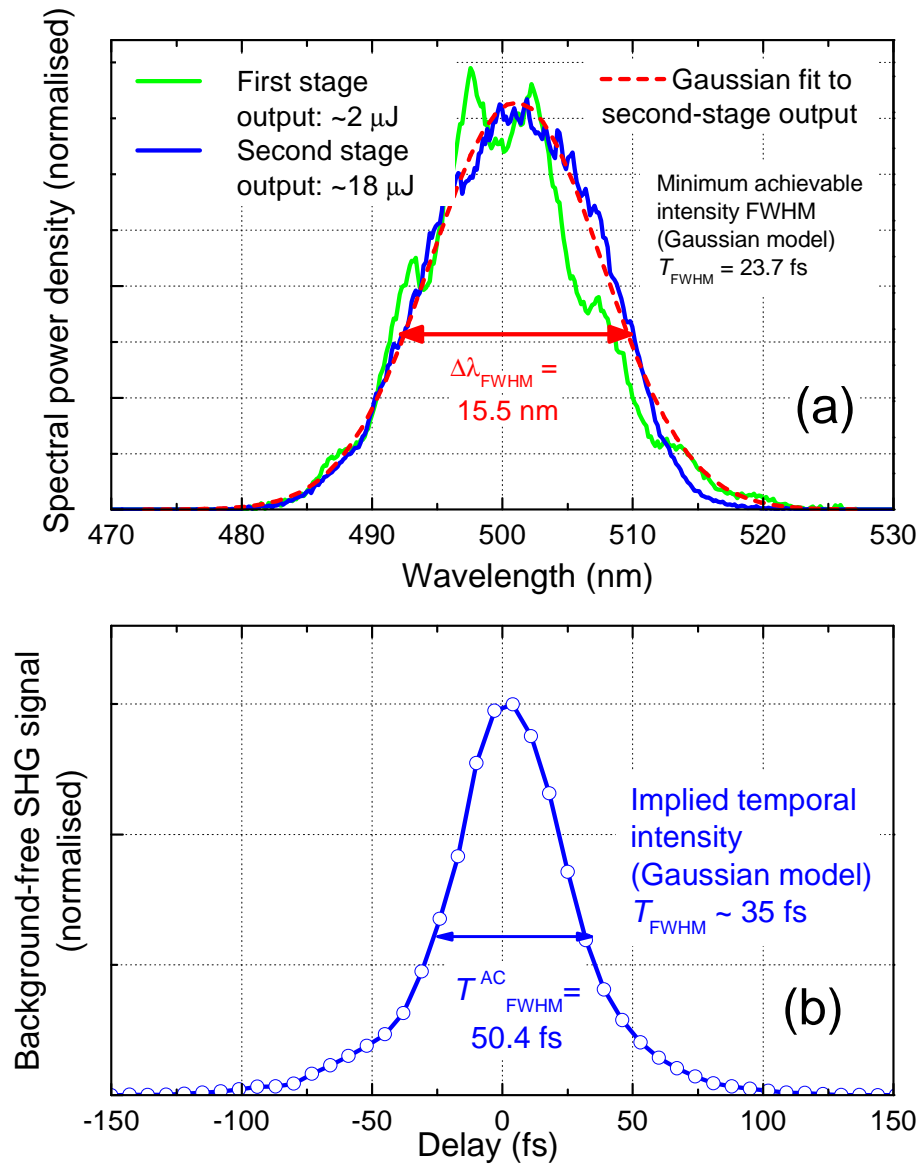


Figure 3.7.: (a) Typical output spectrum for two-stage NOPA (pulse energy $\sim 18 \mu\text{J}$, centre wavelength $\lambda = 500 \text{ nm}$, bandwidth $\Delta\lambda_{\text{FWHM}} = 15.5 \text{ nm}$) including Gaussian fit and spectrum after first-stage amplification). (b) Corresponding intensity autocorrelation (non-collinear SHG signal from $100 \mu\text{m}$ -thick BBO).

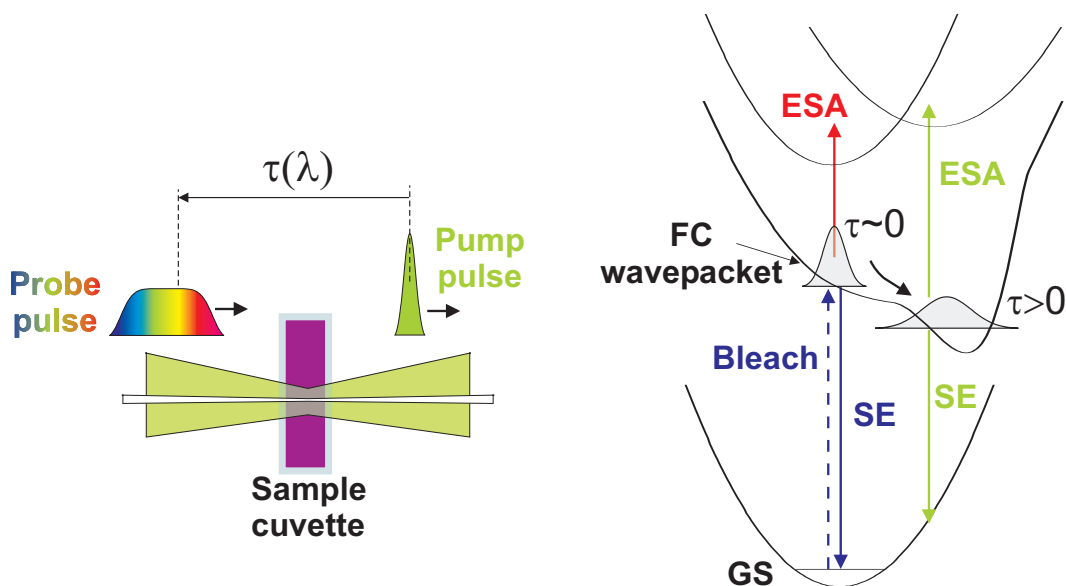


Figure 3.8.: Concept of pump-probe transient absorption measurements. (a) Excitation of sample followed by probing of excited-state absorption changes with variably-delayed broadband WL pulse. (b) Schematic showing various signal components during excited-state evolution: ground-state bleach, stimulated emission to the ground state (SE) and excited-state-absorption (ESA) transitions to higher excited states.

subsequent probe pulse (λ) is measured as a function of the time delay (τ) between the two pulses (which can be varied by changing the relative path length of the two pulses before the sample). The transient absorption signal is composed of several contributions (Figure 3.8(b)), (i) a negative-differential absorption band due to ground-state depopulation (i.e. a ‘bleach’ signal) which will possess the same shape as the ground-state absorption curve (neglecting inhomogeneous broadening), (ii) a negative-differential signal due to stimulated emission (SE) of the excited state (whose spectral properties can change during the excited-state relaxation) and (iii) positive-differential excited-state absorption bands (ESA) involving transitions to higher-lying states. Due to this complex combination of signals, which may overlap at any given probe wavelength, measurement of the transient absorption at only one wavelength (e.g. the ‘degenerate’ case where $\lambda = \lambda_{\text{ex}}$) generally does not yield sufficient information about the corresponding relaxation of the excited state. Hence one usually needs to measure transient absorption *spectra* over a range of probe wavelengths, which facilitates the distinction of characteristic signal bands.

In the design of the measurement system, several options are available, and a subset of these is shown in Figure 3.9. For the probe pulses, one can employ either (i) a WL pulse (Section 3.1.2) or (ii) a tunable pulse source (such as a NOPA, Section 3.1.5). The advantage of using a white-light pulse is that one can in principle measure the transition absorption of the sample across a broad wavelength range in parallel (reducing measurement time), whilst a NOPA must be manually tuned to each probe wavelength of interest. However, the pulse energy for femtosecond WL pulses in a given wavelength interval is limited to much lower levels (i.e. typically < 100 pJ/nm), which results in the measurement of pulse energies where the single-shot quantum fluctuations in the energy can become important for small signals (i.e. with a relative modulation depth of $\sim 10^{-4}$). Moreover, the pulse energy (and spectral) fluctuations are typically larger than for NOPA pulses and

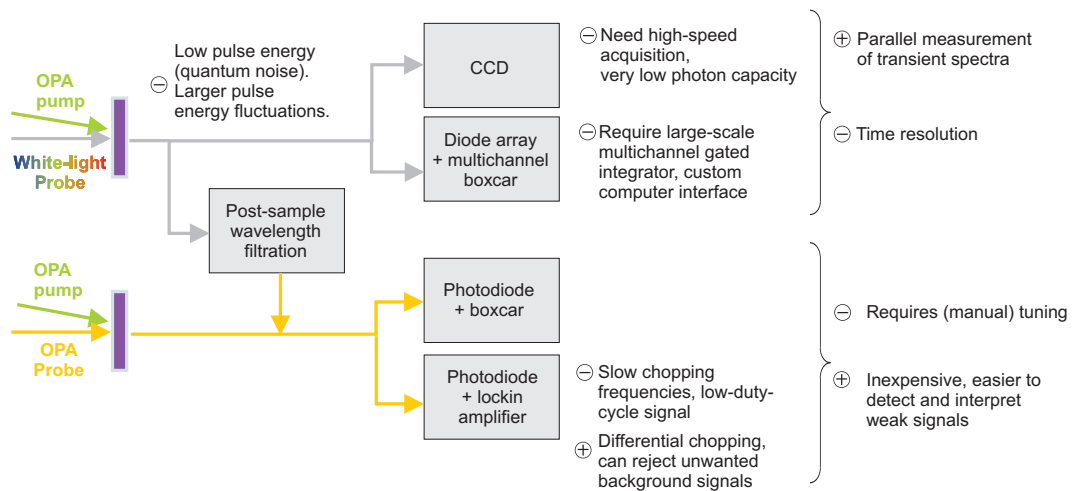


Figure 3.9.: Schematic demonstrating various methods for broadband pump-probe spectroscopy, including single-wavelength vs white-light probing and various post-sample detection options.

normalisation of the signal must be performed carefully on the signal (a discussion of other sources of noise is given below). A major issue in the use of WL pulses is that it is that any dispersive optics will rapidly degrade the time resolution, and the use of simple dispersion-compensating compression techniques (i.e. prism- or grating-based systems) generally cannot rectify the dispersion over the whole spectral range simultaneously. Hence, in using WL pulses, the use of reflective optics for collimating and focussing the WL beam is imperative to maintain a sub-100-fs time resolution (Section 3.3). However, standard reflective focussing optics (i.e. off-axis paraboloidal mirrors) also pose problems (in comparison to lenses) due to aberrations and scattering which degrade the quality of the beam profile.

Following the sample, there are several options for detection of the probe pulse energy (and hence modulation due to the differential absorption of the sample). In the case of a tunable NOPA source (i.e. single probe wavelength), this involves using a single-element photodetector. For the WL pulse, a variable wavelength filter (e.g. monochromator) can also be used in conjunction with a single-element detector (as per the setup used in the experiments presented in this work). The use of single-element detection (or double-element detection in the case where a reference beam is also used for normalisation) allows the use of relatively inexpensive photodetectors and either a boxcar-detector (i.e. a gated integrator) or a lockin-amplifier for registering the detected signal.

Given that the usable probe pulse energy is limited (even for NOPA probe pulses, due to the maximum fluence usable at the sample) and the typical pulse rep-rate in such systems is < 10 kHz, boxcar detection has the advantage that it samples only the peak voltage of the photodetector signal. Hence, a medium-high bandwidth detector can be used (i.e. 1-100 MHz) and the sampled electronic signals are much higher than the average signal (without the need for large amplification factors). For lockin-based techniques, the (average) detected electronic signal is much lower, and the use of electronic amplification is limited by the associated noise penalties. However, we note that lock-in detection can, in principle, possess a far higher dynamic range for the measurement of differential signals due to the use signal averaging in conjunction with optical chopping of the pump and probe pulses (which can also be used to efficiently reject scattered pump signals).

The simplest method for parallel detection of the white-light spectra (following a spectrograph) is a CCD camera. However, despite the low background noise of CCDs, they usually possess very low photon capacities (i.e. $\lesssim 10^6$ photons/pixel) such that single-shot quantum fluctuations of the signal are large, and they are generally not designed to perform well at high acquisition rates (such as the typical 1-kHz pulse repetition rate used in the research work here). In order to obtain the necessary dynamic range and acquisition rates, one can employ a Si-diode array (with typical implementations involving ~ 40 elements). However, the handling of the subsequent parallel electronic signals requires custom multi-channel amplification and sampling electronics, such that this option can be particularly time-consuming and expensive³.

The broadband femtosecond pump-probe setup used for the measurements presented in this work is shown in Figure 3.10⁴. The system is driven by the regenerative-amplifier laser described in Section 3.1.1. A fraction of this output ($250 \mu\text{J}$) is used to pump a two-stage tunable NOPA (Section 3.1.5) which produces the required visible pump pulses ($\lambda_{\text{ex}} = 500 \text{ nm}$ for the measurements presented in Chapter 5) with typical output pulse energies of $10 - 20 \mu\text{J}$, which are compressed using a prism compressor to achieve pulse durations (FWHM) $\sim 35 \text{ fs}$ (at the sample position). The NOPA pump beam passes a computer-controlled mechanical translation stage (which generates the variable pump-probe delay), is reduced to a pulse energy of $\lesssim 100 \text{ nJ}$, and a broadband waveplate is used to prepare the required polarisation relative to the probe polarisation.

A WL pulse (Section 3.1.2) is employed as the probe pulse, using a small fraction ($\sim 2 \mu\text{J}$) of the amplifier laser output for the pump pulses⁵. The WL beam is collimated by an off-axis paraboloidal mirror, and after a 1-mm-thick filter which rejects the 775 nm pump light is split into probe and reference beams (with the probe beam reflected from the front face of the beamsplitter to minimise dispersion).

The NOPA-pump and WL probe beam are brought into parallel alignment with a vertical displacement and focused into the sample using an off-axis paraboloidal mirror. Following the sample, the WL probe beam is recollimated, and sent to one of two detection setups where a small variable wavelength interval ($\Delta\lambda_{\text{FWHM}} \sim 5 \text{ nm}$) is filtered out and detected, in order to measure the corresponding transient absorption for each small probe wavelength range. Two wavelength-selection methods were employed during the research work, as shown in Figure 3.10. The first detection system was based on the use of a prism-pair (SF18 glass, inter-apex separation $\sim 20 \text{ cm}$) to disperse the WL probe light. A variable slit after the prisms mounted on a manual translation stage was used to select the appropriate wavelength range (and bandwidth). Before the prism-pair, a focussing lens ($f = 400 \text{ mm}$) is positioned such that the light is focussed at the position of this slit. We note that despite its low-cost and simplicity (as compared to a aberration-corrected monochromator), this construction provided the necessary wavelength resolution (which could reach down to $\Delta\lambda \sim 1.5 \text{ nm}$). The second post-sample detection setup employed

³Note that another multichannel detector, based on an integrated CMOS array (Hamamatsu) has been investigated, and may be a highly practical alternative to CCDs and diode arrays in that (i) they possess a far higher photon capacity than CCDs, and (ii) the standard integrated electronics deliver a serial signal which can be digitised using a single (or double) channel ADC board.

⁴Note that an overview description of the experimental setup is given here, with the specific parameters used for the presented measurements given in Chapter 5.

⁵Note that another important practical advantage of WL probe pulses is the far smaller pump-power requirement compared to pumping a NOPA (where a vast majority of the output cannot be used in any case, due to the fluence threshold of the molecular samples.)

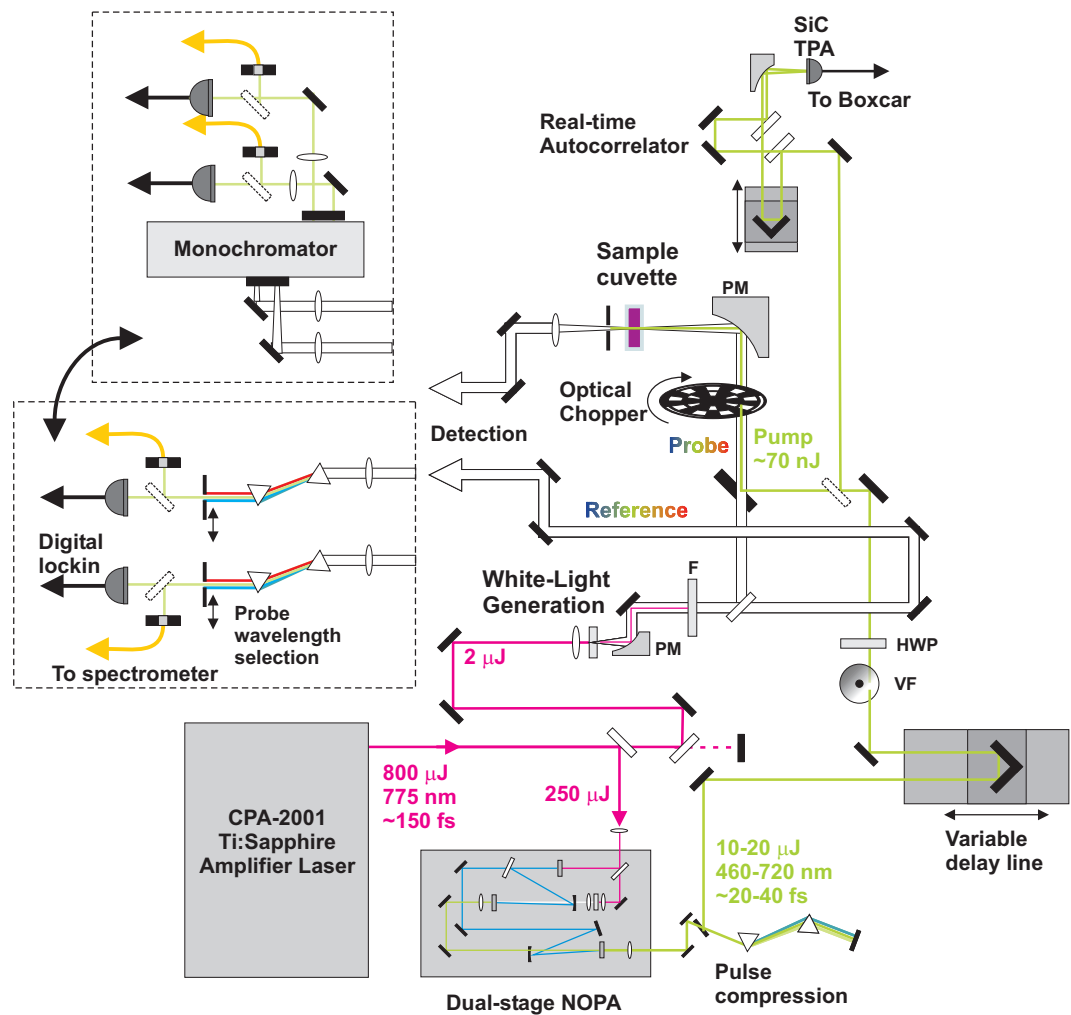


Figure 3.10.: Pump-probe system used for the measurements presented in this work, incorporating (i) a non-collinear parametric amplifier for the visible pump pulses and (ii) WL pulses with different variable post-sample wavelength selection for measurement of the transient spectra.

a computer controlled monochromator in place of the prism-pair. The spectrally filtered beams are then sent to the Si-photodetectors (or optionally directed to a fibre-coupled spectrometer to monitor the filtered spectra).

The measurement of the detected probe (and when used, reference) signals was performed using a digital lock-in amplifier (EG&G 7265). In order to measure the net modulation of the pump-probe signal, different optical chopping methods were used (employing a Thorlabs MC-1000 chopper controller locked to a 1-kHz reference signal from the CPA system). In the earlier measurements, only the pump beam was chopped (at 500 Hz), which rejects the background probe signal in the demodulated lock-in output. However, in this case scattered pump light led to large noise levels for probe wavelengths near the pump wavelength.

We note that normally this problem is combated by the use of differential chopping of both pump and probe beams and lock-in detection at the sum or difference frequency of the two chopping frequencies. However, no suitable commercial product was available for use with the 1-kHz system, where the beams should be chopped at a sub-harmonic of the 1-kHz repetition rate. This led to the design and construction of a custom chopper wheel, with two sets of slots (at different radii on the chopping wheel) which provided a 500-Hz/333-Hz modulation of the probe and pump beams, with a resulting net pump-probe signal at 166 Hz. In order to provide a phase-locked 166-Hz reference signal for the lock-in, we used the frequency-divider built into the front end of the chopper controller to provide a 166-Hz trigger, and then ‘tricked’ the chopper controller to rotate at the required rate with a third set of slots at the outer radius of the chopper wheel (i.e. at the radial position where the optical chopper controller monitors the physical rotation).

In connection with the use of lock-in detection, the photodetector design was particularly critical, due to the very low average power of the filtered WL probe (typically ~ 10 nW). After evaluating many standard photodetectors available in the research group (which were optimised for 100-MHz repetition rate pulse trains with much higher average power), we designed a dual-channel detector based on photodetectors with an integrated 4-kHz-bandwidth FET amplifier (Texas Instruments, Radio-Shack-OPT301M), followed by an additional low-noise amplification stage in the detector housing (with a gain factor of 10). This resulted in $\sim 250 - \mu\text{s}$ electronic signal pulses with a peak voltage of ~ 500 mV (for a detected pulse energy of ~ 10 pJ) as input for the lock-in, with a dark-background noise of 10^{-3} relative to the probe signal (using a 100-ms integration time on the lock-in). However, it should be noted that this dark noise was still the dominant source of noise in the measurements (i.e. more significant than the WL pulse fluctuations for a 100-ms integration time). Hence, for the measurement of the small modulation depths for the Fc-B-bpy samples (with relative modulation depths of $\sim 10^{-4}$), considerable averaging of the transient absorption data was necessary.

3.3. Coherent artifacts and time resolution with white-light continuum probing

The dominant source of coherent artifacts about zero-delay in the transient-absorption signals of solution samples in cuvettes using wavelength-resolved WL probe pulses is due to cross-phase modulation (XPM), i.e. intensity-dependent refractive index changes induced by the pump pulse I_p through third-order non-linear effects [147, 148]. The change in refractive index seen by the probe pulse can be written $\Delta n(z, t) = n_2 I_p(z, t)$ [149], which leads to a deviation in the instantaneous frequency of the probe pulse of $\Delta\Omega(z, t) \propto -\partial I_p / \partial t$. Hence probe wavelength components which overlap temporally with the leading edge of the pump pulse are

red-shifted, whilst those overlapping with the trailing edge are blue-shifted.

As mentioned in Section 3.2, the transient-absorption kinetics are measured by filtering out a small wavelength interval of the WL spectrum after the sample (the same holds in principle whether single-element or parallel-detection is used). Even when the pump pulse does not temporally overlap appreciably with the wavelength interval being measured, the XPM phase modulation leads to a shift in the frequency of neighbouring wavelength regions *into* the measured wavelength interval, giving rise to a structured coherent artifact about the pump-probe zero delay for a given probe wavelength.

An example of these XPM-coherent artifacts (CA) is shown in Figure 3.11 for a pure sample of CH₃CN (in a 1-mm sample-thickness, fused-silica cuvette with 1.25-mm-thick windows). In the case of these earlier measurements, refractive optics (achromatic lenses, $f = 10$ cm) were used for collimating and refocussing the WL beam. The significant temporal dispersion of the WL pulses using refractive optics is evident from the wavelength-dependent position of the centre of each coherent artifact.

Before treating the temporal distribution of the artifacts further, we inspect the dependence of the CA on the relative polarisation between pump and probe in Figure 3.12. Unlike certain CAs that arise in solid-state time-resolved spectroscopy (arising from coherent interference between parallel-polarised pump and probe, which can be largely suppressed by the use of perpendicular polarisations), the XPM-CA persists even for perpendicular polarisation. This is to be expected, due to the fact that in an isotropic medium the magnitude of XPM induced for light with the orthogonal polarisation is given by 1/3 that for parallel polarisations [149]. This reduction in the magnitude of the XPM-CA is reflected in Figure 3.12. Note that in order to eliminate the effects of molecular reorientation on the time-resolved signals on longer time scales (i.e. 100s of picoseconds), one must employ the magic-angle (MA, 54.7°) between pump- and probe-polarisation [150], and hence the relative polarisation cannot be chosen to minimise the amplitude of the CA in any case.

Returning to the temporal distribution of the CA position vs probe wavelength, we note that by extracting the extrema positions one can obtain the temporal distribution of the white-light pulse (i.e. the relative group delay $T(\omega) = -\partial\varphi/\partial\omega$ [138]). In Figure 3.13 we plot the relative temporal position of the CA minimum ($T(\omega)$) vs probe wavelength extracted from the curves in Figure 3.11 (red curve), along with a parabolic fit (vs $\omega = 2\pi c/\lambda$). Given that the spectral phase can be expanded as,

$$\varphi(\omega) \approx \varphi(\omega_0) + \varphi'(\omega_0)\Omega + \frac{1}{2}\varphi''(\omega_0)\Omega^2 + \frac{1}{6}\varphi'''(\omega_0)\Omega^3,$$

then the corresponding group delay will be given by,

$$T(\omega) \approx -(\varphi'(\omega_0) + \varphi''(\omega_0)\Omega + \frac{1}{2}\varphi'''(\omega_0)\Omega^2),$$

such that the parabolic fit provides an estimate of $\varphi''(\omega_0)$ and $\varphi'''(\omega_0)$, which in this case resulted in $\varphi''(\omega_0) = 3090$ fs² and $\varphi'''(\omega_0) = 319$ fs³. These values are consistent with the material dispersion and thickness of the achromatic lenses used (standard LINOS $f=30$ -mm and $f=100$ -mm visible-range doublets, with 8-mm and 22.4-mm diameter, respectively). We note that the dispersion due to the refractive optics results in a ~ 2700 fs relative delay across the probe wavelength range 480 – 650 nm. As mentioned in Section 3.2, the current measurement setup employs off-axis-paraboloidal mirrors for collimating and refocusing of the WL beam. The corresponding temporal distribution of the CA extrema in this case are

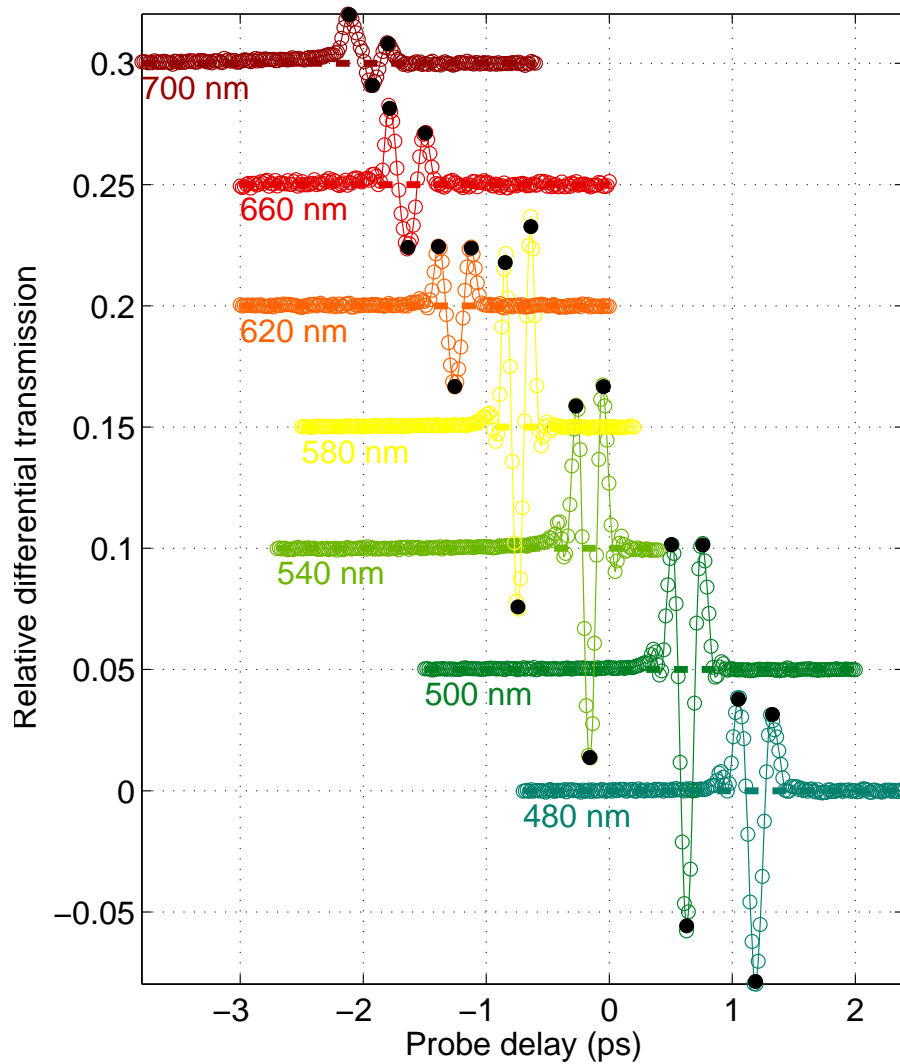


Figure 3.11.: Coherent artifacts vs post-filtered white-light wavelength ($\Delta\lambda_{\text{FWHM}} \sim 6$ nm) for a 1-mm cuvette of pure CH_3CN , with refractive optics (achromatic lenses) between white-light continuum generation and sample. (Pump pulse: 500 nm, ~ 70 nJ).

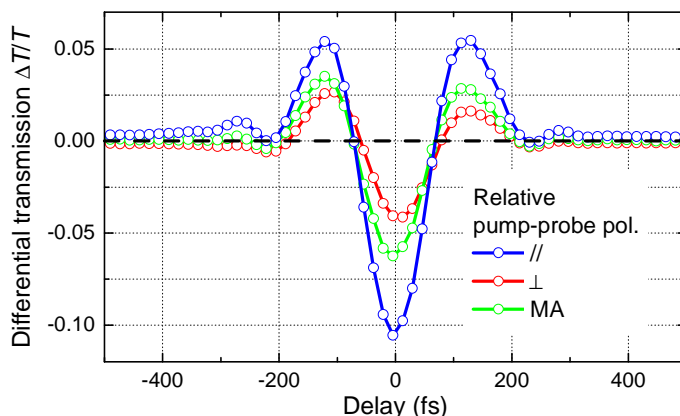


Figure 3.12.: Polarisation dependence of pump-probe coherent artifacts arising from cross-phase modulation of white-light probe by pump intensity in cuvette window/solvent for parallel, perpendicular and magic angle (MA, $\theta = 54.7^\circ$) relative pump-probe polarisation angles.

also included in Figure 3.13, which demonstrate a significant reduction in the WL temporal dispersion, as expected. The residual dispersion is due to a fraction of the sapphire generation medium, a 1-mm short-pass filter and the front window of the cuvette (1.25-mm of fused silica). In this case, the fitted parabolic group delay yields $\varphi''(\omega_0) = 200 \text{ fs}^2$ and $\varphi'''(\omega_0) = 9.3 \text{ fs}^3$, with a temporal shift across the range 480-650 nm of only 330 fs.

The fact that the WL dispersion leads to a wavelength-dependent zero-delay position can be corrected for in the measurements, by a calibration procedure as just shown, independent of the magnitude of the temporal dispersion. The more damaging effect, however, is the temporal width of the XPM-CAs with increasing WL dispersion. This is demonstrated in Figure 3.14, where the CAs for both the

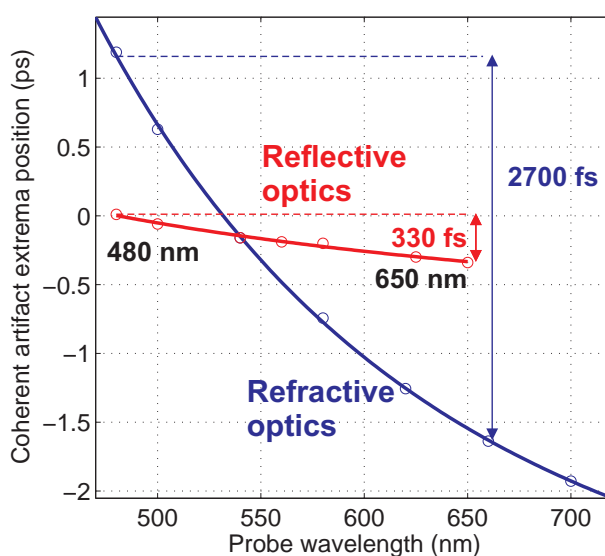


Figure 3.13.: Temporal distribution of coherent artifact minima vs probe wavelength for using (a) refractive optics (achromatic lenses) and (b) reflective optics. Experimental data (open circles) and quadratic fit (solid line) as described in text.

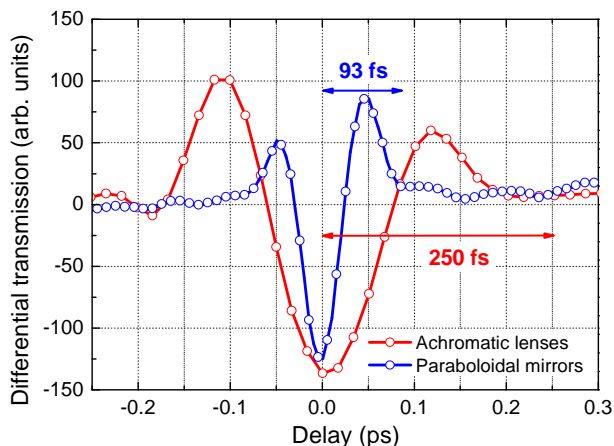


Figure 3.14.: Comparison of coherent artifacts ($\lambda_{\text{ex}} = 500$ nm, $\lambda = 660$ nm, $\Delta\lambda_{\text{FWHM}} \sim 8$ nm) for white-light using (a) refractive optics (achromatic lenses) and (b) reflective optics (off-axis paraboloidal mirrors).

reflective and refractive optics are shown for a pump wavelength $\lambda_{\text{ex}} = 500$ nm and probe wavelength of $\lambda = 660$ nm. Taking the minimum of the CA as the effective zero-delay, the CA is observed to extend ~ 93 fs into the positive delay range for the case of reflective optics, but ~ 250 fs for the case of refractive optics. Hence in order to measure the transient absorption on a sub-picosecond time-scale, the use of reflective optics is extremely important. We note that the residual width of the CA using reflective optics is due to the use of cuvettes with relatively thick window and sample thicknesses (1.25 mm and 1 mm, respectively). This residual width can be further reduced (allowing a sub-50 fs resolution) [148, 151] by the use of custom cuvettes with thin windows and sample thicknesses (e.g. ~ 100 μm). Whilst the time resolution of the existing setup is satisfactory for the measurements on the Fc-B-bpy compounds presented in this work (where the dynamics of particular interest occur with time scales > 400 fs), for future work where dynamics on shorter time-scales may become important, such custom cuvettes should be constructed.

4. CW spectroscopy, electrochemical and quantum chemistry results

4.1. Introduction

In this chapter, we will develop a description of the electronic properties of the Fc-B-bpy compounds (represented by the generic structures in Figure 4.1) based on an analysis of (i) CW UV-vis absorption spectra, (ii) (spectro-)electrochemical, and (iii) theoretical quantum chemistry results. A combined interpretation of these data provide strong evidence that the visible absorption band generally exhibited by the Fc-B-bpy compounds can be attributed to a direct (i.e. Mulliken-) MLCT transition from occupied orbitals predominantly localised on the Fc-donor into unoccupied orbitals predominantly localised on the B-bpy acceptor, with the remaining evidence provided by the time-resolved transient absorption results in Chapter 5.

As mentioned in the Introduction, at the outset of this work, the key derivatives of the Fc-B-bpy compounds ($[\mathbf{nA}](\mathbf{PF}_6)_n$, Figure 4.1¹) had already been well-characterised in terms of single-crystal structure, ¹H, ¹³C and ¹¹B NMR spectra, cyclovoltammetry, general chemical stability/solubility, preliminary semi-empirical calculations and semi-quantitative UV-vis spectroscopy [7]. Moreover, other related Fc-based tetracoordinated-B–N-bridged systems had also been similarly characterised [11, 12, 13, 14, 6, 152], including polymeric derivatives. During the course of the investigation, additional derivatives were synthesised and characterised [10, 4, 3, 5, 1, 9, 2] and incorporated in this spectroscopic study whenever additional relevant information might be gained and samples were made available. In parallel with this work, a considerable level of maturity in the synthetic strategy has evolved, as reflected in some key overview papers (e.g. Ref. [1]) of the broader family of compounds.

The presence of visible absorption near 500 nm generally exhibited by the Fc-B-bpy compounds ($\lambda_{\max} \sim 500$ nm, $\epsilon_{\max} \sim 500$ M⁻¹cm⁻¹ for $[\mathbf{1A}]\mathbf{Br}$, see Figure 4.2 in Section 4.2.1), which gives rise to their dark-red colour in solution/crystal and is absent in the isolated Fc and B-bpy fragments (or in mixed solutions), was tentatively attributed to charge-transfer interactions between the Fc and B-bpy moieties. This was definitely a reasonable conclusion, given that no other electronic interaction in the system appeared to be a plausible candidate for the observed transition². Moreover, the peak absorption strength of the band was observed to increase in almost 1:1 proportion with the number of attached B-bpy groups (i.e. across the series $[\mathbf{nA}](\mathbf{PF}_6)_n$, $n = 1, 2, 4$), with a consistent red-shift with increasing n . Some additional evidence for mixing of the Fe²⁺ and B-bpy orbitals in the radical species $[\mathbf{1A}]^0$ (i.e. $[\mathbf{1A}]\mathbf{PF}_6$ following electrochemical reduction of the B-bpy unit) from ESR measurements was observed. However, a small electronic coupling between the orbitals of the reduced B-bpy unit with the Fe-core does not necessarily imply that the excited state resulting from excitation of the observed visible band corresponds

¹Note that the notation $[\mathbf{nA}](\mathbf{PF}_6)_n$ is adopted from Ref. [7], where \mathbf{n} denotes the number of B-bpy acceptor groups and \mathbf{X} is the counteranion (as shown in Figure 4.1).

²Specifically, it was unlikely that the new/shifted electronic transition arises from (i) *intermolecular* charge transfer from the counteranion to the cationic B-bpy unit, as stated in early reports of B-bpy compounds in the solid state [153], or (ii) charge-transfer from the CH₃ substituents attached to boron.

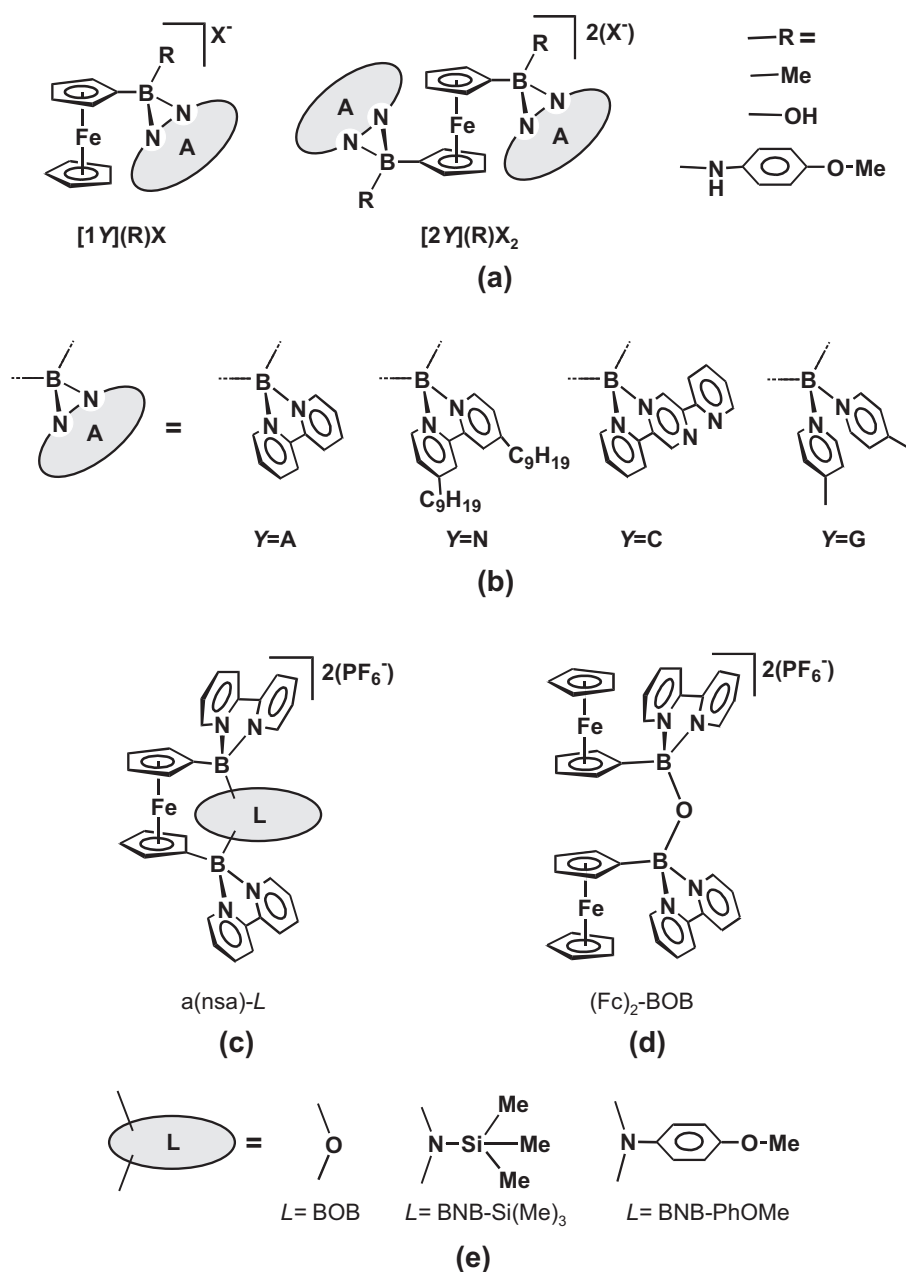


Figure 4.1.: Generic structures of the specific Fc-B-bpy compounds under study. (a) Fc-donor compounds with one and two unbridged B-organic acceptors, $[nY]X_n$. Substituents at B, R (when not specified, $R=CH_3$). Counteranions $X^- = PF_6^-, Br^-$. (b) Particular B-organic acceptors, specified by $Y=A, N, C, G$ (notation selected to be compatible with Ref. [7]). (c) Generic Fc-donor ansa-bridged acceptor compounds $a-L$. (d) Bridged di-ferrocene compound $(Fc)_2BOB$. (e) O- and N-based ansa-bridge components.

to a large-scale charge transfer from Fc into the B-bpy unit.

The possibility that the observed band in these compounds could correspond to a modified version of the existing Fc-I band of unsubstituted Fc ($\lambda_{\max} = 440$ nm, $\epsilon_{\max} \sim 100 \text{ M}^{-1}\text{cm}^{-1}$, Section 2.2.1) corresponding to a predominantly localised excitation on the Fc-unit had to be considered. In principle, the required increase in absorption strength and red-shift of the Fc-I band could result from a combination of the symmetry-lowering and the inductive effects of the cationic B-bpy substituents, as well as only a partial amount of charge-transfer onto the B-bpy unit. Such substituent effects on the absorption band would also be expected to increase with the number of substituents [37].

Perhaps the most compelling existing evidence for the MLCT assignment of the band at the time was the strongly contrasting spectroscopic behaviour of the control compound **[1G]Br** (Figure 4.1), where the B-bpy unit is replaced with two separate pyridine moieties, and the lowest energy band is observed at $\lambda_{\max} = 448$ nm, typical of very weakly-perturbed substituted ferrocenes. The removal of the connecting C-C bridge which forms B-bpy is known to strongly eliminate the electron-accepting nature of the pyridine system due to the requirement of a delocalised electronic system over both pyridine rings [7]. It seems a valid assertion that the purely inductive effects of the cationic B-bpy groups seen by the Fc-unit is not significantly altered in going from **[1A]Br** to **[1G]Br**, hence ruling out the possibility that the electronic transition remains localised on the Fc-unit, but not implying that the excited state involves the degree of charge-transfer such that the LUMO is predominantly localised on the B-bpy substituent in **[1A]Br**.

Given that the molecular systems under study are complex polyatomic metal-organic systems, and most of the argumentation is on a (albeit sound) intuitive chemical basis, a deeper spectroscopic and theoretical investigation was deemed important for further testing the hypothesis of a visible MLCT transition in these compounds, and to determine to what degree charge is transferred to the acceptor in the excited state³. Moreover, through the use of more quantitative spectroscopic measurement and analysis over a set of related Fc-B-bpy derivatives, a superior understanding of the nature of the proposed MLCT transition, including initiatives for design modifications to increase the MLCT absorption strength, was anticipated.

In the following sections, we present a comparison of the specific derivatives identified in Figure 4.1 with (i) measurements and critical analysis of the UV-vis absorption spectra in solution (including a quantitative analysis of the solvent dependence of the MLCT band) and selected derivatives in doped thin films and single-crystal, (ii) analysis of the cyclic voltammetry traces and UV-vis spectral changes accompanying the respective electrochemical oxidation/reduction of the Fc-donor/B-bpy-acceptor (which will also be employed in the interpretation of the excited state transient spectra in Chapter 5) and (iii) the theoretical (TD-)DFT results on a gas phase prototype, including the effects of conformation and electron removal on the predicted electronic structure and a discussion of the predicted excitation energies.

We note that no detectable evidence for photochemistry for the Fc-B-bpy compounds in solution was observed upon prolonged irradiation of the MLCT band. Moreover, tests for photoluminescence in the emission wavelength range $\lambda \leq 900$ nm showed no emission following MLCT excitation from any of the compounds tested (with calibrated sensitivity tests placing an upper bound for any photoluminescent quantum yield at $< 3 \times 10^{-5}$ in this wavelength range). Hence

³Note that in the rest of the text, the term ‘MLCT transition’ will be used to describe the visible absorption band to avoid complication in the discussion, thus foreshadowing the final conclusion of its assignment.

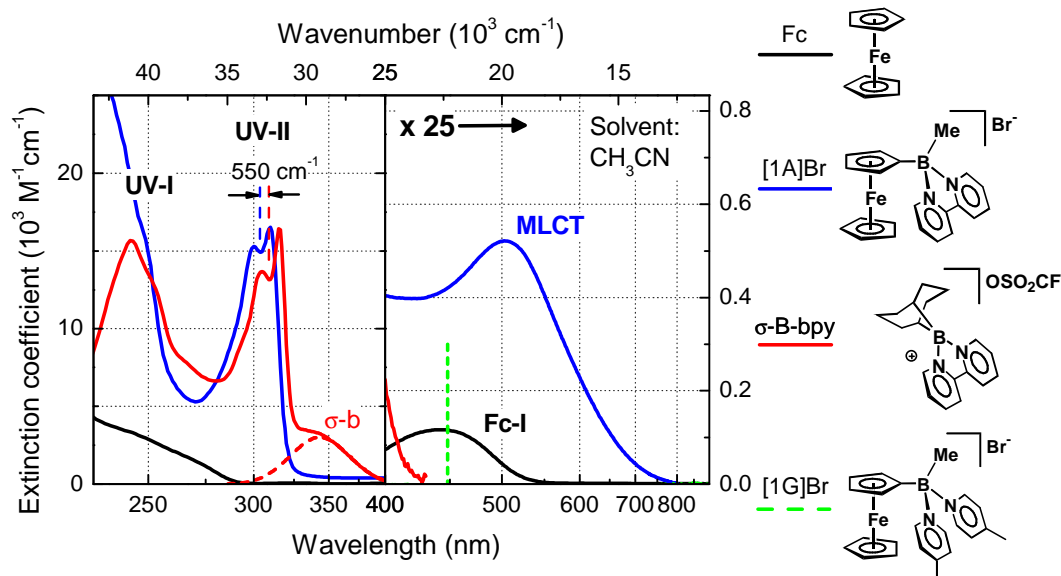


Figure 4.2.: Comparative overview of the UV-vis absorption spectra of prototype Fc-B-bpy compound, **[1A]Br**, and related donor and acceptor “fragment” compounds, as well as an indication of the lowest-energy absorption peak for **[1G]Br** (from [7]).

the experimental spectroscopic data presented in this chapter is based on only the UV-vis absorption characteristics, with a direct probe of the MLCT excited state provided by the time-resolved measurements in the next chapter.

4.2. UV-vis absorption in solution

4.2.1. Extraction of UV-vis absorption bands

Figure 4.2 provides an overview of the UV-vis absorption spectra of the representative prototype **[1A]Br** and those of the two molecular “fragments”, Fc and the acceptor model compound $\sigma\text{-B-bpy}$ (presented in Sections 2.2 and 2.3), as well as the reported absorption maximum position of **[1G]Br** [7]. In the UV range of Figure 4.2, **[1A]Br** exhibits two main regions of partially resolvable absorption, labelled ‘UV-I’ and ‘UV-II’ respectively. The absorption in these regions is seen to correspond approximately additively to the UV bands of the isolated Fc-donor and B-bpy-acceptor fragments, and on this basis we can assign them to localised transitions on the donor or acceptor. The UV-II band corresponds to the $\pi - \pi^*$ -transition localised on the B-bpy unit, which is observed to blue-shift some 550 cm^{-1} ($\cong 0.07 \text{ eV}$) relative to $\sigma\text{-B-bpy}$. From a comparison of the electrochemistry data for **[1A]Br**, $\sigma\text{-B-bpy}$ and **Hf** in Sections 2.3 and 4.5.1 with the corresponding data in [134], the electrochemical reduction potential of $\sigma\text{-B-bpy}$ is less negative than that of **[1A]Br** also by $\sim 0.07 \text{ eV}$, such that this blue-shift of the B-bpy- $\pi - \pi^*$ -transition can be attributed to a destabilisation of the B-bpy LUMO.

In the visible region, one observes the proposed MLCT band (‘MLCT’) for **[1A]Br**— a broad featureless band with a maximum at $\sim 500 \text{ nm}$, resolvable on the low-energy side and with an absorption plateau that extends into the near-UV. The only absorptive feature of the isolated fragments that extends into the visible range is the Fc-I band of the Fc-donor (Section 2.2.1), which exhibits the relatively

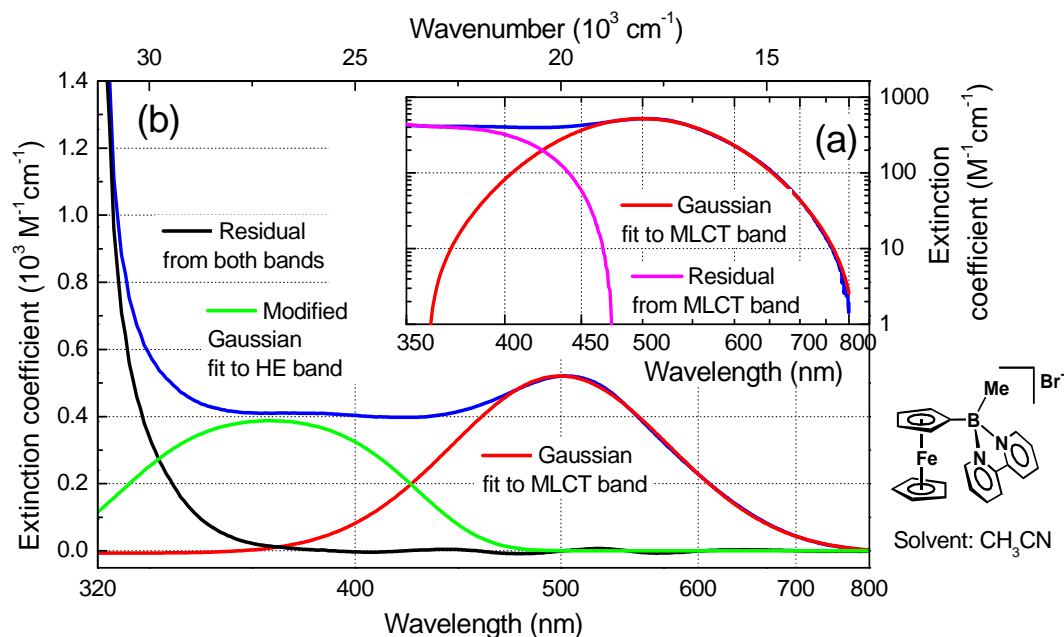


Figure 4.3.: UV-Vis absorption spectra of $[1\mathbf{A}]\mathbf{Br}$ (in CH_3CN) (blue curves) and fitted curves to each region. (a) Initial analysis using only a single Gaussian MLCT band (red) demonstrating non-Gaussian character of residual in the 370 – 470 nm range. (b) Linear plot showing both fitted Gaussian MLCT band (red) and fitted modified Gaussian HE band (green), and residual (black).

weaker absorptive feature due to unresolved predominantly $d-d$ transitions with a maximum at $\lambda_{\text{max}} \sim 440$ nm ($\varepsilon_{\text{max}} \approx 100 \text{ M}^{-1}\text{cm}^{-1}$).

In order to isolate and quantify the individual absorption bands under this envelope, we begin with fitting the low-energy side of the MLCT band for $[1\mathbf{A}]\mathbf{Br}$ with a simple Gaussian function (vs frequency), i.e.

$$\varepsilon(\nu) = \varepsilon_{\text{max}} \exp \left[-4 \ln 2 \frac{(\nu - \nu_0)^2}{\Delta\nu_{\text{FWHM}}^2} \right]. \quad (4.1)$$

The resulting Gaussian least-square fit to the data (using the fitting range 480 – 800 nm) is shown in Figure 4.3⁴, which yields a highly satisfactory fit of the low-energy region (over some 2 orders of magnitude) with a (FWHM) width of $\Delta\nu_{\text{FWHM}} = 6220 \text{ cm}^{-1}$. Note that the Gaussian fit retrieves a peak position of $\lambda_0 = 1/\nu_0 = 499.7$ nm as opposed to that obtained by fitting a quadratic function in a small neighbourhood about the local maximum which yields $\lambda_{\text{max}} = 503.3$ nm. Inspection of the Gaussian fits for the MLCT band across a range of related compounds (presented in the following sections) near the band maximum reveals a systematic small blue-shift of the peak position (due to minor deviations of the MLCT band absorption peak from an ideal Gaussian, but not attributable to the frequency pulling effect of higher energy bands), and hence we will preferentially discuss the position of the local maximum λ_{max} as the centre wavelength whenever one is clearly resolvable (although for the thin film and crystal data to be presented, no local maximum is available, and we must resort to that from the Gaussian fit).

⁴In most cases, the fitting procedures of the absorption bands use the objective function $\chi^2 \equiv \sum (\varepsilon_{\text{exp}} - \varepsilon_{\text{fit}})^2 / \varepsilon_{\text{exp}}$ as opposed to unweighted least-square fitting, in order to lend more weight to the wings of the absorption bands.

The residual absorption, after subtraction of the fitted MLCT band from the raw data, is also shown in Figure 4.3(a) (logarithmic scale), and reveals the low-energy tail of a second higher-energy (HE) band in the range ~ 350 -500 nm. Attempts to fit this region with a second Gaussian resulted in poor agreement with the experimental data. It is evident that the logarithmic curve of the residual after subtraction of the fitted MLCT band (Figure 4.3(a)) does not reflect a simple parabolic shape, but instead conforms to a higher order polynomial. Based on this observation, we attempted to fit this second band region with a modified (higher-order) Gaussian function⁵:

$$\varepsilon(\nu) = \varepsilon_{\max} \exp \left\{ -4 \ln 2 \frac{(\nu - \nu_{\max})^2}{\nu_w^2} \left[1 + \alpha^2 \frac{(\nu - \nu_{\max})^2}{\nu_w^2} \right] \right\}, \quad (4.2)$$

where,

$$\Delta\nu_{\text{FWHM}} = \sqrt{2 \frac{\sqrt{1 + \alpha^2} - 1}{\alpha^2}} \Delta\nu_w, \quad (4.3)$$

which was also used for the fitting of the Fc-I band in Section 2.2.1 (which, we note, was composed of two unresolved, relatively symmetric non-Gaussian bands). Applying this model function results in the fitted HE band shown in Figure 4.3(b) ($\lambda_{\max} = 369.4$ nm, $\varepsilon_{\max} = 388$ M⁻¹cm⁻¹, $\Delta\nu_{\text{FWHM}} = 6940$ cm⁻¹), which matches the residual absorption in this region well and yields a negligible total residual above 370 nm (i.e. after subtraction of both bands), below which the onset of the relatively strong B-bpy UV-absorption band begins. These two model band functions will be used as described here for all the following spectral data, whilst a tabulation of all fitted-spectra parameters for all derivatives presented are given in Table A.2 (Appendix A). In order to have a measure of absorption strength which is independent of a given bandwidth/shape, we can also calculate the oscillator strength f^6 , which for these parameters yields the values $f_{\text{MLCT}} = 0.015$ and $f_{\text{HE}} = 0.012$. Oscillator strengths of this magnitude are generally related to symmetry-forbidden localised transitions in molecules possessing some symmetry elements [37, 98], although in the present case of a proposed CT transition, the weak oscillator strength is also consistent with a low *extensive* spatial overlap of the donor and acceptor MOs.

The fact that the proposed MLCT band conforms to a single Gaussian profile with only slight deviations, suggests that the entire absorption feature corresponds to a single dominant electronic transition (or a number of closely-spaced transitions), although the mechanism leading to the significant line broadening requires further analysis, and will be discussed after presenting the absorption spectra of various derivatives and in various environments.

4.2.2. Solvation effects on the UV-vis absorption spectra

In this section, we analyse the solvent dependence of the UV-vis absorption bands of the Fc-B-bpy compounds. As described in Section 2.1.4, one expects an appreciable rearrangement of the charge density of the solute upon a CT electronic transition,

⁵Note that this higher-order Gaussian function was adopted after the trial of various other common model functions for the HE band, although no rigorous physical derivation of its form was found in the literature. This indicates that several different non-Gaussian broadening mechanisms are associated with the HE bandshape, as well as possibly more than one distinct electronic transition.

⁶The oscillator strength is related to the integrated absorption band via $f \approx 4.32 \times 10^{-9} \int d\nu \varepsilon(\nu)$, where $\varepsilon(\nu)$ is in units of M⁻¹cm⁻¹ and the wavenumber ν in cm⁻¹.

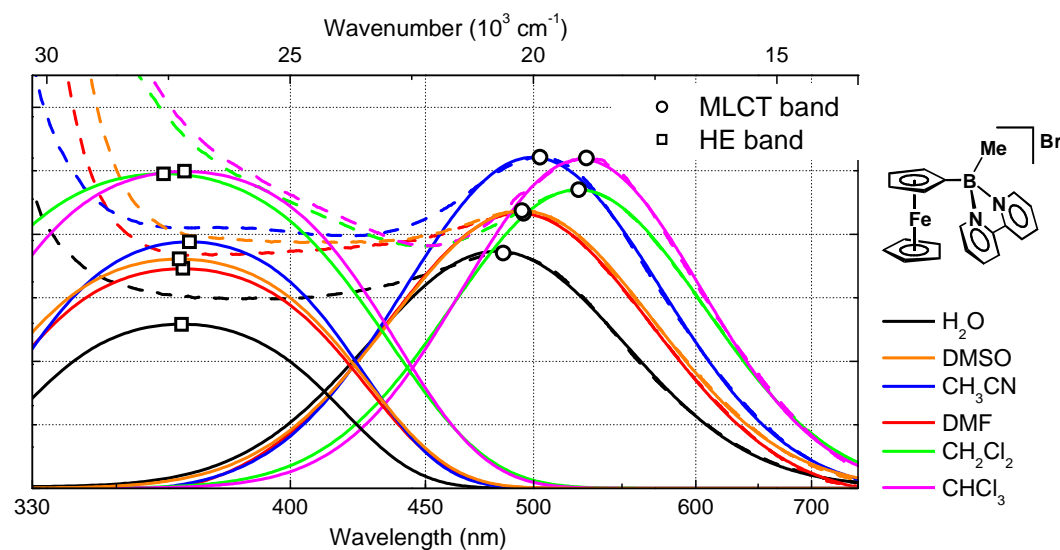


Figure 4.4.: UV-vis absorption spectra of $[1\mathbf{A}]\mathbf{Br}$ in a range of solvents (as indicated), including fitted HE (modified Gaussian) and MLCT (Gaussian) bands (open symbols denote the respective band peak positions).

which should give rise to a dependence of the transition energy on the particular solvent, due to the different electrostatic interaction energies of the ground and excited-state solute with the surrounding solvent molecules. Hence we expect a significant effect upon varying the solvent on the proposed MLCT band in the $[\mathbf{nA}]\mathbf{X}_n$ compounds. Moreover, a quantitative analysis (using the theoretical model derived in Appendix B.3) can yield an estimate of the change in dipole moment between the ground and excited states, as well as the extrapolation of the expected gas-phase absorption (e.g. for comparison with theoretical results). Moreover, we will see that the solvent shift model is important for interpreting the absorption spectral changes that occur upon addition of further B-bpy acceptor groups. In the following, we focus on an analysis of the prototype compound $[1\mathbf{A}]\mathbf{Br}$, which has only a single acceptor group and features more favourable solubility properties in comparison to the corresponding PF_6^- compound.

Figure 4.4 shows the UV-vis absorption spectra and corresponding fitted HE and MLCT bands for a range of polar solvents⁷. As can be readily observed, both the peak wavelength and absorption strength of the MLCT band change significantly in going from H_2O ($\lambda_{\text{max}} = 484.9 \text{ nm}$, $\epsilon_{\text{max}} = 370 \text{ M}^{-1}\text{cm}^{-1}$) to CHCl_3 ($\lambda_{\text{max}} = 528.8 \text{ nm}$, $\epsilon_{\text{max}} = 520 \text{ M}^{-1}\text{cm}^{-1}$) (which is experimentally observable as a pronounced colour change in the solutions). Qualitatively, this corresponds to a blue-shift with increasing solvent dipolarity, i.e. hypsochromism (or negative solvatochromism) [48, 49]. This contrasts with the usual observation of a bathochromic shift (or positive solvatochromism) observed for CT transitions in neutral compounds. This effect has been reported for MLCT transitions in other cationic complexes, and can be rationalised based on the discussion of Section 2.1.4 (c.f. Figures 2.9-2.11), where it was asserted that for cationic compounds, both the ground and

⁷Note that a large number of other solvents, including non-polar solvents, were tested and rejected due to their poor solubility properties for the $[\mathbf{nA}]\mathbf{X}_n$ compounds. The solvents used here may be regarded as a fairly exhaustive selection of appropriate commonly-available solvents, which unfortunately implies a limited degree of statistical performance in the quantitative analysis, i.e. in literature reports, often a robust correlation emerges with the inclusion of $\sim 10 - 20$ solvents

excited state possess antiparallel effective dipole moments, such that the solvent dipole orientation stabilises the ground state and destabilises the Franck-Condon excited state, leading to a blue-shift with increasing solvent interaction.

In order to systematically account for the solvent dependence, we employ the theoretical model for a cationic solute as described in Section 2.1.4 (and derived in Appendix B.3), in terms of the solvent polarity functions $\varphi(\epsilon_s)$ and $\varphi(n^2)$ (see Appendices A.1, B.3) for each solvent (where ϵ_s and n are the static (DC) dielectric constant (permittivity) and optical-frequency refractive index, respectively), which describe the dipolar and polarisability properties of the respective solvents and account for their response to the electronic charge density distribution of the solute. An inspection of the molecular dimensions of each solvent (i.e. in terms of their van der Waals radii) indicated that the effective solute radius a (which is taken as the distance of the centre of the solute ‘sphere’ to the *centre* of the first solvent shell) varied significantly for each solvent (see Table A.1). Hence, in order to account for this effect in the following analysis, we calculated the prefactor of Eq. 2.5,

$$C_s \equiv \frac{\gamma}{a^3} \Xi \left(\frac{a}{\sqrt{B}} \right) (\varphi(\epsilon_s) - \varphi(n^2)), \quad (4.4)$$

with $a = a_0 + r_s$, where a_0 is the effective solute radius, and r_s is an effective radius for each solvent. In keeping with the expected solvent dipole orientation relative to the solute (Figure 2.9) the solvent radii were determined for each solvent by considering the length of each solvent molecule *parallel* to their respective permanent dipole moments⁸. We note that taking the solvent dimensions into account in this way improved the overall correlation of the data. From an analysis of the theoretical structure (Section 4.6), the effective spherical solute radius a_0 of the **[1A]Br** was estimated as $a_0 \simeq 5.56 \text{ \AA}$ ⁹.

Figure 4.5 shows the results of the analysis. In Figure 4.5(a) we plot the calculated solvent pre-factors C_s vs the observed MLCT absorption band peak wavenumber (from the data shown in Figure 4.4). As predicted by Eq. 2.5, a linear fit of C_s vs the transition energy $hc\nu_{\max}$ should yield the quantity $(\Delta\mu)^{-2}$. The linear fit to the data is also shown which yields an estimate of the change in dipole moment of $\Delta\mu = 4.5 \pm 0.2 \times 10^{-29} \text{ C} \cdot \text{m}$ ($\cong 13.4 \text{ D}$). This dipole change corresponds to a displacement of a unit electronic charge by $\Delta\mu/e = 2.8 \text{ \AA}$. In order to put this displacement in perspective, in Figure 4.6 we show the distance as a projected vector with the calculated (gas-phase) structure of **[1]⁺(H)** (see Section 4.6), with a direction parallel to the line passing through the Fe atom and the centroid of the two B-bpy N atoms¹⁰. One observes that the predicted electron displacement amounts to $\sim 70\%$ of the distance between these two points. The fact that the extracted effective electronic displacement upon excitation is somewhat less than the geometric separation between donor and acceptor has been reported for other CT compounds (e.g. Ref. [154]), with the difference attributed to the fact that other electronic orbitals are partially polarised so as to oppose the CT and reduce the net charge displacement.

⁸These ‘dipole-parallel solvent lengths’ were determined by a simple code which employed approximate 3-D structures of each solvent molecule obtained from a chemical database, see Appendix A.1, and tabulated van der Waals radii for the atoms at the extreme positions of the solvent molecule.

⁹This value was derived from the theoretical gas phase structure of **[1]⁺(H)** (Section 4.6). Alternatively, using the crystal structure unit cell volume [7] one arrives at the comparable value of $a \simeq 5.14 \text{ \AA}$.

¹⁰Note that we take these two coordinates as defining the approximate central location of the Fe-donor and B-bpy acceptor, respectively.

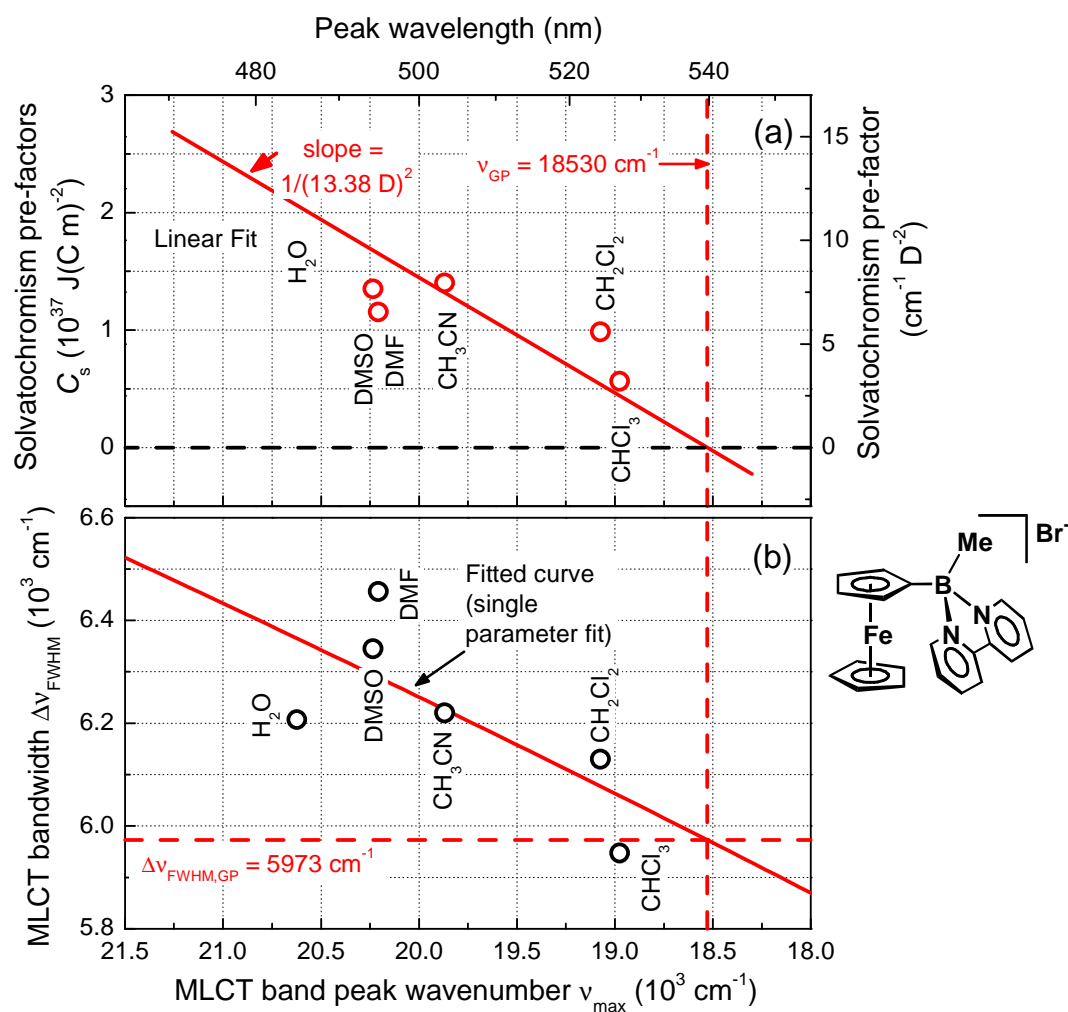


Figure 4.5.: Results of the solvatochromism analysis of the MLCT band of $[\mathbf{1A}]\text{Br}$. (a) Plot of solvent shift prefactor C_s (see RHS of Eq. 2.5) vs experimental MLCT band peak wavenumber, and corresponding linear fit, indicating extrapolated gas phase peak wavenumber. (Note that for graphical reasons, the experimental peak wavenumber is plotted as the x -axis. (b) Corresponding MLCT bandwidth vs peak wavenumber, and fitted model curve (c.f. Eq. 2.6), indicating extrapolated gas phase bandwidth)

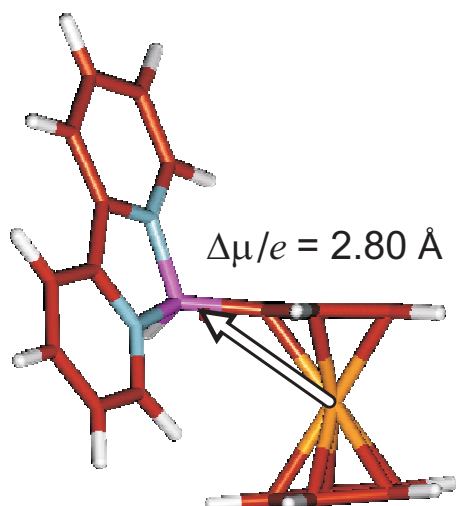


Figure 4.6.: Illustration of the estimated dipole moment change upon MLCT excitation from the solvatochromism analysis of **[1A]Br** (projected dipole vector lengths added to scale with structure, with vector orientation placed parallel to the line connecting the Fe-core and N-N-centroid of the B-bpy unit. The structure shown is the theoretically derived gas-phase structure of the closely related compound **[1]⁺(H)** (c.f. Section 4.6).

Besides an estimate of the change in dipole moment occurring upon excitation, an extrapolation of the linear curve in Figure 4.5(a) also yields an estimate of the expected gas-phase absorption band peak position of $\nu_{\text{GP}} = 18500 \pm 100 \text{ cm}^{-1}$, corresponding to $\lambda_{\text{GP}} = 540 \text{ nm}$. We will refer to this value again in the next section in discussing the dependence of the MLCT absorption spectra on the number of acceptor groups.

We turn now to the fitted MLCT bandwidth vs solvent, which is shown in Figure 4.5(b). The data also show a discernible trend with variation of the solvent (as expected from the theory in Section 2.1.4), with a trend of increasing bandwidth with increasing blue-shift of the band. The observed bandwidth¹¹ is a convolution of both the solvent-induced bandwidth (given by σ_{solv} , Eq. 2.6) and the residual gas-phase bandwidth σ_{GP} (i.e. due to both a Franck-Condon manifold arising from a distribution of vibrational transitions as well any additional broadening from a conformational distribution). Assuming that both the solvent broadening and residual gas-phase bandshapes conform to Gaussian functions, we have,

$$\begin{aligned} \Delta\nu_{\text{FWHM}}^2 &= 8 \ln(2)(\sigma_{\text{GP}}^2 + \sigma_{\text{solv}}^2) = 8 \ln(2)(\sigma_{\text{FC}}^2 + 2kT\Delta E_{\text{solv}}) \\ &= 8 \ln(2)(\sigma_{\text{FC}}^2 + 2hcT(\nu_{\text{max}} - \nu_{\text{GP}})), \end{aligned} \quad (4.5)$$

where we have used $\sigma_{\text{solv}}^2 = 2kT\Delta E_{\text{solv}}$ (i.e. Eq. 2.6). Hence Eq. 4.5 allows us to fit the data with a *single* free parameter (i.e. σ_{GP}) due to the predicted dependence of the solvent broadening on the observed solvent shift (which is available from the analysis in Figure 4.5(a)). The fitted curve (using $T = 300 \text{ K}$) is shown with the data in Figure 4.5(a), which shows a satisfactory correspondence to the experimental MLCT bandwidths, and yields an expected gas-phase bandwidth of $\Delta\nu_{\text{FWHM,GP}} = 5973 \text{ cm}^{-1}$. This correspondence provides a good degree of confidence in the applied solvatochromism model.

¹¹Note that the σ values refer to the second moment of the band, as opposed to the FWHM.

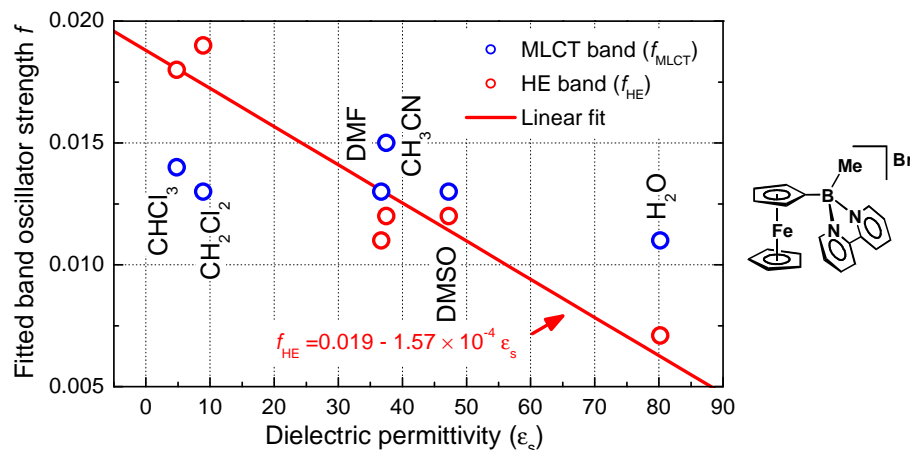


Figure 4.7.: Oscillator strengths from the fitted MLCT and HE band parameters for **[1A]Br** vs solvent dielectric constant. Included is a linear fit for the HE band data.

Considering now the solvent effect on the HE band, we refer back to Figure 4.4(a), where one observes a very distinct behaviour in comparison to the MLCT band. In the case of the HE band, there is no significant shift in the absorption peak energy vs solvent interaction, which suggests that the dipole moment change $\Delta\mu$ for this transition is negligible, i.e. the HE band can be attributed to a localised transition and not to a CT transition. However, a strong dependence of the integrated absorption strength on the solvent dipolarity is observed. In Figure 4.7 we plot the oscillator strengths (obtained from the fitted band parameters) for both the MLCT and HE bands in each solvent vs the solvent static dielectric constant (ϵ_s). As can be seen, the MLCT band oscillator strength does not demonstrate any significant variation with ϵ_s (i.e. the trend in the MLCT peak absorption strength observed in Figure 4.4(a) is mostly a result of the bandwidth variation, and not the integrated absorption intensity). However, the oscillator strength of the HE band shows a marked dependence, with decreasing absorption intensity with increasing solvent dipolarity – a phenomenon referred to as hypsochromism [50]. A linear fit to the HE band oscillator strengths in Figure 4.7 is provided as a visual guide. As shown in the next section, the fitted HE band increases in strength by a factor $\sim 2.3 - 2.8$ upon the addition of a second B-bpy acceptor and hence it is likely that the HE band is due to a transition localised on the B-bpy group(s). Whilst an analysis of the possible causes of this effect lies outside the scope of the current work, the fact that the hypsochromic effect conforms to a fairly well-defined trend with the dipolarity of the solvent tends to argue against specific solvent effects (i.e. due to interaction between chemical groups on the solvent and solute [50]), although the fact that the counteranions in solution will be closer to the solute in solvents with low ϵ_s may be a determining factor.

The cationic solvatochromism model employed here for the MLCT band yields good agreement with experiment, and provides compelling support for the assignment of the MLCT band. However, we should note that despite the fact that electrostatic-based solvatochromism models have enjoyed a considerable amount of popularity and consistency with experiment and theoretical expectations [50, 49, 155, 156, 157, 158, 159, 160, 51, 161, 162], as well as being employed successfully in dynamic solvation models of excited states [163], there is growing attention in the literature to the fact that the solute-solvent interactions are generally more complex than that represented in these relatively simple models and

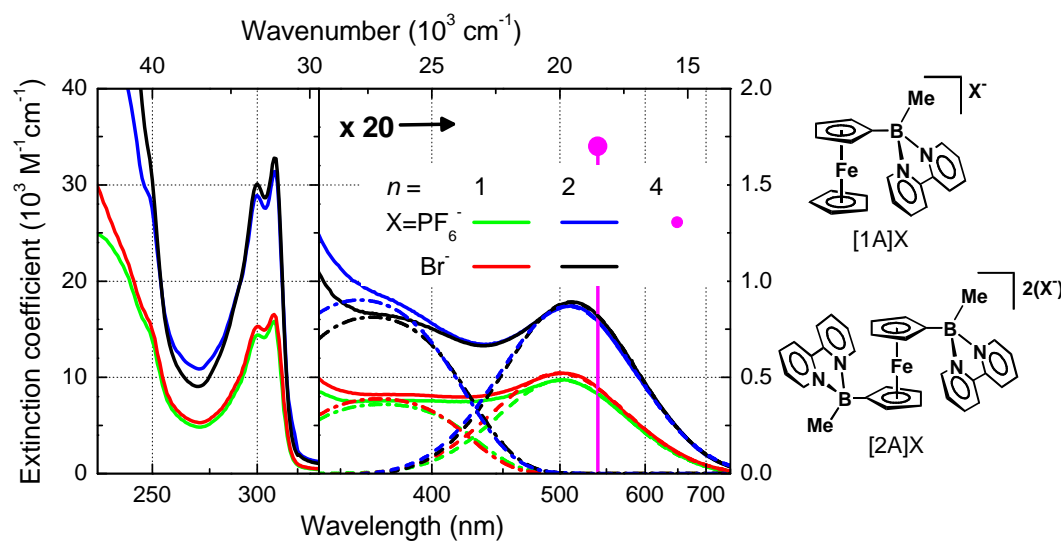


Figure 4.8.: UV-vis absorption spectra of $[nA]X_n$ vs number of acceptors (n) and counteranion, $X = PF_6^-, Br^-$.

additional solvent interaction effects may be important [164, 165, 166, 167, 168]. For instance, as shown in Appendix B.3, such models are effectively based on second-order perturbation theory [48, 169, 170] (although dielectric continuum models, which yield comparable expressions for the solvent shift, are usually based on a simple classical treatments [171, 48, 49, 172, 173, 174]), whereas in the presence of such large electric fields from the surrounding solvent environment (which can be in the range $10^4 - 10^5$ kV/cm), it is possible that these fields could induce significant mixing of excited states [175, 176], and hence observed solvent shifts may be also connected to these higher-order corrections to the electronic states of the solute. Moreover, the role of specific solute-solvent interactions, such as hydrogen-bonding and electron-donation/accepting effects from the first solvent shell could play a significant role. Hence, any truly rigorous analysis of the observed solvent shifts should be accompanied by accurate quantum chemical modelling of the combined solute-solvent system [165, 166, 168, 177, 178]. In closing, we note that the use of Stark spectroscopy of frozen solutions (such as the example in Section 2.2.2) would be an important complementary measurement to confirm the results of the solvatochromism analysis presented here (where the solvent, and hence specific chemical interactions with the solute, is kept constant, and the external electric field applied to the solute can be varied in a controlled manner). Moreover, the synthesis of Fe-B-bpy derivatives with good solubility in *both* polar and non-polar solvents would allow a far more comprehensive investigation.

4.2.3. Comparison of electronic spectra for $[nA]X_n$

Figure 4.8 shows the UV-vis absorption spectra of a set of related derivatives $[nA]X_n$ (in CH_3CN) with a variable (i) number of B-bpy acceptor groups ($n = 1, 2, 4$), and (ii) counteranion ($X = PF_6^-, Br^-$). The variation of the counteranion X is seen to have only a small influence on the absorption spectra across the whole spectral range. This rules out that the near-UV/vis transitions arise from inter-molecular electronic transitions involving the counteranion (although such transitions have been observed in the solid state (and poorly-solvating solvents) for certain B-bpy salts, due to charge transfer from the counteranion [153]). The

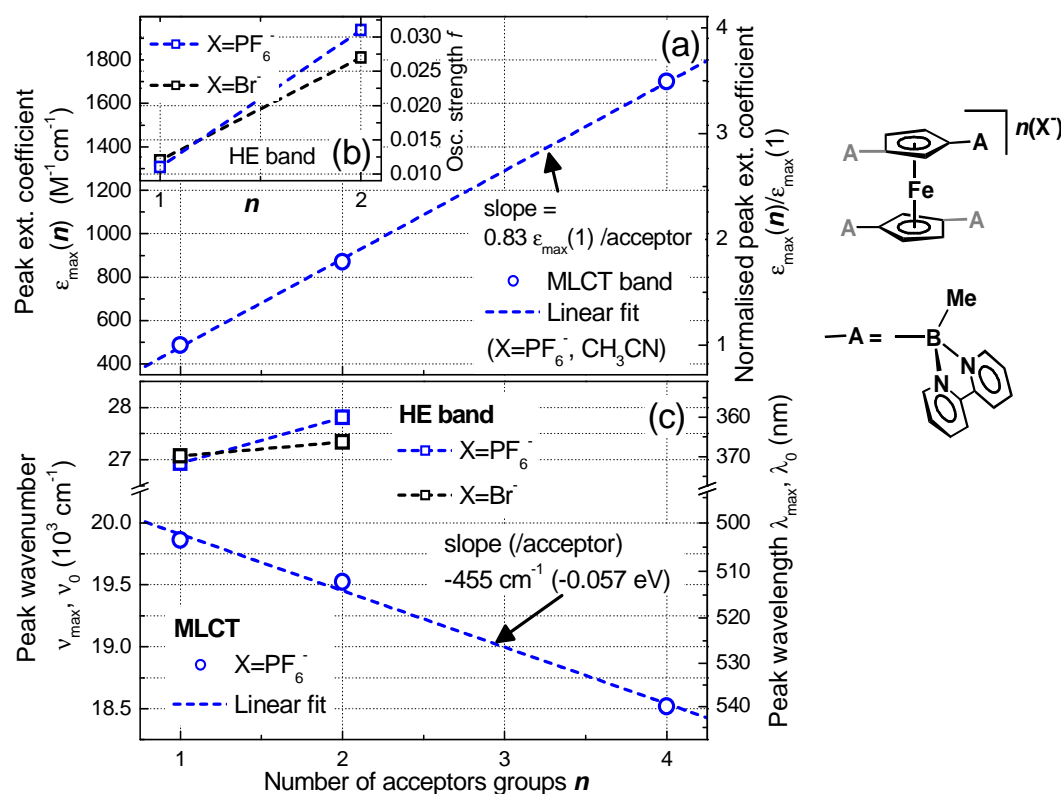


Figure 4.9.: Analysis of UV-vis absorption peaks for $[nA]X_n$ vs number of acceptors (n). (a) Peak extinction coefficient for $[nA](PF_6)_n$ ($n = 1, 2, 4$) (and linear fit). (b) Oscillator strength f for HE band of $[nA]X_n$ ($n = 1, 2$) from fitted band parameters. (c) Peak wavenumber for MLCT band of $[nA](PF_6)_n$ ($n = 1, 2, 4$) (and linear least-squares fit) and the HE band of $[nA]X_n$ ($n = 1, 2$). All data for CH_3CN solvent.

small observed differences resulting from varying the counteranion may well be due to slight differences in sample purity (e.g. due to partial oxidation of the Fc-B-bpy compounds).

Turning now to the dependence of the absorption spectra on the number of acceptors, n , one observes that the addition of a second B-bpy acceptor group leads to an increase of the absorption strength for all the bands present, with a systematic red-shift of the MLCT band energy. Specifically, for $[2A]Br_2$ ($\lambda_{\max} = 512.7 \text{ nm}$, $\epsilon_{\max} = 891 \text{ M}^{-1}\text{cm}^{-1}$) the peak absorption wavelength is shifted by $\Delta\nu = -364 \text{ cm}^{-1}$ relative to $[1A]Br$ ($\lambda_{\max} = 503.3 \text{ nm}$, $\epsilon_{\max} = 521 \text{ M}^{-1}\text{cm}^{-1}$) (the corresponding shift for $[2A](PF_6)_2$ is $\Delta\nu = -338 \text{ cm}^{-1}$, which is consistent within the experimental accuracy). The peak absorption strengths ϵ_{\max} are larger by a factor 1.71 ($[2A]Br_2/[1A]Br$) and 1.79 ($[2A](PF_6)_2/[1A]PF_6$), respectively, with corresponding oscillator-strength ratios of 1.67 and 1.79 (note that the values of ϵ_{\max} are not exactly proportional to f due to small changes in the fitted MLCT bandwidths). From Ref. [7], the corresponding absorption peak data for the compound $[4A](PF_6)_4$ is available¹² ($\lambda_{\max} = 540 \text{ nm}$, $\epsilon_{\max} = 1700 \text{ M}^{-1}\text{cm}^{-1}$), and is added as a data point in Figure 4.8.

The absorption band peak data for both HE and MLCT bands (including $[4A](PF_6)_4$ for the MLCT band) are summarised in Figure 4.9. In Figure 4.9(a),

¹²Note that this compound was not available during the course of this work for independent measurements.

the peak absorption strength of the MLCT band for $[\mathbf{nA}](\mathbf{PF}_6)_n$ ¹³ demonstrates a clear linear trend vs number of acceptor groups, with a best-fit slope corresponding to a factor increase in absorption strength of 0.83 for each additional acceptor group. Although this factor is close to unity, as predicted from the theory in Section 2.1.3, the small deviation implies a finite degree of electronic communication between the acceptor groups (which is evident from analysis of the electrochemistry data in Section 4.5.1).

Figure 4.9(b) also shows the clear linear *red*-shift in the peak photon energy of the MLCT absorption band with increasing number of acceptors, n . A simple linear fit to the data yields a best-fit slope of $-455 \text{ cm}^{-1}/\text{acceptor}$. The fact that a red-shift is observed for the proposed MLCT transition with increasing number of cationic acceptors is somewhat unexpected, and requires a detailed examination. From the simple one-electron (gas-phase) model derived in Appendix B.2.2, we expect that the CT transition energies for the single-acceptor ($\Delta E'_{\text{da}}$) and the linear double-acceptor ($\Delta E'_{\text{d}\beta}$) compounds (in the absence of significant electronic overlap) are related by (Eq. B.63),

$$\Delta E'_{\text{d}\beta} = \Delta E'_{\text{da}} + (V_{\text{aa}}^{\text{B}} - V_{\text{dd}}^{\text{A}}),$$

where V_{dd}^{A} is the interaction energy between the valence electron localised on the donor with either of the cationic acceptors and V_{aa}^{B} is the interaction energy between the electron localised on one acceptor with the other cationic acceptor (with both $V_{\text{dd}}^{\text{A}}, V_{\text{aa}}^{\text{B}} < 0$). Since we expect that $|V_{\text{dd}}^{\text{A}}| > |V_{\text{aa}}^{\text{B}}|$ (mainly because the acceptor-acceptor distance is greater than the donor-acceptor distance), one would expect a blue-shift in the CT transition energy upon the addition of a second acceptor (note that an even larger blue shift is predicted if there is appreciable overlap/mixing between the electronic wavefunctions, due to the resulting stabilisation (destabilisation) of the donor (acceptor) one-electron wavefunctions).

The situation is represented schematically in Figure 4.10, which demonstrates that in the case of two cationic acceptors, the CT transition effectively redistributes the positive molecular charge in an energetically unfavourable way in comparison to the (a) single-acceptor compound (whether or not one assumes a (b) symmetric delocalised wavefunction for the excited state or a (c) localised wavefunction due to a symmetry-lowering imposed by the environment or an asymmetric conformation of the two acceptors). We note that if one applies the concepts of the well-established molecular-exciton theory [45, 179, 180, 181]¹⁴ for a dimer of two *cationic* monomers (with a significant displacement of the positive charge towards the other monomer upon excitation), a net blue-shift would also result for both the ‘symmetric’ and ‘antisymmetric’ transitions.

In general, the observed red-shift in transition energy upon addition of further B-bpy acceptors could be attributed to three main effects: (i) a lowering in the equilibrium HOMO-LUMO separation for the transition (which would have to involve a more complex electronic rearrangement upon CT than that described by the simple one-electron CT picture), (ii) a reduction in the (gas phase) Stokes shift, due to a reduced displacement of the relative conformational equilibria of ground

¹³Note that the MLCT band peak extinction coefficients ε_{max} are analysed as opposed to the extracted oscillator strengths f (the latter being a more objective measure of the strength of the transition), due to the fact that the experimental curve for $[\mathbf{4A}](\mathbf{PF}_6)_4$ was not available. However, given that the fitted MLCT bandwidths do not vary significantly, at least for $[\mathbf{1A}]\mathbf{X}$ and $[\mathbf{2A}]\mathbf{X}_2$, we will take ε_{max} as a reliable measure of the integrated band intensity.

¹⁴Note that many aspects in standard molecular-exciton theory parallel the derivation in Appendix B.2, although in its usual form the exciton theory is applicable only to systems with distinct ground state orbitals.

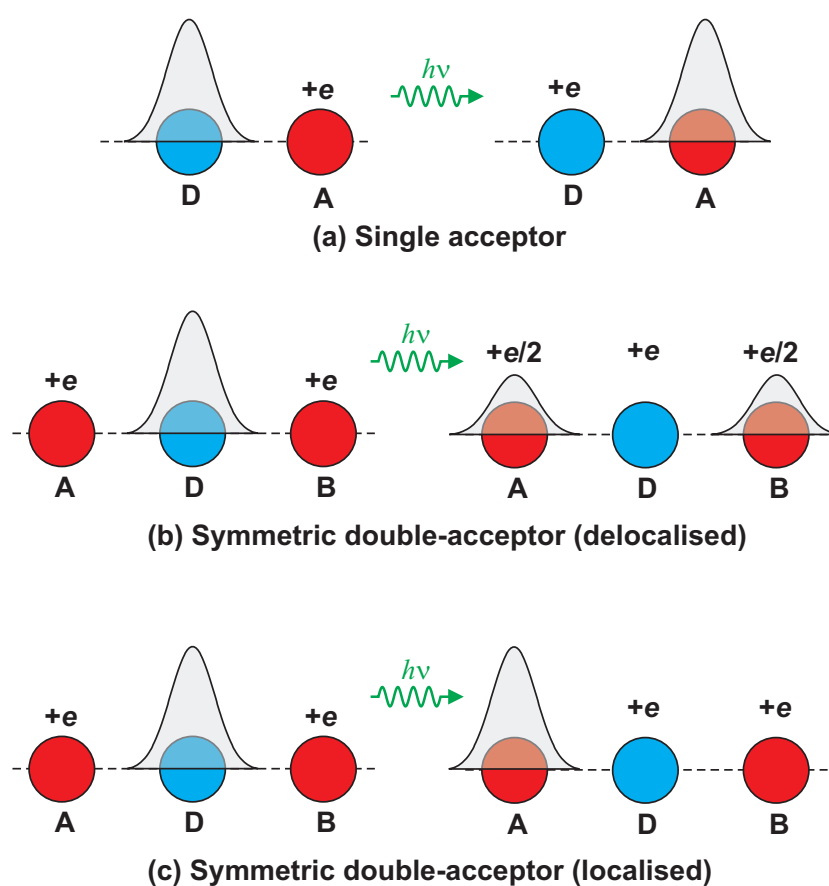


Figure 4.10.: Schematic comparison of CT transition in (a) donor (D)/single cationic acceptor (A) complex and donor/symmetric double acceptor (A,B) complex for both (b) symmetric delocalised and (c) localised excitation, indicating the redistribution of charge.

and excited states (i.e. shifting to smaller values in the presence of additional acceptor groups), or (iii) a reduction in the solvent interaction energy with increasing number of acceptors.

One would tend to argue against a significant relative Stokes shift (mechanism (ii)) as the cause of the red-shifting. The presence of additional (cationic) acceptors is most likely to lead to additional steric constraints on the geometry of the compound in solution, due to e.g. repulsive electrostatic interaction between the B-bpy acceptors (especially in the case of four acceptors, as testified by the significant degeneracy-lifting of the acceptor reduction processes observed in electrochemistry measurements [7]), and hence one could expect a *greater* relative displacement of the reaction coordinates upon excitation with the addition of further acceptor groups (giving rise to a larger Stokes shift of the potential energy surfaces and hence a blue-shifting of the transition energy).

However, a change in the magnitude of solvation interaction vs number of acceptors (mechanism (iii)) could lead to the observed red-shifting. In the previous section, we showed that the MLCT transition in **[1A]Br** exhibits a marked negative solvatochromism, i.e. an increasing blue shift with solvent polarity (ϵ_s) and dipole moment change between ground and excited states ($\Delta\mu$). The calculated solvent-induced blue-shift for **[1A]Br** in CH₃CN was $\Delta\nu_{\text{solv}} = 1340 \text{ cm}^{-1}$ relative to the extrapolated gas-phase value ($\lambda_{\text{GP}} = 540 \text{ nm}$) (See Figure 4.5(a)).

For the case of two acceptors, we expect a fairly high degree of centrosymmetry in the ground state, with the residual asymmetry due to fluctuations in the local solvent environment in combination with the fact that the B-bpy groups possess a distribution of conformations resulting from the relatively unhindered rotation about the B-C(Cp) bonds. Moreover, depending on the degree of instantaneous symmetry between the two acceptors during photon absorption, in general the CT excited-state corresponds to a transfer of electron density from the donor into a wavefunction delocalised to a certain degree over *both* acceptors [42, 44]. Hence we expect that the dipole moment change $\Delta\mu$, and hence the solvatochromic blue-shift, will be reduced in **[2A]Br₂** relative to **[1A]Br** (even more so considering that the effective solvent-shell radius a_0 in **[2A]Br₂** is larger).

The data for the MLCT absorption band of **[2A]Br₂** in various solvents is shown in Figure 4.11, along with the corresponding data for **[1A]Br**. As can be seen (Figure 4.11(a)), in all cases, there is a red-shift of the MLCT band upon addition of the second B-bpy acceptor group, and the data for CH₃CN and DMF are seen to converge, which supports that the solvatochromic shift is strongly reduced. However, we note that the relative changes in the MLCT band peak position and bandwidth for H₂O do not conform to the simple trend that might be expected from the solvatochromism theory, i.e. the relative decrease in solvent blue-shift/bandwidth appears to be too small. Keeping in mind that the solvatochromism model was developed for only a single acceptor group, the lack of a completely consistent behaviour in MLCT band-shifts/-widths for **[2A]Br₂** may well be due to an interaction between the solvent and the degree of symmetry between the two acceptors. One could anticipate that the strongly interacting H₂O molecules lead to a larger instantaneous fluctuation in the relative electronic environment of the two B-bpy substituents, leading to a more localised excited state on one of the acceptors with a resulting larger effective dipole moment change upon excitation (and hence solvent-induced blue-shift, consistent with what is observed).

We note that the reported MLCT band peak position for **[4A](PF₆)₄** in CH₃CN is $\lambda_{\text{max}} = 540 \text{ nm}$, i.e. very close to the extrapolated gas-phase value for **[1A]Br**. This would imply (within the current hypothesis) that both the effective solvent blue-shift *and* the electrostatic penalty for the MLCT electronic rearrangement

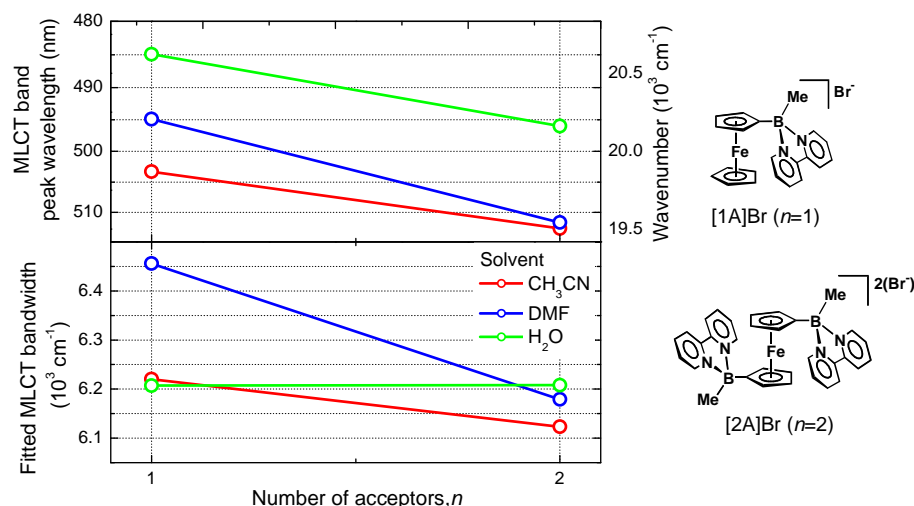


Figure 4.11.: Comparison of (a) MLCT band peak position and (b) fitted MLCT bandwidth, $\Delta\nu_{\text{FWHM}}$ for single ($[1\mathbf{A}]\mathbf{Br}$) and double-acceptor ($[2\mathbf{A}]\mathbf{Br}_2$) compounds vs solvent (as indicated).

are both greatly reduced for the case of four B-bpy acceptors. This is quite an acceptable assertion given the following. (i) We expect a higher degree of relative symmetry between the acceptor groups in the case of four B-bpy acceptors, especially as their relative conformations are now more strongly imposed due to mutual steric interactions (testified by the fact that NMR results show that there is a far larger barrier to rotation of the B-bpy acceptor groups about their respective B-C(Cp) bonds than in $[1\mathbf{A}]\mathbf{PF}_6$ and $[2\mathbf{A}](\mathbf{PF}_6)_2$). Thus we expect $[4\mathbf{A}](\mathbf{PF}_6)_4$ to be highly centrosymmetric in solution, which requires that the ground- and excited-state dipole moments should vanish (and hence suppressing the dominant dipole-dipole interactions with the solvent). (ii) The electrostatic penalty for the CT from the Fc-core into a symmetric delocalised wavefunction over all four acceptors will be far more effectively shielded by the large number of polarisable B-bpy π -systems in $[4\mathbf{A}](\mathbf{PF}_6)_4$, as well as the fact that now adjacent B-bpy acceptor groups are in close proximity and the effective ‘hole’-transfer to the central Fc-core will be partially compensated by a corresponding reduced electrostatic repulsion between cationic acceptors (as demonstrated by the significant Coulomb interaction between acceptors revealed from the electrochemical reduction data [7]).

Returning to the other details in Figure 4.9, we note that the oscillator strength of the fitted HE bands also increases with the addition of a second acceptor, with ratios $[2\mathbf{A}]\mathbf{X}_2:[1\mathbf{A}]\mathbf{X}$ of 2.3 and 2.8 for $\text{X}=\text{PF}_6^-$ and Br^- respectively. However, in contrast to the MLCT band we note that for the fitted HE band peak energy, one observes a consistent *blue*-shift with the addition of the second acceptor amounting to 876 cm^{-1} and 267 cm^{-1} for $\text{X}=\text{PF}_6^-$ and Br^- , respectively. It should be noted that because the HE absorption bands are fitted using only the resolvable low-energy side of the band (i.e. using data in the region 380-500 nm, which is already obtained as the residual after subtraction of the fitted MLCT band from the experimental curve), the fitted values (especially the band peak energies) are subject to possible systematic errors. Hence we do not attempt to draw any quantitative conclusions from the differences in the values for $\text{X}=\text{PF}_6^-$ and Br^- . In any case, the data for the HE band (including the lack of solvatochromism reported in the last section for $[1\mathbf{A}]\mathbf{Br}$) suggests that its origin lies in a transition that is localised on the respective B-bpy units.

4.3. UV-vis absorption in solid state

In this section, we present the absorption spectra of selected Fc-B-bpy compounds in solid-state environments, specifically, the compound $[2\mathbf{N}](\mathbf{PF}_6)_2$ (see Figure 4.1) in a doped-polymer film (at both room temperature and 20 K), and the double-acceptor compound $[2\mathbf{A}](\mathbf{PF}_6)_2$ in a single-crystal sample. The inclusion of doped-polymer thin film measurements serves multiple purposes in the overall investigation of these compounds. Firstly, it allows a convenient medium for the investigation of possible changes in the absorption spectra at low temperature, which were shown to reveal important details for ferrocene in Section 2.2.1 (i.e. reducing the degree of band broadening to the point where two distinct electronic transitions could be resolved). Secondly, for use in practical applications, the ability to incorporate the Fc-B-bpy monomers in thin films is essential, and one must investigate the effect of the new environment on the existing absorption bands (as well as developing appropriate techniques for the preparation of such films, which requires finding compatible solvent/polymer host combinations). The investigation of the $[2\mathbf{A}](\mathbf{PF}_6)_2$ single-crystal sample was specifically chosen because a structure determination based on X-ray diffractometry [7] shows that the conformation of the B-bpy acceptor groups in the crystal is different to that expected in the gas phase/solution, which we anticipated may have an influence on the MLCT band.

4.3.1. $[2\mathbf{N}](\mathbf{PF}_6)_2$ -doped polymer film absorption vs temperature

In approaching the problem of achieving high-quality doped-polymer thin films suitable for optical measurements, several key issues had to be dealt with. Perhaps most critical was finding a suitable polymer/solvent combination, in which the monomer is predissolved before forming the film. As we had extensive experience with spin-coated films employing polystyrene (PS) or PMMA as the host polymer (which allow one to achieve optical-quality thin films, with the required transparency into the UV¹⁵, and where experience had shown that the degree of electronic interaction between the polymer host and dopant monomers was minimised) we attempted to find a suitable solvent (or solvent combination) that would allow good mixing of the PS/PMMA polymer and $[\mathbf{nA}]\mathbf{X}_n$ monomers (and avoid aggregation of the monomer). However, due to the fact that the $[\mathbf{nA}]\mathbf{X}_n$ compounds only dissolve readily in polar solvents, which yielded poor solubility for PS/PMMA, we did not manage to prepare any films of usable quality¹⁶.

Fortunately, an additional derivative $[2\mathbf{N}](\mathbf{PF}_6)_2$ had been synthesised, which differs only from $[2\mathbf{A}](\mathbf{PF}_6)_2$ in that saturated nonyl-chains are attached to the B-bpy-units which renders the compound soluble in non-polar solvents (note that the saturated carbon chains were not expected to have a significant electronic influence on the rest of the compound, although as presented in the following we will show that their presence results in a moderate blue-shift of the MLCT band). Using $[2\mathbf{N}](\mathbf{PF}_6)_2$, we were able to form high-quality doped PS-films by spin-coating from THF solution (which is an extremely suitable solvent for PS films). However, due to the weak absorption strength of the MLCT band, the use of standard spin-coated films (i.e. using a polymer solution of <30 mg/mL with resulting thickness in the range 100-1000 nm) and reasonable monomer-doping concentrations ($\lesssim 5\%$) resulted in a very low optical density of the films (typically <0.01), such that absorption results had extremely low signal-to-noise, and were

¹⁵See Figure A.6 for a typical absorption spectrum of a pure polystyrene film.

¹⁶Note that the solubility of $[1\mathbf{A}]\mathbf{X}$ and $[2\mathbf{A}]\mathbf{X}_2$ was found to be problematic in CHCl_3 for the formation of thin films.

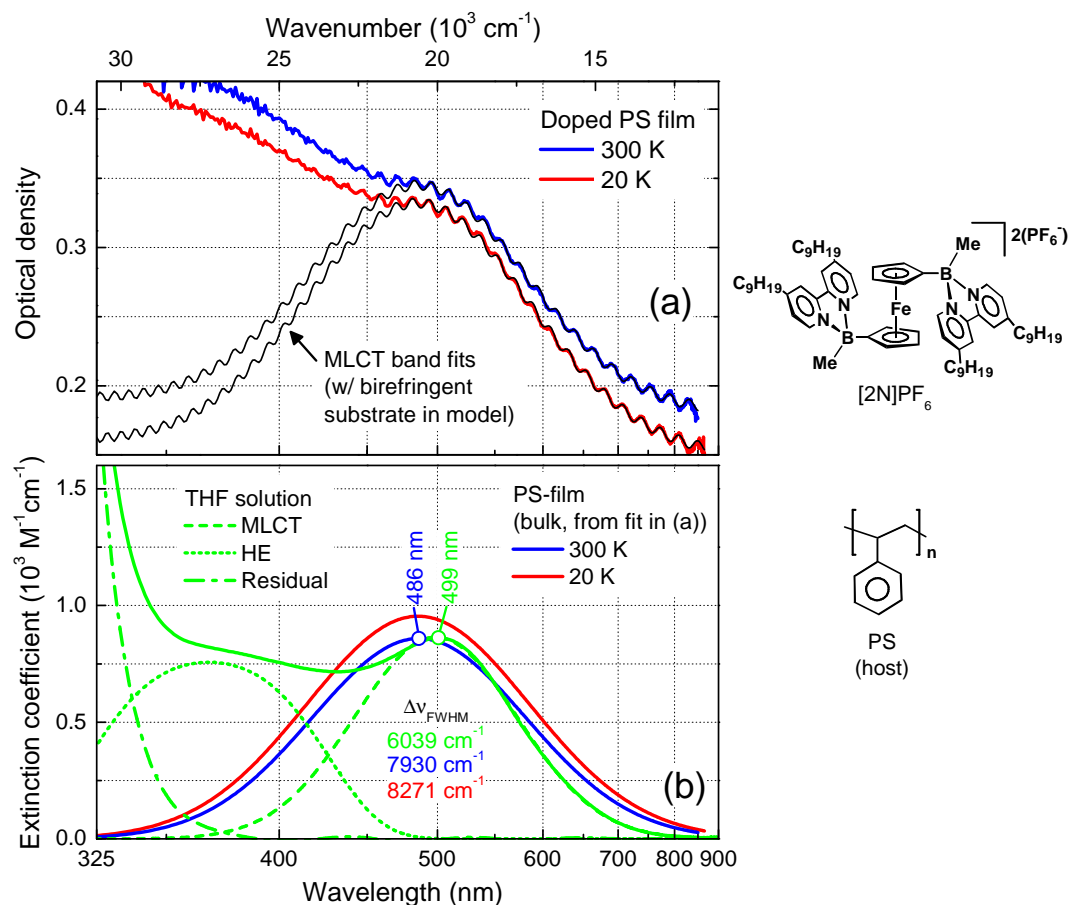


Figure 4.12.: UV-vis absorption of $[2N](PF_6)_2$ -doped polystyrene film (2-wt%, thickness $\sim 30 \mu\text{m}$) for $T=300 \text{ K}$ (blue curve) and 20 K (red). (a) Raw optical density and Gaussian band fit (including modelling of birefringent substrate which gives rise to the oscillation, as described in the text). (b) Comparison of $[2N](PF_6)_2$ molar absorption in THF solution (green) and corresponding calibrated PS-film data extracted from the analysis in (a).

particularly susceptible to background artifacts. Attempts to increase the monomer and/or polymer concentrations resulted in solvation and aggregation problems with unusable results.

As a final solution to the problem, we turned to the method of ‘drop-casting’ films [182], where in contrast to spin-coating, the film is deposited as a solution in an atmosphere of the solvent, and slowly evaporates¹⁷. So long that care is taken in the control of humidity and that the substrate is completely level (achieved using a fine-adjustable kinematic mount), this technique provided high-quality films with the ability to achieve thicknesses of $\gtrsim 30 \mu\text{m}$ which were sufficient for the measurements.

Figure 4.12(a) shows the absorption spectrum of such a drop-cast PS-film doped with $[2N](PF_6)_2$ (drop-cast from a 2-wt-% monomer, 30 mg/mL PS/THF solution), both at $T = 300 \text{ K}$ and $T = 20 \text{ K}$, measured using a small He-cryo head inserted into a standard UV-vis absorption spectrometer. As in solution, one clearly observes the low-energy side of the MLCT absorption band. For the measurements

¹⁷This technique and the necessary details were kindly provided by Prof. Wun-Shain Fann, Institute of Atomic and Molecular Science, Academia Sinica, Taiwan.

shown, we employed a 2-mm-thick sapphire substrate (to avoid any possible shattering at low temperature), with brass contacts to the cryo cold-finger both at the rear of the substrate and a brass contact ring on the upper side, in contact with the film surface (which also was important to prevent the film from detaching at low temperature). Due to an (albeit very weak) polarisation sensitivity in the optics of the spectrometer, the birefringence of the sapphire resulted in the observed oscillatory structure (as confirmed by measurements on a blank substrate and modelling of the effect). (Note that the much finer oscillatory structure due to multiple reflections in the film is not resolvable in Figure 4.12). Using a simple Jones matrix model [139] based on a birefringent substrate and a weak polariser (using literature data for the refractive indices of sapphire), we could fit the experimental curves, as shown in Figure 4.12(a) using a Gaussian absorption band for the bulk thin film absorption and fitting the low-energy region of the band.

The Gaussian MLCT absorption band extracted from the fitted film data are shown in Figure 4.12(b) along with the measured absorption spectrum of $[\mathbf{2N}](\mathbf{PF}_6)_2$ in THF (and fitted MLCT and HE bands). We address the THF solution data first. We note that the MLCT absorption band peak ($\lambda_{\max} = 501$ nm) is significantly *blue*-shifted by 436 cm^{-1} relative to that of $[\mathbf{2A}](\mathbf{PF}_6)_2$ in CH_3CN . This blue-shift was somewhat unexpected, considering the negative solvatochromism expected for any residual dipole moments in $[\mathbf{2A}](\mathbf{PF}_6)_2$ and $[\mathbf{2N}](\mathbf{PF}_6)_2$, and the fact that THF is relatively non-polar ($\epsilon_s = 7.6$) compared to CH_3CN ($\epsilon_s = 37.5$). Instead, the explanation for this might arise from one of several factors: (i) a weak electron-donating effect from the nonyl chains would lead to a small destabilisation of the B-bpy LUMO, and hence a blue shift of the MLCT band, (ii) the bulky nonyl chains may cause significant distortion of the relative conformation between the Fc-core and the B-bpy acceptors leading to a change in the MLCT energy, or (iii) the nonyl chains may affect the location of the counteranions in proximity to the cationic B-bpy acceptors. Whilst insufficient information is available to draw any conclusions in this respect, we note that at least that the Gaussian shape, peak MLCT absorption strength and fitted bandwidth for $[\mathbf{2N}](\mathbf{PF}_6)_2$ in THF ($\Delta\nu_{\text{FWHM}} = 6039$ cm^{-1}) are consistent with $[\mathbf{2A}](\mathbf{PF}_6)_2$, and hence we will assume that the $[\mathbf{2N}](\mathbf{PF}_6)_2$ system is still a representative Fc-B-bpy compound for studying the general effects of the polymer environment on the MLCT transition.

We now turn to the comparison of the solution and variable-temperature film absorption data in Figure 4.12(b). Note that the absolute scaling of the extracted film absorption is based on the experimental monomer-doping concentration, film thickness (~ 30 μm as measured using an interference microscope after creating a ridge in the sample so that the refractive index of the film did not affect the measurement) and the nominal density of polystyrene, allowing a fairly accurate comparison of the absolute absorption strengths between solution and film. As can be seen, for $T = 300$ K, the peak absorption strength in the thin film is very similar to that in THF solution, although the fitted MLCT bandwidth ($\Delta\nu_{\text{FWHM}} = 7930$ cm^{-1}) is significantly larger (by a factor of ~ 1.3), such that the oscillator strength is increased by the same factor (although we note that given the experimental uncertainty in the monomer-concentration in the thin film, at least a 10% error in the absolute absorption strength is possible). Also, a small but significant blue-shift ($\Delta\nu = 540$ cm^{-1}) of in the MLCT band peak ($\lambda_{\max} = 486$ nm) is observed in going to the thin film environment. These moderate but significant increases in MLCT bandwidth and band-peak energy may be attributed to the increase in conformational inhomogeneity of the $[\mathbf{2N}](\mathbf{PF}_6)_2$ solute in the thin film imposed by the relatively rigid and complex PS environment, as well as possibly some electronic

interaction with the C_6H_5 groups in the PS chain. In lowering the temperature to $T = 20\text{ K}$ ¹⁸, the fitted MLCT band peak position did not change significantly (i.e. by less than 1 nm, which is within the accuracy of the band fitting procedure). However, a small increase in MLCT bandwidth ($\Delta\nu_{\text{FWHM}} = 8271\text{ cm}^{-1}$, larger by around 4% than for $T = 300\text{ K}$) and a significant increase in peak absorption strength ($\sim 11\%$) result, such that the fitted oscillator strength is larger by a factor of $\eta \sim 1.15$ % at low temperature. One likely explanation for the increased MLCT absorption strength is due to the contraction to higher densities of the film at low temperature. At a microscopic level, this should lead to a compression of the $[\mathbf{2N}](\text{PF}_6)_2$ molecules, which would force the Fc-donor and B-bpy groups closer together, and increase any through-space contribution to the MLCT transition strength. We assume that the through-bond contribution is relatively constant, which is reasonable considering that the relative changes in bond lengths required to achieve the same increase due to through-bond coupling [183, 184, 185].

We note that these low-T film measurements were originally intended to investigate the possible emergence of resolvable structure under the MLCT band (i.e. due to the possibility of multiple electronic transitions, such as in the case of the Fc-I(a,b) band of ferrocene, Section 2.2.1). Whilst the additional inhomogeneous broadening in thin films, especially at low temperature, definitely worked against this aim, we note that the extremely good fit of the thin-film spectra using a single Gaussian function (at least over the entire low-energy side of the band, see Figure 4.12) for both $T = 20\text{ K}$ and $T = 300\text{ K}$ provides reasonable doubt as to the presence of more than one electronic transition under the MLCT band, where each electronic transition would in general respond differently to the significantly altered environment (and reduction of excited low-frequency vibrations at low T) and lead to some distortion in the band shape. In any case, we can conclude that if more than one electronic transition is present within the MLCT band (with comparable absorption strength), then they must be of similar electronic character, e.g. in terms of their localisation on the Fc and B-bpy units in the ground and excited state.

4.3.2. Single-crystal absorption of $[\mathbf{2A}](\text{PF}_6)_2$

In examining the $[\mathbf{nA}]\mathbf{X}_n$ compounds for any characteristic differences which could lead to a different spectroscopic behaviour, we noted from the X-ray structure determinations that the conformation of the B-bpy unit(s) in $[\mathbf{1A}]\text{PF}_6$ and $[\mathbf{2A}](\text{PF}_6)_2$ differ significantly [7]. Figure 4.13 shows the relevant crystal structures of $[\mathbf{1A}]\text{PF}_6$ and $[\mathbf{2A}](\text{PF}_6)_2$ (reproduced from Ref.[7]). As can be seen, for $[\mathbf{1A}]\text{PF}_6$, the B-bpy unit is facing away from the Fc-unit, consistent with the theoretical ground-state structure (Section 4.6)¹⁹, whilst crystal-packing forces for $[\mathbf{2A}](\text{PF}_6)_2$ enforce the B-bpy acceptors into a conformation where they are bent in towards the Fc-core. Hence measurements on a single-crystal sample of $[\mathbf{2A}](\text{PF}_6)_2$ was seen as a possible probe of the relative role of through-space vs through-bond donor-acceptor coupling on the MLCT transition.

The practical steps in preparation of a suitable single-crystal $[\mathbf{2A}](\text{PF}_6)_2$ sample

¹⁸Note that more than one absorption spectrum was acquired whilst the sample was at low temperature, which provided confidence that the thin-film sample had reached thermal equilibrium. Moreover, the room temperature spectra were measured again after warming the sample, which recovered the original spectrum.

¹⁹Note that the standard 2D representation for $[\mathbf{1A}]\mathbf{X}$ where the B-bpy acceptor is drawn bent down towards the Fc unit is used in this work to be graphically consistent with the literature reports [7, 1, 9], and not to imply the lowest-energy conformation of $[\mathbf{1A}]\text{Br}$, nor necessarily the role of through-space coupling between the Fc and B-bpy units.

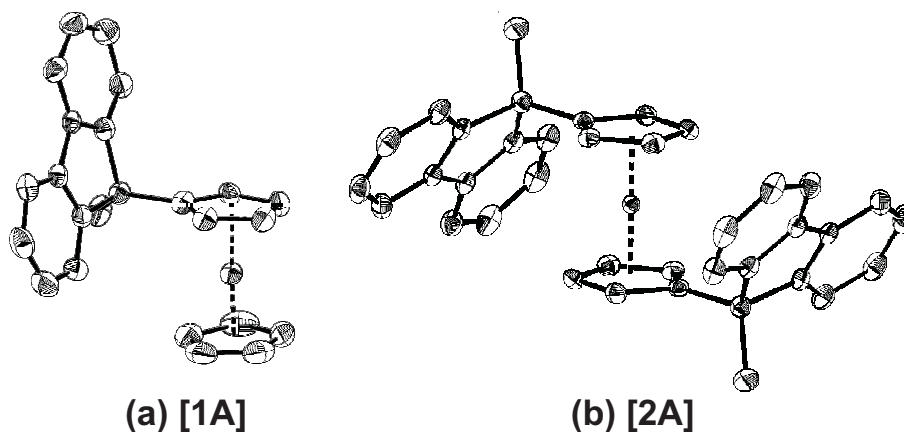


Figure 4.13.: Single-crystal structure of (a) $[1A]PF_6$ and (b) $[2A](PF_6)_2$ [7], demonstrating different relative donor-acceptor conformations.

presented several challenges. Whilst a small collection of irregular-shaped single-crystal fragments, generally with edge dimensions of $\sim 500 \mu\text{m}$, were available, only a small subset possessed a geometry suitable for further processing. The first step in the crystal sample preparation involved setting the crystal in an epoxy disk, and manual polishing of both surfaces to achieve a polished disk with a thickness of a few $100 \mu\text{m}$. However, the optical density of the resulting samples was still far too high for transmission measurements, and further manual polishing resulted in fracturing of the crystal. Moreover, attempts to obtain spectra using diffuse-reflectometry measurements in a suitably-equipped UV-vis spectrometer produced unusable results. Fortunately, a high-precision crystal polishing machine in another research group²⁰ was available for polishing the samples to a thickness of $< 100 \mu\text{m}$, sufficiently thin for transmission measurements of the MLCT band region. The precision polishing procedure involves attaching the crystal-embedded epoxy disk on a silica substrate using an adhesive of suitable transparency. The sample is then polished using a precision-mounted multi-axis rotating lead (Pb) polishing head with an intervening suspension of diamond-powder (grain size $0.25 \mu\text{m}$) in paraffin²¹.

Figure 4.14(a) shows the absorption spectrum of a (randomly oriented) crystal sample of $[2A](PF_6)_2$ with unpolarised light, as well as the fitted HE and MLCT bands. As in the case of the solution and thin-film samples, the low-energy side of the MLCT band conforms very well to a Gaussian profile, and the sum of the two fitted bands yields a negligible residual in the range $> 350 \text{ nm}$. The fitted absorption peak wavelength ($\lambda_{\text{max}} = 480 \text{ nm}$) is significantly blue-shifted by 1310 cm^{-1} relative to CH_3CN solution (512.2 nm) (and hence, based on the negative solvatochromism in these compounds, even more blue-shifted than the

²⁰Institut für Mineralogie, Abteilung für Petrologie und Geochemie, J. W. Goethe-Universität.

²¹It should be noted that even though the polishing process is capable of high-precision processing of inorganic crystals, the inherently low mechanical stability of these organometallic crystals and the small sample cross-section resulted in destruction of the crystal in several initial attempts. Due to the poor success rate of the polishing process, we ended up foregoing the crystal axis pre-orientation procedure, which required a careful absolute orientation of the crystal samples using a sensitive X-ray diffractometer before mounting (note that attempts to orient the samples using the X-ray equipment available within the research institute were not successful, due to the relatively low density of heavy atoms in these crystals). Hence the measurements presented here are on an sample of undetermined orientation. Further optical investigations of such materials in crystal should only be carried out once a process designed specifically for preparing thin fragile organic crystal samples is available.

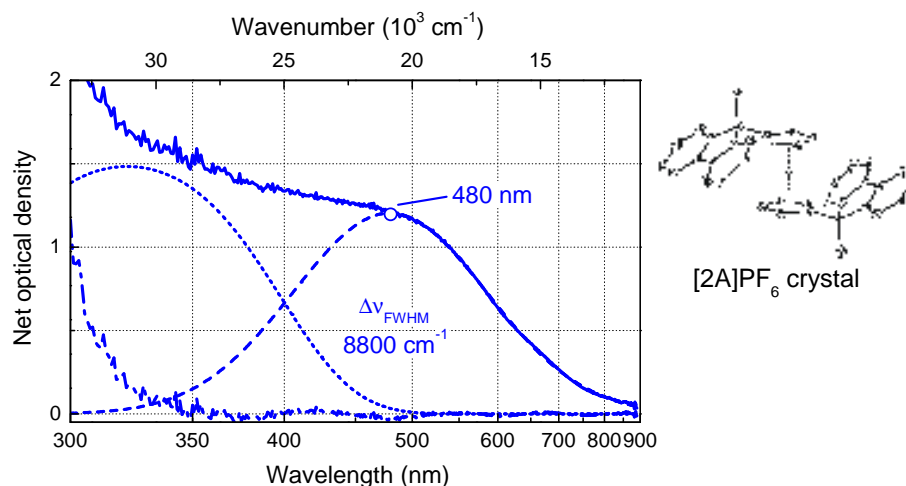


Figure 4.14.: UV-Vis absorption spectrum of $[2\mathbf{A}](\text{PF}_6)_2$ single crystal (arbitrary orientation).

expected gas-phase absorption peak), with a correspondingly larger fitted MLCT bandwidth ($\Delta\nu_{\text{FWHM}} = 8800 \text{ cm}^{-1}$).

As presented in the (gas-phase) theoretical results for the prototype $[1]^+(\text{H})$ (Section 4.6), the relative B-bpy conformation of $[2\mathbf{A}](\text{PF}_6)_2$ in the crystal phase corresponds closely to the geometry where the dihedral angle in the theoretical structure is $\theta_{\text{Fe-C-B-H}} \sim 180^\circ$ (see Figure 4.30, far right column) whereas the expected equilibrium conformation of the B-bpy groups of $[2\mathbf{A}](\text{PF}_6)_2$ in the gas phase (and presumably, in solution) is close to the conformation $\theta_{\text{Fe-C-B-H}} \sim 60^\circ$. From the MO orbital calculations of the ground state (Figure 4.28(d)), the predicted smallest HOMO-LUMO gap is predicted to be slightly lower for the conformation $\theta_{\text{Fe-C-B-H}} \sim 180^\circ$ than that for 60° by approximately 30 meV ($\cong 250 \text{ cm}^{-1}$). Hence, based on this result for a single-acceptor compound in the gas-phase, one could expect a small *red*-shift (or at least, not a *blue*-shift of $> 1300 \text{ cm}^{-1}$) in the MLCT transition energy for the *single*-acceptor compound when the B-bpy group is oriented towards the Fc-core.

However, as discussed in Section 4.2.3, in the case of the two-acceptor compound we expect a significant electrostatic penalty for the CT process relative to the single-acceptor compound due to the relatively unfavourable redistribution of the positive molecular charge. This electrostatic penalty (which in a simple point-charge model should scale with $1/r_{\text{DA}}$) increases as the donor-cationic-acceptor separation is reduced. Hence we attribute the observed blue-shift of $[2\mathbf{A}](\text{PF}_6)_2$ in the crystal to the fact that in this conformation, r_{DA} is significantly reduced relative to the expected gas-phase/solution conformation.

In addressing the source of the increased broadening of the MLCT band for $[2\mathbf{A}](\text{PF}_6)_2$ in the crystal, we cannot invoke conformational/environmental inhomogeneity as its primary source, and must consider additional solid-state effects. However, given that the broadening in the crystal can arise from many different sources, such as molecular-exciton-band formation due to intermolecular interactions, electron-phonon coupling and crystal defects [186], it is not possible to draw any conclusions as to the nature of the additional broadening effects from the data available. It is interesting, however, to note that the MLCT band is still qualitatively similar to that in solution and thin films, such that to a large degree the nature of the MLCT transition is still dominated by intramolecular effects.

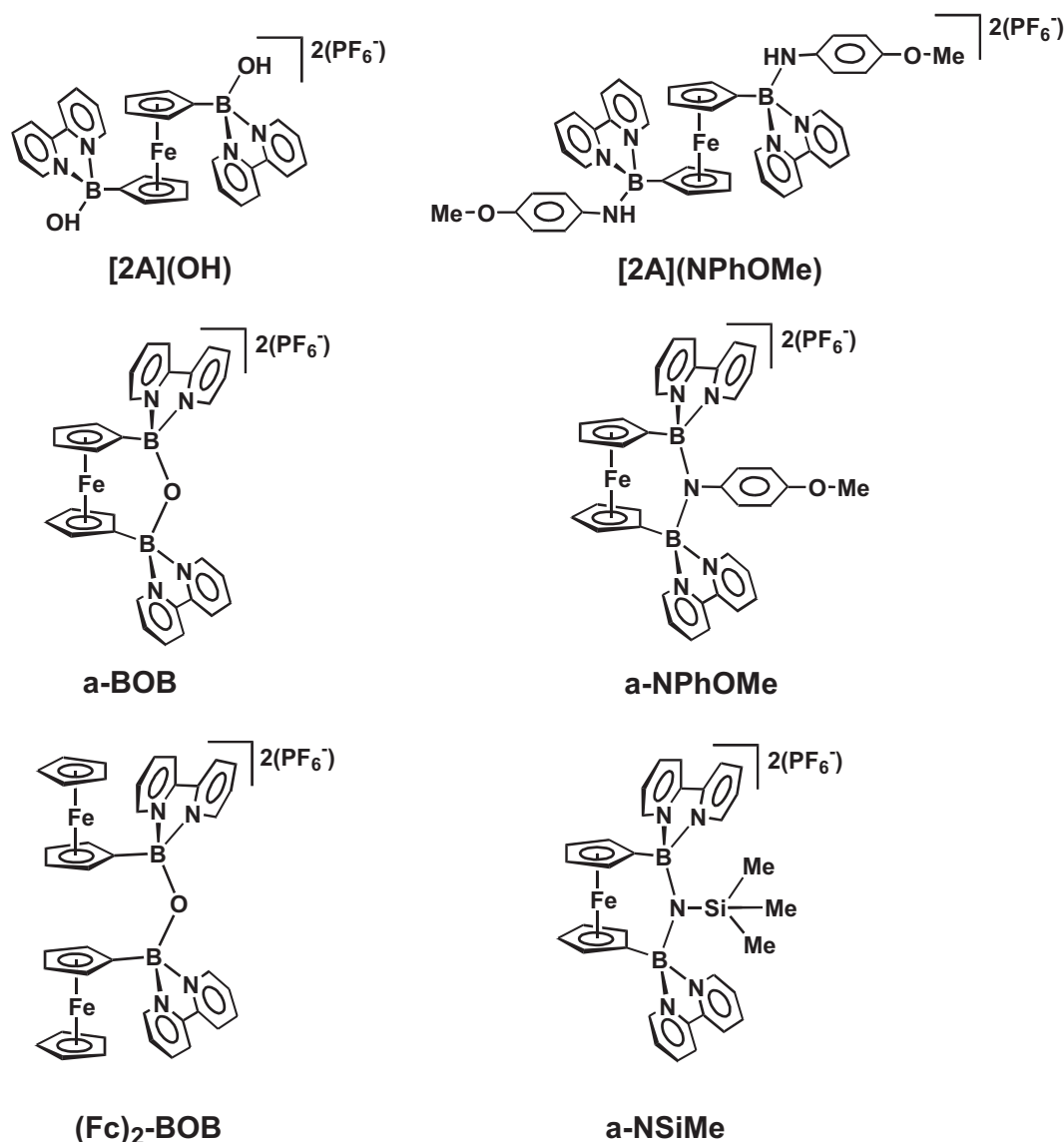


Figure 4.15.: Relevant bridged and unbridged Fc-B-bpy derivatives presented in this section.

We note that an interesting direction for future study includes not only spectral measurements on $[1A]PF_6$, but also on the compound $[2A](OH)$, which is a double-acceptor compound as per $[2A](PF_6)_2$, except the B-bpy groups are bent *away* from the Fc-unit (as per $[1A]PF_6$) [2].

4.4. UV-vis absorption spectra of other Fc-B-bpy derivatives

In this section, we present the UV-vis absorption of the additional Fc-B-bpy derivatives selected for the spectroscopic study (see Figure 4.15). The key comparison presented here is between the MLCT spectra of double-acceptor compounds with a connecting ansa-bridge between the two B-bpy acceptors (either an O-atom in the case of **a-BOB** to form a B-O-B bridge, or a substituted N-atom in the case of **a-NPhOMe** to form a B-N-B bridge) with the corresponding unbridged-acceptor analogs $[2A](OH)$ and $[2A](NPhOMe)$.

In the case of the ansa-bridged compounds, electrochemical studies [3, 2] suggest

a significant (and variable) electronic coupling between the two B-bpy acceptor groups, which is apparent from the splitting of the first two one-e⁻ reduction potentials $E'_{\text{red1(a)}}{}^{\circ}$ and $E'_{\text{red1(b)}}{}^{\circ}$ (which would be degenerate in the case of isolated acceptors), with splittings $\Delta E'_{1\text{a-b}}{}^{\circ} \equiv E'_{\text{red1(b)}}{}^{\circ} - E'_{\text{red1(a)}}{}^{\circ}$ in the range 0.12-0.17 V ($\cong 970 - 1370 \text{ cm}^{-1}$) for the derivatives presented here [2], see Section 4.5.1). In comparison, for the unbridged prototype **[2A](PF₆)₂** these two reduction waves are not resolvable in the cyclic voltammetry data, implying an upper bound of the splitting of $\lesssim 0.05 \text{ V}$. This increased inter-acceptor coupling in the bridged-acceptor derivatives could in principle be due purely to increased Coulomb interaction between the two B-bpy acceptors resulting from their smaller spatial separation enforced by the connecting ansa-bridge. However, no correlation was found between the degree of acceptor interaction and the polarisability of the N-substituent, e.g. Si(Me)₃ in the case of **a-NSiMe** and the π -system PhOMe for **a-NPhOMe**. Because this substituent is spatially located between the two B-bpy acceptors, any through-*space* Coulomb interaction between the acceptor groups should decrease with increasing polarisability of the substituent. This led to the conclusion that the dominant interaction between the B-bpy acceptors across both the B-O-B and B-N-B bridges is due to through-*bond* coupling [2].

From the CT theory presented in Section 2.1.3 (as well as Appendix B.2 and Ref. [187]), the fact that the ansa-bridge enforces a bent formation of the acceptors should result in a finite transition dipole moment for the CT transitions to both the symmetric and anti-symmetric acceptor wavefunctions. With increasing interaction between the acceptors, one expects a splitting between the energies of the symmetric and antisymmetric CT transitions and a corresponding broadening of the band and accompanying red-shift. Whilst a red-shift is consistently observed in comparing the ansa-bridged derivatives with the corresponding ‘free’ acceptor analogs, the MLCT bandwidth consistently *decreases*, indicating that the splitting of the symmetric and antisymmetric wavefunctions is small compared to the MLCT bandwidth and that a conformational mechanism dictates the observed MLCT bandwidth.

This mechanism originates from the fact that, besides the increased acceptor coupling, the ansa-bridge also enforces a different conformation for the B-bpy groups, and strongly hinders any significant geometry changes. The results from the gas-phase theoretical calculations (Section 4.6) suggest that the conformational distribution of rotation about the B-C(Cp) bonds for the prototype single-acceptor compound **[1]⁺(H)** does lead to a degree of broadening on the same order of magnitude as the differences in MLCT bandwidths between the bridged- and unbridged-acceptor compounds, indicating that different conformational distributions dictate the major changes in the MLCT bandwidth amongst the derivatives presented here.

In an additional attempt to distinguish between the acceptor coupling and conformation effects, we also compare the MLCT bandwidth of **a-BOB** with the di-ferrocene compound **(Fc)₂BOB**. For the case of **(Fc)₂BOB**, the B-O-B bridge between the two B-bpy acceptors is still present (although the acceptors are attached to the Cp rings of distinct Fc units), and NMR measurements indicate that in the absence of the constraining ansa-bridge of **a-BOB**, **(Fc)₂BOB** retains the conformational flexibility of the unbridged-acceptor compounds in solution. In this case, the MLCT bandwidth is closer to those of the unbridged-acceptor derivatives, supporting the proposed broadening mechanism as being due to a wider conformational distribution in the absence of the bridge. Another major difference of the ansa-bridged compounds is the greater expected solvatochromic blue-shift, due to the finite change in dipole moment upon excitation (compared to the centrosym-

metric unbridged-acceptor analogs), and an estimate of the expected blue-shift, based on the results in Section 4.2.2 for **[1A]Br**, is presented.

We note that the early spectroscopic measurements of **a-BOB** were severely distorted by the presence of a small concentration of the strongly-absorbing impurity $\text{Fe}(\text{bpy})_3^{2+}$. A comparison with the stringently purified **a-BOB** samples presented in this section is given in Appendix A.5, which demonstrates the potential hazard of even small quantities of impurity when studying compounds with relatively weak absorption.

Finally, we present data for the compound **[1C](PF₆)**, where the B-bpy acceptor group has been replaced with a B-dpp substituent (Section 2.3), which has been shown to possess a more delocalised, lower-energy LUMO relative to bpy, and allows us to examine the effect of this alteration on the MLCT band, which provides a robust test of the dependence of the acceptor-LUMO energy on the energy of the proposed MLCT transition.

In Figure 4.16(a) we present the absorption spectra for **a-BOB**, **(Fc)₂BOB** and **[2A](OH)** (all in CH_3CN), with the fitted HE and MLCT bands in Figure 4.16(b-d). The effect of replacing the CH_3 -substituents on the boron atom of **[2A](PF₆)₂** ($\lambda_{\text{max}} = 512 \text{ nm}$) with the OH substituents of **[2A](OH)** ($\lambda_{\text{max}} = 522 \text{ nm}$) leads to a red-shift of the MLCT band peak energy of $\Delta\nu = 374 \text{ cm}^{-1}$. Hence we can conclude that the OH-substituent leads to a stabilisation of the B-bpy LUMO energy relative to the CH_3 -substituent. From a comparison of **[2A](OH)** and **a-BOB** ($\lambda_{\text{max}} = 522 \text{ nm}$), one sees that the presence of the ansa-bridge results in an additional red-shift of $\Delta\nu = 360 \text{ cm}^{-1}$ (whilst the fitted MLCT bandwidth *reduces* from $\Delta\nu_{\text{FWHM}} = 5841 \text{ cm}^{-1}$ to $\Delta\nu_{\text{FWHM}} = 5260 \text{ cm}^{-1}$).

In Figure 4.17 the visible absorption spectra of the ansa-bridged compound, **a-NPhOMe**, where a substituted N-atom replaces the O-atom in the bridge, is presented, as well as its unbridged analog **[2A](NPhOMe)**. Again, the MLCT absorption band peak of **a-NPhOMe** ($\lambda_{\text{max}} = 532 \text{ nm}$) is red-shifted relative to the unbridged compound **[2A](NPhOMe)** ($\lambda_{\text{max}} = 519 \text{ nm}$) by $\Delta\nu = 471 \text{ cm}^{-1}$, with a decrease in the fitted MLCT bandwidth ($\Delta\nu_{\text{FWHM}} = 6104 \text{ cm}^{-1}$ for **[2A](NPhOMe)** and $\Delta\nu_{\text{FWHM}} = 5753 \text{ cm}^{-1}$ for **a-NPhOMe**).

As mentioned above, given that the ansa-bridged compounds no longer possess a linear arrangement A-D-A, we expect CT transitions to both the non-degenerate symmetric and anti-symmetric delocalised acceptor states. However, no additional structure is observed in the MLCT bands for either **a-BOB** or **a-NPhOMe**, and the MLCT bandwidths are actually significantly less than those of their unbridged-acceptor analogs (**[2A](OH)** and **[2A](NPhOMe)**).

Numerical tests of the form of the superposition of two Gaussian functions vs their peak separation (relative to their FWHM width) suggests that the inter-acceptor coupling cannot be larger than $\sim 0.2\Delta\nu_{\text{FWHM}} \sim 1000 \text{ cm}^{-1} \cong 0.12 \text{ eV}$.

In the case of the double-Fc-donor compound **(Fc)₂BOB** (Figure 4.16), one observes an MLCT band peak position ($\lambda_{\text{max}} = 537 \text{ nm}$), i.e. an additional small red-shift of $\Delta\nu = 175 \text{ cm}^{-1}$ relative to **a-BOB**, but the MLCT bandwidth is $\Delta\nu_{\text{FWHM}} = 6243 \text{ cm}^{-1}$, i.e. comparable to the unbridged-acceptor compounds. Hence the conformational flexibility of the derivative clearly dictates the MLCT bandwidth.

From the theoretical gas-phase calculations on **[1]⁺(H)** (Section 4.6), there is evidence that the fluctuation of the B-C(Cp) rotation angle (which is the main degree of freedom suppressed by the ansa-bridge) will result in a modest broadening of the MLCT transition energy (i.e. $\sim 300 \text{ cm}^{-1}$). However, in solution this value could be significantly modified (i.e. increased), and other displaced vibrational coordinates may also contribute to the total MLCT bandwidth.

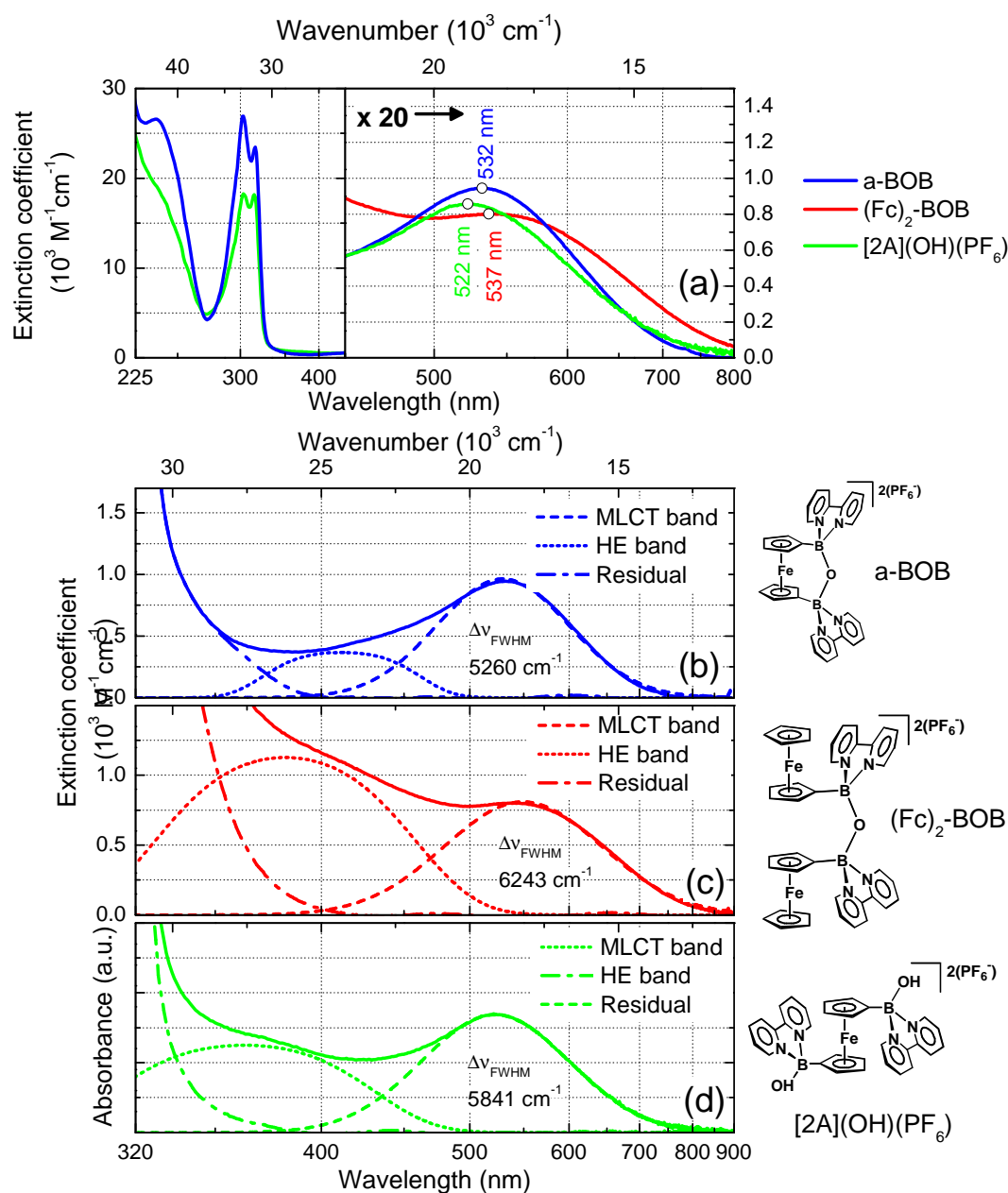


Figure 4.16.: (a) UV-vis spectra for B-O-B-bridged compounds **a-BOB** and **(Fc)₂BOB**, and unbridged-acceptor B-O compound **[2A](OH)** for comparison. Corresponding MLCT and HE band fits (and residual) for (b) **a-BOB**, (c) **(Fc)₂BOB** and (d) **[2A](OH)** (note that the scaling for **[2A](OH)** is arbitrary.)

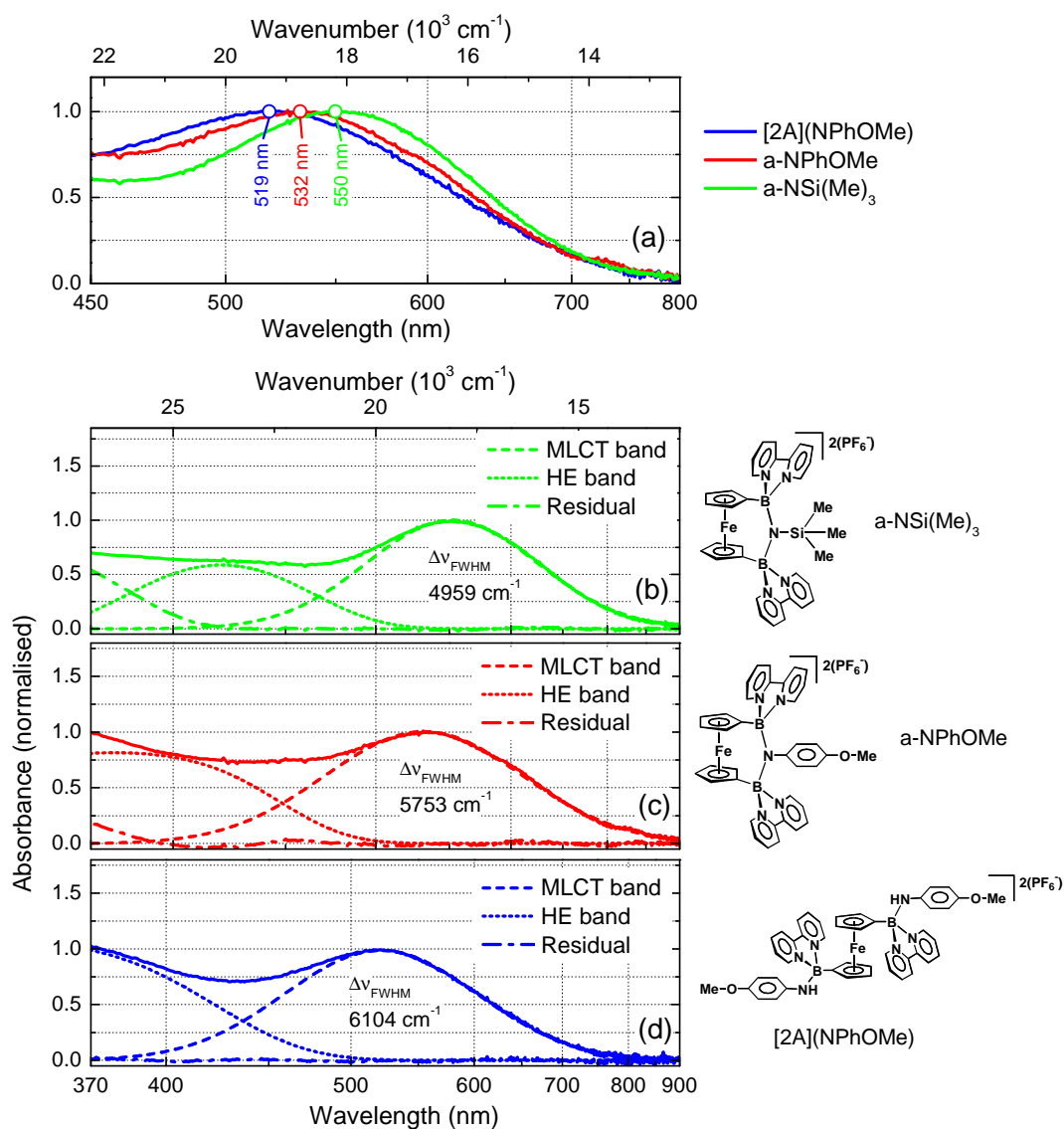


Figure 4.17.: (a) Comparison of UV-vis (normalised) absorption spectra of N-ansa-bridged compounds **a-NSiMe** and **a-NPhOMe**, and **[2A](NPhOMe)** (unbridged acceptor analog to **a-NPhOMe**), indicating MLCT band peak wavelengths. Corresponding MLCT and HE band fits (and residual) for (b) **a-NSiMe**, (c) **a-NPhOMe** and (d) **[2A](NPhOMe)**.

An important comparison arises between the MLCT bands for **a-NSiMe** and **a-NPhOMe** (Figure 4.17). Here we observe that for **a-NSiMe** the MLCT band peak ($\lambda_{\max} = 550$ nm) is even further red-shifted by $\Delta\nu = 615$ cm⁻¹ relative to **a-NPhOMe**, with a significant reduction in MLCT bandwidth ($\Delta\nu_{\text{FWHM}} = 5753$ cm⁻¹ for **a-NPhOMe** and $\Delta\nu_{\text{FWHM}} = 4959$ cm⁻¹ for **a-NSiMe**). We note that the splitting between the two near-degenerate reduction waves for **a-NPhOMe** ($\Delta E'_{1a-b} = 0.17$ V) and **a-NSiMe** ($\Delta E'_{1a-b} = 0.12$ V) is significantly different, by 0.042 V ($\cong 403$ cm⁻¹). The shift and splitting of redox potentials for two coupled acceptors depends somewhat non-trivially on the inter-acceptor interactions in each combination of the two oxidation states (i.e. ‘++’, ‘+0’ and ‘00’, see Figure 4.20), and so this value is not directly applicable to the expected splitting of the symmetric and antisymmetric delocalised acceptor wavefunctions, although it does provide an indication for the approximate magnitude, which is within a factor of 2 of the difference in the MLCT bandwidths of **a-NPhOMe** and **a-NSiMe**. Hence it is reasonable to attribute the reduced MLCT bandwidth for **a-NSiMe** to a reduction in the inter-acceptor interaction, supporting the assertion that the two CT transitions (symmetric and antisymmetric) are hidden under the MLCT absorption band. Note that another contribution to the different MLCT bands for **a-NPhOMe** and **a-NSiMe** could arise due to the presence of the non-planar Si(Me)₃ group, which is effectively bulkier than the planar PhOMe group, as evidenced from small relative differences in the X-ray crystal structures of the two compounds [2] which could be expected to be more significant in solution due to the absence of crystal packing forces.

A more complex issue is the red-shifting of the MLCT band with the addition of the ansa-bridge. We consider first the expected effect of the negative solvatochromism of the Fc-B-bpy compounds. As discussed in Section 4.2.3 for the [**nA**]**X_n** compounds, in the case of two unbridged acceptors, both the effective ground- and excited-state dipole moments should be greatly reduced due to symmetry (with the residual dipole moments being due to symmetry-breaking effects imposed by fluctuations in the environment and relative instantaneous conformation of the two acceptor groups). However, in the case of the ansa-bridged compounds, this *centro*-symmetry is not present, and the MLCT transition should still represent a significant change in dipole moment and result in a significant solvatochromic blue-shift. In order to estimate the expected relative blue-shift for the ansa-compounds **a-BOB**, **a-NPhOMe** compared to the unbridged compounds [**2A**](**OH**), [**2A**](**NPhOMe**) we employ the results of Section 4.2.2. For the single acceptor compound [**1A**]**Br** in CH₃CN, the solvatochromic blue-shift from the extrapolated gas-phase MLCT peak wavelength was calculated to be $\Delta\nu_{\text{solv}} = 1340$ cm⁻¹. Considering the relative geometries, it is reasonable to take the effective dipole moment change $\Delta\mu$ upon MLCT excitation for the ansa-bridged compounds to be a factor $\sqrt{2}$ smaller than that for the single-acceptor compound, which, in light of the quadratic dependence of the solvatochromic shift on $\Delta\mu$ would imply that the solvent-induced blue-shift for the ansa-bridged compounds in CH₃CN is approximately $\Delta\nu_{\text{solv}} = 670$ cm⁻¹ (although, admittedly, no account of the increased effective solute radius is included in this estimate). Moreover, in Section 4.2.3, the observation that the MLCT band of [**2A**](**PF₆**)₂ is blue-shifted relative to the expected gas-phase value for [**1A**]**PF₆** was attributed to the electrostatic penalty for CT in the case of two cationic acceptors, with only a small residual solvatochromic blue-shift. Hence, assuming $\Delta\nu_{\text{solv}} \sim 0$ for all the unbridged double-acceptor compounds, we can estimate the expected gas-phase red-shifts of **a-BOB** (relative to [**2A**](**OH**)) and **a-NPhOMe** (relative to [**2A**](**NPhOMe**))

to be $\Delta\nu_{\text{GP}} \sim 1030 \text{ cm}^{-1}$ and $\Delta\nu_{\text{GP}} \sim 1140 \text{ cm}^{-1}$, respectively²². Thus, accounting approximately for the solvatochromic shift, one expects even larger red-shifts for the gas-phase spectra.

Given that the gas-phase theoretical calculations on $[\mathbf{1}]^+(\text{H})$ indicate significant changes in the expected MLCT transition energy (Section 4.6) should accompany the distortion in the acceptor geometry (i.e. at least for the B-C(Cp) bond rotation), it is not possible to reliably extract the separate contributions to the red-shifts arising from (i) the different acceptor conformation imposed by the ansa-bridge and (ii) the inter-acceptor electronic coupling, for the bridged- and unbridged-acceptor compounds. The fact that both may be significant is accentuated by the observed red-shift of the MLCT band of **a-NSiMe** relative to **a-NPhOMe**. Whereas the reduction in MLCT bandwidth is consistent with the reduced inter-acceptor coupling for **a-NSiMe**, simple CT theory would predict that the MLCT transition for **a-NPhOMe** should be at lower energy, which is not observed.

We turn now to the UV-vis spectra for the derivative $[\mathbf{1C}](\text{PF}_6)$, where the B-bpy group is replaced with a B-dpp-based acceptor group. In Figure 4.18(a) we present a comparison of the visible-range absorption for $[\mathbf{1C}](\text{PF}_6)$ (and fitted HE and MLCT bands) with the B-bpy-acceptor compound $[\mathbf{1A}]\text{PF}_6$. As can be seen, the MLCT absorption peak of $[\mathbf{1C}](\text{PF}_6)$ ($\lambda_{\text{max}} = 605.4 \text{ nm}$) is red-shifted by $\Delta\nu = 3340 \text{ cm}^{-1}$ ($\cong 0.41 \text{ eV}$) with respect to $[\mathbf{1A}]\text{PF}_6$. As described in Section 2.3, comparison of the electrochemical data for the isolated (B-free) acceptor compounds bpy and 2,5-dpp suggests that the LUMO in 2,5-dpp is stabilised by 0.56 eV relative to bpy, and one could anticipate a similar situation for the corresponding B-bpy and B-dpp acceptor groups in $[\mathbf{1A}]\text{PF}_6$ and $[\mathbf{1C}](\text{PF}_6)$. Indeed, the electrochemistry data for $[\mathbf{1A}]\text{PF}_6$ and $[\mathbf{1C}](\text{PF}_6)$ (see Section 4.5.2) indicates that the LUMO for $[\mathbf{1C}](\text{PF}_6)$ is stabilised by 0.5 eV relative to $[\mathbf{1A}]\text{PF}_6$. Whilst this observation alone seems to provide strong evidence for the general assignment of the MLCT band, we note that in Figure 4.18(b), the $\pi - \pi^*$ band for $[\mathbf{1C}](\text{PF}_6)$ is also red-shifted relative to that of $[\mathbf{1A}]\text{PF}_6$ by $\Delta\nu = 4600 \text{ cm}^{-1}$ ($\cong 0.57 \text{ eV}$), which indicates that transitions which are definitely localised on the acceptor also undergo a red-shift of similar magnitude in the three-ring B-dpp system, due to the fact that the highest *occupied* acceptor-MO energy changes by only a small amount ($\sim 0.07 \text{ eV}$, see Section 2.3) in going from B-bpy to the B-dpp acceptor. Hence with this observation alone, it is still possible that the proposed MLCT band would instead be localised on the B-bpy units (and would also be expected to increase with the number of acceptors).

However, an important additional argument for the MLCT assignment arises when considering the relative Fc-based oxidation potentials for $[\mathbf{1A}]\text{PF}_6$ and $[\mathbf{1C}](\text{PF}_6)$ (Section 4.5.2). In this case, the oxidation potential for $[\mathbf{1C}](\text{PF}_6)$ ($E'_{\text{ox}} = 0.50 \text{ V}$) is shifted to a more positive potential relative to $[\mathbf{1A}]\text{PF}_6$ ($E'_{\text{ox}} = 0.40 \text{ V}$) by 0.10 V. This implies that the Fc-based HOMO in $[\mathbf{1C}](\text{PF}_6)$ is stabilised (by 0.10 eV) relative to $[\mathbf{1A}]\text{PF}_6$, so that the net shift between the Fc-HOMO and acceptor-LUMO (relative to $[\mathbf{1A}]\text{PF}_6$) is predicted to be 0.40 eV, in almost exact agreement with the observed MLCT band shift of 0.41 eV. The fact that the MLCT band red-shift for $[\mathbf{1C}](\text{PF}_6)$ relative to $[\mathbf{1A}]\text{PF}_6$ can be explained with a consideration of both changes in the acceptor-LUMO *and* Fc-donor-HOMO provides extremely compelling evidence for the MLCT assignment (perhaps the most *direct* steady-state spectroscopic evidence in this study). As will be seen in Section 4.5.2 where we present a summary of the correlation between the MLCT

²²As per the preceding discussion, these values are calculated by taking the observed red-shifts in CH_3CN solution and adding the estimated negative solvatochromic shift for the ansa-bridged compounds.

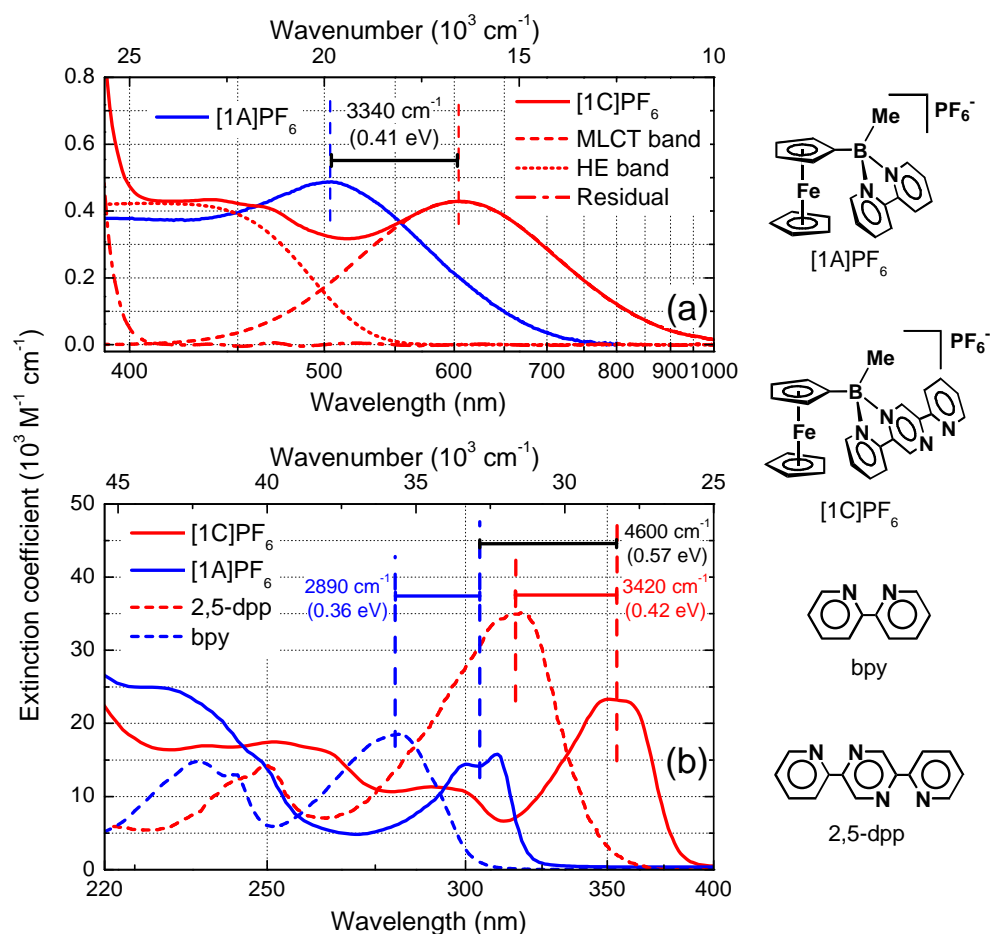


Figure 4.18.: (a) Comparison of UV-vis spectra for corresponding bpy- and 2,5-dpp-based acceptor compounds [1A]PF₆ and [1C](PF₆). (a) Visible range, including fitted MLCT and HE bands for [1C](PF₆), and MLCT absorption peak shift between [1A]PF₆ and [1C](PF₆) (all in CH₃CN). (b) UV range spectra for [1A]PF₆ and [1C](PF₆), including boron-free organic acceptors bpy and 2,5-dpp for comparison, and approximate relevant band peak shifts.

band peak position and the corresponding redox potentials, the inclusion of the derivative $[\mathbf{1C}](\mathbf{PF}_6)$ (with its correspondingly large changes in MLCT band position and redox potentials) is particularly important in establishing the correlation between the two sets of experimental results (whereas effects such as varying solvation and Stokes shifts for the bridged- and unbridged-bpy-acceptor compounds alone somewhat disturbs the ideal linear trend).

We note that within the simple Mulliken-type CT model (Section 2.1.3, Appendix B.2) the relative stabilisation of the Fc-HOMO for $[\mathbf{1C}](\mathbf{PF}_6)$ could well be due to mixing of the Fc-HOMO and dpp-acceptor LUMO (i.e. a greater degree of ground-state charge transfer, and resultant stabilisation of the Fc-HOMO), relative to the bpy-based derivatives where the interpretation of the observed trend of MLCT-band *red*-shifting with increased number of acceptors suggested that this mixing (which should result in an increasing blue-shift of the CT transition) did not play a significant role.

We do note however, that the Mulliken-CT theory also predicts an additional term in the CT transition dipole moment (see Eq. B.43) with significant ground-state mixing, whereas a small decrease in the MLCT oscillator strength is actually observed for $[\mathbf{1C}](\mathbf{PF}_6)$ relative to $[\mathbf{1A}]\mathbf{PF}_6$. We can conclude even though ground-state mixing appears to occur in $[\mathbf{1C}](\mathbf{PF}_6)$, there is a corresponding difference in the spatial distribution of the acceptor orbitals for the B-bpy and B-dpp groups such that the orbital overlap with the Fc-HOMO is actually slightly decreased. This issue remains open for further investigation.

In Figure 4.18(b), we also include the UV absorption spectra of the B-free isolated acceptor groups bpy and 2,5-dpp. Here we observe that the approximate corresponding red-shifts of the $\pi - \pi^*$ band which occur on ‘addition’ of the ‘Fc-B<’-group are $\Delta\nu = 2890 \text{ cm}^{-1}$ (for the bpy-based acceptor) and $\Delta\nu = 3420 \text{ cm}^{-1}$ (for the 2,5-dpp-based acceptor), in both cases due to the delocalisation of the π -bonding and π -anti-bonding orbitals onto the B atom [7]. In Section 4.5.1, we will combine the reported MLCT and $\pi - \pi^*$ spectroscopic data with the corresponding electrochemical data to yield a more detailed comparison of the relative orbital energies of $[\mathbf{1A}]\mathbf{PF}_6$ and $[\mathbf{1C}](\mathbf{PF}_6)$.

4.5. Electrochemistry measurements

In this section we present a summary of the available electrochemical data for selected Fc-B-bpy derivatives, including (i) the cyclic voltammetry traces (from which the redox potentials are extracted) (ii) the correlation of the redox potentials with the MLCT band position, (iii) the changes in UV-vis absorption resulting upon oxidation/reduction.

The cyclic voltammetry data presented here was measured as a standard component of the original characterisation of these compounds [7, 3, 2] due to the fact that it provides a straightforward probe of the electronic coupling between the electroactive fragments in the various derivatives, and hence is included here more for the sake of completeness, due to the importance of this data in the analysis of the spectroscopic data. Due to the fact that we did not devote a theory section in Chapter 2 to electrochemistry, we provide some remarks here on the details of interpreting the redox potentials (in particular the shift and splitting of redox potentials for identical coupled acceptor groups) in order to put some of the comments earlier in this chapter on a more solid footing.

Whilst we have already employed the potentials for the Fc-oxidation and B-bpy-acceptor-reduction processes in interpreting the MLCT band positions on a somewhat ‘derivative-by-derivative’ basis in the previous sections, here we present

a summary of the correlation between the relevant redox potentials and the MLCT band energy for the key derivatives and a simple analysis which demonstrates that the redox potentials provide a robust predictor of the MLCT band energy (which strongly supports the assignment of the band). Finally, we present the differential UV-vis absorption spectra that result upon electrochemical oxidation and reduction of the derivatives **[1A]PF₆**, **[2A](PF₆)₂** and **a-BOB**. A more quantitative measurement of these data was carried out during this study²³, due to the realisation that the new optical transitions that arise upon the Fc-centred oxidation and B-bpy-centred reduction of the Fc-B-bpy compounds would be extremely useful in interpreting the excited-state transient spectra following MLCT excitation (presented in the next chapter), especially in light of the relatively weak coupling between donor and acceptor.

4.5.1. Cyclovoltammetry data and redox potentials

Figure 4.19 displays the measured cyclovoltammetry traces for **[1A]PF₆**, **[2A](PF₆)₂**, **a-BOB** and **(Fc)₂BOB** (under comparable experimental conditions, briefly indicated in the figure caption)²⁴. We begin by identifying the basic features in these traces and the nomenclature indicated in the figure.

At positive potentials (vs SCE²⁵, note the inverted direction of the horizontal axis) we observe the oxidation wave for **[1A]PF₆**, **[2A](PF₆)₂** and **a-BOB** ('ox1') corresponding to electron removal from a predominantly Fc-based HOMO, whilst for the di-ferrocene compound **(Fc)₂BOB** one observes two poorly-resolved near-degenerate oxidation waves ('ox1a' and 'ox1b') corresponding to successive oxidation of the two-Fc system. At negative potential, two reduction wave systems are observed for each compound, each representing the addition of one electron for each B-bpy acceptor present in the compound. Whilst for the single B-bpy acceptor compound **[1A]PF₆**, each sequential process ('red1' and 'red2') involves only one electron per molecule, for the double-acceptor compounds each wave represents the addition of two electrons to the double-acceptor system at near-degenerate potentials ('red1a'/'red1b' and 'red2a'/'red2b')²⁶. The strong acceptor-coupling in the ansa-bridged compounds **a-BOB** and **(Fc)₂BOB** leads to a visible splitting of the two near-degenerate reduction potentials for each wave, but for **[2A](PF₆)₂** they are not resolvable. We note that for the derivatives shown, all these redox

²³Note that preliminary spectra were measured during the initial characterisation of the compounds [7, 3, 2], but only with the express purpose of extracting approximate peak wavelengths for the new bands which emerge upon oxidation/reduction. The spectral data for the compounds **[1A]PF₆** and **[2A](PF₆)₂** presented here were carefully repeated by F. Fabrizi de Biani (AG Zanello, University of Siena, Italy) with an aim to have spectra suitable for more quantitative comparison.

²⁴It should be noted that due to the a number of inherent energy offsets and kinetic terms in solution-phase electrochemical measurements, that depend on experimental factors and the specific systems under study [46], the absolute position of the redox measurements (given relative to a standard redox process of personal choice) does not readily afford the absolute ionisation potential or electron affinity of the compound. However, in most cases the relative redox potentials do possess a fairly well-defined relation to the relative energy changes of the electron-addition and removal processes for a particular compound and related derivatives, and we assume here that the electrochemical potential differences (in V) correspond to the respective energy changes of the solute (in eV). Whilst further details are beyond the scope of the present work, we do stress that the interpretation of the redox data involved was checked with the experience of the electrochemistry group (AG Zanello) who performed the measurements, and the relevant redox potentials were taken from the literature.

²⁵SCE: Standard calomel electrode.

²⁶Note that the absolute number of electrons per molecule involved in each redox wave was confirmed by controlled 'coulometric' tests [7, 3, 2], and is also reflected in the relative amplitude of the corresponding oxidation/reduction peaks.

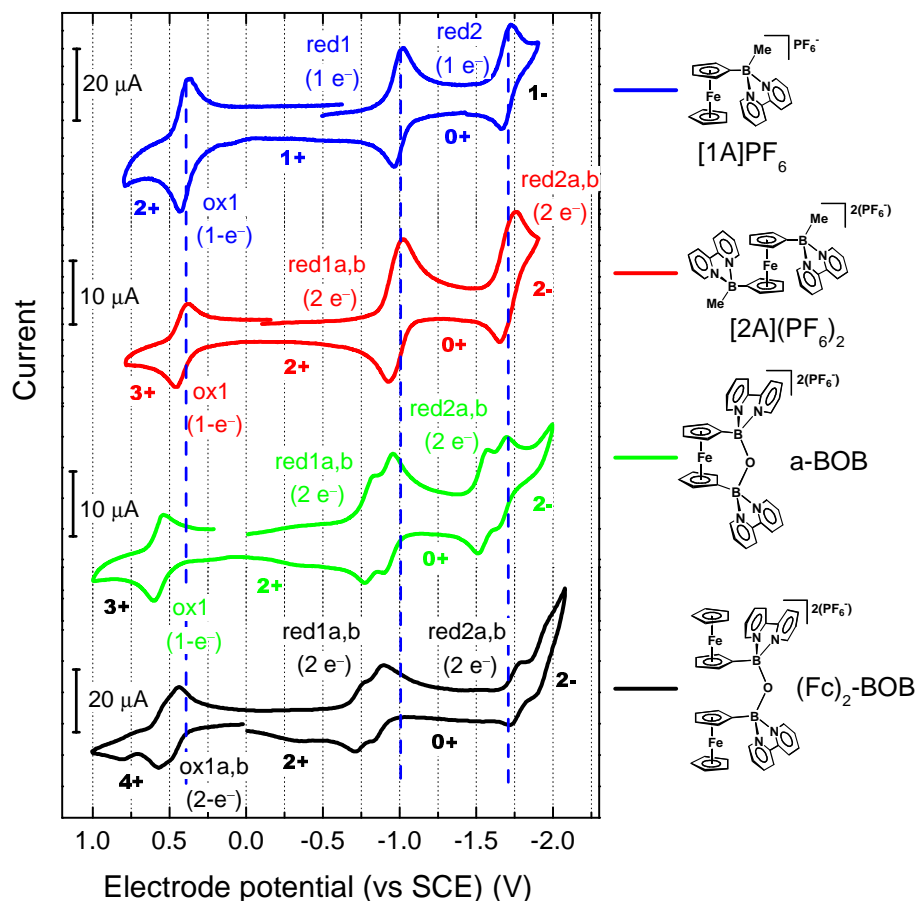


Figure 4.19.: Cyclic voltammograms for **[1A]PF₆**, **[2A](PF₆)₂**, **a-BOB** and **(Fc)₂BOB**, indicating nomenclature for each redox process, the number of electrons involved in each oxidation/reduction wave and the molecular charge in each region (Measurements in DMF containing [NEt₄][PF₆] electrolyte, Pt-electrode [7, 3, 2]). Note the inverted direction of the x-axis (potential)).

Compound	Redox Potentials (V vs SCE)					
	Oxidation		Reduction			
	ox1(a,b)		red1(a,b)	red2(a,b)		
[1A]PF₆	+0.40		-1.02	-1.71		
[2A](PF₆)₂	+0.43		-0.98	-1.71		
[4A](PF₆)₄	+0.38		-1.05	-1.85		
a-BOB	+0.57		-0.80	-0.93	-1.55	-1.67
(Fc)₂BOB	+0.53	+0.47	-0.75	-0.88	-1.78	-1.96
[1C](PF₆)	+0.50		-0.52		-1.25	
σ -B-bpy	-		-0.95		-	
Fc	+0.49		-		-	

Table 4.1.: Formal electrochemical potentials $E'_{\text{ox},1(a,b)}$ and $E'_{\text{red},n(a,b)}$ for relevant Fc-B-bpy compounds and related isolated Fc-donor and σ -B-bpy-acceptor compounds. Note that in the case where the derivative bears multiple acceptor or donor units, the two non-degenerate potentials are given whenever the two waves were resolvable. (Data extracted from [134, 7, 3, 2]).

processes are electrochemically reversible (at least on the experimental time scale of seconds) [7, 3, 2]. The extracted formal electrode potentials are listed in Table 4.1 for reference.

From hereon, we will concentrate only on the *first* of the two n -electron reduction waves (red1(a,b)), which is the only one relevant to the MLCT process. Inspection of the values in Table 4.1 reveals several important variations for the different derivatives (and the control compounds, Fc and σ -B-bpy), as detailed in the following paragraphs.

(i) We note that the oxidation potentials for **[1A]PF₆** ($E'_{\text{ox}} = +0.40$ V), **[2A](PF₆)₂** ($E'_{\text{ox}} = +0.43$ V) and **[4A](PF₆)₄** ($E'_{\text{ox}} = +0.38$ V) all occur at slightly lower positive values in comparison to Fc, indicating that the electron removal is slightly energetically more favourable, which suggests that the B-bpy group(s) actually donate some electron density to the Cp-ring(s) of the Fc unit despite their formal positive charge [7]. The lack of a trend for $n = 1, 2, 4$ however deserves some attention, if one considers the increasing formal positive charge of these cationic compounds with increasing number of B-bpy acceptors. In the gas-phase (i.e. in the absence of counteranions or surrounding dielectric solvent), the ionisation potential of these compounds would demonstrate a very large Coulomb barrier for electron removal (depending on the effective solute radius and the degree of intramolecular shielding of the electron from the formal positive charge during removal). In the electrochemical solution however, the large excess of counteranions in the electrolyte will render this Coulombic escape energy almost negligible (especially considering the additional electric field shielding afforded by the DMF solvent ($\epsilon_s = 36.7$)). However, the fact that the UV-vis spectra are measured in solution in the absence of the excess electrolyte (with only a 1:1 concentration of counteranions, which need not be within the first solvent shell of the solute) could lead to some deviations in the correlation between the measured MLCT band energy and oxidation potential. We return to this point in the next section when presenting this correlation.

(ii) For the di-ferrocene compound **(Fc)₂BOB**, the splitting in the oxidation

potentials ($E'_{\text{ox,a}} = +0.47$ V, $E'_{\text{ox,b}} = +0.53$ V) is $\Delta E'_{\text{ox,a-b}} = 0.06$ V ($\cong 480$ cm⁻¹) indicates that a small (presumably through-space) coupling exists between the two Fc units. We note that the degree of this splitting is a critical parameter if one attempts to electrochemically prepare a mixed-valence compound [188, 189, 190, 191, 192, 15, 193] (i.e. with oxidation of only one of the two Fc units). The average of the two oxidation peaks, however, is close to that in Fc, and does not reproduce the less-positive value for the unbridged double-acceptor compound **[2A](PF₆)₂**.

(iii) The oxidation potential for **a-BOB** ($E'_{\text{ox}} = +0.57$ V) is shifted to considerably more positive potential, such that the Fc-HOMO is stabilised by the presence of the ansa-bridged B-bpy-system. However, we note that the fact that both B-O-B bridged derivatives, **a-BOB** and **(Fc)₂BOB**, do not demonstrate the destabilisation of the Fc-HOMO witnessed in **[nA](PF₆)_n** might suggest that any electron density from the B-bpy groups which extends onto the Cp⁻ rings for the **[nA](PF₆)_n** series is ‘diverted’ onto the B-O-B bridge (consistent with the through-bond coupling hypothesis for the B-O-B bridged compounds).

(iv) Turning now to the corresponding reduction processes, we note that for the unbridged-B-bpy-acceptor derivatives **[1A]PF₆** ($E'_{\text{red1}} = -1.02$ V), **[2A](PF₆)₂** ($E'_{\text{red1}} = -0.98$ V) and **[4A](PF₆)₄** ($E'_{\text{red1}} = -1.05$ V) the reduction processes all occur at more negative potential than the control compound σ -B-bpy, indicating a destabilisation of the B-bpy LUMO when the saturated carbon network in σ -B-bpy is replaced by the Fc unit (note that for **[2A](PF₆)₂** and **[4A](PF₆)₄**, these values are the average of the near-degenerate 2- and 4-e⁻ reduction processes). There seems to be no simple explanation for the observed destabilisation of both Fc-HOMO and B-bpy-LUMO for these derivatives. We note that in comparison to the oxidation process, which involves a Fc-HOMO which is localised on the Fe²⁺-core, the B-bpy-LUMO involves a highly delocalised LUMO, such that electronic distortion due to the presence of the Fc-unit leads to an inherently more complex influence on the reduction potential. Hence it is foreseeable that the electronic distortion of the bpy HOMOs in **[nA](PF₆)_n** (which is associated also with the slight donation of electron density to the Fc) leads to resulting π -orbitals which possess a higher degree of repulsion with the π^* orbital.

(v) In contrast to the unbridged compounds, for the B-O-B bridged compounds **a-BOB** and **(Fc)₂BOB** there is both a well-resolved splitting in the near-degenerate reduction potentials ($\Delta E'_{\text{red1a-b}} = 0.13$ V) in both cases, and the average of the two split potentials $\overline{E'_{\text{red1}}}$ (0.865 V for **a-BOB** and 0.815 V for **(Fc)₂BOB**) is shifted to less-negative values for both derivatives relative to σ -B-bpy (by 0.085 V for **a-BOB** and 0.135 V for **(Fc)₂BOB**). In order to discuss these shifts, we refer to Figure 4.20 which provides a schematic for the expected splitting of the reduction potentials for a system with two identical acceptors (in a symmetric environment), with a small perturbation due to interaction matrix elements V_{11} and V_{12} in each combination of oxidation states (‘++’, ‘+0’ and ‘00’). (We note that the schematic in Figure 4.20 is derived from simple perturbation theory analogous to that in Appendix B.1.2 assuming the wavefunction overlap is small).

As indicated, the splitting depends in a somewhat non-trivial way on the interaction between acceptors for all three possible combinations of (distinguishable) oxidation states. Assuming that $V_{11} \gg V_{12}$, we have $\Delta E_{\text{red,a-b}} = 1/e(V_{11}^{00} + V_{11}^{++} - 2V_{11}^{+0})$ for the potential splitting whilst the shift of the average potential is given by $\overline{E'_{\text{red}}} = E_{\text{red}} + 1/(2e)(V_{11}^{00} - V_{11}^{++})$. Hence, neglecting wavefunction overlap, the shift of the average reduction potential $\overline{E'_{\text{red1}}}$ for both **a-BOB** and **(Fc)₂BOB** is due to a combination of the dominant repulsive cation-cation interaction ($V_{11}^{++} > 0$)

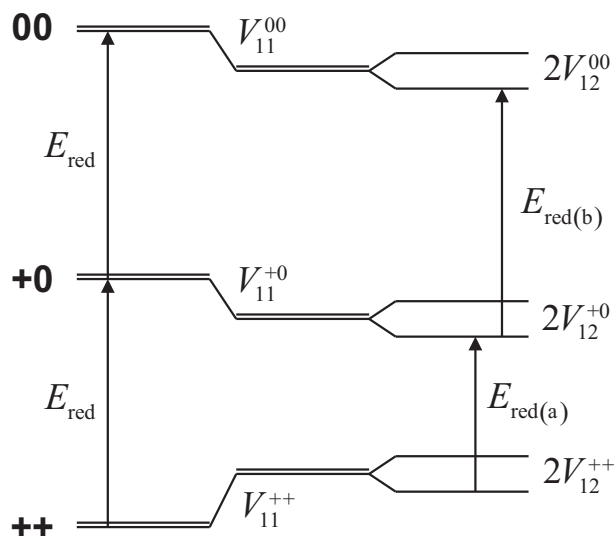


Figure 4.20.: Schematic demonstrating the expected non-degenerate reduction potentials for two *coupled* cationic acceptors ($E_{\text{red(a)}}^{\circ}$ and $E_{\text{red(b)}}^{\circ}$) in comparison with two isolated cationic acceptors (with degenerate reduction potentials E_{red}°).

and a smaller contribution from the attractive dipole-dipole interaction of the two neutral (reduced) acceptors ($V_{11}^{00} < 0$), whilst the splitting $\Delta E_{\text{red(a-b)}}$ also includes a contribution from the attractive ion-dipole interaction ($V_{11}^{+0} < 0$).

We note that in the case of purely through-space interaction, for the more flexible **(Fc)₂BOB** derivative the relative location of the B-bpy acceptors should be able to adjust more readily to reduce the magnitude of the repulsive cation-cation interaction ($|V_{11}^{++}|$). However, given that the splitting of the near-degenerate redox potentials for **(Fc)₂BOB** and **a-BOB** are so similar, this would imply that the chief mechanism for the inter-acceptor coupling must be due to through-bond interactions, i.e. the relevant wavefunctions of each B-bpy group extend significantly onto the intervening B-O-B bridge, where the bond lengths across the B-O-B bridge in each case are comparable.

The cyclovoltammetry trace for **[1C](PF₆)** is shown in Figure 4.21 (with that of **[1A]PF₆** included for comparison). As already mentioned in Section 4.4, the reduction potential $E_{\text{red1}}^{\circ} = -0.52$ V is shifted to significantly less negative values relative to **[1A]PF₆** (i.e. by 0.50 V) due to the inherently lower energy LUMO in 2,5-dpp compared with bpy (which is also presumably the case in their corresponding cationic B-derivatives). However in Section 2.3 we showed that the relative shift between the reduction potentials of bpy and 2,5-dpp was slightly larger, i.e. 0.56 V. Whilst little weight can be given to this observation alone, we note also that the oxidation potential for **[1C](PF₆)** ($E_{\text{ox}}^{\circ} = +0.50$ V) is more positive than that for **[1A]PF₆** by 0.1 V. Taken together, these shifts imply a comparable Fc-HOMO stabilisation and B-dpp-LUMO destabilisation. As mentioned in Section 4.4 in examining the UV-vis spectrum of **[1C](PF₆)**, such an effect is in accord with the Mulliken-type CT theory (also presented in this work, Appendix B.2) in the case where there is a finite degree of mixing between the Fc-HOMO and B-dpp-LUMO in the ground state. This increased mixing is to be expected (see Eq.s B.40 and B.42) based on the fact that the unperturbed donor and acceptor orbital energies are much closer for **[1C](PF₆)** in comparison to the B-bpy-acceptor compounds.

If we combine the estimates for relative energy level positions and separations

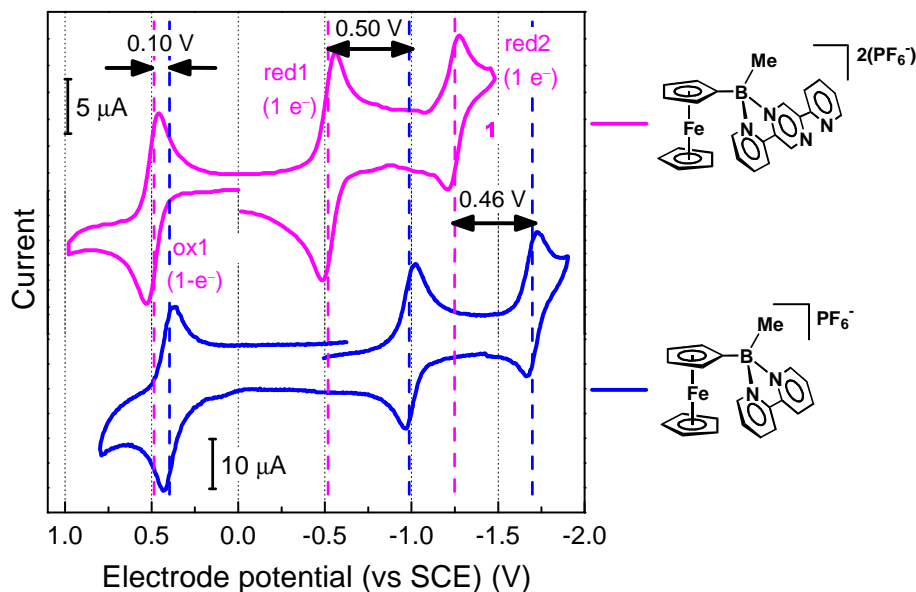


Figure 4.21.: Cyclic voltammetry traces for 2,5-dpp-acceptor derivative **[1C](PF₆)** for comparison with corresponding bpy-acceptor compound **[1A]PF₆**. (Measurements in DMF containing [NEt₄][PF₆] electrolyte, Pt-electrode [9].)

from UV-vis and electrochemical data for **[1A]PF₆** and **[1C](PF₆)**, we can construct an approximate energy level diagram for the Fc-HOMO, B-bpy- and B-dpp-HOMO and -LUMO, as shown in Figure 4.22. The deduction of this energy diagram is actually overdetermined from the available data, yet all observed transitions and relative shifts for the Fc-HOMO and acceptor-LUMO are consistent with the scheme to within 0.01 eV. We do note, however, that the energy level of the highest-occupied π -orbitals on the B-bpy and B-dpp acceptors are determined only by the estimates of the UV $\pi - \pi^*$ absorption bands, and lead to an implied relative stabilisation of this orbital energy by ~ 0.07 eV. It is hoped that this scheme will provide a useful comparison with future theoretical modelling of the **[1C](PF₆)** derivative.

4.5.2. Correlation between MLCT transition energies and redox potentials

One of the most robust experimental tests for the assignment of a CT transition is given by a comparison of the CT transition energy ($\propto \nu_{\text{MLCT}}$) and the difference between donor-oxidation and acceptor-reduction electrochemical potentials $\Delta E'^{\circ} = E'_{\text{ox}} - E'_{\text{red}}$ [194, 47, 195, 196, 197, 198, 199, 200, 201, 202, 203, 204, 205]. As stated in Section 2.1.3, whereas the CT absorption process takes place on a time scale much shorter than the time for nuclear rearrangement (Franck-Condon principle), the electrochemical potentials correspond to *adiabatic* processes [47], such that we assume that the internal and solvent conformation can adopt their new equilibrium positions *during* the course of electron addition/removal. Hence the observed MLCT transition energy E_{MLCT} in solution and the redox potential difference $\Delta E'^{\circ}$ are related by (Eq. 2.4),

$$E_{\text{MLCT}} = e\Delta E'^{\circ} + \chi_e + \Delta E_{\text{FC}} - C, \quad (4.6)$$

where χ_e is the difference between the excited-state solvent interaction energies for the Franck-Condon (i.e. ground-state) and CT (excited-state) solvent equilib-

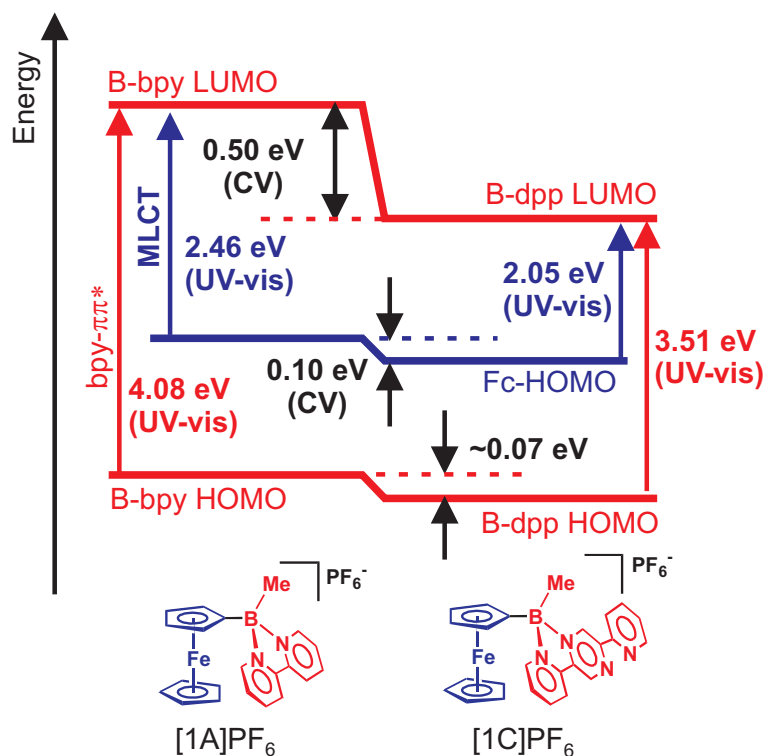


Figure 4.22.: Schematic of frontier Fc/acceptor orbital energies for $[1A]PF_6$ vs $[1C](PF_6)$ derived from the UV-vis and CV data (as indicated).

ria. ΔE_{FC} is the one-half Stokes shift for the transition (i.e. due to the difference between internal equilibrium nuclear coordinates) (see Section 2.1.1). The electrostatic interaction term $C > 0$ corresponds to the difference between the hypothetical reduction potential for the acceptor $E'_{red1(a),D+}$ in the case where the donor is *oxidised* (a situation not realisable in practice) and that measured with a neutral donor, $E'_{red1(a)}$. Note that this term corresponds to the value that would be measured in the same solute environment as the other redox potentials appearing in Eq. 4.6, i.e. in the presence of a high concentration of counteranions, and not a gas-phase value which would include a significant additional Coulomb term (discussed further below). We note that using the simple model of symmetric charge displacement for the CT in a cationic compound, we have $\chi_e = \Delta E_{solv}$ (Section 2.1.4).

In Figure 4.23 we plot the (a) first electrochemical oxidation potential ($E'_{ox1(a)}$), (b) first reduction potential ($E'_{red1(a)}$) and (c) the difference between these two quantities ($\Delta E'^o$) vs the corresponding observed MLCT band peak energy E_{MLCT} . (We note that the redox data are measured all in DMF, whilst the MLCT data are all measured in CH_3CN , which we will address below). One observes an overall correlation between the data, although the data for some derivatives deviate significantly. Including the data for all derivatives, a linear regression of the reduction potential data $E'_{red1(a)}$ (Figure 4.23(b)) yields a slope of -1.18 V/eV, whilst the regression of the more weakly dependent (and less correlated) oxidation potential data $E'_{ox1(a)}$ (Figure 4.23(a)) yields a slope of -0.19 V/eV²⁷, such that the regression of the redox potential *difference* $\Delta E'^o$ (Figure 4.23(c)) yields a slope of

²⁷Note that in an earlier report [206] the data for $[1C](PF_6)$ was not included, such that the correlation between the MLCT transition energy and the oxidation potentials was not identified.

+0.99 V/eV – in very close agreement to the expected value of unity. The regression has a correlation coefficient $r = 0.88$ for the fit of $\Delta E'^o$, with an horizontal intercept of $E_{\text{MLCT},0} = 0.98$ eV.

We note that from Eq. 4.6, any differences in solvent interaction energy, Stokes shift or electrostatic donor-acceptor interaction amongst the derivatives should give rise to displacements from an ideal correlation (whilst one should also bear in mind that the various total molecular charges for the different derivatives could also significantly affect the electrochemical potentials, although certain factors should be expected to cancel between the oxidation and reduction potentials).

Upon inspection of the potential difference data $\Delta E'^o$ (Figure 4.23(c)) for the derivatives $[\mathbf{nA}](\text{PF}_6)_n$ ($n = 1, 2, 4$) alone, we note that a fitted line through these points would be almost flat (i.e. no correlation at all). However, from the discussion and analysis of Section 4.2.3, we came to the conclusion that the red-shifting of the MLCT band with increasing n was due to the decrease in the solvent blue-shift. Hence, from Eq. 4.6 the deviation for $[\mathbf{4A}](\text{PF}_6)_4$ is to be expected.

Inspecting Eq. 4.6, we can extract further information from the extrapolated intercept $E_{\text{MLCT},0}$, i.e.,

$$E_{\text{MLCT},0} = \Delta E_{\text{solv}} + \Delta E_{\text{FC}} - C. \quad (4.7)$$

From the solvatochromism analysis of Section 4.2.2, we can estimate the contribution from the solvent ΔE_{solv} , even though it must be recognised that this term is not constant for each derivative (due to differences in the expected dipole moment changes, as discussed in Section 4.2.3), and that the MLCT absorption band data is taken in CH_3CN as opposed to DMF (although due to the similar dielectric constants of CH_3CN and DMF, this leads to a relatively small correction). In order to produce a reasonable estimate, we use the following approach (using the available experimental data directly, as appropriate, in precedence to fitted curves).

The measured MLCT band peak wavelengths for $[\mathbf{1A}]\text{PF}_6$ are $\lambda_{\text{max}} = 503.5$ cm^{-1} for CH_3CN and $\lambda_{\text{max}} = 497.7$ cm^{-1} for DMF, which suggests that we must shift the fitted line in Figure 4.23(c) horizontally (and hence also $E_{\text{MLCT},0}$) by $\sim +0.029$ eV to approximately account for the difference in solvent between the two measurements (note that such a shift actually slightly improves the agreement of the fitted line with the data points for $[\mathbf{1A}]\text{PF}_6$ and $[\mathbf{1C}](\text{PF}_6)$). Moreover, we adopt the value of solvent blue-shift observed for $[\mathbf{1A}]\text{Br}$ in DMF of $\Delta\nu_{\text{solv}} = 1676$ cm^{-1} (relative to the extrapolated gas-phase value of ν) which corresponds to $\Delta E_{\text{solv}} = 0.21$ eV. Hence, we can estimate the remaining quantities in Eq. 4.7 as,

$$\Delta E_{\text{FC}} - C \sim 0.81 \text{ eV},$$

which is consistent in magnitude with reports on other MLCT systems (see Ref. [47] for a fairly comprehensive list), although no data was found for similar Fc-donor compounds for a critical comparison.

Unfortunately, a means to estimate the quantity C is not accessible with the available experimental/theoretical results. Although in Section 4.6 we present the theoretical gas-phase LUMO energies for both the prototype cation ($[\mathbf{1}]^+(\text{H})$) and dication ($[\mathbf{1}]^{2+}(\text{H})$), which shows that the acceptor-LUMO is stabilised by $\Delta E_{\text{LUMO}} = 3.44$ eV upon oxidation of the Fc unit, this value is not readily usable in the estimate of C because it includes a dominating contribution from the Coulomb escape potential in the gas phase, where no counteranions are in close contact with the cationic solute. Note that an attempt to compensate for the escape potential present in the calculated gas-phase LUMO energies (relative to the required situation where counteranions are in close contact with the solute) using

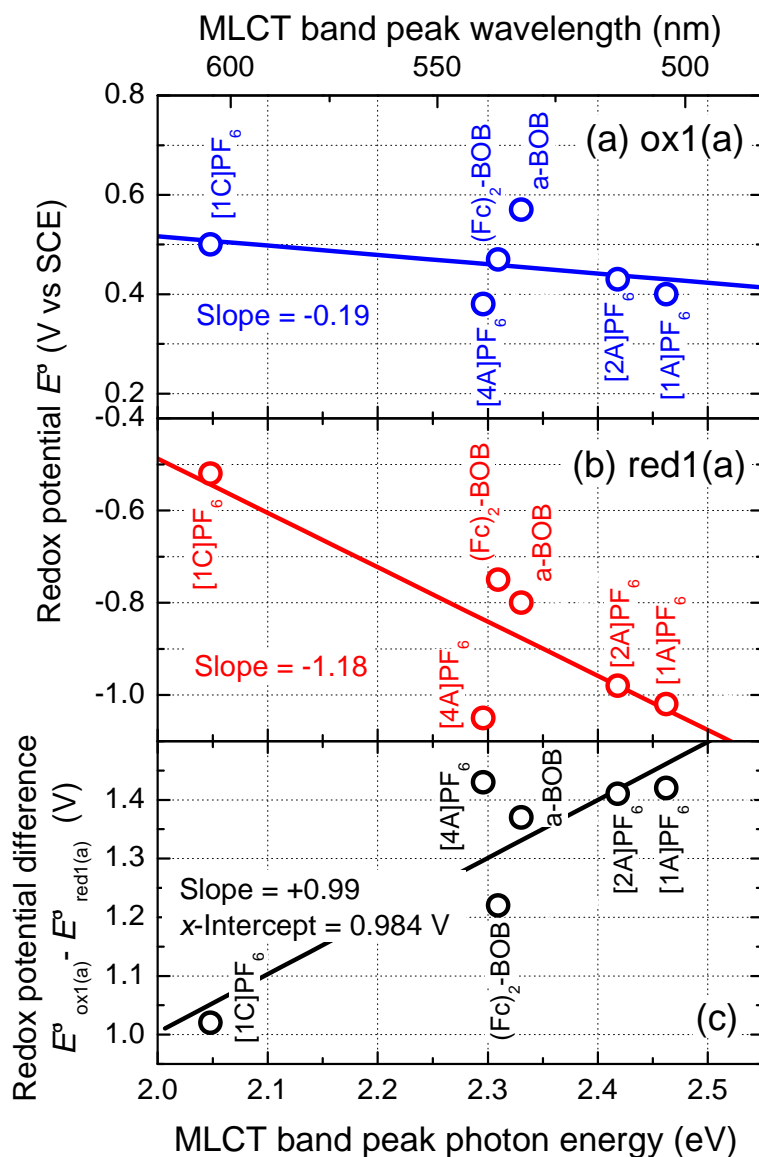


Figure 4.23.: Formal electrochemical redox potentials E° (in DMF) vs MLCT band peak transition energies $h\nu_{\text{max}}$ (in CH₃CN), and linear fits to the data (fitting parameters as indicated). (a) (First) oxidation potential $E^{\circ}_{\text{ox,1(a)}}$, (b) (first) reduction potential $E^{\circ}_{\text{red,1(a)}}$, and (c) potential difference $\Delta E^{\circ} = E^{\circ}_{\text{ox,1(a)}} - E^{\circ}_{\text{red,1(a)}}$.

a simple Coulomb point-charge model is open to significant uncertainty depending on the estimates used for the unknown parameters, i.e. an effective radius for the molecule and the proximity of the counteranions to the solute in the electrochemical solution. Hence in order to accurately estimate C would require additional theoretical calculations of both the cation and dication with an accurate inclusion of surrounding counteranions/solvent.

However, we do at least have a lower bound for the Stokes (blue-)shift of the MLCT transition $\Delta E_{\text{FC}} > 0.81$ eV ($\cong 6490$ cm⁻¹). Given our existing estimate for the MLCT band peak for **[1A]Br** in the gas-phase of $\nu_{\text{GP}} = 18530$ cm⁻¹, we predict a HOMO-LUMO spacing (i.e. the origin of the MLCT transition) of $\nu_{\text{GP}}^{\text{HOMO-LUMO}} < 12040$ cm⁻¹, corresponding in wavelength to $\lambda_{\text{GP}}^{\text{HOMO-LUMO}} > 830$ nm). The fact that the appreciable Stokes shift (which is actually of a fairly typical magnitude for MLCT systems [47]), and to a lesser degree the solvatochromic blue-shift, lead to a prediction for the HOMO-LUMO energy separation significantly lower than the experimentally observed MLCT band peak photon energy should be kept in mind when considering such systems. We note that based on this lower bound for the origin of the MLCT transition, it is not surprising that no photoluminescence (PL) was detected in the range $\lambda < 900$ nm, which motivates future PL measurements with the necessary near-IR equipment. We will consider the large magnitude of this Stokes shift (i.e. excited-state internal reorganisation energy) in interpreting the excited-state transient absorption kinetics in Chapter 5.

We conclude this section by noting an interesting point for future synthesis of Fc-B-bpy derivatives. As given above, the extrapolated gas-phase equilibrium HOMO-LUMO spacing for **[1A]Br** is predicted to be $E_{\text{GP}}^{\text{HOMO-LUMO}} + C = hc\nu_{\text{GP}}^{\text{HOMO-LUMO}} \approx 1.5$ eV. Given that the acceptor LUMO of the corresponding B-dpp-based acceptor compound **[1C](PF₆)** is predicted to be ~ 0.5 eV lower in energy (see Figure 4.22), we can expect that for **[1C](PF₆)** $E_{\text{GP}}^{\text{HOMO-LUMO}} + C \sim 1.0$ eV. Moreover, if the Fc-donor was replaced with an octamethylated-Fc donor ('OMFc', i.e. with 8 CH₃ groups on the Cp⁻ rings [104, 105]), then this should destabilise the donor HOMO by approximately 0.4 eV (given the approximate additive shift of the Fc-based HOMO with increasing number of CH₃ groups, see Section 2.2.1). Hence, in such a OMFc-donor/B-dpp-acceptor derivative, we could expect $E_{\text{GP}}^{\text{HOMO-LUMO}} + C \sim 0.6$ eV. Given that typical values of the electrostatic term C for MLCT compounds are often reported on the order of $C \sim 0.5$ V [47], this opens the question of whether $E_{\text{GP}}^{\text{HOMO-LUMO}}$ may actually become *negative* for a OMFc-B-dpp compound, which would result in a stable MLCT *ground* state for such a derivative. Based on the analysis presented here, investigation into the possible synthesis of such a derivative are currently being pursued.

4.5.3. UV-vis spectroelectrochemistry results

Due to the weakly-coupled nature of the donor and acceptor in the Fc-B-bpy compounds, we should expect that the localised electronic transitions present on the electrochemically oxidised-donor and reduced-acceptor should also be present in the CT excited state of the donor-acceptor complex, depending on the influence of the different net molecular charge in each case (i.e. D⁺A/DA⁻ and D⁺A⁻). Such correlations between the absorption spectra of the oxidised/reduced species and the CT excited-state have been observed for other MLCT compounds [207, 195]. Hence, for comparison with the excited-state transient spectra presented in Chapter 5, a series of UV-vis spectroelectrochemistry (SEC) measurements were performed²⁸ (i.e.

²⁸F. Fabrizi de Biani, AG Zanello, University of Siena, Italy.

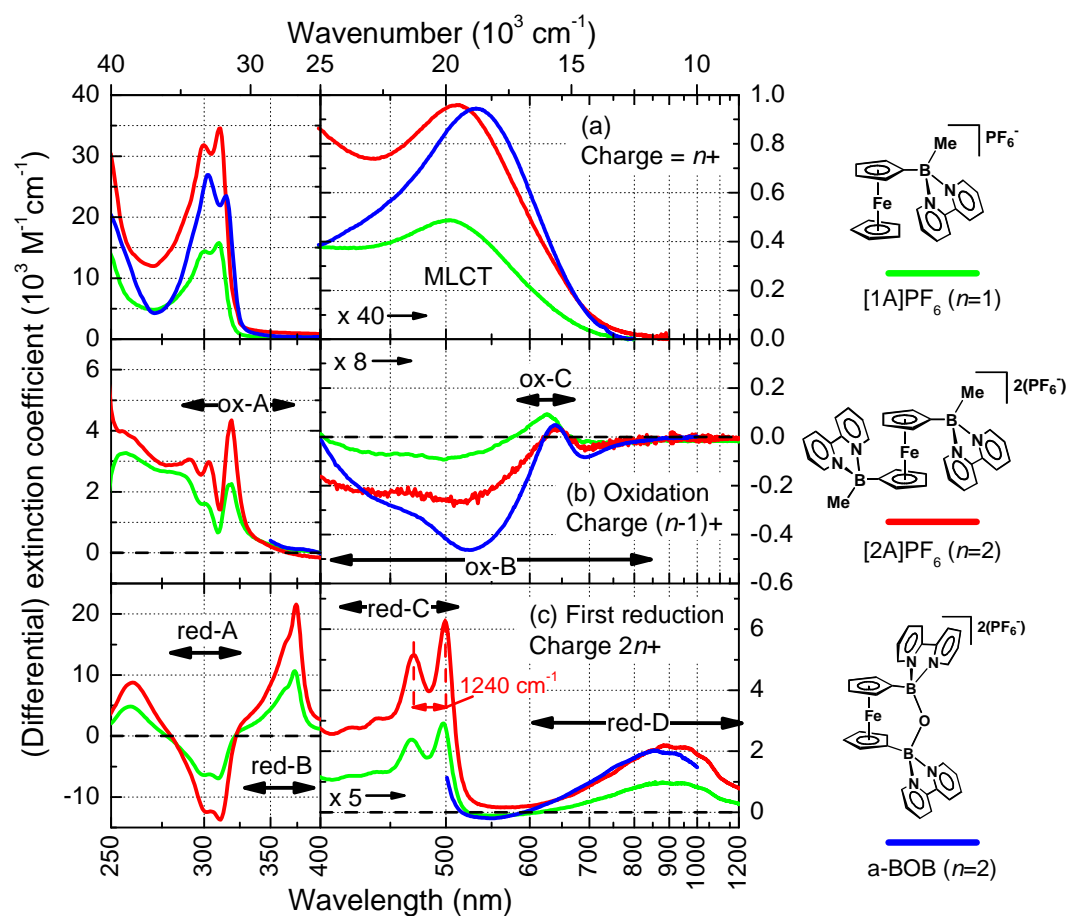


Figure 4.24.: Differential UV-vis spectra upon exhaustive first electrochemical (b) oxidation (ox1) and (c) reduction (red1(a,b)), for comparison with (a) spectra in ‘normal’ redox state (cationic charge $n+$), for compounds $[1A]PF_6$, $[2A](PF_6)_2$ and **a-BOB** (in DMF) as indicated. (See Figures A.2 and A.3 for time series spectra, and fixed redox potentials). Different qualitative regions of the spectra are labelled ‘ox- X ’ and ‘red- X ’ to aid discussion in the text (the spanning arrows only indicate the general spectral region, which are specified more clearly in the text for each compound).

a measurement of the absorption spectra upon electrochemical oxidation or reduction at a static electrode potential) on the compounds $[1A]PF_6$ and $[2A](PF_6)_2$, whilst some provisional data for **a-BOB** were also available from an earlier characterisation [3].

The time-series differential UV-vis spectra during oxidation and reduction of $[1A]PF_6$ and $[2A](PF_6)_2$ are presented in Figures A.2 and A.3 in Appendix A.3, which demonstrate that the oxidation/reduction of the samples was almost exhaustive and that the form of the differential spectra does not change during the measurement (indicating that no secondary reactions take place on the time scale of the measurement). In Figure 4.24 we present a summary of the differential spectra for $[1A]PF_6$, $[2A](PF_6)_2$ and **a-BOB**. Figure 4.24(a) shows the spectra of the compounds before oxidation/reduction (as already presented in Sections 4.2.3 and 4.4) for comparison.

In Figure 4.24(b) (oxidation), several differential absorption features can be ob-

served which are qualitatively similar for the three derivatives presented²⁹, and even though these changes are comprised of unresolved overlapping absorption bands we have added a labelling scheme ('ox-*X*') to the approximate wavelength regions to aid in their discussion (please note the different vertical scales/zero levels for each panel). In the wavelength region 'ox-A', the structured differential absorption increase arises from a small increase in strength and broadening of the existing $\pi - \pi^*$ transition localised on the B-bpy acceptor(s), which we attribute to the influence from the increased electronegativity of the oxidised Fc. Extending deeper into the UV ($\lambda \lesssim 300$ nm), a broad region of unresolved positive absorption arises, which we attribute to the LMCT transitions observed in the UV absorption spectrum of unsubstituted Fc^+ (i.e. from the occupied π -orbitals of the Cp^- rings into the vacated Fe^{3+} *d*-based orbitals, see Figure 2.16, Section 2.2.1 for the UV-vis spectrum of Fc^+). In the visible range, the broad region of negative differential absorption ('ox-B') corresponds in part to the suppression of the MLCT band. However, from the magnitude of the negative absorption changes in comparison to the MLCT band (c.f. Figure 4.24(a)), it is clear that additional new absorption features arise in this region, which is exemplified by the net absorption *increase* (with a peak occurring in the range $\sim 600 - 650$ nm) labelled 'ox-C'. We note that these new features are highly consistent with the visible absorption spectrum for Fc^+ (Figure 2.16), where a similar peak in the absorption is observed at $\lambda_{\text{max}} = 618$ nm associated with the lowest-energy LMCT band of Fc^+ , with a broad, weakly structured absorption plateau extending down to 400 nm (which consists of several unresolved residual *d-d* transitions centred on the Fe^{3+} -core [57]). We note that any residual MLCT transitions are expected to be strongly blue-shifted due to the positive charge on the Fc-unit after oxidation.

Turning now to the differential spectra upon the first *n*-electron reduction in Figure 4.24(c) (note that the electrochemical potentials used were some 100s of mV beyond the near-degenerate first reduction wave, such that *both* B-bpy groups received one electron in **[2A](PF₆)₂** and **a-BOB**). Across the entire UV-vis range, the magnitude of the absorption changes is significantly greater than those occurring upon oxidation. In the region 'red-A', a negative differential feature which represents the suppression of the original B-bpy $\pi - \pi^*$ band dominates. The structured differential absorption features which dominate in the ranges $\lambda \gtrsim 325 - 400$ nm ('red-B') and $\sim 400 - 550$ nm ('red-C') are highly consistent with the absorption peak positions of the Fc-free B-bpy derivatives presented in Figure 2.25. For instance, upon reduction, the derivative σ -B-bpy possesses absorption peaks at 378 nm and at 463/494 nm³⁰, whilst the differential spectra for the reduced-**[2A](PF₆)₂** derivative (Figure 4.24) possesses well-defined peaks at 374 nm (red-B) and 470/499 nm (red-C) (note that these two latter peaks would appear to represent the vibrational manifold of the same electronic transition). We make the important note that for the case of Fc-free B-bpy-derivatives with electron-withdrawing substituents attached to B (i.e. compounds 'Hc' and 'He' in Figure 2.25), the 'red-C' absorption band is significantly blue-shifted, with the lowest-energy absorption peak occurring at $\lambda \approx 460$ nm. Hence we could anticipate that the presence of a simultaneously oxidised Fc unit attached to the reduced B-bpy acceptor would also result in a significant blue-shift of this band – a point we will return to in interpreting the

²⁹Note that certain experimental problems in the measurement for **a-BOB** resulted in significant background artifacts, and the spectra shown here are recovered after a careful background subtraction from the data. Hence it is possible that the spectra for **a-BOB** shown are still slightly distorted, and if required for more a more critical analysis, should be remeasured.

³⁰Note that in the original report for the UV-vis spectra of these compounds [134], only peak wavelengths were reported, without any detailed interpretation.

excited-state transient spectra in the next chapter.

The final feature upon reduction is the broad band (red-D) extending from $\lambda \sim 600$ nm into the near-IR. We note that no mention of such a band was made for reduced-B-bpy derivatives in the only existing literature report [134], although this paper was mostly devoted to synthetic issues, and no mention of the wavelength range used in the measurements was reported. In a simple MO picture, we expect that addition of an electron to the B-bpy-acceptors should significantly destabilise the next lowest unoccupied orbital, such that any MLCT transitions should be significantly blue-shifted (relative to the original MLCT band in the non-reduced Fc-B-bpy derivatives), and hence not be a likely assignment for the ‘red-D’ band. In our original reports on this band [206, 8], we concluded that this red-D band is due to a localised transition on the reduced B-bpy-acceptors, both in considering the energy of the band and the fact that the absorption strength increases in proportion to the number of B-bpy groups in each derivative (see Figure 4.24(c)). However, from the broad featureless nature of this band, it is also conceivable that it corresponds to a transition involving significant LMCT character *from* the newly occupied orbital on the B-bpy units into an unoccupied orbital which is also delocalised onto the Fc unit. This remaining uncertainty strongly motivates the measurement of the vis-NIR absorption of the σ -B-bpy derivative following electrochemical reduction in future work. In any case, the presence of this band can be taken as an indicator of the presence of reduced B-bpy acceptor(s), and we will show that a similar band also appears in the excited-state transient spectra of all the Fc-B-bpy compounds presented in Chapter 5.

4.6. Quantum chemistry results

As demonstrated in the preceding sections, a great deal of insight into the electronic structure and photophysics of these medium-sized-polyatomic metal-organic compounds can be derived from comparative experimental measurements of related derivatives, in conjunction with simplified generic models which avoid an explicit description of the interaction of the weakly-coupled molecular fragments and their internal electronic structure. However, in general, only in conjunction with results from accurate quantum-chemical calculations can the interpretation of the observed physical properties be made more concrete.

A great deal of progress in the last decade in the development of ab-initio DFT methods for metal-organic systems [84, 85, 83, 82, 81, 76, 75, 79, 87, 208] has led to a situation where the results for ground-state properties are in almost quantitative agreement with experiment. Moreover, the extended time-dependent DFT (TD-DFT) methods can provide accurate predictions of excited-state properties (i.e. optical transition energies and excited-state potential energy surfaces) for organic [209, 210, 211] and metal-organic systems (including Fc) [177, 212, 213, 214, 178, 41, 215, 216, 217, 218, 219, 220, 86]. We note however, that recent reports demonstrate that purely TD-DFT-based methods possess an inherent error for large-scale CT transitions (i.e. where the net spatial displacement of charge density upon excitation is comparable to the spatial extent of the related molecular orbitals) due to the treatment of the exchange energy [221, 41] such that it should predict transition energies that are systematically too low (with possible errors of 1-2 eV [221]). Existing reports which show fair agreement between theory and experiment for such CT transitions [177, 178] may well involve an interplay of other systematic errors in the calculation (although this question remains at the frontier of investigation of TD-DFT methods). Moreover, the predicted oscillator strengths for optical transitions are generally weaker than those observed experi-

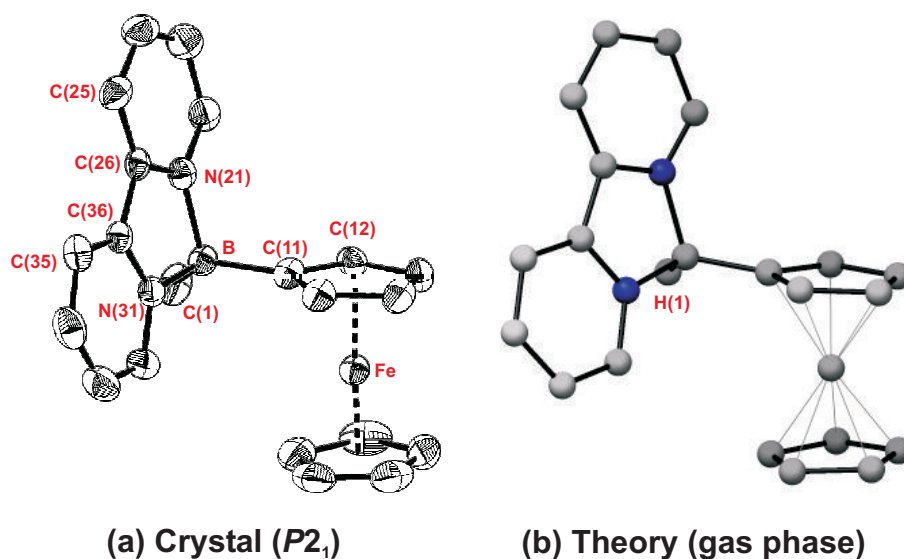


Figure 4.25.: Comparison of (a) experimentally-determined crystal structure of $[1\mathbf{A}]\mathbf{PF}_6$ and (b) theoretical (gas-phase) structure of model compound $[1]^+(\text{H})$ (structure obtained from independent geometry optimisation). Atoms relevant to the geometry comparison in Table C.1 indicated in (a) (using the same indices as in [7]). Counteranion position for the crystal structure of $[1\mathbf{A}]\mathbf{PF}_6$ is omitted.

mentally [212, 218]. In any case, a comparison of theory and experimental transition energies is important to gauge the accuracy of TD-DFT methods for the Fc-B-bpy systems.

In this section, we present results of the prototype Fc-B-bpy derivative $[1]^+(\text{H})$ ³¹ including (i) the (gas-phase) ground-state conformation and molecular-orbital electronic structure, (ii) the predicted low-energy electronic transitions from a TD-DFT calculation, (iii) the potential energy contour of the ground-state vs the rotation about the B-C(Cp) bond bridging the donor and acceptor, (iv) a comparison of the electronic structure with the corresponding dication $[1]^{2+}(\text{H})$ (in order to predict the changes that occur upon oxidation) and (v) the ground-state electrostatic potential surfaces of $[1]^+(\text{H})$ (which reflects the distribution of the formal positive charge in these cationic species). The technical details of the (TD-)DFT calculations are given in Ref. [206] and references therein [222, 223, 224]³².

The equilibrium geometry calculated for $[1]^+(\text{H})$ is shown in Figure 4.25 for comparison with the reported crystal structure of $[1\mathbf{A}]\mathbf{PF}_6$ from Ref. [7]. We note that the prototype $[1]^+(\text{H})$ differs from $[1\mathbf{A}]\mathbf{PF}_6$ only in that the CH₃-substituent attached to the B atom is replaced with a single H-atom, which is not expected to lead to significant differences in conformation/electronic structure (although the slightly more electron-rich CH₃ group could have a small effect on the B atom). From visual inspection, the theoretical structure is shown to be in excellent agreement with the structure of $[1\mathbf{A}]\mathbf{PF}_6$ in the crystal phase, with a consistent relative conformation of the B-bpy and Fc groups, and the almost eclipsed (D_{5h}) rela-

³¹The theoretical results presented here were performed by T. Müller, Anorganische Chemie, J. W. Goethe-Universität, Frankfurt.

³²We note that the theoretical results presented here (excepting the TD-DFT electronic transition results) are actually from more recent calculations than those presented in Ref. [206], although they differ only in that the B3LYP basis-set has been used, as opposed to the B3P86 basis-set used for the results in Ref. [206].

tive conformation of the Fc Cp⁻-rings. A more quantitative comparison of bond lengths/angles is given in Table C.1. The fact that the predicted equilibrium gas-phase structure for [1]⁺(H) is consistent with the crystal structure of [1A]PF₆ indicates that the crystal structure of [1A]PF₆ is dominated by intramolecular constraints, as opposed to crystal-packing forces.

The corresponding frontier Kohn-Sham³³ occupied (HOMO) and unoccupied (LUMO) molecular orbitals and their respective vacuum energy eigenvalues are shown in Figure 4.26. As is observed, the highest five occupied molecular orbitals (HOMO[0]-HOMO[-4]) are localised on the Fc moiety, whilst the four lowest unoccupied orbitals (LUMO[0]-LUMO[+3]) are all localised on the B-bpy moiety, such that in a simplified MO picture we expect the lowest-energy transitions to be of Fc→B-bpy MLCT character.

It is instructive to compare the Fc-based HOMOs in Figure 4.26 with those calculated for Fc in Figure 2.13, although one must consider that somewhat different DFT calculation methods were used in each case [206, 84], and that the calculation for Fc was performed for the staggered (*D*_{5d}) relative conformation of the Fc Cp⁻-rings, although this should not lead to any significant differences after accounting for the modified symmetry of the orbitals (see Section 2.2.1). We note that for Fc, the frontier orbitals HOMO[-1] (a_{1g}) and (doubly-degenerate) HOMO[0] (e_{2g}) possess significant *d*_{z²} and *d*_{xy}, *d*_{x²-y²} character, in qualitative agreement to the HOMO[-2]-HOMO[0] molecular orbitals for [1]⁺(H)³⁴, which shows that the presence of the cationic B-bpy groups does not strongly affect the electronic character of the frontier occupied Fc-orbitals, although as can be seen in Figure 4.26 the MOs are somewhat distorted. Moreover, the lower-lying HOMO[-3,-4] are also similar to those reported in Ref. [84] (not shown in Figure 2.13), in that they are delocalised over the whole Fc unit (we note that a small admixture of these orbitals in the electronic excitations, either through vibronic coupling or configuration interaction (CI), could be important for achieving the degree of overlap with the B-bpy-based LUMOs).

The fact that a modified analog of the e_{1g}^{*} LUMO[0] of unsubstituted Fc (which is the dominant LUMO contribution to the lowest-energy *d-d*-transitions in Fc [77, 86]) is *absent* in the frontier LUMOs shown for [1]⁺(H) suggests that it is significantly destabilised by the presence of the cationic B-bpy group, which also explains the absence of the Fc-I band in the analysis of the UV-vis absorption spectra for [nA](PF₆)_n in Section 4.2.3. We note that there is only a small delocalisation of the frontier MOs onto the intervening B-C(Cp) bridge between the Fc-donor and B-bpy-acceptor, which is consistent with the fact that no strongly-allowed MLCT transitions (i.e. *f* ≳ 0.1) are observed in these compounds.

The calculated TD-DFT transition energies, oscillator strengths and dominant contributing HOMO-LUMO terms for [1]⁺(H) are listed in Table C.2 (Appendix C), and presented graphically in Figure 4.27. Included in Figure 4.27 are the experimental visible absorption spectrum of [1A]Br (in CH₃CN) and the extrapolated gas-phase absorption band from the solvatochromism analysis in Section 4.2.2.

We note that since the TD-DFT transition energies are calculated for the fixed (gas-phase) ground-state geometry, they correspond to the experimental transition

³³Note that the Kohn-Sham molecular orbitals extracted from DFT theory have a modified interpretation to those from Hartree-Fock methods [208], although their physical interpretation in the literature is usually treated on an equal footing.

³⁴Note that there is a possible source of confusion in the indexing schemes for the HOMOs of Fc and those of [1]⁺(H). Due to the molecular symmetry in unsubstituted Fc, the doubly-degenerate HOMO[0] actually corresponds to the non-degenerate HOMO[-1] and HOMO[0] in [1]⁺(H).

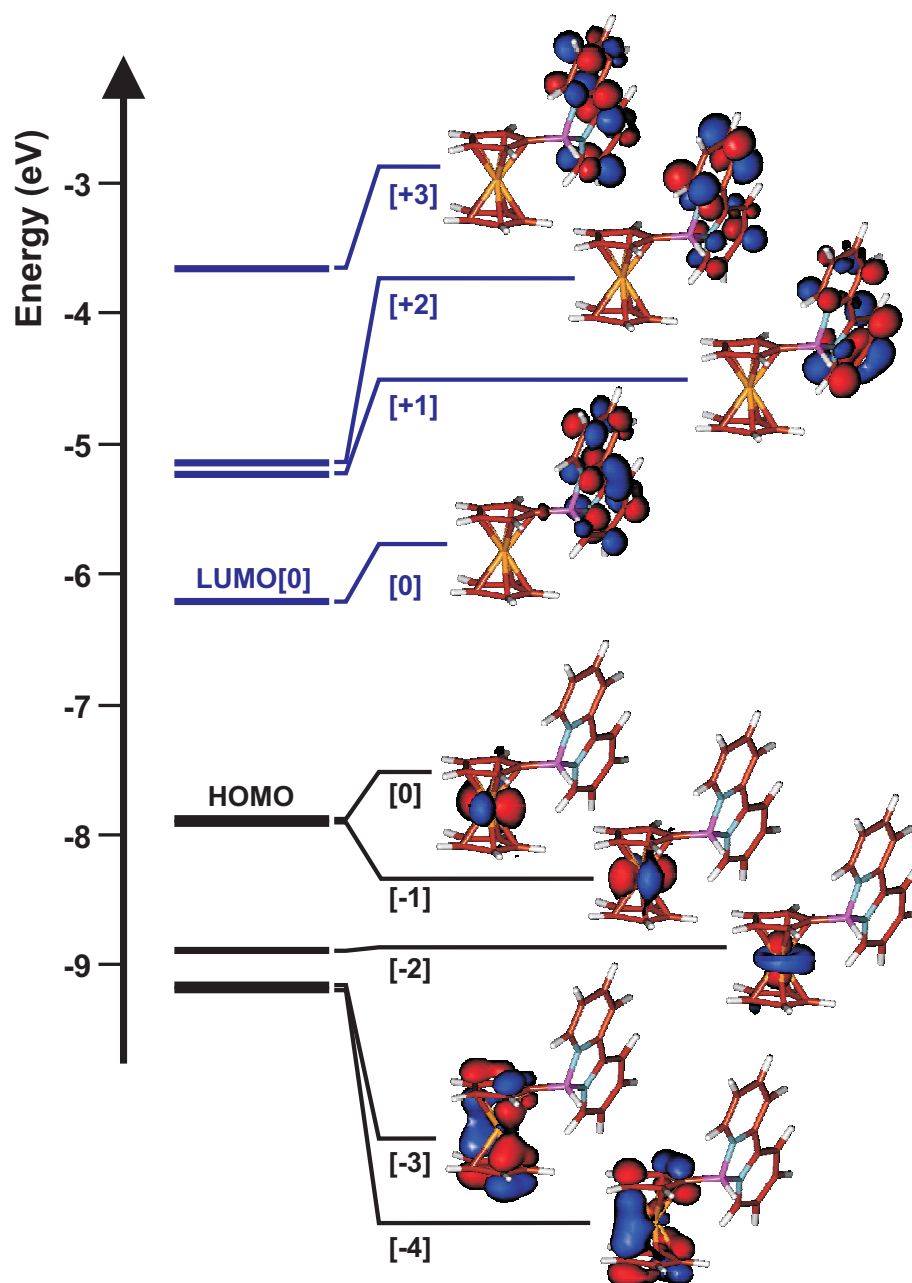


Figure 4.26.: Frontier Kohn-Sham molecular orbitals and energy eigenvalues for (geometry-optimised) $[1]^+(\text{H})$ extracted from DFT calculations. (Iso-surfaces encompass 0.95 of total normalised electron density.)

energy, including the Stokes shift energy (i.e. excess vibrational energy). From a comparison with the extrapolated gas-phase MLCT band maximum for the gas phase (with $\lambda_{\max} = 540.0 \text{ nm} \cong 2.30 \text{ eV}$) we observe that the lowest-energy transitions predicted by TD-DFT are at significantly lower photon energy. Specifically, the lowest two TD-DFT transitions (labelled ‘MLCT-1’ and ‘MLCT-2’ in Figure 4.27) occur at $\lambda_{\max} = 1058 \text{ nm} \cong 1.17 \text{ eV}$ and $\lambda_{\max} = 1029 \text{ nm} \cong 1.20 \text{ eV}$, respectively. As for all the first seven lowest-energy predicted transitions, these excitations involve a dominant contribution from a single HOMO-LUMO pair with normalised amplitudes in the range 0.6-0.7 (see Table C.2)³⁵, with the next largest amplitude < 0.2 . As could be expected from an inspection of the orbital energies in Figure 4.26, for transitions MLCT-1 and MLCT-2 the major contributing HOMO-LUMO pairs are HOMO[0]→LUMO[0] and HOMO[-1]→LUMO[0], respectively. Nevertheless, there is a significant admixture of lower-lying-HOMOs and higher-lying LUMOs in each excitation, such that the more delocalised Fc-HOMO[-3,-4] may play an important role in increasing the transition dipole moment for these transitions. Besides the fact that the lowest-energy TD-DFT transitions MLCT-1 and MLCT-2 are some 1.1 eV red-shifted from that expected from analysed experimental data, we also note that the predicted oscillator strengths are significantly smaller than that calculated for the MLCT band by a factor of 5 (i.e. $f = 0.0006$ and $f = 0.0028$ for transitions MLCT-1 and MLCT-2, respectively, compared to $f_{\text{MLCT}} = 0.014$ for the experimental MLCT band).

We do note, however, that transition MLCT-3 is far more consistent with the experimental MLCT transition, both in terms of transition energy and oscillator strength ($\lambda_{\max} = 699 \text{ nm} \cong 2.01 \text{ eV}$, $f = 0.0084$, major contribution HOMO[-2]→LUMO[0]). Hence, in our previous literature report [206], we tentatively assigned the MLCT band to transition MLCT-3³⁶. However, since learning of the errors inherent in current implementations of TD-DFT for long-range CT transitions – i.e. systematically low predicted energies, with 1-2 eV not being unusual [41], and low estimates for the oscillator strengths by up to a factor ~ 10 (see e.g. [212, 218]) – we must reconsider this assignment³⁷. Given that the comparison of electrochemical potentials and MLCT band positions for the extended range of Fc-B-bpy derivatives in this work shows a correlation between the MLCT transition energies and corresponding oxidation potentials, it seems likely that the near-degenerate frontier orbitals HOMO[0] and HOMO[-1] are involved in the MLCT transition, and hence we must consider that the TD-DFT transitions MLCT-1 and/or MLCT-2 correspond to the experimental MLCT band. (We note that in the solution phase, the environmental perturbation may lead to considerable mixing between the close-lying HOMO[0] and HOMO[-1], which are separated by only 0.027 eV).

We note that similar deviations from experiment have been observed in additional preliminary TD-DFT calculations carried out for the derivative **a-BOB** [221], with similar or even larger resultant red-shifts in the predicted lowest-energy

³⁵Note that the TD-DFT transitions are constructed from a linear combination of single HOMO-LUMO pair excitations, with the ‘amplitudes’ representing the coefficients in this linear combination.

³⁶Note that the previous assignment of the MLCT band to transition MLCT-3 was also consistent with the fact that no clear correlation between the electrochemical oxidation potential and the MLCT band position was observed, due to the exclusion of the data for **[1C](PF₆)**, which indicated that a lower-lying HOMO might be involved in the MLCT transition as opposed to the frontier HOMO (which in a simple MO picture was assumed the dominant orbital involved in the oxidation process).

³⁷Note that the systematic transition-energy errors in TD-DFT for CT transitions is still not universally recognised in the literature [221].

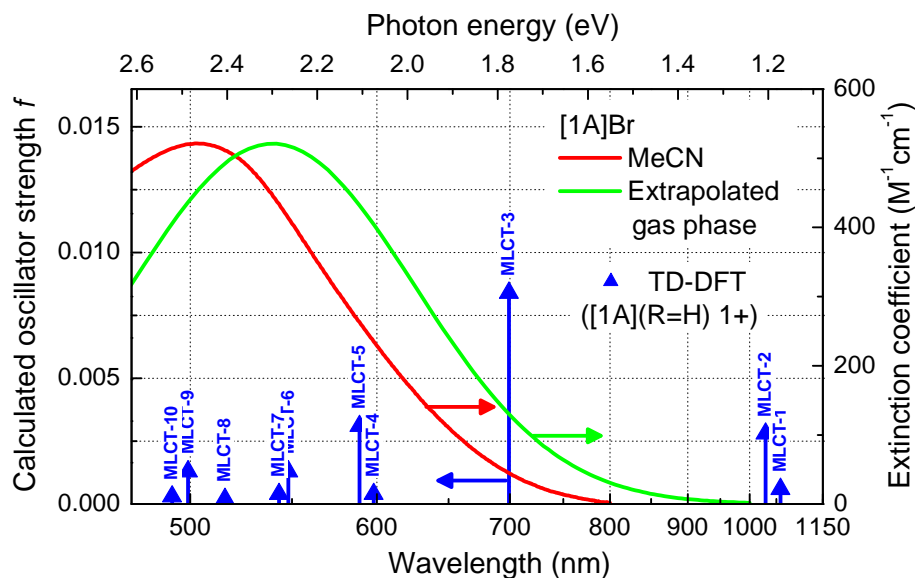


Figure 4.27.: Spectrum of lowest-energy electronic transitions for $[1]^+(\text{H})$ predicted by TD-DFT (gas phase) calculations. For comparison, the experimental absorption spectrum of $[1\text{A}]\text{Br}$ in CH_3CN is included, as well the extrapolated gas-phase spectrum from the solvatochromism analysis of Section 4.2.2. (Note that the scale for the oscillator strength (left) is chosen to match the extinction coefficient range (right) assuming a Gaussian band with width $\Delta\nu_{\text{FWHM}} = 5970 \text{ cm}^{-1}$, i.e. the extrapolated gas-phase bandwidth for $[1\text{A}]\text{Br}$).

transitions, depending on the exact method used (the lowest-energy transition did still correspond to CT states). Moreover, preliminary calculations based on the Hartree-Fock configuration-interaction-singles (SCI) method (which does not suffer from the systematically low-energies, but does not account for dynamical electron correlation included in DFT-based methods[41]) predicted transition energies much *larger* than those observed (i.e. $< 300 \text{ nm}$).

In summary, whilst the existing TD-DFT results do at least support that the lowest-energy transitions in the Fc-B-bpy compounds arise from MLCT transitions from Fc-based orbitals into B-bpy orbitals, the predicted energies and strengths are systematically incorrect, perhaps even to the point where even comparison of theoretical excitation energies amongst related derivatives may be hazardous.

We turn now to an investigation of the dependence of the (nuclear) potential energy U (Eq. 2.1) and frontier molecular orbitals on the relative Fc-B-bpy conformation in the ground state. The specific coordinate chosen for study was the dihedral angle $\theta_{\text{Fe-C-B-H}}$ (i.e. the minimum angle between the planes containing Fe-C(11)-B and C(11)-B-H(1), as per the atom labelling in Figure 4.25), which is representative of the rotation about the B-C(11) bond. This coordinate was chosen for study based on the deduction from NMR spectra [7] that rotation about the B-C(11) bond is relatively unhindered for $[1\text{A}]\text{PF}_6$ and $[2\text{A}](\text{PF}_6)_2$ (in solution). A better understanding of the possible motion/oscillation along this coordinate can be gained from an analysis of the theoretical potential energy curve $U(\theta_{\text{Fe-C-B-H}})$ and an estimate for the corresponding rotational inertia for each molecular fragment, as is presented below. Moreover, it is important to consider the possible effect of motion along this coordinate on the frontier molecular orbitals, and hence the expected MLCT absorption transition energy (and intensity), which will in general

contribute to broadening of the absorption spectrum.

In Figure 4.28, we give a summary of the calculated DFT results for $[1]^+(\text{H})$ for a set of selected dihedral angles $\theta_{\text{Fe-C-B-H}}$ (note that from the symmetry of Fc, the results are invariant for $\theta_{\text{Fe-C-B-H}} = -\theta_{\text{Fe-C-B-H}}$). In Figure 4.28(a) we plot the relative potential energy curve (for static nuclei, with a constrained optimisation of the remaining geometry in each case) $U = U(\theta_{\text{Fe-C-B-H}})$ vs the dihedral angle (with a spline-interpolation between the calculated values). The interpolated curve demonstrates a well-defined minimum near $\theta_{\text{Fe-C-B-H}} = 60^\circ$, and a peak barrier for large scale motion of ~ 0.2 eV (near $\theta_{\text{Fe-C-B-H}} = 0^\circ$, note that we include the corresponding scale in kcal mol $^{-1}$ at right, due to its common usage in transition-state theory).

If we treat the thermal motion about the equilibrium as a classical vibration (see below) then we can calculate the expected relative Boltzmann probability distribution ($\propto \exp(-U/kT)$) vs a quasi-static displacement from the equilibrium, as is indicated by the inset in Figure 4.28(b), which indicates that, neglecting tunnelling, the motion is constrained to a fairly small region about the equilibrium dihedral angle at room temperature (we will return to this point shortly). In Figures 4.28(b,c), we plot the corresponding frontier LUMO and HOMO energies vs $\theta_{\text{Fe-C-B-H}}$, with the corresponding HOMO[0]-LUMO[0] energy separation $\Delta E_{\text{H}[0]-\text{L}[0]}$ in Figure 4.28(d), which we can consider as a measure of the variation of the expected lowest-energy electronic transition energy. We note, as could be generally expected, that the frontier orbital energies bear a distinct dependence on the dihedral angle to that of the potential energy U . We will return to the nature of the frontier orbitals vs dihedral angle shortly.

In order to gain a better description for the expected motion along this coordinate, we need an estimate for the characteristic frequency of vibration ω_θ expected about the equilibrium position³⁸. In order to simplify the calculation, we assume that small displacements in the dihedral angle are equivalent to rotation about the B-C(11) bond, and calculate the rotational inertia ($I_k = \sum m_j r_{\perp,j}^2$) of the two molecular fragments (i.e. Fc ($k = 1$) and B-bpy ($k = 2$) groups) with respect to this axis³⁹. Using the Z -matrix of the geometry optimised molecular structure for $\theta_{\text{Fe-C-B-H}} = 60^\circ$, this gives values of $I_1 = 5.57 \times 10^{-44}$ kg \cdot m 2 and $I_2 = 8.08 \times 10^{-44}$ kg \cdot m 2 . In analogy to a diatomic vibration, the effective rotational inertia for counter-rotation between the two molecular fragments is the reduced rotational inertia $I = (I_1^{-1} + I_2^{-1})^{-1} = 3.30 \times 10^{-44}$ kg \cdot m 2 . Fitting a quadratic function $U \approx \frac{1}{2}K\theta^2$ to the interpolated curve about the equilibrium positions yields an estimate of $K = 1.31 \times 10^{-19}$ N \cdot m \cdot rad $^{-1}$. Hence we can estimate the vibrational frequency quantum as $\omega_\theta = \sqrt{K/I} \approx 2\pi \times 320$ GHz, with a corresponding energy of $\hbar\omega_\theta = 0.0013$ eV⁴⁰. Hence the energy quanta for vibration $\hbar\omega_\theta \ll kT$ (for $T = 300$ K), hence justifying a classical treatment of the motion along this dihedral. In Figure 4.29(a), a magnified section of the data in Figure 4.28(a) about the equilibrium dihedral position is presented, as well as the a portion of the vibration manifold U_M^θ from the foregoing analysis, and the

³⁸Note that the vibrational frequency along this coordinate was not requested as an output from the quantum calculations, and hence we calculate an estimate manually from the given potential energy curve $U(\theta)$ and the given molecular structure

³⁹Note that this approximation is also employed in many high-level quantum chemistry packages [225].

⁴⁰Note that given that the analysis involved the interpolated curve through the data for a small number of calculated geometries, this value is only a tentative estimate. However, given that the frequency calculated in this way depends on \sqrt{K} (where the source for possible error arises) and that we can expect the potential to vary as a smooth function of the geometry, a rigorously-determined probably does not deviate by more than some 10's of %.)

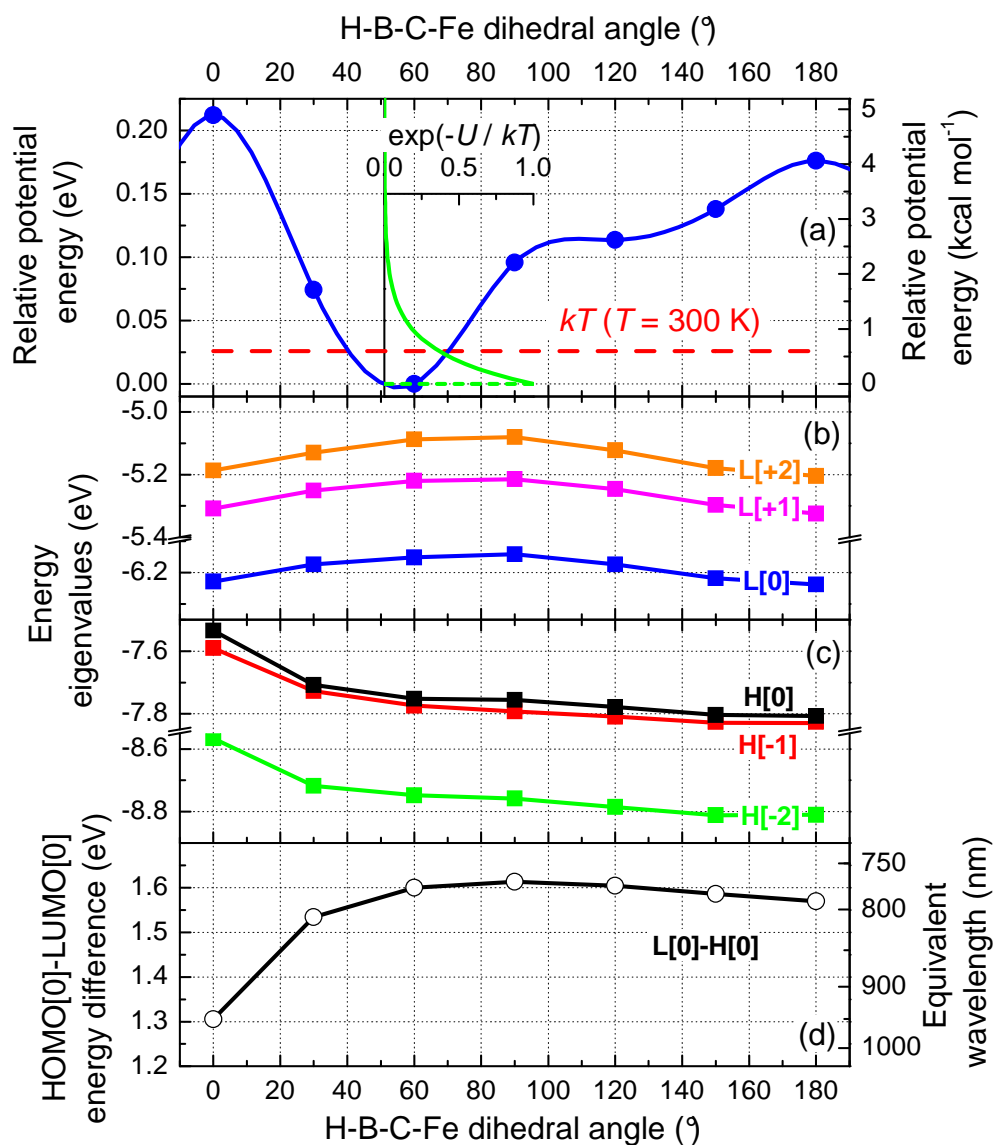


Figure 4.28.: Analysis of theoretical results for $[1]^+(\text{H})$ vs Fe-C(11)-B-H(1) dihedral angle $\theta_{\text{Fe-C-B-H}}$ (constrained geometry optimisation). (a) (Nuclear) potential energy U relative to the conformation $\theta_{\text{Fe-C-B-H}} = 60^\circ$. Inset shows the relative Boltzmann probability ($\exp(-U/kT)$) for $T = 300 \text{ K}$ in the absence of coupling to other degrees of freedom. (b,c) Energy eigenvalues for selected frontier orbitals (as indicated) (Note that the local scale is preserved within each range). (d) Energy difference between frontier orbital energies of HOMO[0]-LUMO[0] vs dihedral angle. Scale at right demonstrates the corresponding magnitude of wavelength variation (pragmatically assuming no systematic shift between true transition energies and HOMO-LUMO spacing).

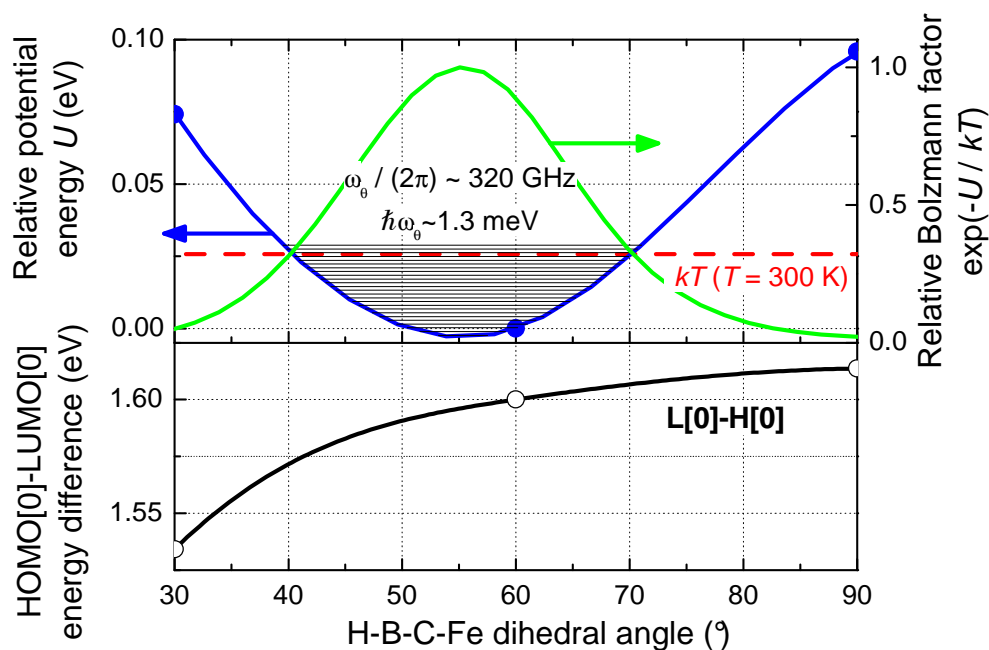


Figure 4.29.: Closer inspection of the potential energy curve vs $\theta_{\text{Fe-C-B-H}}$ near the equilibrium. (a) Interpolated potential energy (blue curve), and corresponding Boltzmann probability distribution (green curve). Also included is a representation of the lowest estimated vibrational energy levels $U_M^{\theta} = (M + 1/2)\hbar\omega_{\theta}$. (b) Interpolated HOMO[0]-LUMO[0] spacing vs $\theta_{\text{Fe-C-B-H}}$.

corresponding Boltzmann probability distribution (now plotted as a function of $\theta_{\text{Fe-C-B-H}}$). The interpolated HOMO[0]-LUMO[0] energy separation $\Delta E_{\text{H}[0]-\text{L}[0]}$ is plotted below in 4.29(b). Using the Boltzmann distribution (as opposed to a finite-amplitude classical oscillation with amplitude $\theta_{\text{max}} = 2kT/K$), we can calculate the expected second moment $\sigma_{\text{H}[0]-\text{L}[0]}$ of $\Delta E_{\text{H}[0]-\text{L}[0]}$. This results in the value $\sigma_{\text{H}[0]-\text{L}[0]} = 0.016$ eV $\cong 130$ cm^{-1} , which corresponds to an expected line broadening of $\Delta\nu_{\text{FWHM}} = \sqrt{8 \ln(2)} \sigma_{\text{H}[0]-\text{L}[0]} \sim 300$ cm^{-1} for the associated electronic transition. Compared to the observed MLCT bandwidth in solution (e.g. for **[1A]PF₆** $\Delta\nu_{\text{FWHM}} = 6220$ cm^{-1} , Section 4.2.3), this small fluctuation in the electronic band gap due to conformational fluctuations along $\theta_{\text{Fe-C-B-H}}$ is rather small, and the predicted gas-phase bandwidth (i.e. after deconvolving the expected solvent broadening, Section 4.2.2) is mostly due to a large Stokes shift between the ground- and excited-state conformational equilibria. However, it should be noted that this conformational distribution appears to play a role in the MLCT bandwidth changes between the unbridged- and bridged-acceptor compounds (Section 4.4), such that either this gas-phase potential does not reflect the situation in polar solution, or other conformational degrees of freedom are also involved in the MLCT band broadening.

In addressing the unhindered rotation (deduced from NMR [7]) about the B-C(11) bond, these theoretical results imply that the gas-phase situation would be described by only a small vibration about either of the two equilibria $\theta_{\text{Fe-C-B-H}} \approx \pm 60^{\circ}$, with tunnelling to the symmetric minimum at $\theta_{\text{Fe-C-B-H}} \approx \mp 60^{\circ}$. We note that the transformation between these two equilibria corresponds to an exchange of the two pyridine rings of the B-bpy group and a reflection of the C atoms in the substituted Cp ring, consistent with the observed degenerate ^1H and ^{13}C

NMR signals for the relevant atoms. Whilst an accurate estimate for the expected barrier-crossing rate between these two minima requires a rigorous application of transition-state theory [226] (which is beyond the scope of the current investigation), given the calculated characteristic vibrational frequency $\omega_{\theta} \approx 2\pi \times 320$ GHz we can assume that even if the semi-classical ‘single-encounter’ tunnelling probability across the barrier is only $\sim 10^{-3}$, this would still result in many barrier crossings within the effective measurement time of the NMR (assumed to be on the order of μs). Note that two important issues remain open in terms of the motion along this dihedral coordinate: (i) In solution, it is quite plausible that solvent interaction will lead to a modification of the gas-phase potential presented here, and (ii) we can anticipate a significantly modified potential in the MLCT excited state. As we will show in the next chapter, it is likely that large-scale rotation about the B-C(Cp) bond occurs on a ~ 20 ps time-scale following excitation in solution for the unbridged-acceptor compound **[2A](PF₆)₂**.

In Figure 4.30 we plot the frontier molecular orbitals for a subset of the calculated fixed-dihedral conformations. An inspection of the nature of these orbitals against the dihedral coordinate can help provide an indication for close approaches between the ground- and excited-state potentials (where, due to the fact that we consider the adiabatic ground-state wavefunctions [37], one can expect to observe a change in the nature of the total electronic wavefunction upon passing near a potential surface crossing). As can be seen from an inspection of the LUMOs in Figure 4.30 and their corresponding energies in Figure 4.28, only minor changes result in the (B-bpy-localised) orbitals with varying dihedral angle, and the LUMO energies remain well-apart and maintain a relatively constant separation. For the HOMOs in Figure 4.30, we note that the spatial character of the two frontier HOMOs exchange approximately upon going from $\theta_{\text{Fe-C-B-H}} = 0^{\circ} \rightarrow 180^{\circ}$, with the orbital containing a large orbital density lobe on the Fc unit beneath the B-bonded-C-atom being HOMO[-1] for $\theta_{\text{Fe-C-B-H}} = 0^{\circ}$, and HOMO[0] for $\theta_{\text{Fe-C-B-H}} = 180^{\circ}$. Whilst from the energy curve in Figure 4.28(a) we do not expect the molecule to spend a significant amount of time in either of these conformations, it is interesting to note that the spatial distribution of Fc-based HOMOs with respect to the bpy LUMOs (which should have a direct influence on the HOMO-LUMO overlap and hence the absorption strength) is dependent in this way on the conformation. Comparison of the lowest HOMO-LUMO energy separation vs dihedral angle in Figure 4.28(d) reflects the fact that any MLCT band transition energy could be strongly influenced by enforcing a different dihedral angle (e.g. through synthetic modification). An open question that also emerges is to whether the stabilised LUMO of the ansa-bridge compounds (Sections 4.4) might be due in part to the different conformation between Fc-donor and B-bpy-acceptors (as opposed to the existing hypothesis that this stabilisation results mainly from inter-acceptor coupling across the -B-X-B-bridge). Additional theoretical calculations would be needed to investigate this further (e.g. to see if the molecular orbitals and HOMO/LUMO energies in the ansa-compounds are significantly different to those presented here for the single-acceptor compound **[1]⁺(H)**).

We now present the corresponding ground-state electronic structure of the dication **[1]²⁺(H)**, i.e. **[1]⁺(H)** following electron removal. These results were of interest for several reasons. Perhaps most importantly, most envisioned applications for polymeric systems based on the Fc-B-bpy monomers will involve the oxidised state of the Fc-unit in some way (such as following an optically-driven CT into an attached macromolecular system or electrochemical oxidation to generate a proportion of paramagnetic Fc⁺ centres), and hence it is important to know what effect this electron removal has on the overall electronic structure of the donor-acceptor

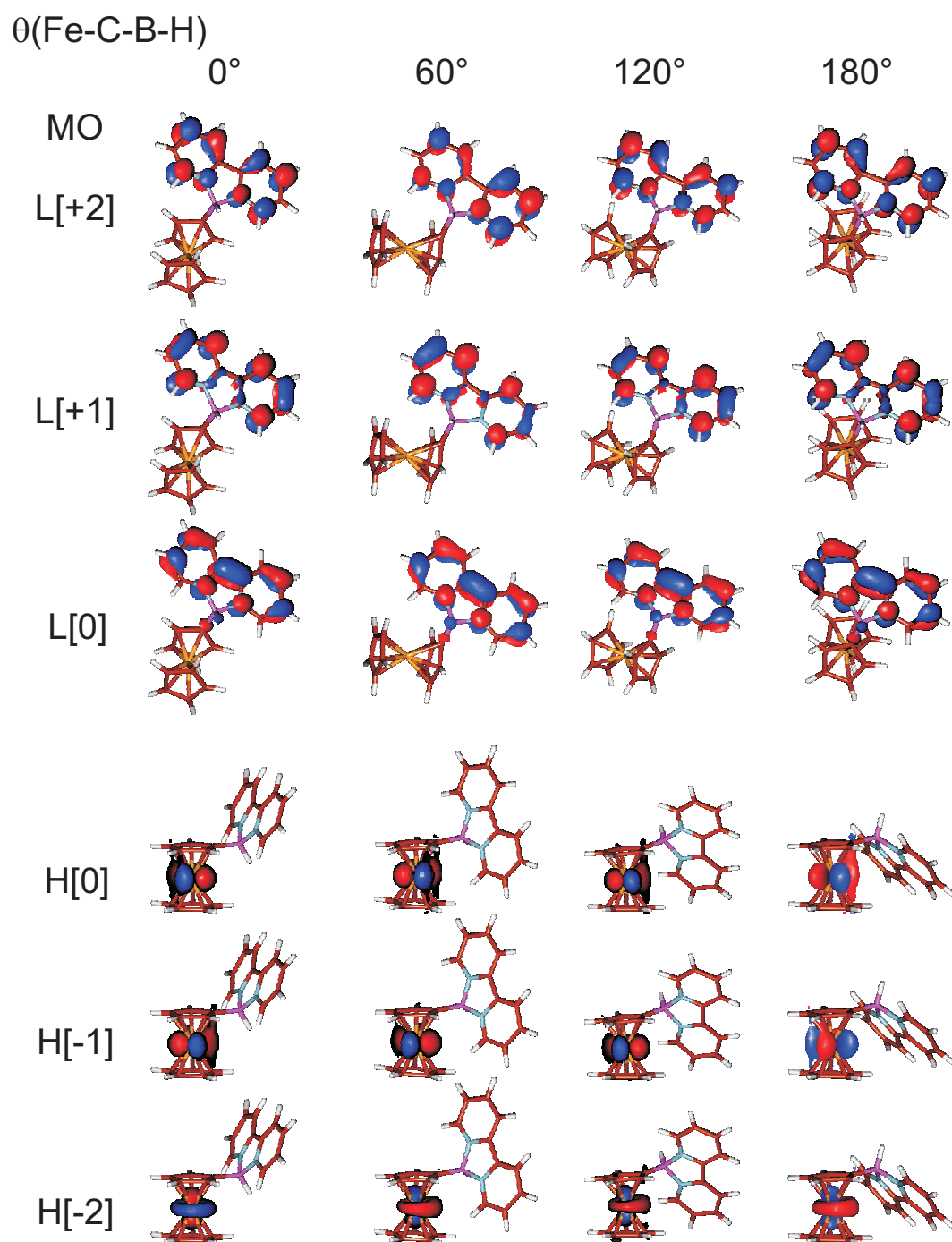


Figure 4.30.: Calculated Kohn-Sham frontier molecular orbital isosurfaces vs selected dihedral angles $\theta_{\text{Fe-C-B-H}}$ for $[\mathbf{1}]^+(\text{H})$ (orbital energies shown in Figure 4.28). Note that in order to aid visual inspection, the approximate graphical orientation of the Fe-unit is constant for the HOMOs, whilst for the LUMOs the B-bpy-unit orientation is approximately constant.

complex. To a lesser degree, these data also provide a comparison for the UV-vis spectroelectrochemistry data in Section 4.5.3 for the oxidised species $[\mathbf{1A}]\text{PF}_6$ and $[\mathbf{2A}](\text{PF}_6)_2$.

In Figure 4.31 we present the molecular orbitals and their energies for $[\mathbf{1}]^{2+}(\text{H})$ for comparison with $[\mathbf{1}]^+(\text{H})$. Several important differences exist between $[\mathbf{1}]^+(\text{H})$ and $[\mathbf{1}]^{2+}(\text{H})$. Due to the fact that the total electron spin momentum is no longer zero, the α -spin- and β -spin-orbitals are no longer degenerate in the paramagnetic radical $[\mathbf{1}]^{2+}(\text{H})$ (note that the dication possesses net α -spin, i.e. there is one additional α -spin orbital). The vacuum energies of all orbitals fall significantly to more negative (bound) values. This is to be expected due to the increased coulomb binding of the more positively charged solute. However, the HOMOs of both spin are stabilised far more strongly than the LUMOs, which results in an increase of 3.09 eV in the smallest HOMO-LUMO separation from 1.66 eV (for the cation $[\mathbf{1}]^+(\text{H})$) to 4.75 eV (for the dication $[\mathbf{1}]^{2+}(\text{H})$). It is clear however, that using these observed HOMO-LUMO separations for $[\mathbf{1}]^{2+}(\text{H})$ to predict the energy of actual electronic transitions is clearly hazardous in this case, due to the fact the resulting energies would be inconsistent with the fact that visible range absorption is still observed in the oxidised compound $[\mathbf{1A}]\text{PF}_6$ (Section 4.5.3) due to Fc-localised transitions.

Of considerable interest is the effect of oxidation on the spatial character and delocalisation of the frontier molecular orbitals, which bear only scarce correspondence to those of the cation $[\mathbf{1}]^+(\text{H})$, and reflect the complex redistribution of charge density that occurs upon electron removal. We note that whilst the lowest energy unoccupied orbital (α -LUMO[0]) is still of the same character as the LUMO[0] for $[\mathbf{1}]^+(\text{H})$, there is a number of closely-spaced HOMOs which are delocalised over both the Fc and B-bpy fragments, with the highest ‘singly-occupied molecular orbital’ (α -H[0]) actually localised on the B-bpy acceptor, as opposed to on the Fc unit. We note that we cannot generalise these results directly to the case of the MLCT excited-state (where the charge displaced from the Fc-centre is still present in the molecule). However, an important implication arises when we consider the expected behaviour of mixed-valence [188, 189, 190, 191, 192, 15, 193] macromolecular systems incorporating the Fc-B-bpy monomers in both oxidation states. Based on the theoretical orbitals presented here, we expect that the molecular orbitals associated with oxidised centres should possess increased delocalisation over Fc-donor and B-bpy acceptor, which should promote electronic coupling between adjacent donor and acceptor groups in related oligomeric/polymeric systems.

In conclusion to this section, we present in Figure 4.32 the calculated electrostatic potential of the cation $[\mathbf{1}]^+(\text{H})$ calculated on the isosurfaces of total electron density for several tolerances, as indicated (with two perspectives in each case). For the tight tolerance of $r = 0.1$ (far right), one observes the relative positive potential of the hydrogen atoms and a large relative positive potential in the neighbourhood of the B atom. For increasing tolerance r (and correspondingly larger distance from the molecular centre), the average positive potential falls away as expected, and one sees clearly that approaching the van der Waals surface, the spatial region near the B-bpy acceptor reflects more of the net positive charge on the cation, with a significantly higher relative potential to near the unsubstituted Cp^- ring. Hence we can conclude that the effective charge density seen by the surrounding solvent molecules for the single-B-bpy-acceptor derivatives $[\mathbf{1A}]\text{X}$ does correspond to a superposition of a monopole/dipole distribution, hence supporting (at least for the ground state) the solvatochromism model employed in Section 4.2.2.

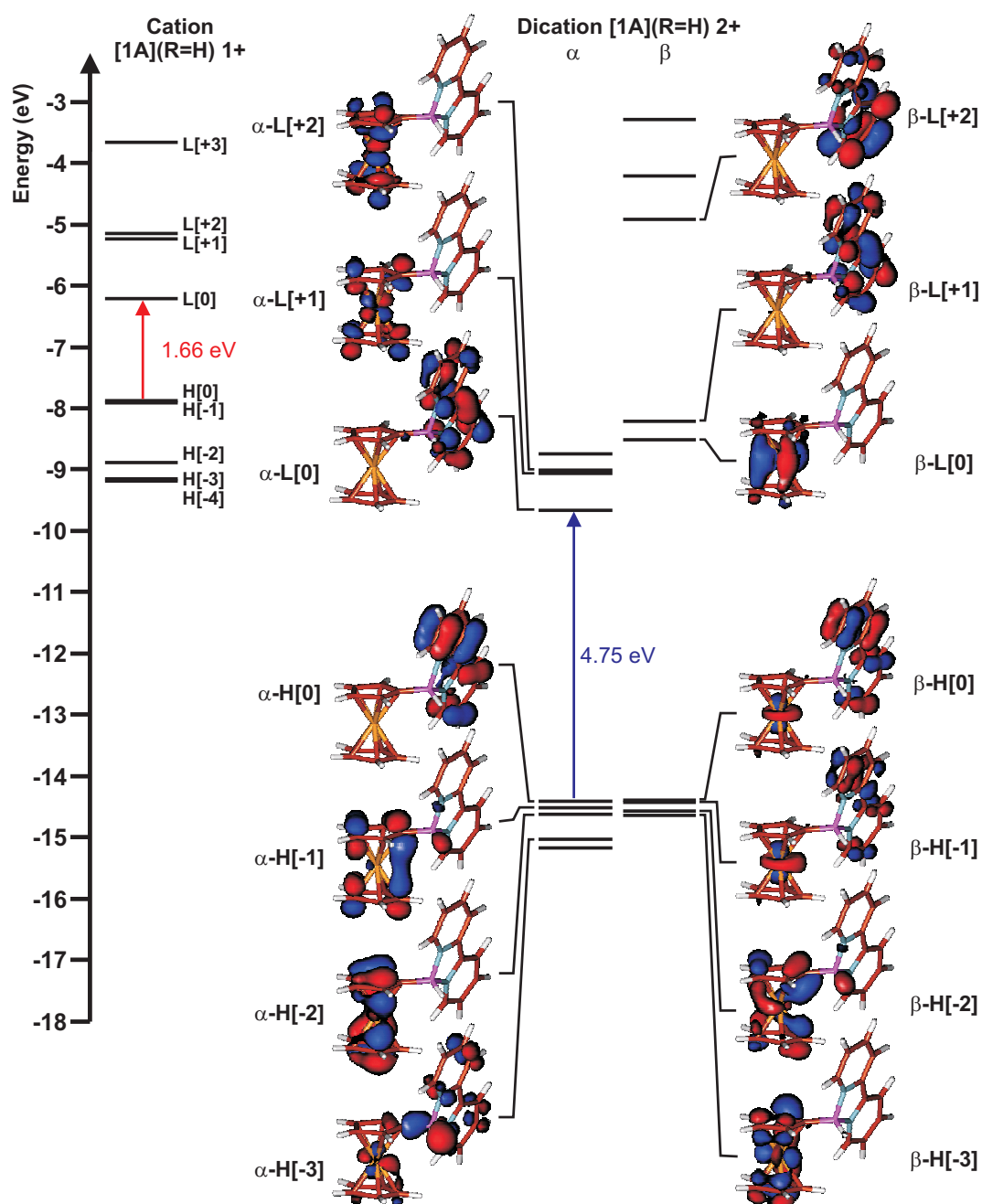


Figure 4.31.: Frontier Kohn-Sham molecular and energies for the dication $[1]^{2+}(\text{H})$ extracted from DFT calculations. Shown on the left are the MO energies for the cation $[1]^+(\text{H})$ for comparison.

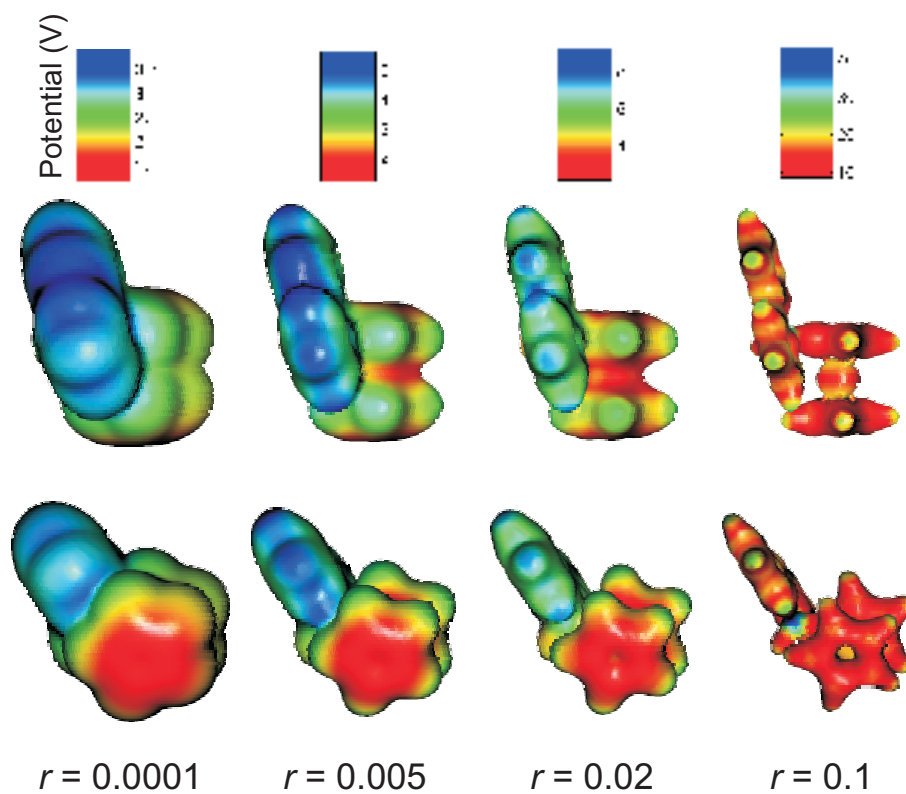


Figure 4.32.: Electrostatic potential for $[1]^+(\text{H})$ (calculated from the theoretical gas-phase ground state) plotted on the total electron density isosurfaces for several tolerances, as indicated (r represents the fraction of remaining electron density not encompassed by the surface). Note the colour scaling differs for each isosurface.

5. Time-resolved transient-absorption spectroscopy of Fc-B-bpy compounds in solution

In this chapter, we present the time-resolved excited-state absorption characteristics of several Fc-B-bpy derivatives in solution following direct excitation of the MLCT band. Whilst the previous chapter provided many key details in understanding the electronic properties of the ground-state (and to a lesser degree, the excited-state) and strongly supports the assignment of the MLCT band, a direct probe of the properties of the transient MLCT excited state can only be gained from ultra-fast time-resolved measurements. The properties of MLCT excited states in medium-size polyatomic metal-organic compounds can display a range of interesting excited-state phenomena, such as ultrafast intersystem-crossing and electronic localisation [207], which can be directly observed with ultrafast excited-state spectroscopy. Our key interests in probing the excited-state dynamics of the Fc-B-bpy compounds was two-fold: (i) in order to look for spectral characteristics that support the assignment of the MLCT band, and (ii) to gain knowledge of the relaxation mechanisms (including the possible role of intermediate excited states) and related time-scales for decay of the excited CT state. This latter point is extremely relevant for the design of related derivatives for the optically-driven injection of charge into an attached macromolecular system, as the efficiency of electron injection will be determined by the relative magnitudes of the effective back-electron transfer (b-ET) relaxation rate $\sum k_{b-ET,i}$ and the rate for secondary transfer k_{sec} of the excited electron into a delocalised channel in the macromolecular framework, or into an adjacent oxidised donor. Moreover, even in the simpler case where the directly-excited CT state is itself the target excited state, the steady-state fraction of excited molecules in a sample (for a given constant optical excitation level) will be proportional to the excited-state lifetime.

In the following, we present (i) the transient-absorption spectra of compounds **[2A](PF₆)₂**, **a-BOB** and **(Fc)₂BOB** (in the range $\lambda = 450 - 760$ nm, on a time scale from 1-1000 ps), (ii) a comparison of these excited-state transient spectra with UV-vis spectroelectrochemistry data (from Section 4.5.3), and (iii) the corresponding transient-absorption kinetics for several characteristic wavelengths (including a global fitting analysis). We discuss certain models for the relaxation mechanism consistent with the observed excited-state dynamics. These three derivatives (Figure 5.1) were selected for the comparative time-resolved study based on the fact that both (i) conformational flexibility and (ii) the electronic coupling between acceptors across the B-O-B bridge, could contribute to the differences in observed excited-state relaxation behaviour. As will be presented in the following sections, the transient absorption data suggest relaxation dynamics for both **[2A](PF₆)₂** and **(Fc)₂BOB** which include an efficient non-radiative transition to the ground state (at least for a fraction of the excited-state ensemble of **[2A](PF₆)₂**) on time scales in the range $\sim 18 - 45$ ps due to large-scale conformational rearrangement in the excited-state, whilst the ground-state recovery for **a-BOB** proceeds only on a ~ 780 ps time scale, indicating that the critical factor in the excited-state relaxation behaviour is dictated by conformational freedom as opposed to an influence on the excited-state electronic wavefunction due to the presence of the B-O-B bridge.

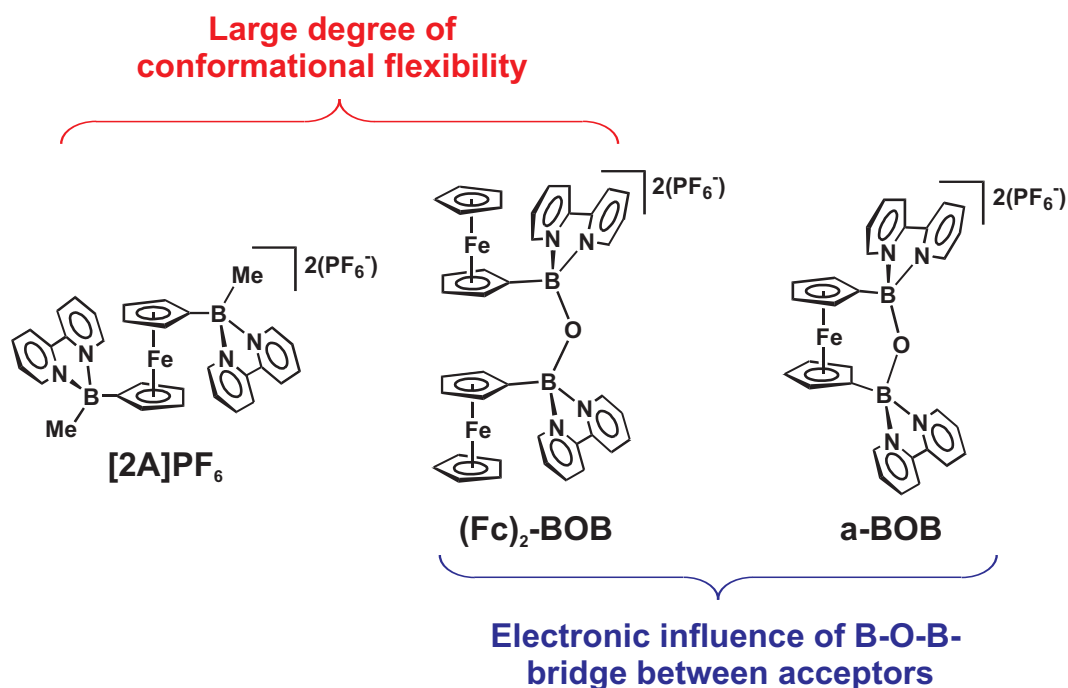


Figure 5.1.: Fc-B-bpy derivatives studied in the transient absorption measurements, $[2\mathbf{A}](\text{PF}_6)_2$, $\mathbf{a-BOB}$ and $(\text{Fc})_2\text{BOB}$. The excited-state dynamics of these three derivatives are compared in order to better distinguish between excited-state effects from (i) conformational flexibility and (ii) possible electronic influence of the B-O-B bridge between coupled acceptors.

5.1. Additional experimental details

The experimental setup used for the measurements in this chapter was outlined in Section 3.2 (see Figure 3.10), although here we give the details for the specific measurements presented in this chapter. For the excitation pulses, we employed a NOPA source (Section 3.1.5) tuned to a centre wavelength of $\lambda = 500$ nm (typically with $\Delta\lambda_{\text{FWHM}} = 15.6$ nm), and compressed to a pulse width of ~ 35 fs (at the sample position). A two-lens telescope arrangement was used to collimate the NOPA beam, with a beam diameter of approximately 3 mm (FWHM).

For the probe source, we employed white-light continuum pulses (Section 3.1.2) generated in a 3-mm-thick sapphire disk using the near-IR pulses from the CPA amplifier laser (~ 2 μJ pulse energy, $\lambda = 775$ nm) (Section 3.1.1). The white-light continuum beam was collimated by an 90° off-axis paraboloidal mirror (Ag-coated) with off-axis-distance of 25.4 mm, with a beam diameter of ~ 7 mm (although this was slightly wavelength-dependent). Optimal adjustment of the collimating mirror was achieved by inspecting the beam profile at a distance ~ 8 m after the mirror (i.e. by diverting the probe beam from the sample into a long path traversing the lab). A thin IR-blocking filter (with a 1-mm BK7 substrate) was used to suppress the residual 775 nm pump light in the white-light-continuum spectrum. A long-range manual delay-stage (providing up to 1 m of adjustable delay) was used to adjust the relative total path lengths of the pump and probe such that almost the full travel of the translation stage corresponded to positive pump-probe delays (i.e. allowing the measurement of the transient probe absorption up to 1000 ps following excitation).

The pump and probe beams were brought into parallel alignment (with a separation between the two beam centres of ~ 6 mm), and focussed into the sample using a second 90° off-axis paraboloidal mirror with an off-axis-distance of 100 mm. The probe beam was incident on the centre of the paraboloidal mirror, whilst the pump beam was displaced vertically, such that the beams cross in the vertical direction at the focus. This arrangement is essential due to the significant scattering of the pump beam from the (diamond-turned) paraboloidal mirror, which leads to scattering in the horizontal direction. Fine tuning of the spatial overlap of the pump and probe beams was first achieved using a $25 - \mu\text{m}$ -diameter pinhole positioned at the focal plane (confirmed by optimising the probe beam transmission through the pinhole). Further optimisation in the presence of a sample cuvette was performed using a rhodamine-6G sample.

The alignment of the NOPA pump beam to the mechanical translation stage (upon which a retroreflector was mounted) was fined-tuned by diverting a fraction of the pump beam after the translation stage directly onto a CCD camera chip and monitoring the beam motion (using a dedicated measurement program) as the translation stage was moved over its full travel of 20 cm (c.a. $\cong 1300$ ps double pass). In this way, the alignment could be compensated including systematic mechanical defects in the translation stage resulting in a residual beam-walk of ~ 40 μm over the full travel range (and a resulting negligible beam-walk at the sample focal position). The relative polarisation of the pump and probe beams was checked using a Glan-Taylor polariser, and a broadband $\lambda/2$ -waveplate in the pump beam path was used to achieve the desired relative polarisation between pump and probe (for the measurements presented here, this was the magic angle 54.7°).

The solution samples were in static quartz cuvettes with a 1-mm sample thickness (and standard front/back window thickness of 1.25 mm). The Fc-B-bpy sample concentrations were typically ~ 3.5 mM, which resulted in a sample optical density of ~ 0.3 at the pump wavelength (corresponding to $\sim 50\%$ absorption). Tests were

performed to ensure that no detectable concentration dependence of the form of the transient absorption signals resulted for these levels of sample concentration.

For the measurements presented here, an incident pump pulse energy of $J_0 \approx 70$ nJ was employed at the sample. Assuming a nominal pump-beam focal diameter of 100 μm (Gaussian FWHM) at the sample, this corresponds to an on-axis incident pump fluence of $F_0 = 6.2 \mu\text{J} \cdot \text{mm}^{-2}$. Given the molecular absorption strength of the Fc-B-bpy derivatives at the probe wavelength $\epsilon \sim 900 \text{ M}^{-1}\text{cm}^{-1}$ (which corresponds to an absorption cross-section of $\sigma = \ln(10)/(10N_A)\epsilon \sim 3.4 \times 10^{-22} \text{ m}^{-2}$), at the front surface of the sample we have an approximate relative excitation density of,

$$\frac{\Delta n}{n} = \frac{\lambda \sigma F_0}{hc} \sim 0.0054,$$

which is consistent with the magnitude of the observed maximum transient-absorption modulation depth(s) ($\Delta OD \lesssim 10^{-3}$).

Tests of the pump-probe signal vs incident pump pulse energy confirmed that the form of the signals did not change significantly in reducing the pump energy by a factor of 5 (below which the signal-to-noise of the transients was too low for meaningful comparison), hence indicating that the level of two-photon excitation was negligible for the pump energies used (as supported by the low relative excitation density estimated above). However, attempts to increase the pump-pulse energy above $F_0 = 10 \mu\text{Jmm}^{-2}$ (i.e. to increase the signal modulation) resulted in significant non-linear effects in the sample (which was evident from the production of a super-broadened pump spectrum after the cuvette), and resulted in extremely noisy, distorted pump-probe signals. We note that the fact that the onset of significant thermal (i.e. average pump-power) effects were observed at slightly higher pump-fluences than the onset of non-linear (instantaneous intensity) effects was taken to justify the use of static cuvettes.

Following the sample, the diverging probe beam passed through an adjustable aperture (to reject scattered pump light) and was recollimated by a plano-convex lens ($f = 100$ mm). The probe beam was then focussed (using an $f = 80$ mm lens) at the entrance slit of the computer-controlled monochromator (0.5 m, entrance slit 200 μm 600 lines/mm grating, blaze wavelength 500 nm). At the output of the monochromator, a manually adjustable slit was used to provide a bandpass of $\Delta\lambda_{\text{FWHM}} \sim 5$ nm for the probe light. For the measurements here, the filtered probe beam was recollimated (by a $f = 50$ mm lens), and coupled into a multimode-fibre via a fibre-coupler. In this way, the filtered probe light could be coupled either to the optical detector or to a home-built fibre-coupled spectrometer (in the latter case, to allow for an accurate calibration of the monochromator).

As mentioned in Section 3.2, the optical detector for the probe beam used for these measurements is based on a Si-photodiode (sensitivity range 250-1100 nm) with an integrated 4-kHz-bandwidth FET-amplifier, and an additional $\times 10$ amplifier section in the detector housing. The electronic signal was then sent to a digital lock-in amplifier (Perkin Elmer, 7265). Before the sample, the NOPA-pump and white-light-probe pulses passed through a custom-built two-phase optical chopper (synchronised to the pulse train, Section 3.2) which downsampled the 1-kHz pulse trains to 333 Hz and 500 Hz, respectively. Hence the net pump-probe signal modulation is encoded on the detected probe signal with a fundamental frequency of 166 Hz. The optical chopper provided a synchronised 166-Hz TTL reference directly to the lockin amplifier. Note that extensive tests were performed using different time constants for the analog integration of the demodulated lock-in signals. From statistical analyses of the signal fluctuations vs different lock-in time constants (in the range 10-2000 ms), a value of 100 ms was determined to be near optimal, due

to the fact that for longer integration times, sources of sub-Hz-bandwidth noise became important, and the convergence of the relative standard deviation of the signal fluctuations tended to diverge from the central-limit theorem behaviour vs integration time observed for shorter integration times.

In order to determine the absolute modulation depth of the transient absorption signals, the measurement programs regularly monitored the absolute probe pulse signal, which was achieved by setting the lock-in amplifier to detect the 3rd harmonic of the 166 Hz reference signal (i.e. the probe modulation frequency of 500 Hz), and scaling the value by the appropriate factor of 3 (due to the different duty cycle of the pump-probe and probe-only signals).

In the measurements shown here, no reference beam was used, as the dominant source of noise on the pump-probe signals was determined to be due to the residual dark electronic noise from the detector, pre-amplifier and lock-in amplifier electronics. (Note that due to the finite correlation between neighbouring white-light pulses, the lock-in detection effectively performs a quasi-normalisation using adjacent modulated and unmodulated probe pulse signals).

The data-acquisition computer programs¹ mediated control of the monochromator position (i.e. detected probe wavelength), translation-stage position (i.e. pump-probe delay) and acquisition of the transient-absorption signals from the lock-in amplifier.

We note that the transient absorption spectra presented here, are not corrected for the temporal chirp of the white-light continuum (this functionality has been put into more recent measurement programs), such that the effective pump-probe delay varies by ~ 500 fs across the probe wavelength range (i.e. with the effective pump-probe delay being more positive at the blue end of the spectrum). This results in some distortion of the transient spectra for the nominal $\tau = 1$ ps delay (which is defined for $\lambda = 520$ nm). Any confusion resulting from this distortion can be resolved by inspection of the corresponding single-wavelength kinetics, which are corrected from analysis of the coherent artifacts (which are also removed in the data presented).

Due to the fact that the transient-absorption kinetics exhibit changes on several distinct time scales (i.e. with the coherent artifacts and initial relaxation on sub-picosecond time scales, and complete ground-state recovery on a time scale approaching 1000 ps), the sub-routines handling the pump-probe delay scanning were adapted to allow for the definition of multiple scan ranges with different scan speeds (i.e. in ps-delay/sec), such that a single scan program acquired kinetics with the appropriate delay resolution in each delay range. Moreover, due to the possible occurrence of burst noise during the measurements, the data from each repeated delay scan was stored in auxiliary data files, allowing the removal of obvious outliers from the data in the analysis stage, as well as providing the possibility to estimate the standard error of the averaged transient absorption data.

5.2. Transient absorption spectra

Figure 5.2 shows the excited-state transient absorption spectra for the compounds (a) **[2A](PF₆)₂**, (b) **a-BOB** and (c) **(Fc)₂BOB** (in CH₃CN) following excitation with $\lambda_{\text{ex}} = 500$ nm (as described in the previous section), for selected pump-probe delays in the range $\tau = 1-1000$ ps. For comparison, the corresponding CW ground-state absorption spectra (as well as the fitted HE and MLCT bands) are shown in Figure 5.2(d), as well as the excitation pulse spectrum. For both **[2A](PF₆)₂**

¹The self-written data-acquisition programs used here were coded in Labview.

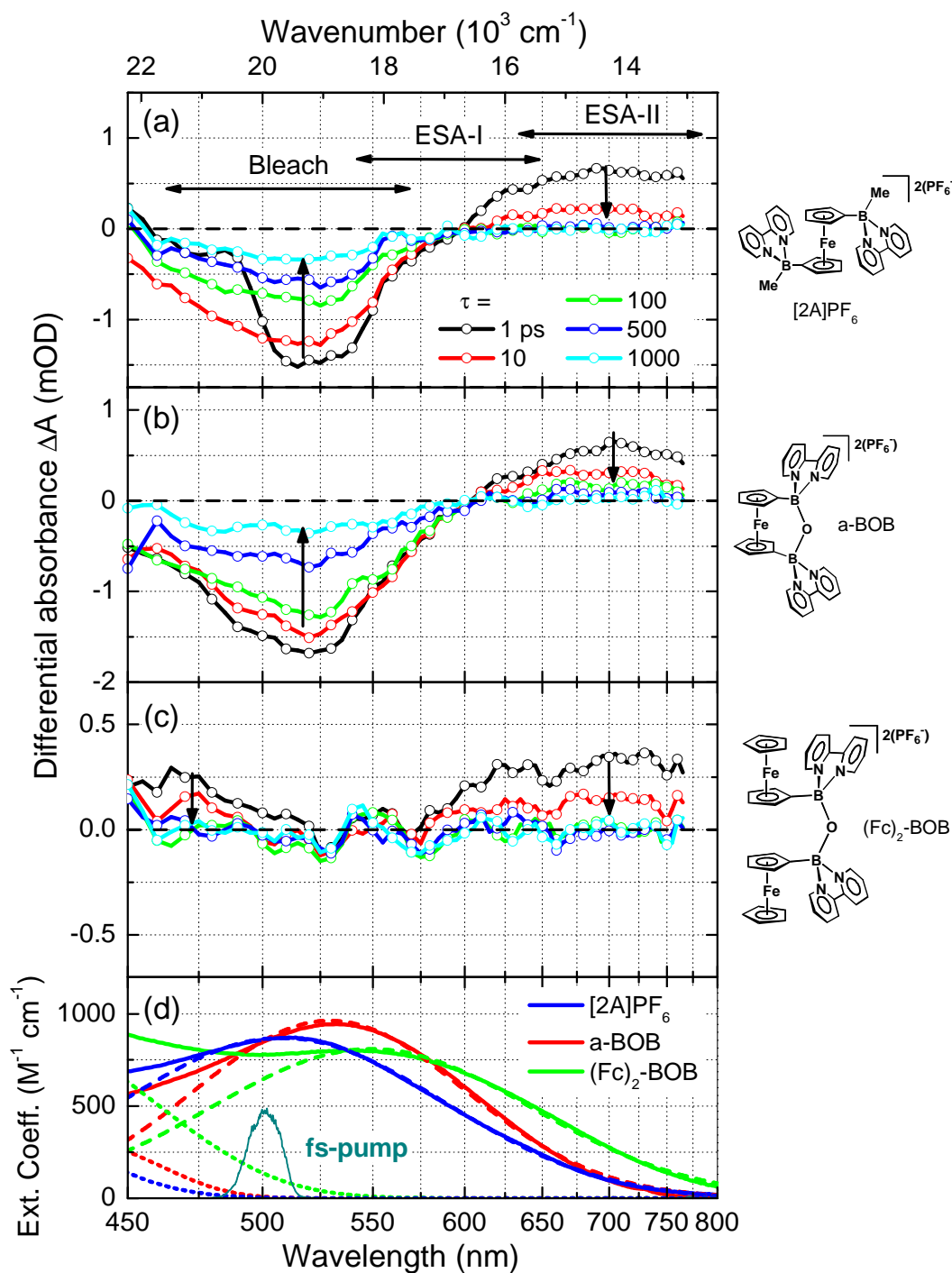


Figure 5.2.: Transient absorption spectra for (a) $[2A](PF_6)_2$, (b) *a*-BOB and (c) $(Fc)_2$ BOB (in CH_3CN) following excitation at $\lambda_{ex} = 500 \text{ nm}$ for selected pump-probe delays (as indicated) (relative pump-probe polarisation: magic angle). Approximate regions of predominant bleach and two regions of overlapping excited-state absorption (ESA-I, ESA-II) are indicated in (a). (d) Corresponding ground-state absorption spectra and excitation-pulse spectrum.

and **a-BOB**, one observes a region of negative differential absorption (ground-state bleach signal) in the range $\lambda \sim 460 - 600$ nm, whereas for wavelengths above a quasi-isosbestic point at $\lambda \approx 600$ nm the transient absorption is dominated by excited-state absorption, extending to the red-edge of the measurement wavelength window at $\lambda = 760$ nm. It is apparent that whilst the transient-absorption bleach band for **[2A](PF₆)₂** and **a-BOB** is no longer dominant for $\lambda \gtrsim 600$ nm, from an inspection of the ground-state absorption curves in Figure 5.2(d) the ground-state absorption strength at this wavelength is still $\sim 50\%$ that of the absorption maximum, which indicates that the ESA band extends into the region $\lambda < 600$ nm.

Also evident is that despite the fact that the regions of predominant bleach and ESA decay at clearly different rates in the spectra of **[2A](PF₆)₂** (with only a negligible residual net ESA signal for $\tau \geq 100$ ps) the position of the zero crossing does not red-shift significantly with increasing delay. In the case where all ESA bands would decay more rapidly and leave only a residual ground-state bleach (due to the involvement of a ‘dark’ intermediate excited state), one would expect the negative bleach band to expand progressively into the region $\lambda > 600$ nm and acquire the same form as the ground-state absorption spectrum, which is not observed.

One possible explanation for this would be that the excitation at $\lambda_{\text{ex}} = 500$ nm excites only a spectroscopically distinct portion of the ground-state ensemble, i.e. that a bleach band of reduced width results from ‘hole-burning’ of an inhomogeneously-broadened ground state ensemble. However, given that no red-shifting of the bleach band is observed over the full delay range ($\tau \rightarrow 1000$ ps) for **[2A](PF₆)₂**, this would imply a characteristic time scale for the redistribution of the inhomogeneity of $\tau \gg 1000$ ps. It is conceivable that such a slowly-fluctuating broadening mechanism could arise in **[2A](PF₆)₂** from a distribution of relative conformations between the Fc-donor and B-bpy-acceptor groups due to variable rotation about the B-C(Cp) bridging bonds. However, the fact that the transient spectra for **a-BOB** (where the conformational distribution of the B-bpy groups relative to the Fc-donor is constrained by the connecting -O- bridge) also exhibit the same deviation between the predominant bleach band and the ground-state absorption tends to rule out such an inhomogeneous broadening mechanism.

Hence, in order to explain the persistent reduced wavelength range of predominant bleach signal for both **[2A](PF₆)₂** and **a-BOB**, we are led to conclude that there are actually two distinct overlapping ESA bands (which we will refer to as ‘ESA-I’ and ‘ESA-II’) contributing to the transient spectra. The first band (ESA-I) is dominant in the region $\lambda \sim 550 - 650$ nm and suppresses the bleach band in this region, whilst the ESA-II band dominates the signal for $\lambda \gtrsim 650$ nm and is responsible for the observed net-positive differential absorption in this region. We note that based on the spectra for **[2A](PF₆)₂**, this implies that the ESA-I band decays on the same (or comparable) time scale as the ground-state recovery (i.e. bleach band decay).

Concerning the origin of these two ESA bands, we consider certain differential absorption features in the UV-vis spectra that appear upon electrochemical oxidation/reduction of **[2A](PF₆)₂** and **a-BOB** (Figure 4.24). We note that upon oxidation of these compounds, one also does not observe a negative differential absorption of the same shape as the MLCT band in the visible range (ox-B in Figure 4.24(b)), due to the presence of the new electronic transitions that arise for the Fc⁺-centre in this wavelength range, and that also lead to a suppression of the negative differential absorption on the red-side of the MLCT band. Hence we propose that the ESA-I band is associated with analogous localised transitions on the Fc-unit of **[2A](PF₆)₂** and **a-BOB** in the MLCT excited state, which corresponds

to the transient oxidised species Fc^+ (assuming that the electronic displacement upon excitation corresponds to almost complete removal of a unit electronic charge from the Fc-centre and neglecting the coupling to the B-bpy unit). Moreover, this is consistent with the fact that the ESA-I band possesses the same relaxation kinetics as the ground-state recovery.

In considering the possible origin of the ESA-II band, we consider the corresponding changes in UV-vis absorption for $[\mathbf{2A}](\text{PF}_6)_2$ and **a-BOB** that occur upon electrochemical reduction (Figure 4.24(c)). Here we observe an analogous differential absorption band (red-D) that arises in the near-IR (and extends down to $\lambda \sim 600$ nm), which (based on the discussion in Section 4.5.3) we can assign to the presence of an additional electron on the B-bpy acceptor. Hence we assign the ESA-II band to the presence of an excess unit electronic charge distributed on the B-bpy units in the initial MLCT excited-state. Both the assignment of the ESA-I band and the ESA-II band in terms of the corresponding spectroelectrochemistry data strongly support an almost complete charge transfer of an electron upon excitation of the proposed MLCT band.

In order to investigate more critically the comparison of the excited-state transient differential spectra with the spectra upon oxidation/reduction, in Figure 5.3 we present the results of a regression analysis of the excited-state transient spectrum of $[\mathbf{2A}](\text{PF}_6)_2$ (for $\tau = 10$ ps) using the corresponding oxidised- $[\mathbf{2A}](\text{PF}_6)_2$ /reduced- $[\mathbf{2A}](\text{PF}_6)_2$ spectra as basis functions. We note that from the discussion of the UV-vis spectra of reduced-B-bpy derivatives (Sections 2.3 and 4.5.3), we expect a blue-shifting of second lowest-energy band in the reduced- $[\mathbf{2A}](\text{PF}_6)_2$ -spectrum (red-C, which has its first vibrational peak at $\lambda = 499$ nm) in the presence of an electron-withdrawing group, which we can expect to be the case in a MLCT excited-state where the Fc unit is formally oxidised. Hence in the fitting process, we allowed a variable blue-shift of the reduced- $[\mathbf{2A}](\text{PF}_6)_2$ spectrum as a fitting parameter. As shown in Figure 5.3, a reasonable agreement between the experimental excited-state transient spectrum and the hybrid-oxidised/reduced- $[\mathbf{2A}](\text{PF}_6)_2$ spectrum is obtained, if we allow for a blue shift of the reduced- $[\mathbf{2A}](\text{PF}_6)_2$ spectrum of $\Delta\nu = 2470$ cm^{-1} , which is somewhat larger than the blue-shift of the red-C band in substituting electron-withdrawing substituents ($\Delta\nu \sim 1600$ cm^{-1}) (see Section 2.3). We note that the relative weighting of each redox spectrum in the fit involves a significantly smaller weight for the reduced- $[\mathbf{2A}](\text{PF}_6)_2$ spectrum than for the oxidised- $[\mathbf{2A}](\text{PF}_6)_2$ spectrum. Accounting for the fact that the ESA-II region has already decayed significantly by $\tau = 10$ ps, we can extrapolate a ratio for the two spectra of $\sim 4:1$ (oxidised:reduced) for the initial excited state. However, given that the differential spectra of the oxidised-donor- $[\mathbf{2A}](\text{PF}_6)_2$ and reduced-acceptor- $[\mathbf{2A}](\text{PF}_6)_2$ correspond to the case of $\text{A-D}^+\text{-A}$ and $\text{A}^-\text{-D-A}^-$, respectively, whilst the MLCT excited-state of $[\mathbf{2A}](\text{PF}_6)_2$ corresponds formally to $\text{A-D}^+\text{-A}^-$, it is foreseeable that the differences in electrostatic influence between in donor and acceptor in each case (and the accompanying difference in equilibrium conformation) will lead to distortions in the energy and strength of the related electronic transitions².

Returning to Figure 5.2, one observes that the transient spectra of the ferrocene compound $(\text{Fc})_2\text{BOB}$ (Figure 5.2(c)) differ significantly from those of $[\mathbf{2A}](\text{PF}_6)_2$ and **a-BOB**. Whilst the ESA-II band region is still discernible, it is clear that additional excited-state absorption bands arise in the same wavelength region as the bleach band with similar magnitude, such that no clear region of negative differential absorption is observed, although the depression in the spectrum

²Note that we describe the MLCT excited state in terms of a localised CT onto one of the two B-bpy acceptors, which we will address later in this chapter.

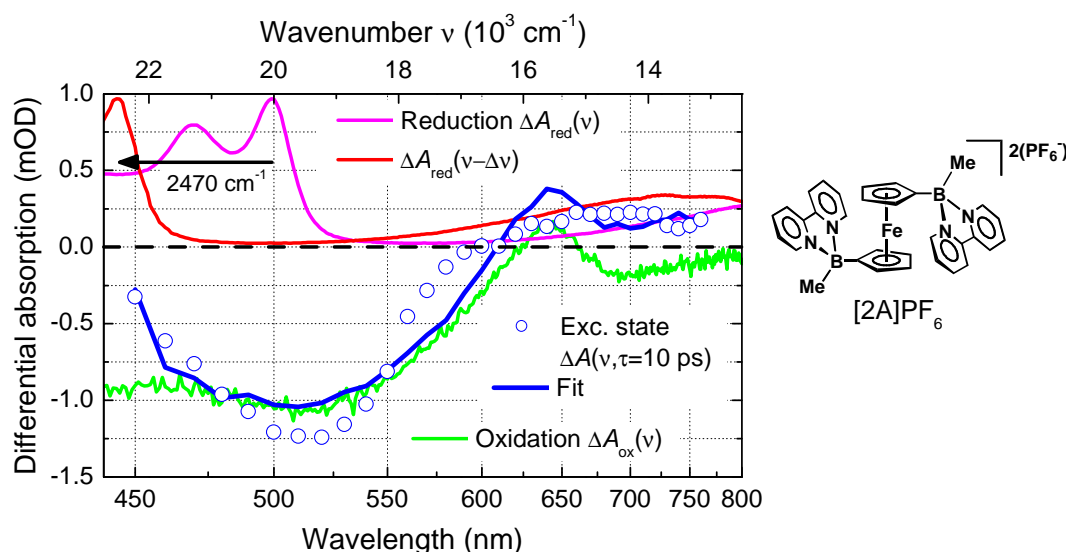


Figure 5.3.: Results of a regression analysis of differential excited state absorption spectrum of $[2\mathbf{A}](\text{PF}_6)_2$ ($\tau=10$ ps following $\lambda_{\text{ex}} = 500$ nm excitation) based on a weighted sum of the differential absorption upon electrochemical oxidation and reduction (Figure 4.24) (with a fitted blue-shift of the reduction spectrum of 2470 cm^{-1} as indicated).

between $\lambda \sim 470 - 600$ nm does again reflect the presence of the bleach band³. Moreover, despite the comparatively low signal-to-noise of the data (which is due to the generally weaker signal modulation across the spectrum), it is also evident that the entire transient spectrum decays by $\tau = 100$ ps (see the corresponding transient-absorption kinetics and analysis in the next section).

We note that from the electrochemistry data for $(\text{Fc})_2\text{BOB}$ (Section 4.5.1) there is evidence for a finite degree of electronic coupling between the two Fc-units. Hence, it is reasonable to expect additional excited-state transitions between the Fc/Fc⁺ pair in $(\text{Fc})_2\text{BOB}$, in analogy to mixed-valence Fc-Fc⁺ compounds [188, 189, 190, 191, 192, 15, 193]. Moreover, such intervalence transitions normally possess extremely broad diffuse absorption bands, which is consistent with the fact that no characteristic band structure is observed for the additional ESA contributions in the transient spectra of $(\text{Fc})_2\text{BOB}$. One can anticipate from these results for $(\text{Fc})_2\text{BOB}$ that far more complex excited-state spectra may be encountered in the Fc-B-bpy-based oligomeric systems to be studied in the future where multiple Fc units can interact.

5.3. Transient absorption kinetics

In this section, we present the time-resolved transient-absorption kinetics for $[2\mathbf{A}](\text{PF}_6)_2$, $\mathbf{a}\text{-BOB}$ and $(\text{Fc})_2\text{BOB}$ following MLCT excitation ($\lambda_{\text{ex}} = 500$ nm), in order to better quantify the different relaxation characteristics of the MLCT excited state. For each derivative, we present the data for three characteristic probe wavelengths, (i) $\lambda = 470$ nm (high-energy side of predominant bleach band), (ii)

³We note that the transient spectra for $(\text{Fc})_2\text{BOB}$ were performed during the same measurement run as those for $[2\mathbf{A}](\text{PF}_6)_2$ and $\mathbf{a}\text{-BOB}$, and similar transient spectra for $(\text{Fc})_2\text{BOB}$ were produced in earlier preliminary measurements, such that it is unlikely that the significant differences in the transient spectra compared to the other derivatives are due to spurious artifacts in the measurement.

$\lambda = 540$ nm (near-degenerate predominant bleach), and (iii) $\lambda = 660$ nm (ESA-II band). The results are shown in Figures 5.4 (**[2A](PF₆)₂**), 5.5 (**a-BOB**) and 5.6 (**(Fc)₂BOB**). The transient-absorption kinetics for all derivatives exhibit multi-exponential relaxation characteristics on several distinct time scales, including an initial sub-picosecond transient (τ_1), and depending on the derivative, 1-2 slower components (τ_2 , τ_3) which vary over a broad range of from several ps to almost 1 ns. In order to extract meaningful parameters from the curves, we fit the data for each derivative with global time scales for all probe wavelengths, i.e.,

$$\Delta A(\lambda, \tau) = \sum_j A_{0j}(\lambda) \exp(-\tau/\tau_j).$$

The fitted multi-exponential curves are shown with the experimental data in the corresponding figures. The fitted parameters for each derivative are listed in Table 5.1, where we have normalised the amplitudes of each fitted exponential component to the unsigned sum of the amplitudes for the τ_2 and τ_3 components, i.e. $A_{0j}(\lambda) \rightarrow A_{0j}(\lambda)/(|A_{02}(\lambda)| + |A_{03}(\lambda)|)$, in order to more readily evaluate their relative contribution. In certain cases, a particular exponential component did not improve the fit to the data (i.e. $A_{03}(\lambda = 660 \text{ nm})$ for **[2A](PF₆)₂** and $A_{02}(\lambda = 540 \text{ nm})$ for **a-BOB**), and were omitted from the fitting procedure for these curves.

We note that the fitted multi-exponential parameters differ somewhat from our previous report [206]. This is due to two reasons. Firstly, for the weak absorption changes here, the presence of a small vertical offsets (associated with residual pump-only and probe-only signals not completely rejected by the lock-in detection) can significantly affect the fitting parameters for the weak components, and these offsets were carefully reanalysed (using the data for negative pump-probe delays).

Secondly, the analyses employed here for the global fitting of the data for each derivative employed an improved algorithm, where only the global time constants τ_j are treated as parameters in the non-linear optimisation problem. For each guess of the global time constants, the corresponding amplitudes $A_{0j}(\lambda)$ for each probe wavelength are determined by linear regression. This leads to a greatly improved performance of the fitting algorithm over a ‘standard’ implementation where all parameters are included in the non-linear search⁴. For the robust fitting of (noisy) experimental data, a Nelder-Mead simplex algorithm is generally preferable over Levenberg-Marquardt methods [227]. However, with increasing number of fit parameters, simplex-based methods become slow and less reliable, with the possibility of stagnation (i.e. convergence on a set of parameters that correspond to a *local* minimum of the misfit between the model curve and the experiment data). By using linear regression for the amplitudes of each exponential (i.e. using the more stable singular-value decomposition method [227]) in each iteration, the dimensionality of the algorithm search space is reduced considerably (e.g. from a maximum of 12 parameters, to only 3) resulting in faster and more reliable convergence.

For all derivatives, large-amplitude sub-ps transients are observed, with a small but significant variation in fitted time constant for each derivative ($\tau_1 = 0.67$ ps for **[2A](PF₆)₂**, $\tau_1 = 0.52$ ps for **a-BOB** and $\tau_1 = 0.46$ ps for **(Fc)₂BOB**). From the analysis of the MLCT spectra and electrochemical potentials in Section 4.5.2, we expect that the initial (Franck-Condon, FC) MLCT-excited state is significantly displaced from the excited-state equilibrium intramolecular and solvent geometry. The time scale for the associated initial cooling (vibrational energy redistribution)

⁴For example, the standard fitting routines in applications such as Origin®, both the non-linear and linear parameters are treated as non-linear search parameters in the fitting algorithms.

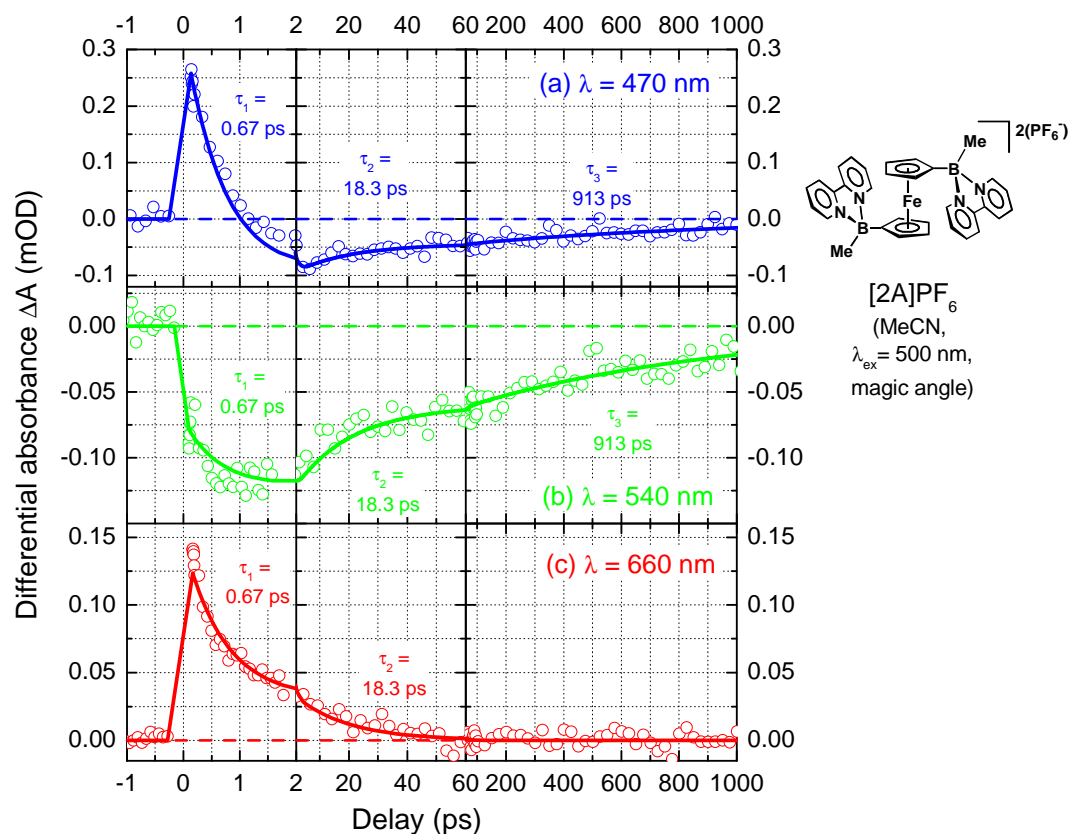


Figure 5.4.: Transient absorption kinetics for $[2\mathbf{A}](\text{PF}_6)_2$ (in CH_3CN) following excitation at $\lambda_{\text{ex}} = 500 \text{ nm}$ for selected probe wavelengths (a) $\lambda = 470 \text{ nm}$, (b) $\lambda = 540 \text{ nm}$ and (c) $\lambda = 660 \text{ nm}$ (relative pump-probe polarisation: magic angle). Global time scales (when employed for each probe wavelength) as indicated.

Derivative	τ_j (ps)	σ_{τ_j} (ps)	$\lambda = 470 \text{ nm}$		$\lambda = 540 \text{ nm}$		$\lambda = 660 \text{ nm}$	
			A_j	σ_{A_j}	A_j	σ_{A_j}	A_j	σ_{A_j}
$[2\mathbf{A}](\text{PF}_6)_2$	0.67	0.03	4.43	0.03	0.44	0.02	3.13	0.04
	18.3	1.7	-0.52	0.02	-0.49	0.01	1	0.01
	913	63	-0.48	0.01	-0.51	0.003	–	–
a-BOB	0.52	0.02	4.10	0.02	-0.58	0.02	3.41	0.04
	5.4	1.8	-0.30	0.01	–	–	0.45	0.02
	779	28	-0.70	0.003	-1	0.004	0.55	0.005
(Fc)₂BOB	0.46	0.02	15.1	0.1	3.8	0.5	5.29	0.06
	44.8	4.5	1	0.02	1	0.1	1	0.02

Table 5.1.: Normalised amplitudes and global time constants (and standard errors, σ_X) from multiexponential regression of the transient absorption kinetics for $[2\mathbf{A}](\text{PF}_6)_2$, **a-BOB** and **(Fc)₂BOB** (in CH_3CN , $\lambda_{\text{ex}} = 500 \text{ nm}$).

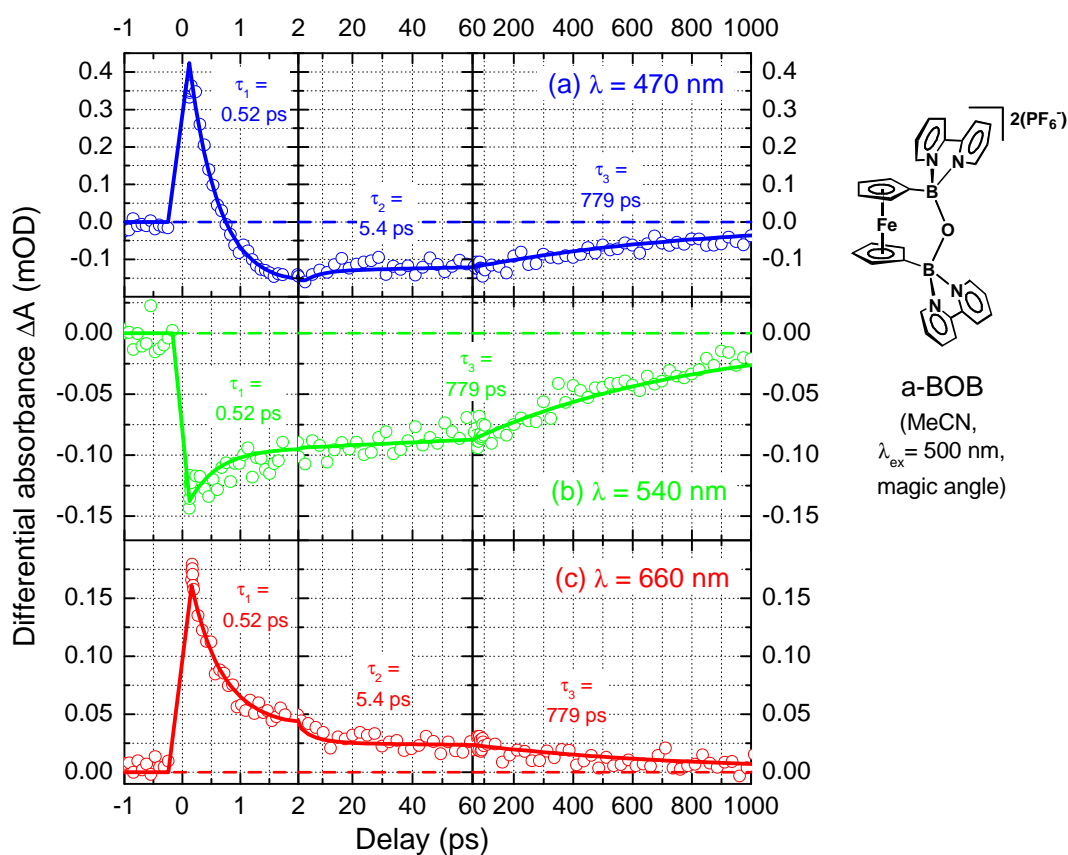


Figure 5.5.: Transient absorption kinetics for **a-BOB** (in CH_3CN) following excitation at $\lambda_{\text{ex}} = 500 \text{ nm}$ for selected probe wavelengths (a) $\lambda = 470 \text{ nm}$, (b) $\lambda = 540 \text{ nm}$ and (c) $\lambda = 600 \text{ nm}$ (relative pump-probe polarisation: magic angle). Global time scales (when employed for each probe wavelength) as indicated.

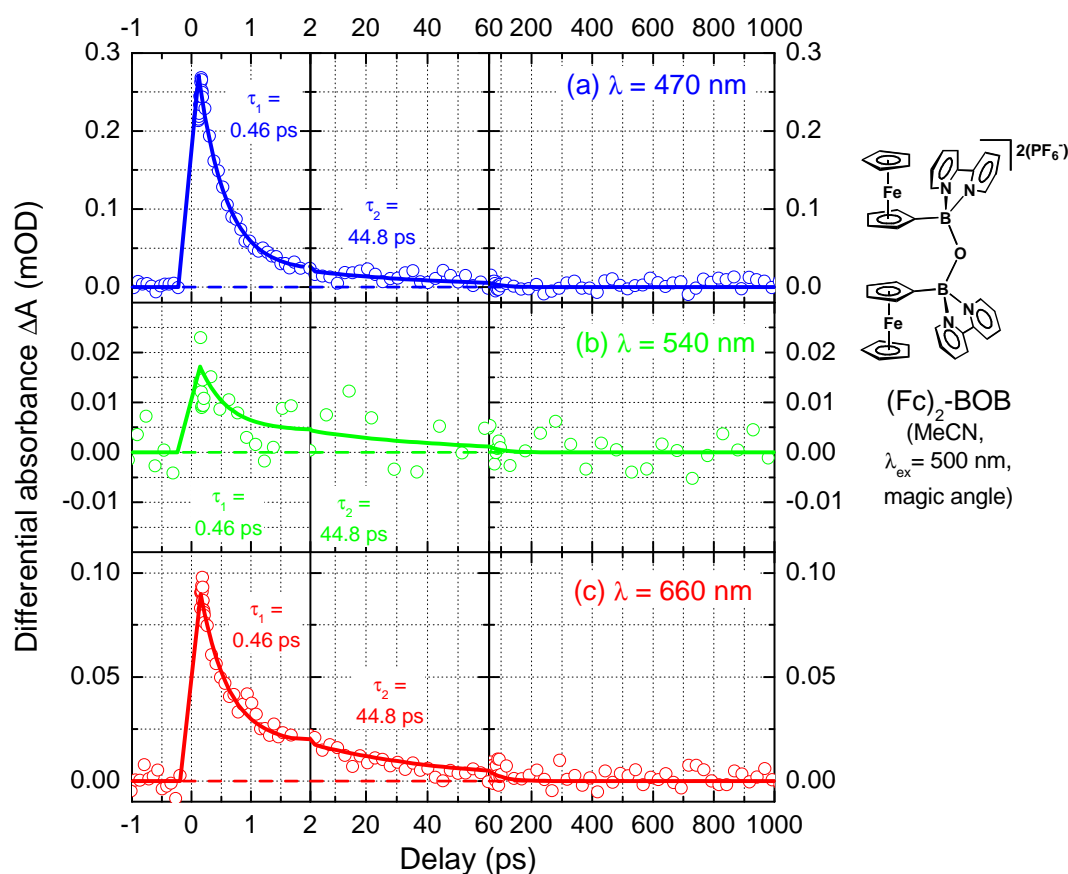


Figure 5.6.: Transient absorption kinetics for $(\text{Fc})_2\text{BOB}$ (in CH_3CN) following excitation at $\lambda_{\text{ex}} = 500 \text{ nm}$ for selected probe wavelengths (a) $\lambda = 470 \text{ nm}$, (b) $\lambda = 540 \text{ nm}$ and (c) $\lambda = 660 \text{ nm}$ (relative pump-probe polarisation: magic angle). Global time scales (when employed for each probe wavelength) as indicated.

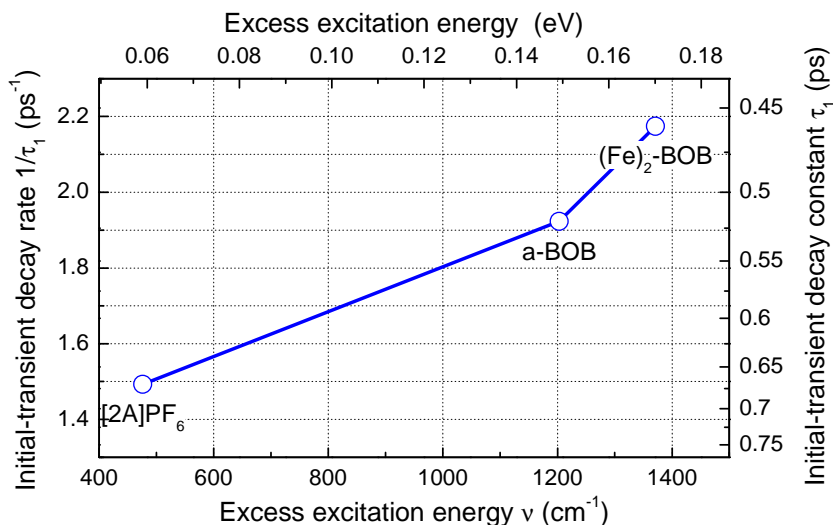


Figure 5.7.: Comparison of initial sub-ps decay rates for **[2A](PF₆)₂**, **a-BOB** and **(Fc)₂BOB** (obtained from global time constant fitting for each derivative) vs excess excitation energy (i.e. obtained from $\lambda_{\text{ex}} = 500$ nm MLCT band peak position)

for medium-sized polyatomic solutes and polar solvent reorientation are generally observed on such time scales of 0.1-1 ps [228, 229]. Moreover, we note that the time constant τ_1 decreases as we go from **[2A](PF₆)₂** \rightarrow **a-BOB** \rightarrow **(Fc)₂BOB**, whilst from Figure 5.2(d) we see that the MLCT band peak position shifts to progressively lower energy (with respect to the pump wavelength $\lambda_{\text{ex}} = 500$ nm) in this same order. Hence the excess vibrational energy of the initial excited state increases in the order **[2A](PF₆)₂** \rightarrow **a-BOB** \rightarrow **(Fc)₂BOB**, which is consistent with the observed increase in the fitted rates $1/\tau_1$ for the sub-ps transients. In Figure 5.7 we show a plot of these decay rates ($1/\tau_1$) against a proportional measure of the relative excess excitation energy $\Delta\nu_{\text{ex}}$ (taken as the difference between the centre wavenumber of the pump spectrum and the MLCT band peak position, i.e. $\Delta\nu_{\text{ex}} = 1/\lambda_{\text{ex}} - 1/\lambda_{\text{max}}$) for each derivative.

Given that the estimated Stokes shift for the MLCT band of **[1A]X** (i.e. excess initial excited-state vibrational energy upon excitation at the MLCT band peak) was determined to be large ($\Delta E_{\text{FC}} > 0.81$ eV $\cong 6490$ cm^{-1} , see Section 4.5.2) compared to the range of additional excess energies here ($\Delta\nu_{\text{ex}} \cong 470 - 1370$ cm^{-1}), it is interesting that such a strong dependence is observed and suggests that the observed trend in these sub-ps transients may also be affected by inherent differences in the excited-state potential surface for each derivative. This question should be studied in future measurements of these sub-ps transients vs excitation wavelength. For all derivatives, the amplitudes of the sub-ps transients are generally positive (except for **[2A](PF₆)₂**, $\lambda = 540$ nm), and much larger for $\lambda = 470$ nm and $\lambda = 660$ nm than for $\lambda = 540$ nm, indicating that these transients are associated with transient excited-state absorption accessible in the initial hot excited state, and not partial relaxation to the ground state. Hence, we concentrate in the following on the 1-2 longer time scales in discussing the relaxation to the ground state.

For **[2A](PF₆)₂**, the near-degenerate (predominant bleach) transient absorption decay ($\lambda = 540$ nm, Figure 5.4(b)) is composed of a nearly 1:1 combination of the two longer global time scales ($\tau_2 = 18.3$ ps, $\tau_3 = 913$ ps, $A_{02} : A_{03} = -0.49 :$

–0.51). Similar values are obtained at the blue-edge of the predominant bleach band ($\lambda = 470$ nm, Figure 5.4(a)) ($A_{02} : A_{03} = -0.52 : -0.48$). Most striking of all in the kinetics for **[2A](PF₆)₂** is that the predominant ESA-II signal ($\lambda = 660$ nm, Figure 5.4(c)) decays completely on the shorter of the two time scales ($\tau_2 = 18.3$ ps), which indicates that following the initial sub-ps relaxation, an additional significant relaxation process occurs on this 18.3 ps time scale. In general, this could be related to (i) a strong displacement in reaction coordinates away from the initially-equilibrated excited state⁵ due to slower conformational dynamics whilst remaining in the same (adiabatic) electronic state, or a non-radiative transition to either (ii) an intermediate electronic state or (iii) return to the electronic ground-state. We will return to a discussion of these possibilities in presenting the proposed relaxation models in the next section.

For **a-BOB** the two longer time scales are $\tau_2 = 5.4$ ps and $\tau_3 = 779$ ps, i.e. with τ_2 significantly smaller than that for **[2A](PF₆)₂** although with a comparable time scale for the complete ground-state recovery τ_3 (note the associated 1- σ errors for these fitted time constants in Table 5.1). Whilst the faster of these two time scales contributes significantly to the blue-edge ($\lambda = 470$ nm, Figure 5.5(a)) and ESA-II ($\lambda = 660$ nm, Figure 5.5(c)) kinetics (with $A_{02} : A_{03} = -0.3 : -0.7$ and $A_{02} : A_{03} = -0.45 : -0.55$, respectively), no detectable τ_2 -component is present in the predominant-bleach signal⁶ ($\lambda = 540$ nm, Figure 5.5(b)). This indicates that despite some additional excited-state dynamics on this τ_2 -time scale for **a-BOB**, the nature of the excited state remains relatively constant, and all relaxation to the ground state occurs on the longer $\tau_3 = 779$ ps time scale. Combined with the fact that more than half of the ESA-II signal persists on the τ_3 -time scale (in stark contrast to **[2A](PF₆)₂**), we are led to conclude that the relaxation dynamics for **a-BOB** following initial equilibration are confined to a only small rearrangements in a single excited electronic state.

For **(Fc)₂BOB** (Figure 5.6), a third distinct behaviour in the relaxation dynamics is observed. In this case, following equilibration, all kinetics decay completely on a single $\tau_2 = 44.8$ ps time scale. This indicates that complete ground-state recovery due to non-radiative decay⁷ occurs on this relatively fast time scale. The fact that the flexible **(Fc)₂BOB** can reach a conformation where such an efficient non-radiative coupling to the ground-state occurs will be used in the next section to aid in the interpretation of the relaxation dynamics for **[2A](PF₆)₂**.

5.4. Interpretation of time-resolved data and proposed relaxation models

In this section, we discuss the observed transient-absorption data in more detail, and attempt to develop a more explicit model of the excited-state relaxation dynamics for each derivative consistent with the observed kinetics/spectra.

We note that the foundations for a rigorous model of the excited-state electronic and conformational dynamics would require extensive investigation of a wider range of derivatives and test compounds, and information from other time-resolved spectroscopies (e.g. optical-pump infrared-probe). In addition, extensive (ground- and excited-state) theoretical calculation would be required to identify all possible ac-

⁵Note that we will use the term ‘initially-equilibrated excited state’ to describe the situation directly following the initial sub-ps transient.

⁶More precisely, the inclusion of the τ_2 component did not assist in measurably reducing the misfit of the **a-BOB** transient absorption curve for $\lambda = 540$ nm.

⁷Note that considering the MLCT absorption strength, any radiative decay times for these compounds is expected to be on a far longer time scale, $\gg 1000$ ps [230].

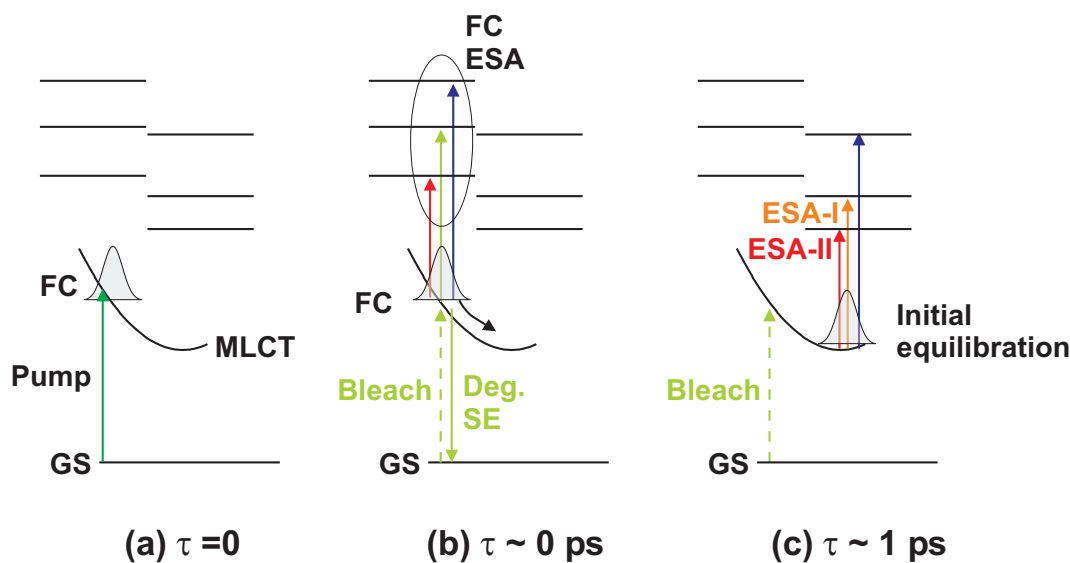


Figure 5.8.: Schematic representation of the excited states and resulting signal components during the initial relaxation following excitation. (a) Excitation. (b) Initial Franck-Condon (FC) wavepacket, and corresponding transient ESA signals (FC-ESA), ground-state depopulation (bleach) and degenerate stimulated emission (SE). (c) Wavepacket following initial equilibration, and ps-time-scale signal components (see Figure 5.2).

tive degrees of freedom and the dependence of the excited state(s) on these coordinates for each derivative.

Hence, we must confine ourselves to a more qualitative approach, i.e. constructing minimalistic schematic reaction-coordinate-energy diagrams consistent with the observed transient-absorption data without an explicit description of the exact nuclear motion corresponding to each reaction coordinate. Moreover, whilst the transient spectra appear to be composed of a small number of ESA bands (which we have assigned to analogous electronic transitions in the oxidised/reduced compounds), we stress the fact that with such broad, featureless transient spectra, there may well be additional superposed ESA bands (with their own specific temporal behaviour) which would complicate the situation and possibly lead to modified relaxation models and interpretation to that presented here [231, 232]. Nevertheless, the approach employed here will serve to clarify the proposed relaxation mechanisms that may be present in these systems, and provide a reference for future theoretical/experimental investigation.

We begin by addressing the sub-ps transient absorption signals present in the measured kinetics of $[2\mathbf{A}](\mathbf{PF}_6)_2$ (Figure 5.4), $\mathbf{a-BOB}$ (Figure 5.5) and $(\mathbf{Fc})_2\mathbf{BOB}$ (Figure 5.6). As presented in the last section, all derivatives exhibit large-amplitude transient ESA signals with decay times in the range 0.46 – 0.67 ps (see Table 5.1). These time scales are typical for both (i) intra-molecular cooling of excited vibrational modes that are displaced from equilibrium in the Franck-Condon excited state (with the vibrational energy being redistributed into the large number of other modes present in the polyatomic molecule), and (ii) reorientation of the solvent (and corresponding coupling with the internal motion) due to the new electron distribution in the excited-state. Given the appreciable magnitude of both the Stokes shift and solvent reorganisation energies for the Fc-B-bpy systems (Section

4.2.2 and 4.5.2), we can expect both to contribute significantly to the observed sub-ps transient behaviour.

In Figure 5.8, we present a schematic of the sub-ps development of the initial excited state and the relevant contributions to the transient signals. In Figure 5.8(a), the Franck-Condon excited state (prepared by absorption of the pump photon) will rapidly dissipate the excess vibrational energy, corresponding to a downhill propagation of the depicted wavepacket along the relevant reaction coordinates.

We note that the relatively large sub-ps transient-absorption changes for each derivative imply that the accessible electronic transitions to higher excited states changes significantly during this initial equilibration (and that these initial accessible transitions possess a far larger transition dipole moment). In Figure 5.8(b) we indicate the corresponding accessible ESA transitions in the Franck-Condon region (FC-ESA). Moreover, in the FC state, we expect two additional negative-differential contributions in the transient spectra, due to the ground-state depopulation (which corresponds to our working definition of ‘bleach’) and an equal contribution from degenerate stimulated emission (SE) of the initial excited-state population⁸. Whilst the ‘bleach’ component persists until ground-state recovery is achieved, for the current systems where a large displacement occurs during the initial equilibration, the degenerate-SE signal is expected to decay during the initial relaxation.

In a fluorescent dye (where radiative coupling to the ground state remains significant even after cooling, and generally only small Stokes shifts are involved) this is usually accompanied by the emergence of red-shifted negative-differential absorption, i.e. non-degenerate stimulated emission, which acquires the spectral form of the fluorescence spectrum. However, in the Fc-B-bpy systems under study, the degree of rearrangement is expected to be large, and the initially-equilibrated state may possess a far weaker radiative coupling to the ground state, such that no red-shifted stimulated emission signal emerges.

In inspecting the relative amplitudes of the sub-ps transients in Figures 5.4-5.6, we see at the near-degenerate probe wavelength ($\lambda = 540$ nm) the ESA transients are significantly smaller than those for $\lambda = 470$ nm and $\lambda = 660$ nm, with the actual sign of the amplitude for $\lambda = 540$ nm depending on the derivative (for **[2A](PF₆)₂** and **(Fc)₂BOB**, the amplitude represents a small net positive absorption, whilst for **a-BOB** a small net absorption decrease results). Based on the foregoing discussion, we assign these smaller amplitude transients for $\lambda = 540$ nm to a near cancellation of the FC-ESA and degenerate stimulated emission components, both of which decay with a similar time dependence as the wavepacket leaves the FC region. For the probe wavelengths $\lambda = 470$ nm and $\lambda = 660$ nm, the FC-ESA signals dominate the signals. As shown in Figure 5.8(c), after this initial rapid equilibration, the ESA components corresponding to those identified in the longer-time transient spectra in Figure 5.2 are established, and the temporal behaviour of these signals indicates the subsequent slower excited state dynamics in returning to the ground electronic state.

At this point, we address briefly the question of the delocalisation of the excitation in these double-acceptor compounds. Comparison with preliminary measurements on the single-acceptor compound **[1A]PF₆** demonstrated no significant differences in the transient-absorption spectra compared to the double-unbridged-

⁸Note that in the following discussion, we define ‘bleach’ signals as the negative-differential absorption contribution arising only from ground-state depopulation (and not degenerate stimulated emission) although in the literature both are often referred to collectively as the ‘bleach signal’, which is perhaps a more natural terminology, considering that for a idealised two level system it is their combined presence which leads to transparency of a molecular ensemble when half the molecules are excited, i.e. $n_g = n_{ex} = \frac{1}{2}n_0$.

acceptor compound $[\mathbf{2A}](\mathbf{PF}_6)_2$ (although the comparison could only be made in the > 1 ps delay range). Moreover, it has been observed for the MLCT excited states in other systems with degenerate acceptors that the excitation becomes localised on a single acceptor on a sub-ps time scale [207, 233].

A semi-quantitative theory for approaching these issues is provided from molecular exciton theory for a coupled dimer (i.e. in the case of two chromophores with a finite electrostatic interaction), when the treatment is extended to include a representative reaction coordinate for each acceptor with a Stokes shift for the electronic transition [44] (as opposed to pure electronic wavefunctions).

In this treatment, the fact that the excited-state energy of the two chromophores (before including their coupling) can possess non-degenerate energies (through their respective dependence on distinct reaction coordinates) leads to symmetry-breaking in the coupled system, such that the delocalisation of the two coupled-dimer wavefunctions decreases as the difference in the reaction coordinates (and hence energies) of the two chromophores increases. This in turn leads to one excited-state dimer wavefunction that is lower in energy (i.e. the one more localised on the chromophore with the more energetically favourable reaction coordinate). This state is even further stabilised by increasing the difference between the reaction coordinates of the two chromophores. In the ‘weak-coupling’ case (where the magnitude of the Stokes shift is much larger than the inter-chromophore coupling), this type of instability leads to two minima in the excited-state energy surface, i.e. where the excitation is completely localised on one chromophore (at the excited-state equilibrium geometry), whilst the other chromophore is in its ground electronic state (and ground-state equilibrium geometry). This situation is depicted in Figure 5.9, which shows both the degenerate ground-state minimum and the two symmetric localised-excitation minima in the excited-state.

Given the analogy to the case of a donor with two identical acceptors, this suggests that dynamic localisation of the MLCT excitation on a single acceptor will occur in the case of $[\mathbf{2A}](\mathbf{PF}_6)_2$ (and presumably for $\mathbf{a-BOB}$ and $(\mathbf{Fc})_2\mathbf{BOB}$), where the energy changes due to conformational rearrangement in the excited state are significantly larger than the magnitude of the inter-acceptor coupling (Section 4.4 and 4.5.2). Since we expect this localisation to occur on the time scale of the initial conformational changes, it is quite likely that this dynamic localisation occurs during the initial equilibration, i.e. that the MLCT excitation is localised on a single acceptor after 1 ps. This time-scale is consistent with that reported for other MLCT compounds [207, 233].

We turn now to the relaxation dynamics that occur after the initial equilibration, i.e. on the time scales τ_2 (and τ_3 for $[\mathbf{2A}](\mathbf{PF}_6)_2$ and $\mathbf{a-BOB}$). As described in the last section, for $[\mathbf{2A}](\mathbf{PF}_6)_2$ the near-degenerate transient absorption signal ($\lambda = 540$ ps) decays on two time scales $\tau_2 = 18.3$ ps and $\tau_3 = 913$ ps with approximately equal amplitudes for the two components ($A_{02} : A_{03} = -0.49 : -0.51$), with a similar ratio for the $\lambda = 470$ ps kinetics ($A_{02} : A_{03} = -0.52 : -0.48$). Moreover, the ESA-II signal decays completely on the shorter τ_2 time scale, indicating that the wavepacket leaves the initially-equilibrated region completely, into a reaction coordinate region where the ESA-II transition no longer possesses an appreciable transition dipole moment, which could involve an distinct intermediate electronic state. We will refer to this new excited-state situation as the ‘intermediate state’ (IS).

We note that the τ_2 decay of the predominant bleach signal (both at $\lambda = 470$ nm and 540 nm) could in general be due to one of two influences: (i) the presence of a new ESA signal for the IS in this wavelength range, or (ii) return of a portion of the wavepacket to the ground-state (due to the encounter with a near-crossing

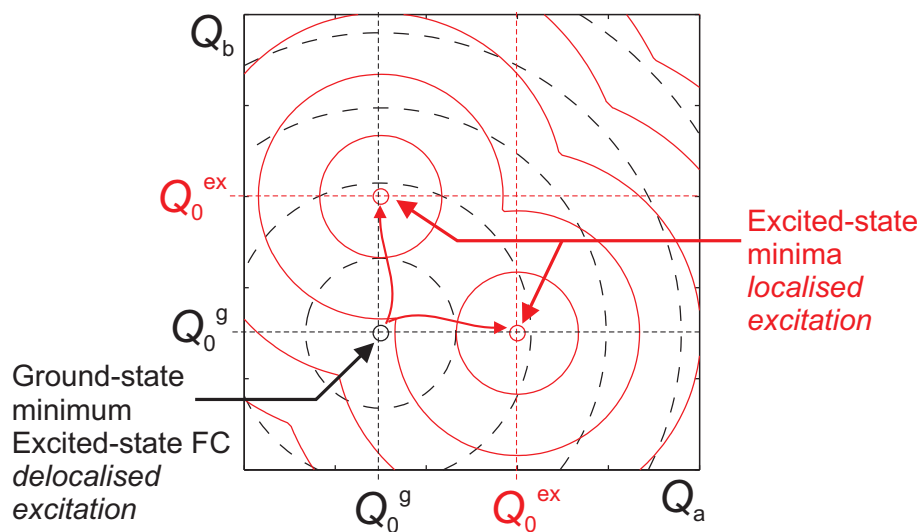


Figure 5.9.: Qualitative reaction-coordinate energy diagram for a system with two weakly-interacting acceptors (a,b) compound, indicating the motion from the ground-state equilibrium (i.e. Franck-Condon coordinates directly following excitation) ($Q^a = Q^b = Q_0^g$) where the MLCT excitation is delocalised on both acceptors, towards one of two degenerate excited-state minima (e.g. ($Q^a = Q_0^{ex}$, $Q^b = Q_0^g$)) where the excitation is localised on a single acceptor. (Adapted from [44]).

or conical intersection with the ground state energy surface). However, from an inspection of the relevant transient spectra for $[2\mathbf{A}](\mathbf{PF}_6)_2$ (Figure 5.2(a)), for $\tau \leq 100$ ps there is no evidence for the emergence of a new ESA band that could account for case (i). Hence we conclude that the τ_2 decay component in the $\lambda = 540$ nm signal is due to partial ground-state recovery (involving ~ 0.50 of the excited ensemble). The remaining fraction of the excited ensemble then reaches the IS where a far slower transition to the ground-state occurs. Due to the fact that no photoluminescence measurements were performed in the range $\lambda > 900$ nm we cannot rule out that this slower component of the ground-state recovery is due to a radiative transition. However, as discussed below in relation to the proposed reaction coordinate diagrams, if the IS for $[2\mathbf{A}](\mathbf{PF}_6)_2$ corresponds to an excited-state equilibrium strongly displaced from the ground-state with an energy lower than the ground state for this geometry, then only non-radiative transitions can occur, due to thermal excitation to the ground-state crossing. We summarise the conclusions drawn so far for $[2\mathbf{A}](\mathbf{PF}_6)_2$ in the Jablonski diagram in Figure 5.10(a). We return to a discussion of the nature of the conformational dynamics below.

From the transient absorption data, the interpretation of the relaxation dynamics of $\mathbf{a-BOB}$ and $(\mathbf{Fc})_2\mathbf{BOB}$ is somewhat more straightforward. For $\mathbf{a-BOB}$, whilst there is a finite decay component in the transient-absorption kinetics for $\lambda = 470$ nm (blue-edge of bleach band) and 660 nm (ESA-II) on a $\tau_2 = 5.4$ ps time scale, there is no evidence for any ground-state recovery in the predominant bleach signal ($\lambda = 540$ nm). Moreover, as less than half the ESA-II signal decays on this time scale, this indicates that these τ_2 -dynamics involve only a small conformational change to a slightly displaced IS which affects the strength of the ESA transitions. The subsequent decay of all transient-absorption kinetics on the $\tau_3 = 779$ ps time scale implies that from this IS, there is a single slower mechanism for coupling to the ground-state (as per the slower relaxation of $[2\mathbf{A}](\mathbf{PF}_6)_2$). A

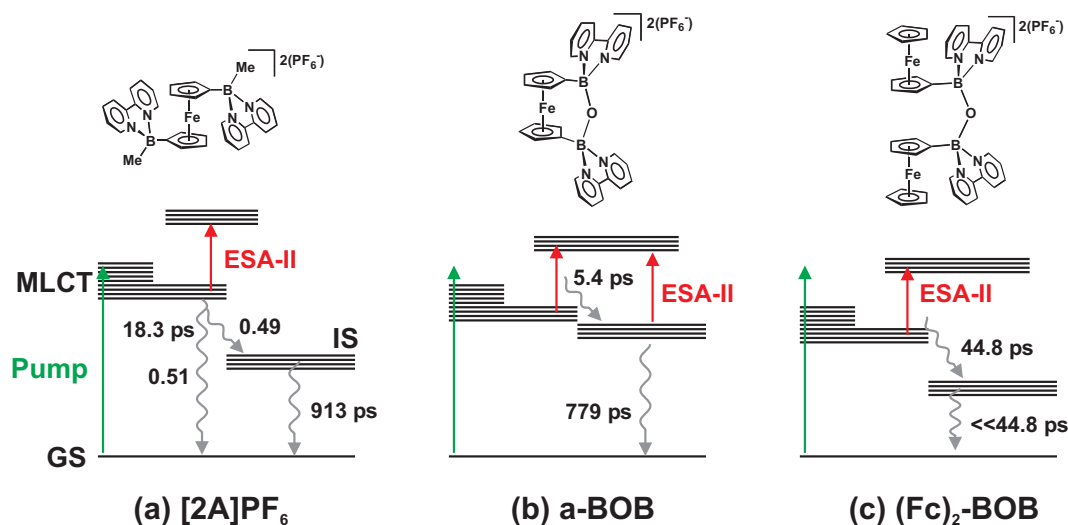


Figure 5.10.: Jablonski diagram depicting the proposed excited-state relaxation behaviour and time scales (following initial equilibration) for each derivative (a) $[2\mathbf{A}](\text{PF}_6)_2$, (b) $\mathbf{a}\text{-BOB}$ and (c) $(\mathbf{Fc})_2\text{BOB}$. In (a), the wavepacket-splitting fractions (deduced from the global fit of the kinetics and the proposed model) are indicated (0.49,0.51).

representation of these relaxation steps is given in Figure 5.10.

For $(\mathbf{Fc})_2\text{BOB}$, the fact that only a single exponential decay with $\tau_2 = 44.8$ ps is present in the kinetics following the initial equilibration signifies that the entire excited-state ensemble evolves to a conformation where efficient coupling to the ground state occurs, with no trapping of a fraction of the excited-state ensemble in an IS with a slower ground-state recovery time. We note that because the ESA-II ($\lambda = 660$ nm) signal decays on the same time scale as the bleach signal, this implies that the ground-state recovery occurs promptly as the wavepacket leaves the initially-equilibrated state, due to encountering a conformation where a highly efficient non-radiative transition to the ground state (i.e. a near-crossing or conical intersection) occurs. The corresponding Jablonski diagram for $(\mathbf{Fc})_2\text{BOB}$ is given in Figure 5.10.

The fact that complete ground state recovery occurs with sub-nanosecond time constants for all the derivatives presented here, tends to rule out the occurrence of an intersystem crossing (i.e. singlet-triplet conversion, $S_1 \rightarrow T_1$) in the MLCT excited state. Although ‘forward’ intersystem crossing can occur for MLCT excited states in medium-sized organometallic compounds on even sub-picosecond time scales [207], the resulting triplet state generally has a lifetime of at least 10’s of ns (and typically in the range of μs) [37].

Up to this point, we have constructed schematic Jablonski diagrams to provide an overview of the proposed relaxation pathways of the MLCT state. In concluding this chapter, we attempt to specify the situation more explicitly in terms of the conformational dynamics associated with the identified relaxation pathways. Given that there is evidence for a very rapid internal conversion between the excited- and ground-state potential energy surfaces for $[2\mathbf{A}](\text{PF}_6)_2$ and $(\mathbf{Fc})_2\text{BOB}$, it is our working hypothesis that the excited-state wavepackets encounter, or closely approach, a conical intersection during their relaxation, which have been shown recently to be far more likely than avoided crossings in polyatomics of this size (once it is established that a close approach of the potential surfaces exists), based

on a general formal treatment [40]. In constructing a minimalistic potential energy diagram we employ schematic diagrams involving two active reaction coordinates [37, 38].

A schematic of the proposed potential energy surfaces for **[2A](PF₆)₂** is depicted in Figure 5.11 (note that certain likely conformational modes that may be active in the relaxation dynamics are indicated on the 2D structure in the figure). In this model, following the initial equilibration, a slower (i.e. more weakly driven) conformational change along a coordinate Q_2 occurs on a $\tau_2 = 18.3$ ps time scale, which corresponds to the propagation of the wavepacket along a path where it encounters an intersection with the ground state potential surface. Given that rotation about the B-C(Cp) bond would reasonably be expected to lead to significant changes in the electronic coupling between the ground (D-A⁺) and excited state (D-A⁺)⁹, due to the large resulting change in the D-A separation, we propose that the reaction coordinate Q_2 corresponds to a form of motion which involves the B-C(Cp) bond rotation. In general the excited-state potential (in solution) should be modified significantly with respect to the gas-phase ground-state potential involving the B-C(Cp) bond rotation calculated in Section 4.6 (which possessed a fundamental vibrational period estimated as $2\pi/\omega_\theta \sim 3$ ps). If we assume that the excited-state potential is significantly ‘flattened’ relative to the ground-state potential, then B-C(Cp) rotation in the excited state on a time scale of $\tau_2 = 18.3$ ps would be a reasonable value.

We anticipate that other relatively ‘loose’ degrees of freedom e.g. involving tilting of the B-bpy planes and counter-rotation of the Cp-rings of the Fc will also affect the energy of the excited state, such that the conical intersection occurs with respect to the B-C(Cp) bond rotation and another coordinate, Q_1 , based on these other degrees of freedom. As depicted in Figure 5.11, we assume that only a fraction (0.51) of the wavepacket is directed to the ground (diabatic) state, whilst the remaining fraction (0.49) continues to propagate to a lower, displaced excited-state minimum (IS). From this position, the only available mechanism for ground-state recovery is through thermal/solvent-induced activation to the ground-state intersection with a characteristic time scale of $\tau_3 = 913$ ps.

For the case of **a-BOB**, the fact that all ground-state recovery is observed on the $\tau_3 = 779$ ps time scale indicates that no close approach to the ground-state potential surface occurs in the excited state. This is reasonable in comparison to our proposed model for **[2A](PF₆)₂**, where significant rotation of the B-C(Cp) bond along a relatively unconstrained potential curve was required in order to reach the conical intersection. The corresponding ground-/excited-state potential energy curves along this coordinate for **a-BOB** will instead feature extreme energetic barriers beyond a certain degree of B-C(Cp) rotation (due to significant bond stretching).

However, due to the fact that **a-BOB** still possesses a finite flexibility of the B-C(Cp) bond (with a concerted bending of the B-O-B bridge and counter-rotation of the Cp rings of the Fc-unit), it is plausible that small scale motion along this reaction coordinate occurs after initial equilibration on the $\tau_2 = 5.4$ ps time scale, which leads to the changes observed in the ESA signals on this time scale. Hence we propose the schematic potential energy surfaces for **a-BOB** in Figure 5.12, where the wavepacket proceeds on a 5.4 ps time scale along Q_2 to a more stable, distorted, excited-state IS, from where relaxation to the ground state occurs on

⁹Note that it would be hazardous to draw strong conclusions about the excited-state coupling between donor and acceptor vs the B-C(Cp) rotation angle from the ground-state HOMO/LUMO theoretical DFT results in Section 4.6, which did not show any strong dependence of the donor-acceptor HOMO-LUMO overlap upon rotation of the B-C(Cp) bond.

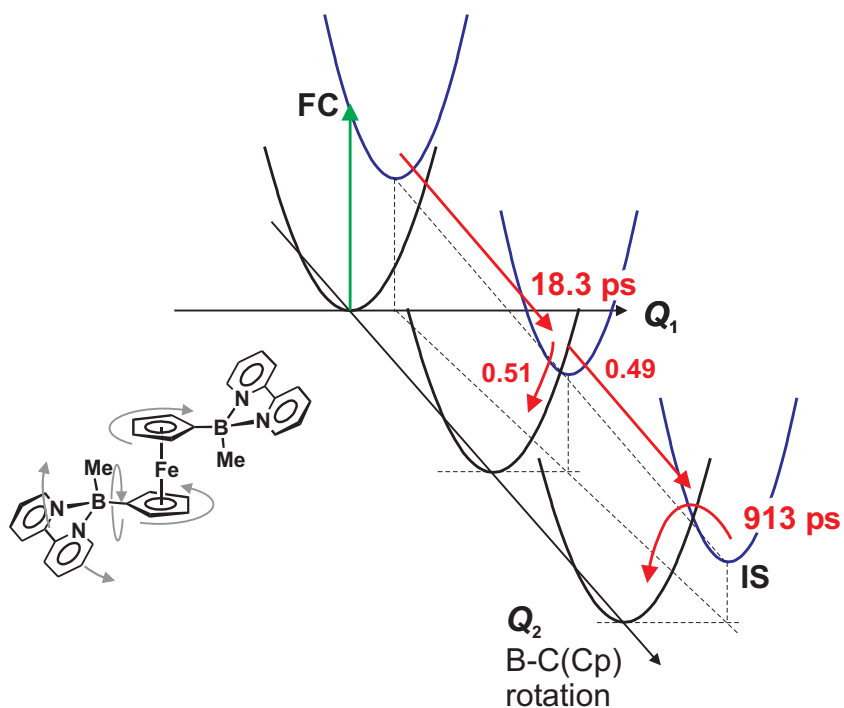


Figure 5.11.: Schematic reaction coordinate diagram to describe proposed relaxation dynamics of $[2A](PF_6)_2$. Relatively unhindered rotation about the B-C(Cp) bond (Q_2) on an 18.3 ps time-scale takes wavepacket to a metastable intermediate state (IS) (with non-radiative decay to the ground-state on a ~ 913 ps time scale) via a conical intersection to the ground state.

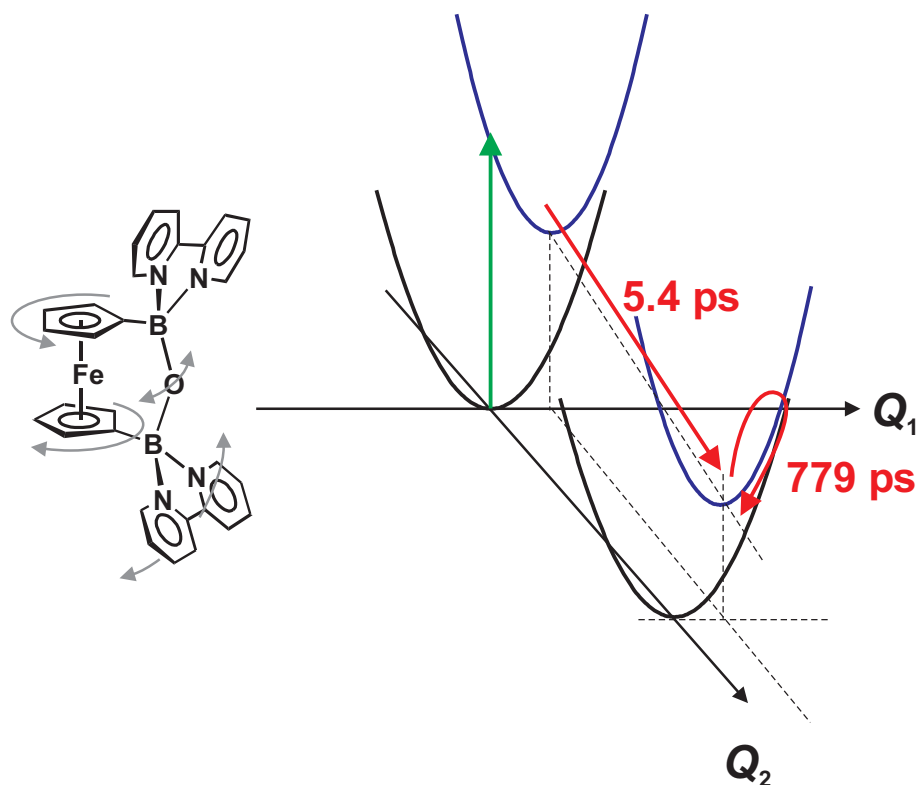


Figure 5.12.: Schematic reaction coordinate to describe proposed relaxation dynamics of **a-BOB**. Following small scale excited-state rearrangement on a ~ 5.4 ps time-scale, wavepacket reaches metastable intermediate state (with non-radiative decay to the ground-state on a 779 ps time scale). Close intersections with the ground-state potential are prevented due to the limited motion enforced by the ansa-bridge.

the slower $\tau_3 = 779$ ps time scale. We note that based on the schematic in Figure 5.12, where the displacement of the reaction coordinate Q_1 is far smaller than for $[\mathbf{2A}](\mathbf{PF}_6)_2$ (due to the limited motion along Q_2), it is possible that this IS is still energetically higher than the corresponding ground-state potential. Hence both non-radiative and radiative coupling to the ground state would be possible. As mentioned earlier, an important future measurement would be to perform sensitive near-IR luminescence measurements (in the range $\lambda > 900$ nm) to see if any radiative relaxation is observed for **a-BOB**.

For the case of $(\mathbf{Fc})_2\mathbf{BOB}$, we propose the situation shown in Figure 5.13. In the case of $(\mathbf{Fc})_2\mathbf{BOB}$, the additional relatively unhindered degrees of conformational freedom (involving bending and twisting of the loose B-O-B bridge) will result in an effective reaction coordinate Q_2 composed of several forms of motion, in addition to rotation about the B-C(Cp) bonds. We assume then that motion along this complex hybrid coordinate towards a conical intersection is less direct than for $[\mathbf{2A}](\mathbf{PF}_6)_2$ (or involving a greater inertia for the conformational rearrangement), such that the time scale for reaching the intersection is slowed down (relative to $[\mathbf{2A}](\mathbf{PF}_6)_2$) to the observed time scale of $\tau_2 = 44.8$ ps. Moreover, unlike $[\mathbf{2A}](\mathbf{PF}_6)_2$, we assume that the region where an intersection to the ground state potential occurs corresponds to a point near the minimum in the excited-state potential, such that complete non-radiative relaxation to the ground state results, without any fraction reaching a displaced excited-state minimum where slower relaxation takes place.

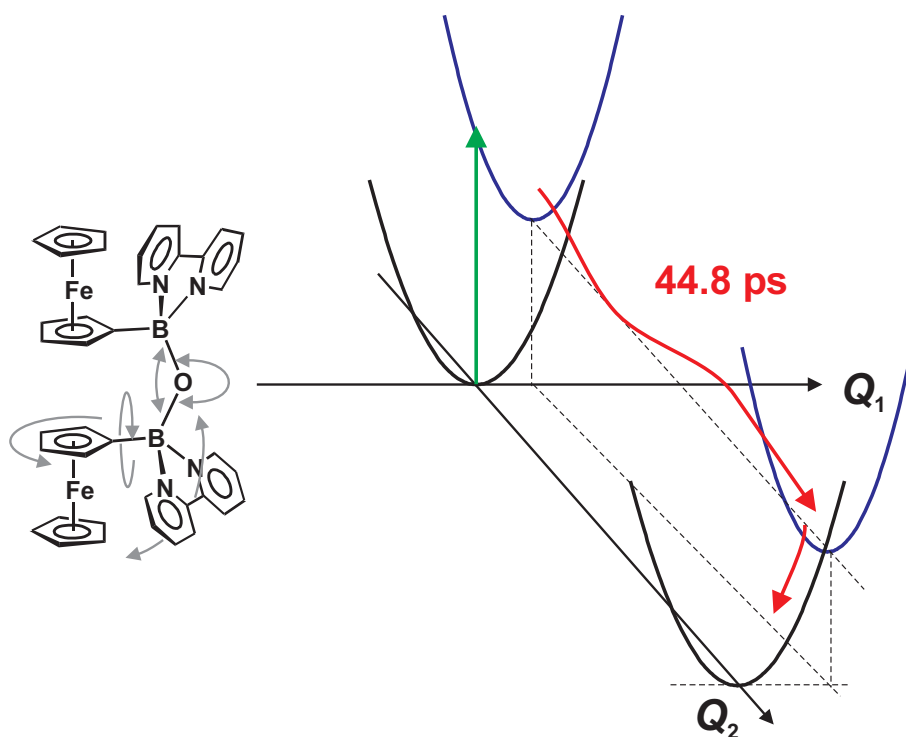


Figure 5.13.: Schematic reaction coordinate to describe proposed relaxation dynamics of $(\text{Fc})_2\text{BOB}$. Following significant rearrangement on a 44.8 ps time-scale, wavepacket reaches metastable intermediate state with conical intersection to ground-state. Note that the reaction coordinates Q_j are not assumed to be normal-mode coordinates.

In summary, from the experimental data and proposed models for the relaxation dynamics of the three derivatives presented here, we can draw several conclusions. (1) The correlation between the MLCT excited-state transient-absorption spectra for $[\mathbf{2A}](\mathbf{PF}_6)_2$ and $\mathbf{a-BOB}$ and the absorption bands of the corresponding oxidised/reduced species strongly supports that the MLCT excited state involves an almost complete transfer of an electron from the Fc-donor to the B-bpy-acceptor(s). (2) The electronic effects of the B-O-B bridge connecting the two acceptors in $\mathbf{a-BOB}$ and $(\mathbf{Fc})_2\mathbf{BOB}$ does not result in any clear characteristic differences in the relaxation dynamics in comparison to $[\mathbf{2A}](\mathbf{PF}_6)_2$. This may be due to the fact that upon excitation, the excited-state wavefunction becomes localised on only one of the two acceptors due to the symmetry reduction introduced from instantaneous fluctuations in the two acceptor conformations, hence leading to an electronic behaviour similar to the case of uncoupled acceptors. (3) The relatively unhindered distortion of bridging bonds for $[\mathbf{2A}](\mathbf{PF}_6)_2$ and $(\mathbf{Fc})_2\mathbf{BOB}$ (in particular, rotation of the B-C(Cp) bonds between Fc-donor and B-bpy-acceptors) is a determining factor in the relaxation to the ground-state (i.e. back-electron transfer to the Fc-donor), due to the ability of the excited-state wavepacket to encounter an efficient non-radiative coupling to the ground state. This final point indicates that in order to maximise the lifetime of the MLCT state, target derivatives should possess a rigid structure linking donor and acceptor to prevent excited-state geometry changes which lead to an encounter with efficient non-radiative decay channels.

6. Conclusions

A combined interpretation of the results and analysis presented in this work strongly support the assignment of the MLCT band in the Fc-B-bpy compounds, with the excited state involving an almost complete transfer of an electron from the Fc-donor to the B-bpy-acceptor. The key results supporting this conclusion are,

- (i) the observed solvatochromic behaviour of **[1A]Br** (Section 4.2.2), which suggests a dipole moment change between the ground and excited state corresponding to the displacement of the molecular electron density by an amount approaching the donor-acceptor separation upon optical excitation,
- (ii) the correlation between redox potentials and the observed MLCT transition for a range of derivatives (Section 4.5.2),
- (iii) the nature of the theoretical frontier molecular orbitals for the prototype **[1]⁺(H)** (Section 4.6), and,
- (iv) the comparison of the UV-vis spectral changes upon electrochemical donor-oxidation/acceptor-reduction with the MLCT excited-state transient absorption spectra (Section 5.2).

A number of additional results emerge which will aid the rational design of future derivatives, for both (i) inclusion as functional pendant groups for optically-induced CT into macromolecular systems, and (ii) polymers employing the Fc-B-bpy monomers directly in the polymer backbone.

From the time-resolved transient absorption measurements, we can conclude that the degree of conformational flexibility for different Fc-B-bpy derivatives critically affects the relaxation (back-electron transfer) rate from the B-bpy acceptor to the Fc-donor, where those derivatives with flexible linkage between donor and acceptor (i.e. **[2A](PF₆)₂** and **(Fc)₂BOB**) undergo partial (or complete for **(Fc)₂BOB**) relaxation on a time scale of $\sim 18 - 45$ ps, whilst for the derivative **a-BOB** with a constraining chemical bridge between the two acceptors, the ground-state recovery occurs only on a 770 ps time scale. This strong dependence of relaxation time vs structural rigidity can be traced to the presence of efficient non-radiative relaxation pathways (potential energy surface-crossings) to the ground state, which involve excited-state geometries which can only be encountered for those compounds where significant excited-state geometric rearrangement is possible. Hence, in order to achieve longer CT lifetimes and higher efficiencies for the optically-induced injection and subsequent propagation of the transferred charge in macromolecular networks, an important design principle is to ensure a rigid molecular framework linking donor and acceptor.

A detailed comparison of the MLCT spectra of derivatives with bridged- and unbridged-acceptors led to a conclusion supporting significant inter-acceptor coupling between bpy-groups linked by -B-N-B and -B-O-B- bridges, which is an important factor for the design of macromolecular systems where electron transfer between acceptor groups can be employed to provide a channel for charge propagation. Moreover, from the theoretical results of the dication **[1]²⁺(H)**, there is evidence that oxidation of the Fc unit results in frontier molecular orbitals delocalised over both donor and acceptor, such that the inclusion of the oxidised Fc-B-bpy units in polymeric systems may result in a greater delocalisation over the whole Fc-B-bpy structure and hence enhance electronic-coupling between remote electronic systems connected via these Fc-B-bpy monomers.

The future direction of this research is aimed at low-dimensional solid-state systems incorporating these monomers for the optical control of electronic charge injection into delocalised electronic channels. In this respect, the synthesis of model materials, where the Fc-B-bpy compounds are attached to a well-established oligomeric/polymeric system is anticipated. An example of a such system (poly(m-phenylenefuchson)) where strong ferromagnetic interactions result from the injection of additional charge was given in the Introduction, although many possible candidate systems should be considered, where the unique synthetic advantages of B-N bonding could be explored for incorporating the Fc-donor.

In pursuit of highly efficient optically-driven CT derivatives, the existing Fc-B-bpy compounds still require additional synthetic modification to achieve a stronger MLCT absorption strength, such that the required levels of optical irradiation to maintain a significant fraction of CT excited states in the molecular ensemble can be reduced. As demonstrated in Section 2.2.2, the incorporation of conjugated π -systems into Fc-donor derivatives can lead to excellent optical properties ($\epsilon_{\max} \sim 40000 \text{ M}^{-1}\text{cm}^{-1}$, $\lambda_{\max} \sim 850 \text{ nm}$), through the participation of π -bridge electronic states in enhancing the electronic coupling between donor and acceptor via intensity borrowing. Hence the development of modified derivatives incorporating conjugated π -systems in conjunction with the B-N linkage (e.g. with the conjugated C chain linking Fc-donor and B-bpy acceptor), could result in a significant enhancement of the optical properties.

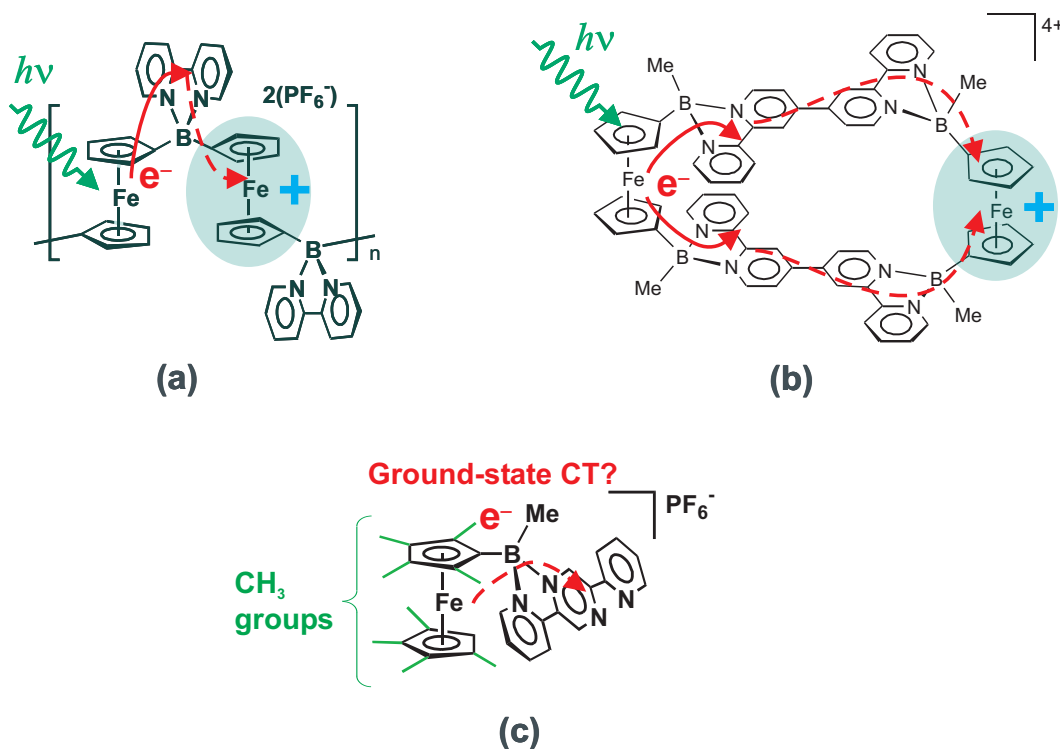


Figure 6.1.: Fc-B-bpy systems for future investigation. (a) Recently synthesised Fc-B-bpy-polymer. Possibility to prepare statistically oxidised Fc⁺-centres, such that irradiation of the MLCT band of the remaining unoxidised Fc-centres may result in photoconductivity. (b) Existing Fc-B-bpy macrocycle compounds prepared as a mixed-valence Fc/Fc⁺ pair. (c) Target Fc-B-bpy monomer with octamethylated-Fc-donor and B-dpp acceptor, where MLCT could occur in the ground state.

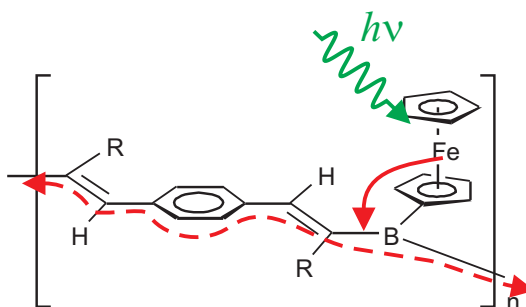


Figure 6.2.: Target polymers containing Fc-donors attached to *tri*-coordinated B-atoms integrated into the polymer π -system backbone.

Very recently, the successful synthesis of the Fc-B-bpy-based polymer (Figure 6.1(a)) has been achieved within the group of our synthetic collaborators (AG Wagner, Anorganische Chemie, J. W. Goethe-Universität, Frankfurt am Main), and is currently undergoing preliminary characterisation. As depicted in Figure 6.1(a), one anticipated area for study involves preparing a statistical mixture of oxidised Fc^+ -centres along the polymer backbone (either by chemical or electrochemical means). In this case, excitation of the MLCT band of remaining unoxidised Fc-centres will allow for electron transfer along the polymer backbone (i.e. photoconductivity) in the presence of an external bias field. Similar parallel studies of the existing Fc-B-bpy macrocycle compounds (Figure 6.1(b)), involving optically-induced CT between a mixed-valence Fc/ Fc^+ pair will also be useful in investigating the possible transfer of charge between two Fc-centres following MLCT excitation. The application of ultrafast time-resolved optical studies will be particularly suited to probe the processes following MLCT excitation in these systems.

In terms of interesting possible magnetic phenomena, the synthesis of a modified Fc-B-bpy compound with an octamethylated-Fc donor (OMFc) and B-dpp acceptor (Figure 6.1(c)) is being considered. As discussed in Section 4.5.2, there is some indication that for this compound (with a significantly destabilised OMFc-donor HOMO and stabilised B-dpp acceptor LUMO) the MLCT state might well be the ground state of the system. In such a case, this ground state would be composed of both a cationic radical Fc^+ and anionic radical B-dpp^- which could interact either ferro- or antiferromagnetically [18].

In parallel with the future development of materials with tetra-coordinated-B linkage, current work with our synthetic collaborators is underway to produce polymers incorporating *tri*-coordinated-B in the backbone, with Fc attached as a pendant group to the B atom, such as the structure shown in Figure 6.2. In these systems, the empty p-orbital of the B atom allows it to participate in electronic states delocalised along the polymer chain, as suggested from studies of related polymers [234]. We anticipate that the CT excitation of the Fc-group should result in optical injection of an electron into the delocalised states on the polymer backbone. Future time-resolved optical studies will also be applied to these systems.

A. Auxiliary spectroscopic data and results

A.1. Solvent data for solvatochromism analysis

Table A.1 gives the relevant solvent parameters [50], including effective solvent dimensions determined by analysis of 3D solvent approximate solvent structures and dipole moments obtained from www.nist.gov/srd. Figure A.1 shows the solvent polarity functions $\varphi(\epsilon_s)$ and $\varphi(n^2)$ as defined in Eq. B.102 for the solvents employed in the solvatochromism study of **[1A]Br** in Section 4.2.2.

Solvent		Property						
Name	Formula	Optical refractive index n	Static dielectric constant ϵ_s	Dipole moment μ (D)	Density ρ (kg m ³)	Molar mass M (g mol ⁻¹)	Average van der Waals radius (Å)	Van der Waals radius $\perp \mu$ (Å)
Water	H ₂ O	1.333	80.1	1.85	1	18.02	1.35	1.59
N,N'-dimethylformamide	DMF	1.4305	36.7	3.82	0.944	73.09	2.54	3.22
Acetonitrile	CH ₃ CN	1.3442	37.5	3.52	0.7857	41.05	2.07	2.85
Chloroform	CHCl ₃	1.4459	4.806	1.04	1.489	119.38	2.52	2.31
Dichloromethane	CH ₂ Cl ₂	1.4242	8.93	1.6	1.3266	84.93	2.33	2.28
Dimethylsulfoxide	DMSO	1.4785	47.24	3.96	1.1014	78.14	2.51	2.81

Table A.1.: Refractive index, $\lambda = 589$ nm) static dielectric constant (ϵ_s) data for the solvents employed in the study of the Fc-B-bpy compounds [50].

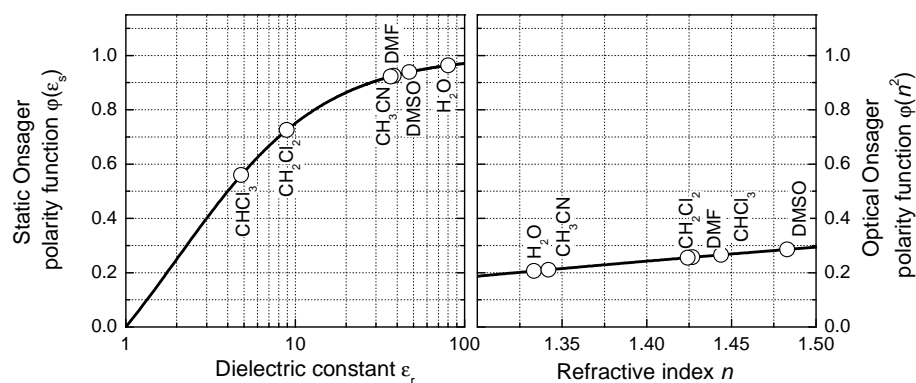


Figure A.1.: Onsager polarity functions $\varphi(\epsilon_s)$ and $\varphi(n^2)$ for the solvents used in the solvatochromism study of **[1A]Br** in Section 4.2.

A.2. Fc-B-bpy UV-vis absorption data and fitted band parameters

A complete listing of the fitted MLCT and HE bands for the Fc-B-bpy compounds is given in Table A.2.

Compound	Solvent	MLCT band						HE band				
		λ_{\max} (nm)	ϵ_{\max} ($M^{-1}cm^{-1}$)	λ_0 (nm)	ϵ_0 ($M^{-1}cm^{-1}$)	$\Delta\nu_{FWHM}$ (cm^{-1})	f	λ_0 (nm)	ϵ_0 ($M^{-1}cm^{-1}$)	$\Delta\nu_{FWHM}$ (cm^{-1})	α	f
[1A]Br	CH ₃ CN	503.3	521	499.7	528	6220	0.015	369.4	388	6935	2.35	0.012
	DMF	494.9	433	492.5	449	6456	0.013	367.6	346	7297	2.41	0.011
	H ₂ O	484.9	370	481.8	371	6207	0.011	367.2	258	6464	2.18	0.0071
[1A]PF ₆	DMF	494.2	437	494.1	437	6345	0.013	366.6	361	7468	2.41	0.012
	CHCl ₃	527.0	520	525.1	525	5948	0.014	368.4	504	8158	2.77	0.018
	CH ₂ Cl ₂	524.3	470	523.9	470	6130	0.013	362.3	495	8979	2.46	0.019
[2A]Br ₂	CH ₃ CN	512.7	891	510.9	905	6123	0.025	365.8	813	7602	2.12	0.027
	DMF	511.7	778	511.2	799	6179	0.023	368.8	730	7704	2.44	0.026
[2A](PF ₆) ₂	H ₂ O	496.0	670	493.2	671	6208	0.019	362.7	598.1	7318	1.97	0.019
	CH ₃ CN	512.2	871	508.3	880	6255	0.025	359.6	902	7933	1.95	0.031
a-BOB	DMF	511.2	770	511.8	778	5971	0.021	372.9	678	7659	2.88	0.022
	CH ₃ CN	532.0	944	529.4	963	5260	0.023	411.2	367	7483	3.06	0.017
a-NSiMe	DMF	531.3	918	533.3	933	5065	0.022	419.9	434	5084	1.69	0.014
	CH ₃ CN	549.9	-	551.9	-	4959	-	419.9	-	5219	0.847	-
a-NPhOMe	CH ₃ CN	532.8	-	531.6	-	5753	-	378.0	-	7885	3.17	-
	CH ₃ CN	536.8	801	549.1	809	6243	0.023	381.6	1127	8510	1.99	0.059
[1C](PF ₆)	CH ₃ CN	605.4	429	604.0	429	5994	0.012	407.9	423	8213	25.57	0.022
[2A](NPhOMe)	CH ₃ CN	518.7	-	521.1	-	6104	-	348.0	-	9862	1.79	-
[2A](OH)	CH ₃ CN	522.0	-	522.3	-	5841	-	362.3	-	8552	2.29	-
[2N](PF ₆) ₂	THF	501.0	862	498.9	864	6039	0.024	367.3	757	7318	2.34	0.046
	PS film, 300 K	-	-	485.9	859	7928	(0.031)	-	-	-	-	-
	PS film, 20 K	-	-	485.2	954	8270	(0.036)	-	-	-	-	-

Table A.2.: Fitted MLCT and HE band parameters for the Fc-B-bpy derivatives.

A.3. Fc-B-bpy UV-vis spectroelectrochemical time-series

The UV-vis spectro-electrochemistry time-series data for $[1A]PF_6$ and $[2A](PF_6)_2$ is shown in Figures A.2 and A.3.

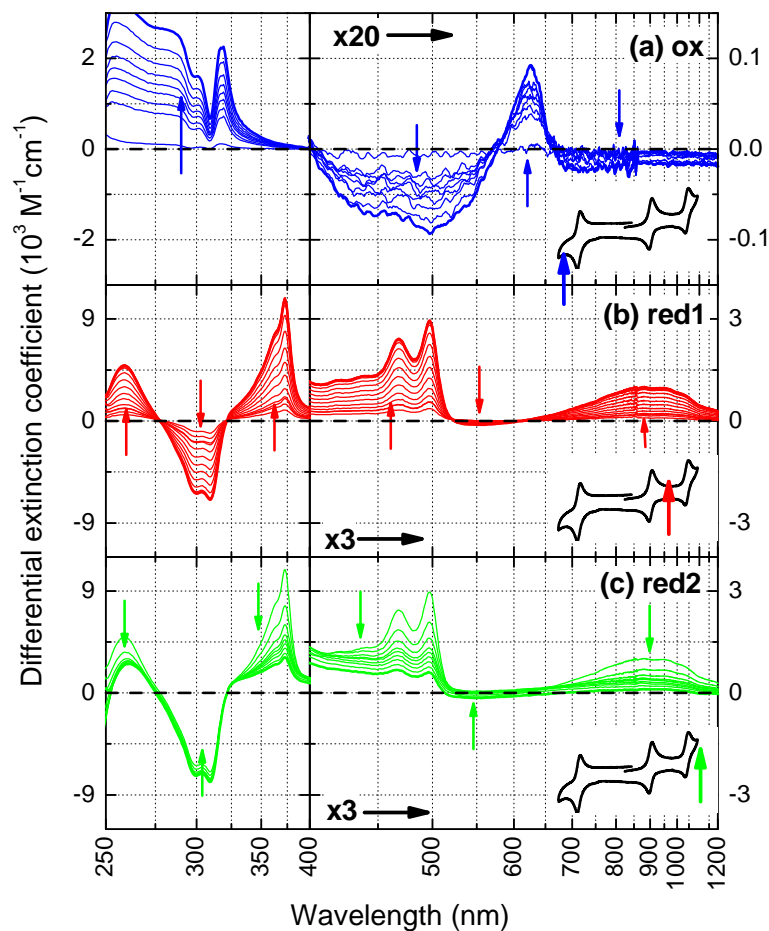


Figure A.2.: Time-series differential UV-vis absorption of $[1A]PF_6$ (in DMF) during electrochemical processes (a) 1-e⁻oxidation (ox1), (b) first 1-e⁻reduction (red1) and (c) second 1-e⁻(red2) reduction. Bold lines denote the final absorption curve, whilst small arrows indicate direction of change with time. Static redox potentials are for each set of spectra are indicated in the inset of each panel.

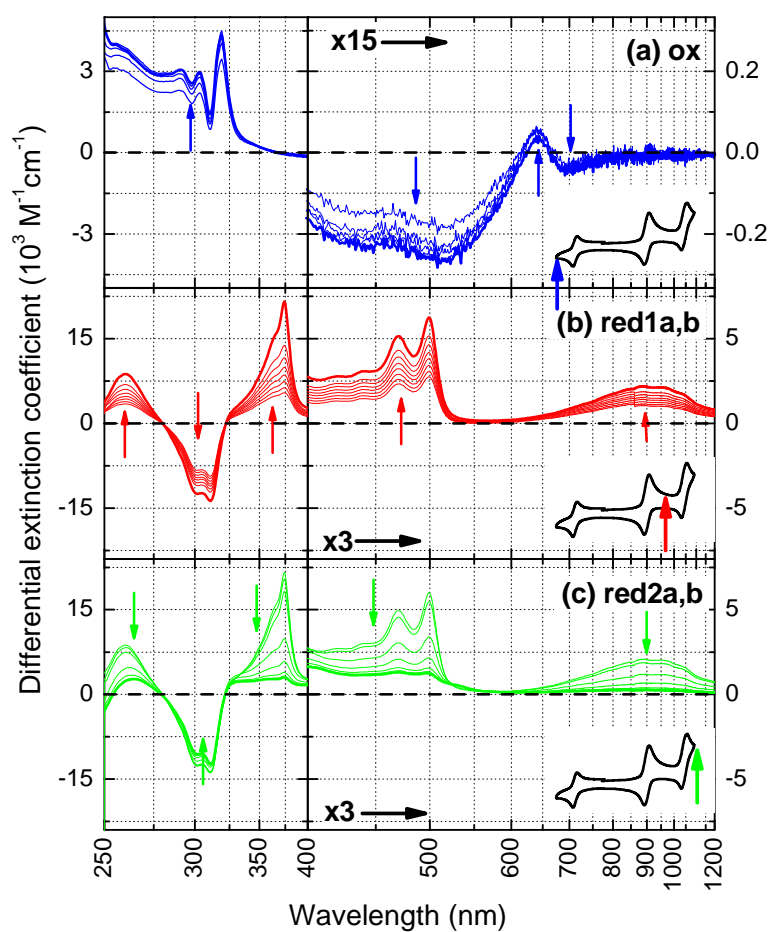


Figure A.3.: Time-series differential UV-vis absorption of $[2A](PF_6)_2$ (in DMF) during electrochemical processes (a) 1- e^- oxidation (ox1), (b) first 2- e^- reduction (red1) and (c) second 2- e^- reduction.

A.4. Expressions for the initial degenerate transient-absorption signal of a two-component sample

We consider a sample composed of a dilute mixture of two (non-interacting) compounds, with molar fractions f_i and absorption cross-sections σ_i and a total molecular density n_0 . In the following, we assume identical non-diverging, cylindrical pump/probe beams (cross-section A). The pump pulse energy vs distance z in the cuvette can be written,

$$J(z) = J_0 e^{-(\alpha_1 + \alpha_2)z}, \quad (\text{A.1})$$

where the absorption coefficients are given by $\alpha_i = \sigma_i f_i n_0$. The differential pump pulse energy absorbed by each compound is given by,

$$\frac{dJ_i}{dz} = \alpha_i J(z) = \alpha_i J_0 e^{-(\alpha_1 + \alpha_2)L}, \quad (\text{A.2})$$

which yields the initial excitation density profile for each compound,

$$\Delta n_i(z) = \frac{\alpha_i J_0}{h\nu A} e^{-(\alpha_1 + \alpha_2)z}. \quad (\text{A.3})$$

The initial change in sample absorption (at the pump wavelength) due to each compound is given by,

$$\Delta\alpha_i = -2\Delta n_i \sigma_i, \quad (\text{A.4})$$

so that the probe pulse energy obeys,

$$\frac{dJ_p}{dz} = -[(\alpha_1 + \Delta\alpha_1(z)) + (\alpha_2 + \Delta\alpha_2(z))] J_p, \quad (\text{A.5})$$

or,

$$J_p(z) = J_{p0} e^{-(\alpha_1 + \alpha_2)L} \exp \left[- \int_0^L dz (\Delta\alpha_1 + \Delta\alpha_2) \right]. \quad (\text{A.6})$$

This yields the differential transmitted probe pulse energy (i.e. relative to that in the absence of the pump),

$$\Delta J_p = J_{p0} e^{-(\alpha_1 + \alpha_2)L} \left\{ \exp \left[- \int_0^L dz (\Delta\alpha_1 + \Delta\alpha_2) \right] - 1 \right\}. \quad (\text{A.7})$$

The normalised differential signal is thus given by,

$$\frac{\Delta S}{S_0} = \frac{\Delta J_p}{J_{p0} e^{-(\alpha_1 + \alpha_2)L}} = \exp \left[- \int_0^L dz (\Delta\alpha_1 + \Delta\alpha_2) \right] - 1, \quad (\text{A.8})$$

or, to a good approximation for typical differential signals,

$$\frac{\Delta S}{S_0} \approx - \int_0^L dz (\Delta\alpha_1 + \Delta\alpha_2). \quad (\text{A.9})$$

From Eq.s A.3 and A.4 we have,

$$\Delta\alpha_i(z) = -2 \frac{J_0}{h\nu A} f_i \sigma_i^2 n_0 e^{-(f_1 \sigma_1 + f_2 \sigma_2) n_0 z}, \quad (\text{A.10})$$

so that,

$$\begin{aligned} \frac{\Delta S}{S_0} &\approx 2 \frac{J_0}{h\nu A} n_0 (f_1 \sigma_1^2 + f_2 \sigma_2^2) \int_0^L dz e^{-(f_1 \sigma_1 + f_2 \sigma_2) n_0 z} \\ &= 2 \frac{J_0}{h\nu A} \frac{(f_1 \sigma_1^2 + f_2 \sigma_2^2)}{f_1 \sigma_1 + f_2 \sigma_2} \left[1 - e^{-(f_1 \sigma_1 + f_2 \sigma_2) n_0 L} \right], \end{aligned} \quad (\text{A.11})$$

or for a weakly absorbing sample,

$$\frac{\Delta S}{S_0} \approx 2 \frac{J_0}{h\nu A} n_0 L (f_1 \sigma_1^2 + f_2 \sigma_2^2). \quad (\text{A.12})$$

Writing the approximate single-component signals as $\left(\frac{\Delta S}{S_0}\right)_i \approx 2 \frac{J_0}{h\nu A} n_0 L f_i \sigma_i^2$, the relative contribution from each compound is given by,

$$\left(\frac{\Delta S}{S_0}\right)_2 / \left(\frac{\Delta S}{S_0}\right)_1 \approx \frac{f_2 \sigma_2^2}{f_1 \sigma_1^2}. \quad (\text{A.13})$$

Eq. A.13 demonstrates that the presence of a small quantity of impurity compound (with a molar absorption strength greater than the non-impurity compound) in the sample can lead to a relative contribution to the transient absorption which is not given simply by the ratio of the ground-state absorptivities, i.e. $\alpha_2/\alpha_1 = f_2 \sigma_2 / f_1 \sigma_1$, but is larger by a factor σ_2/σ_1 . A numerical case study is given in Section A.5 for the case of **a-BOB** and the impurity $\text{Fe}(\text{bpy})_3^{2+}$.

A.5. Spectroscopic comparison of contaminated/purified samples of **a-BOB**

As mentioned in Section 4.4, the original samples of **a-BOB** contained a small fraction of the impurity $\text{Fe}(\text{bpy})_3^{2+}$. Considerable effort was required to isolate a usable-pure **a-BOB** sample with a low yield (carried out by our synthetic collaborators, AG Wagner, J. W. Goethe-Universität). Here we demonstrate the importance of high sample purity for spectroscopic studies of relatively weak absorption bands (such as the MLCT band of the **Fe-B-bpy** compounds) in the presence of contaminants (with far stronger absorption).

A regression analysis of the contaminated **a-BOB**-sample absorption spectrum ε_{tot} using the spectra of purified **a-BOB** (ε_1) and $\text{Fe}(\text{bpy})_3^{2+}$ (ε'_2) as per, $\varepsilon_{\text{tot}} = \eta_1 \varepsilon_1 + \eta_2 \varepsilon_2$, yielded the molecular number fractions $\eta_1 = 0.961$ and $\eta_2 = 0.038$. Note that $\eta_1 + \eta_2 = 1.00$, which was not constrained in the regression analysis, and testifies an accurate calibration of the spectra. This analysis demonstrates the critical distinction between “synthetic purity (i.e. with $f_2 \sim 0.038$ molar impurity)” and “spectroscopic purity” (in this case, ~ 0.26 of total absorption is due to impurity at 500 nm) for (relatively) strongly absorbing contaminants. Moreover, from an inspection of the spectra in Figure A.4 it emphasises the specific hazard that the impurities (which generally possess common moieties) may often have an absorption profile which is similar to that of the target chromophore, and hence remain undetected without careful quantitative analysis.

The far more drastic impact of relatively small quantities of such strongly-absorbing contaminants arises when one considers the expected impurity contribution to a transient-absorption signal (due to the quadratic dependence of the molar absorbance). Using the values above, and Eq. A.13, we can predict the relative contributions to the degenerate (bleach) signal. This is demonstrated in Figure

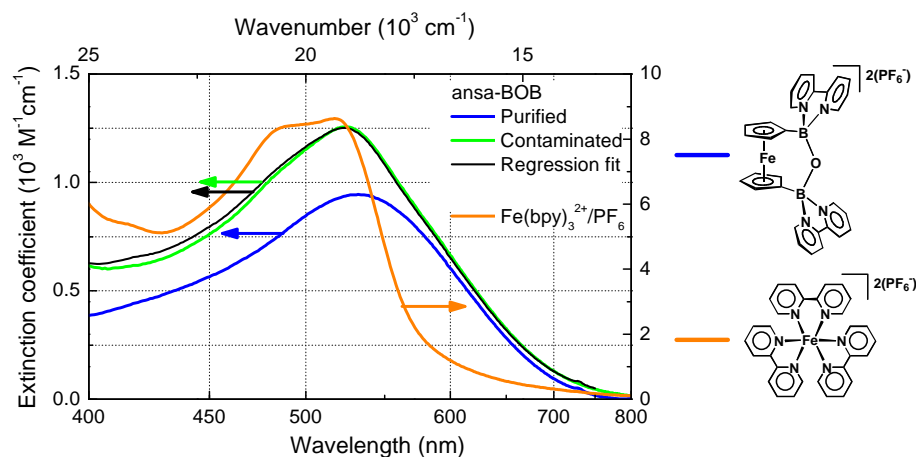


Figure A.4.: UV-vis absorption of contaminated **a-BOB** samples and stringently purified samples, and spectra of predominant contaminant $\text{Fe}(\text{bpy})_3^{2+}$. Included is a regression of the spectra of purified **a-BOB** and $\text{Fe}(\text{bpy})_3^{2+}$.

A.5, which shows the expected relative initial bleach signal amplitude (relative to a pure sample of **a-BOB**) as a function of the impurity concentration of $\text{Fe}(\text{bpy})_3^{2+}$. For the impurity concentration derived above of $f_2 \sim 0.038$, Eq. A.13 predicts that the $\text{Fe}(\text{bpy})_3^{2+}$ -impurity contribution to the initial bleach signal (for a pump wavelength $\lambda_{\text{ex}} = 500 \text{ nm}$) is ~ 2.5 times that from the target **a-BOB** chromophore. An comparison of transient absorption traces taken for the contaminated sample, and purified samples of $\text{Fe}(\text{bpy})_3^{2+}$ and **a-BOB** (obtained only near the end of the study) are consistent with this magnitude of distortion. Whilst in principle it would be possible to remove the $\text{Fe}(\text{bpy})_3^{2+}$ contributions from the earlier transient absorption measurements on **a-BOB**, this was not pursued due to the fact that such a decomposition analysis depends critically on the relative excitation density, beam geometry and concentrations in each set of measurements.

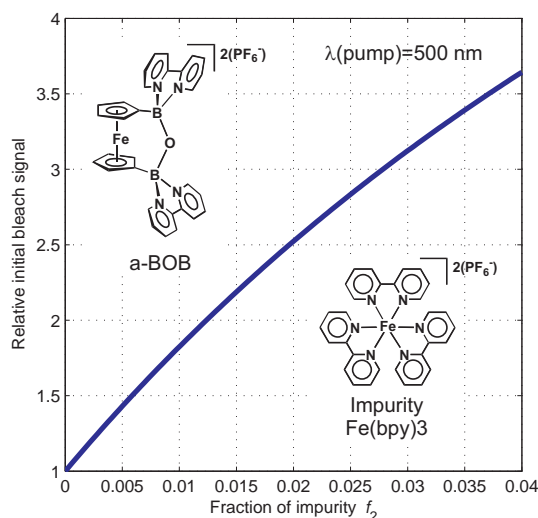


Figure A.5.: Predicted initial degenerate transient absorption (bleach) signal (c.f. Eq A.13) for an **a-BOB** sample contaminated with $\text{Fe}(\text{bpy})_3^{2+}$ vs impurity fraction f_2 relative to a pure **a-BOB** sample, using the molar extinction coefficients for $\lambda_{\text{ex}} = 500 \text{ nm}$.

A.6. Additional materials

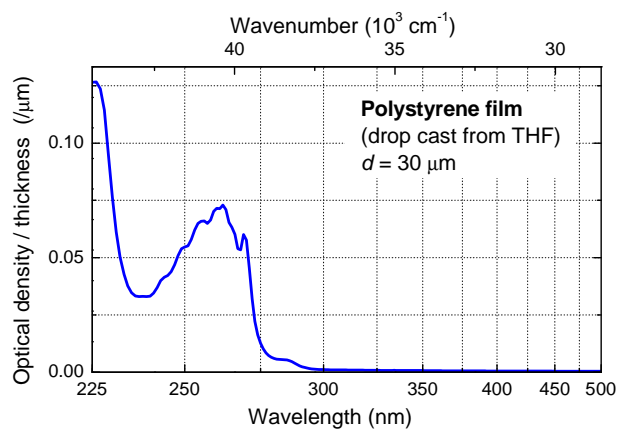


Figure A.6.: UV-vis absorption of neat polystyrene film (drop-cast from THF solution (concentration 30 mg/mL)).

B. Derivation of theoretical results

B.1. Perturbation theory results for D-Aⁿ complexes

B.1.1. Donor–single-acceptor complex, D-A

In order to obtain useful semiquantitative expressions for the energies and wavefunctions of a donor-acceptor (D-A) system in terms of the isolated donor and acceptor (and their interaction) using low-order perturbation theory, an approach is needed which is appropriate for unperturbed wavefunctions which are not eigenfunctions of a common hamiltonian (and hence are also not in general orthogonal). The results of the following perturbation treatment for a donor–*single*-acceptor system was first presented in Ref. [42] without derivation, except for stating that it is based on a ‘generalisation’ of a derivation in Ref. [235] for the simpler case of a set of orthogonal eigenfunctions of a common unperturbed hamiltonian (and perturbation). Moreover, whilst a modern reference [187] addressing the case of a donor–*double*-acceptor complex exists, they avoid any explicit expressions for the corresponding energies of the system. Hence it is deemed appropriate to present a clear derivation of all required results here¹.

The approach is based on an approximate simplification of the finite-basis secular determinant (which is limited to the unperturbed, one-electron ground state wavefunctions), which is shown to parallel standard Rayleigh-Schrödinger perturbation theory, only allowing more readily for the use of non-orthogonal unperturbed wavefunctions, for which different terms in the hamiltonian represent the perturbation.

We assume we have two one-electron wavefunctions, φ_j ($j = 1, 2$), which are the ground-state eigenfunctions of the isolated donor and acceptor, respectively, and use these as an approximate basis to describe the two lowest one-electron wavefunctions of the weakly-coupled D-A system:

$$\varphi'_j = \sum_{i=1}^2 c_{ji} \varphi_i. \quad (\text{B.1})$$

In terms of the hamiltonian for the combined D-A system, H , we require:

$$H\varphi'_j = E'_j \varphi'_j \quad (\text{B.2})$$

Switching to Dirac notation, this requires for $i, j = 1, 2$:

$$\begin{aligned} \langle \varphi_i | H | \varphi'_j \rangle &= c_{j1} \langle \varphi_i | H | \varphi_1 \rangle + c_{j2} \langle \varphi_i | H | \varphi_2 \rangle \\ &= c_{j1} H_{i1} + c_{j2} H_{i2} \\ &= E'_j (c_{j1} \langle \varphi_i | \varphi_1 \rangle + c_{j2} \langle \varphi_i | \varphi_2 \rangle) \\ &= E'_j (c_{j1} S_{i1} + c_{j2} S_{i2}) \end{aligned} \quad (\text{B.3})$$

or,

$$c_{j1} (H_{i1} - E'_j S_{i1}) + c_{j2} (H_{i2} - E'_j S_{i2}) = 0 \quad (\text{B.4})$$

or in matrix form for $j = 1, 2$,

$$\begin{bmatrix} H_{11} - E'_j S_{11} & H_{12} - E'_j S_{12} \\ H_{21} - E'_j S_{21} & H_{22} - E'_j S_{22} \end{bmatrix} \begin{bmatrix} c_{j1} \\ c_{j2} \end{bmatrix} = \begin{bmatrix} H_{11} - E'_j & H_{12} - E'_j S_{12} \\ H_{12} - E'_j S_{12} & H_{22} - E'_j \end{bmatrix} \begin{bmatrix} c_{j1} \\ c_{j2} \end{bmatrix} = \mathbf{0} \quad (\text{B.5})$$

¹Moreover, it should be noted that in the more modern account in Ref. [43] it appears that the first-order perturbation terms are simply discarded, due to the emphasis on the second-order effects (i.e. wavefunction mixing), which makes this habitually-cited reference potentially misleading.

where we used the fact that H is hermitian, as well specifying $\varphi_j \in \mathbb{R}$, so that $H_{12} = H_{21}^*$, $S_{ij} = S_{ji}^* = S_{ji}$ and have taken normalised unperturbed wavefunctions, i.e. $S_{ii} = 1$. (Note that these assumptions only simplify the algebraic form of the following expressions, and do not affect the principle results.) Non-trivial solutions to Eq. B.1.1 require:

$$\begin{vmatrix} H_{11} - E'_j & H_{12} - E'_j S_{12} \\ H_{21} - E'_j S_{12} & H_{22} - E'_j \end{vmatrix} = 0, \quad (\text{B.6})$$

which is the standard secular equation.

In the present case, the eigenvalues and eigenfunctions could be obtained exactly (within the approximation of the finite basis set). However, in order to prepare for the case of a larger basis, we want to develop the diagonalisation problem approximately, in a way that parallels standard low-order perturbation theory (although the standard Rayleigh-Schrödinger or Brillouin-Wigner results are not directly applicable, as we are dealing with a non-orthogonal basis of unperturbed wavefunctions which do not share a common unperturbed hamiltonian).

The application of perturbation theory is as follows [235]. We assume that the unperturbed wavefunctions φ_j are only weakly mixed by their respective perturbations in H . In order to find approximate E'_j and φ'_j , we assume that $E'_j \approx H_{jj}$ for all elements in the secular determinant except at the (j, j) position. Moreover, all terms away from the j -th row and j -th column are set to zero. (Note that these rather seemingly drastic simplifications still maintain a level of approximation equal to standard low-order perturbation theory.) For $j = 1$:

$$\begin{vmatrix} H_{11} - E'_1 & H_{12} - H_{11} S_{12} \\ H_{12} - H_{11} S_{12} & H_{22} - H_{11} \end{vmatrix} = 0 \quad (\text{B.7})$$

or,

$$E'_1 = H_{11} - \frac{(H_{12} - H_{11} S_{12})^2}{H_{22} - H_{11}}. \quad (\text{B.8})$$

This yields for the coefficients,

$$\frac{c_{12}}{c_{11}} = -\frac{H_{12} - H_{11} S_{12}}{H_{22} - H_{11}}. \quad (\text{B.9})$$

Similarly, for $j = 2$:

$$E'_2 = H_{22} + \frac{(H_{12} - H_{22} S_{12})^2}{H_{22} - H_{11}}, \quad (\text{B.10})$$

and

$$\frac{c_{21}}{c_{22}} = \frac{H_{12} - H_{22} S_{12}}{H_{22} - H_{11}}. \quad (\text{B.11})$$

We can demonstrate that these equations are consistent with standard perturbation theory (with orthogonal eigenfunctions of an unperturbed Hamiltonian, $H^{(0)}$). If we write $H = H^{(0)} + H^{(1)}$ then,

$$H_{jj} = H_{jj}^{(0)} + H_{jj}^{(1)} = E_j + H_{jj}^{(1)},$$

$$H_{21} = H_{21}^{(0)} + H_{21}^{(1)} = H_{21}^{(1)},$$

and

$$S_{12} = 0.$$

Substituting these expressions into Eq.s B.1.1-B.1.1 e.g., for $j = 1$ yields,

$$E'_1 = E_1 + H_{11}^{(1)} - \frac{(H_{21}^{(1)})^2}{(E_2 + H_{22}^{(1)}) - (E_1 + H_{11}^{(1)})}, \quad (\text{B.12})$$

and,

$$c_{12} = -\frac{H_{21}^{(1)}}{(E_2 + H_{22}^{(1)}) - (E_1 + H_{11}^{(1)})} c_{11}, \quad (\text{B.13})$$

which are consistent with the standard results of Rayleigh-Schrödinger perturbation theory (first-order wavefunctions, second-order energies).

B.1.2. Symmetric double-acceptor complex, A-D-A

We now employ three-dimensional bases and write: $\varphi'_j = \sum_{i=1}^3 c_{ji} \varphi_i$. The secular equations now read,

$$\begin{bmatrix} H_{11} - E'_j & H_{12} - E'_j S_{12} & H_{13} - E'_j S_{13} \\ H_{21} - E'_j S_{21} & H_{22} - E'_j & H_{23} - E'_j S_{23} \\ H_{31} - E'_j S_{31} & H_{32} - E'_j S_{32} & H_{33} - E'_j \end{bmatrix} \begin{bmatrix} c_{j1} \\ c_{j2} \\ c_{j3} \end{bmatrix} = \mathbf{0} \quad (\text{B.14})$$

We assume that the two isolated acceptors are identical, i.e. the unperturbed wavefunctions φ_2, φ_3 are degenerate (but centred on different origins). For the case to be treated (i.e. a sum of three independent effective potentials, one from each isolated system), it is possible to write the total hamiltonian for the A-D-A complex as $H = H' + H^{(2,3)}$, and we can first treat the degenerate (2,3)-subsystem alone. If we carry out this part of the problem without approximation, then the results can be used in the subsequent perturbation treatment for the full A-D-A system as per the D-A case without requiring any special additional considerations. For the 2-3 degenerate system we have,

$$\begin{vmatrix} H_{22}^{(2,3)} - E'_j & H_{23}^{(2,3)} - E'_j S_{23} \\ H_{23}^{(2,3)} - E'_j S_{23} & H_{33}^{(2,3)} - E'_j \end{vmatrix} = 0, \quad (\text{B.15})$$

where, in the present case, the two acceptors are interchangeable, and hence $H_{22}^{(2,3)} = H_{33}^{(2,3)}$. Solving Eq. B.1.2 yields,

$$(H_{22}^{(2,3)} - E'_j)^2 - (H_{23}^{(2,3)} - E'_j S_{23})^2 = 0,$$

or,

$$E_{\alpha,\beta} = \frac{H_{22}^{(2,3)} \pm H_{23}^{(2,3)}}{1 \pm S_{23}}, \quad (\text{B.16})$$

which is exactly the same result as for the simple MO treatment for H_2^+ [98]. The corresponding coefficients yield symmetric (α) and antisymmetric (β) eigenfunctions,

$$c_{\alpha,\beta 2} = \frac{1}{\sqrt{2}} = \pm c_{\alpha,\beta 3},$$

which defines

$$\varphi_{\alpha,\beta} = \frac{1}{\sqrt{2}} (\varphi_2 \pm \varphi_3). \quad (\text{B.17})$$

Now we use this new non-degenerate basis in the full A-D-A problem:

$$\begin{bmatrix} H_{11} - E'_j & H_{1\alpha} - E'_j S_{1\alpha} & H_{1\beta} - E'_j S_{1\beta} \\ H_{1\alpha} - E'_j S_{1\alpha} & H_{\alpha\alpha} - E'_j & H_{\alpha\beta} \\ H_{1\beta} - E'_j S_{1\beta} & H_{\alpha\beta} & H_{\beta\beta} - E'_j \end{bmatrix} \begin{bmatrix} c_{j1} \\ c_{j\alpha} \\ c_{j\beta} \end{bmatrix} = \mathbf{0}, \quad (\text{B.18})$$

where $S_{\alpha\beta} = 0$. Following the previous implementation of perturbation theory from the D-A case, we solve the approximate secular determinant equation, which reads for $j = 1$,

$$\begin{vmatrix} H_{11} - E'_1 & H_{1\alpha} - H_{11} S_{1\alpha} & H_{1\beta} - H_{11} S_{1\beta} \\ H_{1\alpha} - H_{11} S_{1\alpha} & H_{\alpha\alpha} - H_{11} & 0 \\ H_{1\beta} - H_{11} S_{1\beta} & 0 & H_{\beta\beta} - H_{11} \end{vmatrix} = 0, \quad (\text{B.19})$$

which upon rearrangement gives,

$$E'_1 = H_{11} - \frac{(H_{1\alpha} - H_{11} S_{1\alpha})^2}{H_{\alpha\alpha} - H_{11}} - \frac{(H_{1\beta} - H_{11} S_{1\beta})^2}{H_{\beta\beta} - H_{11}}, \quad (\text{B.20})$$

$$\frac{c_{1\alpha}}{c_{11}} = -\frac{H_{1\alpha} - H_{11} S_{1\alpha}}{H_{\alpha\alpha} - H_{11}}, \quad (\text{B.21})$$

and,

$$\frac{c_{1\beta}}{c_{11}} = -\frac{H_{1\beta} - H_{11} S_{1\beta}}{H_{\beta\beta} - H_{11}}. \quad (\text{B.22})$$

Likewise for $j = \alpha$,

$$E'_\alpha = H_{\alpha\alpha} + \frac{(H_{1\alpha} - H_{\alpha\alpha}S_{1\alpha})^2}{H_{\alpha\alpha} - H_{11}} - \frac{(H_{\alpha\beta})^2}{H_{\beta\beta} - H_{\alpha\alpha}}, \quad (\text{B.23})$$

$$\frac{c_{\alpha 1}}{c_{\alpha\alpha}} = + \frac{H_{1\alpha} - H_{\alpha\alpha}S_{1\alpha}}{H_{\alpha\alpha} - H_{11}}, \quad (\text{B.24})$$

and,

$$\frac{c_{\alpha\beta}}{c_{\alpha\alpha}} = - \frac{H_{\alpha\beta}}{H_{\beta\beta} - H_{\alpha\alpha}}; \quad (\text{B.25})$$

and for $j = \beta$,

$$E'_\beta = H_{\beta\beta} + \frac{(H_{1\beta} - H_{\beta\beta}S_{1\beta})^2}{H_{\beta\beta} - H_{11}} + \frac{(H_{\alpha\beta})^2}{H_{\beta\beta} - H_{\alpha\alpha}}, \quad (\text{B.26})$$

$$\frac{c_{\beta 1}}{c_{\beta\beta}} = + \frac{H_{1\beta} - H_{\beta\beta}S_{1\beta}}{H_{\beta\beta} - H_{11}}, \quad (\text{B.27})$$

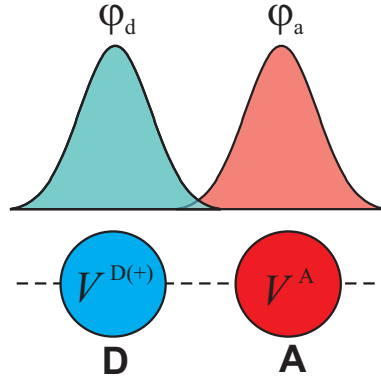
and,

$$\frac{c_{\beta\alpha}}{c_{\beta\beta}} = + \frac{H_{\alpha\beta}}{H_{\beta\beta} - H_{\alpha\alpha}}. \quad (\text{B.28})$$

When we consider the single-electron hamiltonian as $H = T + V^{(1)} + V^{(2)} + V^{(3)}$, some of these expressions are considerably simplified (due to the symmetrised properties of φ_α and φ_β).

B.2. One-electron wavefunctions and charge transfer transitions of D-Aⁿ complexes

B.2.1. Donor–single-acceptor complex, D-A



We describe the D-A system using one-electron wavefunctions and an effective potential composed of the sum of the isolated donor (*excluding* the valence electron under consideration), V^D , and acceptor, V^A , with no response of either potential to the wavefunction occupied by the electron. (Note that this is quite a severe approximation, in that the remaining electrons on the donor cannot relax upon charge transfer, which is the major assumption in this model. The neglect of using correctly antisymmetrised wavefunctions also results in the neglect of the exchange energy contribution, although due to the small overlap of the wavefunctions this is expected to be only a small correction).

The hamiltonian is written as,

$$H = T + V^D + V^A, \quad (\text{B.29})$$

where $(T + V^D) \varphi_d = E_d \varphi_d$ and $(T + V^A) \varphi_a = E_a \varphi_a$. From Eq.s B.1.1-B.1.1 we have,

$$\varphi'_d = \varphi_d + c_{da} \varphi_a, \quad (\text{B.30})$$

with,

$$c_{da} = -\frac{H_{ad} - H_{dd} S_{ad}}{H_{aa} - H_{dd}}, \quad (\text{B.31})$$

and,

$$E'_d = H_{dd} - \frac{(H_{ad} - H_{dd} S_{ad})^2}{H_{aa} - H_{dd}} = H_{dd} - (H_{aa} - H_{dd}) c_{da}^2. \quad (\text{B.32})$$

Also,

$$\varphi'_a = \varphi_a + c_{ad} \varphi_d, \quad (\text{B.33})$$

with,

$$c_{ad} = \frac{H_{ad} - H_{aa} S_{ad}}{H_{aa} - H_{dd}}, \quad (\text{B.34})$$

and,

$$E'_a = H_{aa} + \frac{(H_{ad} - H_{dd} S_{ad})^2}{H_{aa} - H_{dd}} = H_{aa} + (H_{aa} - H_{dd}) c_{ad}^2, \quad (\text{B.35})$$

where from hereon we will always take $c_{jj} = 1$ (and leave the resultant perturbed wavefunctions slightly unnormalised).

Substituting the unperturbed eigenfunctions gives:

$$\begin{aligned} H_{ad} &= \langle \varphi_a | T + V^D + V^A | \varphi_d \rangle = E_d \langle \varphi_a | \varphi_d \rangle + \langle \varphi_a | V^A | \varphi_d \rangle \\ &= E_d S_{ad} + V_{ad}^A \\ &= H_{da} \\ &= \langle \varphi_d | T + V^D + V^A | \varphi_a \rangle = E_a \langle \varphi_a | \varphi_d \rangle + \langle \varphi_a | V^D | \varphi_d \rangle \\ &= E_a S_{ad} + V_{ad}^D, \end{aligned} \quad (\text{B.36})$$

$$\begin{aligned} H_{dd} &= \langle \varphi_d | T + V^D + V^A | \varphi_d \rangle = E_d \langle \varphi_d | \varphi_d \rangle + \langle \varphi_d | V^A | \varphi_d \rangle \\ &= E_d + V_{dd}^A, \end{aligned} \quad (\text{B.37})$$

and,

$$\begin{aligned} H_{aa} &= \langle \varphi_a | T + V^D + V^A | \varphi_a \rangle = E_a \langle \varphi_a | \varphi_a \rangle + \langle \varphi_a | V^D | \varphi_a \rangle \\ &= E_a + V_{aa}^D. \end{aligned} \quad (\text{B.38})$$

For φ'_d this gives,

$$c_{da} = -\frac{V_{ad}^A - V_{dd}^A S_{ad}}{(E_a - E_d) + (V_{aa}^D - V_{dd}^A)}, \quad (\text{B.39})$$

and,

$$E'_d = E_d + V_{dd}^A - c_{da}^2 [(E_a - E_d) + (V_{aa}^D - V_{dd}^A)], \quad (\text{B.40})$$

whilst for φ'_a ,

$$c_{ad} = \frac{V_{da}^D - V_{aa}^D S_{ad}}{(E_a - E_d) + (V_{aa}^D - V_{dd}^A)}, \quad (\text{B.41})$$

and,

$$E'_a = E_a + V_{aa}^D + c_{ad}^2 [(E_a - E_d) + (V_{aa}^D - V_{dd}^A)]. \quad (\text{B.42})$$

For the transition dipole moment we have,

$$\begin{aligned} \mu'_{da} &= \langle \varphi'_d | \mathbf{M} | \varphi'_a \rangle = (\langle \varphi_d | + c_{da} \langle \varphi_a |) \mathbf{M} (|\varphi_a \rangle + c_{ad} |\varphi_d \rangle) \\ &= \langle \varphi_d | \mathbf{M} | \varphi_a \rangle + c_{da} \langle \varphi_a | \mathbf{M} | \varphi_a \rangle + c_{ad} \langle \varphi_d | \mathbf{M} | \varphi_d \rangle + O(c^2) \\ &\approx \boldsymbol{\mu}_{da} + c_{da} \boldsymbol{\mu}_{aa} + c_{ad} \boldsymbol{\mu}_{dd} \\ &= (\boldsymbol{\mu}_{da} - S_{ad} \boldsymbol{\mu}_{dd}) + c_{da} (\boldsymbol{\mu}_{aa} - \boldsymbol{\mu}_{dd}), \end{aligned} \quad (\text{B.43})$$

using $c_{da} + c_{ad} + S_{ad} = 0$. This result represents an important result for charge-transfer transitions between the interacting donor and acceptor, which demonstrates that the finite oscillator strength for the transition results from two terms, (i) the ‘contact’ term ($\mu_{da} - S_{ad}\mu_{dd}$) due to the finite overlap of the unperturbed donor and acceptor wavefunctions, and (ii) the ‘transfer’ term $c_{da}(\mu_{aa} - \mu_{dd})$, which results due to mixing of the donor and acceptor orbitals. Due to the fact that the transfer term effectively contains local transition dipole moments, for appreciable mixing of the donor and acceptor wavefunctions this term is expected to dominate.

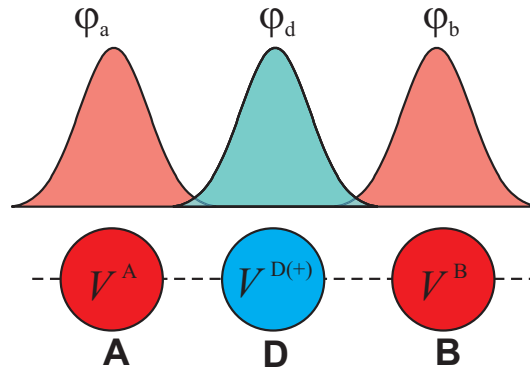
Assuming that the mixing of the unperturbed orbitals is negligible (due to a large energetic separation), then $c_{da} \approx c_{ad} \approx 0$ and from Eq.s B.40 and B.42 the energy separation of the two perturbed states is given by,

$$\Delta E'_{da} \approx (E_a - E_d) + (V_{aa}^D - V_{dd}^A). \quad (\text{B.44})$$

This shows that the approximate photon energy for the transition is shifted by two terms, (i) V_{aa}^D , i.e. the electrostatic interaction of the valence electron on the acceptor with the *oxidised* donor (which will lead to a red-shift of the CT transition), and (ii) V_{dd}^A , the electrostatic interaction of the valence electron on the donor with the acceptor.

In the case where the ground-state donor and acceptor are both neutral, we have $V_{dd}^A \approx 0$, and the transition energy is lowered by $V_{aa}^D < 0$. However, in the case of a ground state with neutral-donor and cationic-acceptor, then $V_{aa}^D \approx V_{dd}^A$ and no significant red-shift results from the interaction terms. However, in general, a cationic acceptor will have a greater electron affinity, i.e. E_a will generally be lower in energy. Note that inclusion of the mixing terms c will in general result in an additional blue-shift of the CT transition (due to the resulting stabilisation of the donor and destabilisation of the acceptor wavefunctions).

B.2.2. Symmetric donor–double-acceptor complex, A-D-A



The total hamiltonian can be written,

$$H = T + V^D + V^A + V^B, \quad (\text{B.45})$$

where $(T + V^D)\varphi_d = E_d\varphi_d$, $(T + V^A)\varphi_a = E_a\varphi_a$ and $(T + V^B)\varphi_b = E_a\varphi_b$ ($E_b = E_a$).

Using the perturbation results for the symmetrised-acceptor basis, for φ'_d ,

$$c_{d\alpha} = -\frac{H_{\alpha d} - H_{dd}S_{d\alpha}}{H_{\alpha\alpha} - H_{dd}} = -2\frac{V_{\alpha d}^A - V_{dd}^A S_{d\alpha}}{(E_\alpha - E_d) + (V_{\alpha\alpha}^D - 2V_{dd}^A)}, \quad (\text{B.46})$$

where $V_{dd}^A = V_{dd}^B$ and $V_{\alpha d}^A = V_{\alpha d}^B$. From the antisymmetry of ϕ_β it is clear that,

$$c_{d\beta} = 0. \quad (\text{B.47})$$

The corresponding energy is given by,

$$E'_d = E_d + 2V_{dd}^A - c_{d\alpha}^2 [(E_\alpha - E_d) + (V_{\alpha\alpha}^D - 2V_{dd}^A)]. \quad (\text{B.48})$$

For φ'_α ,

$$c_{\alpha d} = \frac{H_{d\alpha} - H_{\alpha\alpha}S_{d\alpha}}{H_{\alpha\alpha} - H_{dd}} = \frac{V_{d\alpha}^D - V_{\alpha\alpha}^D S_{d\alpha}}{(E_\alpha - E_d) + (V_{\alpha\alpha}^D - 2V_{dd}^A)}. \quad (\text{B.49})$$

Again, from symmetry (i.e. $V_{\beta\alpha}^D = 0$),

$$c_{\alpha\beta} = 0. \quad (\text{B.50})$$

The corresponding energy is then given by,

$$E'_\alpha = E_\alpha + V_{\alpha\alpha}^D + c_{\alpha d}^2 [(E_\alpha - E_d) + (V_{\alpha\alpha}^D - 2V_{dd}^A)] \quad (\text{B.51})$$

For φ'_β , from symmetry we have,

$$c_{\beta d} = 0, \quad (\text{B.52})$$

$$c_{\beta\alpha} = 0, \quad (\text{B.53})$$

and,

$$E'_\beta = E_\beta + V_{\beta\beta}^D, \quad (\text{B.54})$$

i.e. the antisymmetric acceptor wavefunction does not mix with the donor wavefunction.

We now express these relations in terms of the original single acceptor wavefunctions and energies. We need the following results,

$$E_{\alpha,\beta} = \frac{H_{aa}^{AB} \pm H_{ab}^{AB}}{1 \pm S_{ab}} = E_a + \frac{V_{aa}^B \pm V_{ba}^B}{1 \pm S_{ab}} = E_a + \frac{V_{aa}^B - V_{ba}^B S_{ab}}{1 - S_{ab}^2} \pm \frac{V_{ba}^B - V_{aa}^B S_{ab}}{1 - S_{ab}^2},$$

$$V_{\alpha d}^A = \frac{1}{\sqrt{2}} (V_{ad}^A + V_{bd}^A),$$

$$V_{\alpha d}^B = V_{\alpha d}^A,$$

$$S_{d\alpha} = \frac{1}{\sqrt{2}} (S_{da} + S_{db}) = \sqrt{2}S_{da},$$

$$V_{d\alpha}^D = \frac{1}{\sqrt{2}} (V_{da}^D + V_{db}^D),$$

and,

$$V_{\alpha\alpha}^D = \frac{1}{2} (V_{aa}^D + V_{bb}^D + V_{ab}^D + V_{ba}^D) = V_{aa}^D + V_{ab}^D.$$

Substitution yields, for φ'_d ,

$$c_{d\alpha} = -\sqrt{2} \frac{(V_{ad}^A + V_{bd}^A) - 2V_{dd}^A S_{da}}{(E_a - E_d) + \left(\frac{V_{aa}^B + V_{ba}^B}{1 + S_{ab}} + V_{aa}^D + V_{ab}^D - 2V_{dd}^A \right)} \quad (\text{B.55})$$

and,

$$E'_d = E_d + 2V_{dd}^A - c_{d\alpha}^2 \left[\left(E_a - E_d + \frac{V_{aa}^B + V_{ba}^B}{1 + S_{ab}} \right) + (V_{aa}^D + V_{ab}^D - 2V_{dd}^A) \right]. \quad (\text{B.56})$$

For φ'_α ,

$$c_{\alpha d} = \sqrt{2} \frac{V_{da}^D - (V_{aa}^D + V_{ab}^D) S_{da}}{\left(E_a - E_d + \frac{V_{aa}^B + V_{ba}^B}{1 + S_{ab}} \right) + (V_{aa}^D + V_{ab}^D - 2V_{dd}^A)}, \quad (\text{B.57})$$

and,

$$E'_\alpha = E_a + \frac{V_{aa}^B + V_{ba}^B}{1 + S_{ab}} + V_{aa}^D + V_{ab}^D + c_{\alpha d}^2 \left[\left(E_a - E_d + \frac{V_{aa}^B + V_{ba}^B}{1 + S_{ab}} \right) + (V_{aa}^D + V_{ab}^D - 2V_{dd}^A) \right]. \quad (\text{B.58})$$

For $\varphi'_\beta = \varphi_\beta$,

$$E'_\beta = E_a + \frac{V_{aa}^B - V_{ba}^B}{1 - S_{ab}} + V_{aa}^D - V_{ab}^D. \quad (\text{B.59})$$

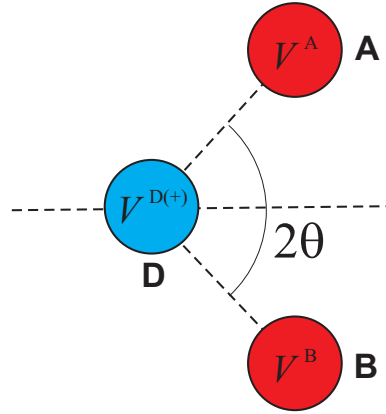


Figure B.1.: Non-linear double-acceptor CT complex.

The transition dipole moment for the symmetric acceptor wavefunction vanishes due to the antisymmetry of the transition dipole moment operator, i.e.,

$$\boldsymbol{\mu}'_{d\alpha} = 0, \quad (\text{B.60})$$

whereas for the antisymmetric acceptor wavefunction,

$$\begin{aligned} \boldsymbol{\mu}'_{d\beta} &= \langle \varphi'_d | \mathbf{M} | \varphi'_\beta \rangle = (\langle \varphi_d | + c_{d\alpha} \langle \varphi_\alpha |) \mathbf{M} (|\varphi_\beta\rangle + c_{\beta\alpha} |\varphi_\alpha\rangle) \\ &= \langle \varphi_d | \mathbf{M} | \varphi_\beta \rangle + c_{d\alpha} \langle \varphi_\alpha | \mathbf{M} | \varphi_\beta \rangle \\ &= \frac{1}{\sqrt{2}} \langle \varphi_d | \mathbf{M} | \varphi_a \rangle - \frac{1}{\sqrt{2}} \langle \varphi_d | \mathbf{M} | \varphi_b \rangle + \frac{1}{2} c_{d\alpha} (\langle \varphi_a | + \langle \varphi_b |) \mathbf{M} (|\varphi_a\rangle - |\varphi_b\rangle) \\ &= \frac{1}{\sqrt{2}} (\boldsymbol{\mu}_{da} - \boldsymbol{\mu}_{db}) + \frac{1}{2} c_{d\alpha} (\boldsymbol{\mu}_{aa} + \boldsymbol{\mu}_{ba} - \boldsymbol{\mu}_{ab} - \boldsymbol{\mu}_{bb}) \\ &= \sqrt{2} \boldsymbol{\mu}_{da} + c_{d\alpha} \boldsymbol{\mu}_{aa}. \end{aligned} \quad (\text{B.61})$$

This result exemplifies the situation in a symmetric linear donor–double-acceptor complex, i.e. whilst mixing with donor wavefunction occurs only for the symmetric acceptor wavefunctions, the CT transition to this state is forbidden, whilst for the antisymmetric wavefunction, the opposite situation holds. However, this latter transition can also gain intensity through mixing of the donor and symmetric acceptor wavefunction due to the finite transition dipole moment between the symmetric and antisymmetric wavefunctions.

We note that if we neglect mixing, then the predicted transition dipole between the donor and antisymmetric acceptor wavefunction is given by $\boldsymbol{\mu}'_{d\beta} = \sqrt{2} \boldsymbol{\mu}_{da}$, and the oscillator strength $f \propto |\boldsymbol{\mu}'_{d\beta}|^2$ for the CT transition is twice that for the single-acceptor transition. The energy separation for each state, also assuming negligible mixing, is given by,

$$\begin{aligned} \Delta E'_{d\beta} &= (E_a - E_d) + (V_{aa}^D - 2V_{dd}^A + V_{aa}^B) \\ &= (E_a - E_d) + (V_{aa}^D - V_{dd}^A) + (V_{aa}^B - V_{dd}^A) \end{aligned} \quad (\text{B.62})$$

Comparing this result to the single-acceptor $\Delta E'_{da}$ (Eq. B.62), we have,

$$\Delta E'_{d\beta} = \Delta E'_{da} + (V_{aa}^B - V_{dd}^A) \quad (\text{B.63})$$

For a neutral-donor–neutral-double-acceptor complex, we have $|V_{dd}^A| \gtrsim |V_{aa}^B| \approx 0$ and we expect a small blue shift (due to the fact that the donor-acceptor distance is smaller than the acceptor-acceptor distance). However, for a donor with two cationic acceptors, we expect much larger electrostatic interactions with $|V_{dd}^A|$ significantly larger than $|V_{aa}^B|$ due to the smaller separation, and a significant blue-shift of the CT transition should result.

An important difference arises when the A-D-A complex is not linear, but form an angle 2θ as in Figure B.1. In this case, the transition dipole moment to the symmetric acceptor

wavefunction does not vanish, and the CT transitions to the symmetric and antisymmetric acceptor wavefunctions will vary with $\cos^2(\theta)$ and $\sin^2(\theta)$, respectively [187].

If we return to the energies of the symmetric (E'_α) and antisymmetric (E'_β) wavefunctions (Eq.s B.58 and B.59), then neglecting mixing these two energies should be separated by,

$$\Delta E'_{\alpha\beta} \equiv E'_\alpha - E'_\beta = \frac{V_{aa}^B + V_{ba}^B}{1 + S_{ab}} - \frac{V_{aa}^B - V_{ba}^B}{1 - S_{ab}} + 2V_{ab}^D = 2\frac{V_{ba}^B - S_{ab}V_{aa}^B}{1 - S_{ab}^2} + 2V_{ab}^D. \quad (\text{B.64})$$

B.3. Solvatochromic shift and broadening of a symmetric charge-transfer electronic transition for a charged-solute

The following derivation for the expected solvent shift and broadening of a charge-transfer electronic transition, using second-order perturbation theory and subsequent classical averaging of the perturbation terms, is based closely on the treatment in Ref. [48]. However, in order to treat the case of a solute with net charge, we need to include additional terms arising from ion-dipole interactions. Moreover, the classical averaging is now performed with the dominant ion-dipole term in the Boltzmann factor, which, after retaining only the most dominant terms, leads to a correction to the result for neutral solute molecules [48]. It should be noted that the neglect of solvent-solvent interactions is quite a significant approximation, although this is approximately accounted for through the use of the solvent dielectric properties through the Clausius-Mossotti and Clausius-Debye relations [48] (as opposed to the explicit solvent dipole moments).

For a single solute molecule and a set of solvent molecules n , and neglecting solvent-solvent interactions, we have $H = H_0 + \sum_n H_{0n} + \sum_n V_n$ where,

$$\begin{aligned} V_n &= (V_{\text{nuc-nuc}})_n + (V_{\text{el-nuc}})_n + (V_{\text{el-el}})_n \\ &= \sum_{I,J} \frac{Z_I Z_{nJ}}{|\mathbf{r}_I - \mathbf{r}_{nJ}|} - \sum_{i,J} \frac{Z_{nJ}}{|\mathbf{r}_i - \mathbf{r}_{nJ}|} - \sum_{I,j} \frac{Z_I}{|\mathbf{r}_I - \mathbf{r}_{nj}|} + \sum_{i,j} \frac{1}{|\mathbf{r}_i - \mathbf{r}_{nj}|}, \end{aligned} \quad (\text{B.65})$$

and the sum is over all solute/ n -th solvent nuclei (charge Z_I, Z_{nJ} , position $\mathbf{r}_I, \mathbf{r}_{nJ}$) and electrons ($\mathbf{r}_i, \mathbf{r}_{nj}$). In each solute/ n -th-solvent reference frame where the vector $R\hat{\mathbf{z}}_n$ is the displacement from the molecular centre of 1 to the molecular centre of 2, each distance can be expressed as in terms of the local coordinates,

$$r_{12} = R \left[1 + \frac{2(z_1 - z_2)}{R} + \frac{(x_1 - x_2)^2 + (y_1 - y_2)^2 + (z_1 - z_2)^2}{R^2} \right]^{\frac{1}{2}}.$$

Taking an inverse power expansion yields:

$$\frac{1}{r_{12}} \rightarrow \frac{1}{R} + \frac{(z_1 - z_2)}{R^2} + \frac{1}{R^3} \left(-\frac{1}{2} (x_1^2 + x_2^2 + y_1^2 + y_2^2 - 2z_1^2 - 2z_2^2) + x_1 x_2 + y_1 y_2 - 2z_1 z_2 \right) + O\left(\frac{1}{R^4}\right) \quad (\text{B.66})$$

Now we evaluate each term in the expansion, $V_n^{(n)}$.

$$\begin{aligned} V_n^{(1)} &= \frac{1}{R_n} \left(\sum_{I,J} Z_I Z_{nJ} - \sum_{i,J} Z_{nJ} - \sum_{I,j} Z_I + \sum_{i,j} 1 \right) \\ &= \frac{1}{R_n} (PP_n - NP_n - PN_n + NN_n) \\ &= \frac{1}{R_n} (P - N) (P_n - N_n) \\ &= \frac{1}{R_n} QQ_n \end{aligned} \quad (\text{B.67})$$

where P and P_n are the total nuclear charge on the solute and n -th solvent, respectively, N and N_n the corresponding total electronic charges, and $Q_x = P_x - N_x$ are the net molecular charges. This term clearly corresponds to the ion-ion contribution. If one or both molecules are neutral, $V_n^{(1)} = 0$.

$$\begin{aligned} V_n^{(2)} &= \frac{1}{R_n^2} \left(\sum_{I,J} Z_I Z_{nJ} (z_I - z_{nJ}) - \sum_{i,J} Z_{nJ} (z_i - z_{nJ}) - \sum_{I,j} Z_I (z_I - z_{nj}) + \sum_{i,j} (z_i - z_{nj}) \right) \\ &= \frac{1}{R_n^2} \left[Q_n \left(\sum_I Z_I z_I - \sum_i z_i \right) - Q \left(\sum_J Z_{nJ} z_{nJ} - \sum_j z_{nj} \right) \right] \end{aligned} \quad (\text{B.68})$$

These terms correspond to ion-dipole interaction. For neutral solvent molecules $Q_n = 0$, and,

$$V_n^{(2)} = -\frac{Q}{R_n^2} \left(\sum_J Z_{nJ} z_{nJ} - \sum_j z_{nj} \right). \quad (\text{B.69})$$

$$\begin{aligned} V_n^{(3)} &= -\frac{1}{2R_n^3} \left[\sum_{I,J} Z_I Z_{nJ} (x_I^2 + x_{nJ}^2 + y_I^2 + y_{nJ}^2 - 2z_I^2 - 2z_{nJ}^2) - \sum_{i,J} Z_{nJ} (x_i^2 + x_{nJ}^2 + y_i^2 + y_{nJ}^2 - 2z_i^2 - 2z_{nJ}^2) \right. \\ &\quad \left. - \sum_{I,j} Z_I (x_I^2 + x_{nj}^2 + y_I^2 + y_{nj}^2 - 2z_I^2 - 2z_{nj}^2) + \sum_{i,j} (x_i^2 + x_{nj}^2 + y_i^2 + y_{nj}^2 - 2z_i^2 - 2z_{nj}^2) \right] \\ &\quad + \frac{1}{R_n^3} \left[\sum_{I,J} Z_I Z_{nJ} (x_I x_{nJ} + y_I y_{nJ} - 2z_I z_{nJ}) - \sum_{i,J} Z_{nJ} (x_i x_{nJ} + y_i y_{nJ} - 2z_i z_{nJ}) \right. \\ &\quad \left. - \sum_{I,j} Z_I (x_I x_{nj} + y_I y_{nj} - 2z_I z_{nj}) + \sum_{i,j} (x_i x_{nj} + y_i y_{nj} - 2z_i z_{nj}) \right] \\ &= -\frac{1}{2R_n^3} \left[Q_n \left\{ \sum_I Z_I (x_I^2 + y_I^2 - 2z_I^2) - \sum_i (x_i^2 + y_i^2 - 2z_i^2) \right\} \right. \\ &\quad \left. + Q \left\{ \sum_J Z_{nJ} (x_{nJ}^2 + y_{nJ}^2 - 2z_{nJ}^2) - \sum_j (x_{nj}^2 + y_{nj}^2 - 2z_{nj}^2) \right\} \right] \\ &\quad + \frac{1}{R_n^3} \left[\sum_{I,J} Z_I Z_{nJ} I_{I,nJ} - \sum_{i,J} Z_{nJ} I_{i,nJ} - \sum_{I,j} Z_I I_{I,nj} + \sum_{i,j} I_{i,nj} \right], \end{aligned} \quad (\text{B.70})$$

where $I_{A,nB} \equiv x_A x_{nB} + y_A y_{nB} - 2z_A z_{nB}$. For $Q_n = 0$,

$$\begin{aligned} V_n^{(3)} &= -\frac{1}{2R_n^3} Q \left[\sum_J Z_{nJ} (x_{nJ}^2 + y_{nJ}^2 - 2z_{nJ}^2) - \sum_j (x_{nj}^2 + y_{nj}^2 - 2z_{nj}^2) \right] \\ &\quad + \frac{1}{R_n^3} \left[\sum_{I,J} Z_I Z_{nJ} I_{I,nJ} - \sum_{i,J} Z_{nJ} I_{i,nJ} - \sum_{I,j} Z_I I_{I,nj} + \sum_{i,j} I_{i,nj} \right] \end{aligned} \quad (\text{B.71})$$

Assuming that the spatial distribution of the solvent charge density is small compared to the distance between the solvent and solute, we can neglect the remaining ion-quadrupole term:

$$V_n^{(3)} \rightarrow \frac{1}{R_n^3} \left[\sum_{I,J} Z_I Z_{nJ} I_{I,nJ} - \sum_{i,J} Z_{nJ} I_{i,nJ} - \sum_{I,j} Z_I I_{I,nj} + \sum_{i,j} I_{i,nj} \right] \quad (\text{B.72})$$

We introduce the dipole operators,

$$\mathbf{M} = \sum_I Z_I \mathbf{r}_I - \sum_i \mathbf{r}_i$$

and

$$\mathbf{M}^n = \sum_J Z_{nJ} \mathbf{r}_{nJ} - \sum_j \mathbf{r}_{nj}.$$

If we define the matrix: $\mathbf{T}_n = \mathbf{I} - 3\mathbf{k}_n \mathbf{k}_n^T$ (where \mathbf{k}_n is the unit vector along the z_n -axis), then we can rewrite Eq.s B.69 and B.72 as,

$$V_n^{(2)} = -\frac{Q}{R_n^2} \mathbf{k}_n \cdot \mathbf{M}^n, \quad (\text{B.73})$$

and,

$$V_n^{(3)} = \frac{1}{R_n^3} \mathbf{M} \cdot \mathbf{T}_n \cdot \mathbf{M}^n. \quad (\text{B.74})$$

These are the two interaction terms we employ in the following second-order perturbation theory.

We take a ground state electronic wavefunction of the form $\Psi_g = \left(\prod_n \varphi_g^n \right) \cdot \psi_g$, where ψ_g and φ_g^n refer to the isolated solute and n -th solvent molecule, respectively. The interaction Hamiltonian term for all solvent molecules is given by

$$V = \sum_n V_n = \sum_n \frac{1}{R_n^3} \mathbf{M} \cdot \mathbf{T}_n \cdot \mathbf{M}^n - Q \sum_n \frac{1}{R_n^2} \mathbf{k}_n \cdot \mathbf{M}^n \quad (\text{B.75})$$

The only excited wavefunctions that will contribute to the energy perturbation (to second order), involve at most one solvent excitation, i.e. we need consider only the electronic wavefunctions,

$$\Psi_e' = \left(\prod_n \varphi_g^n \right) \cdot \psi_e, \quad \Psi_e'' = \left(\prod_{n \neq p} \varphi_g^n \right) \cdot \varphi_e^p \cdot \psi_g, \quad \text{and}, \quad \Psi_e''' = \left(\prod_{j \neq p} \varphi_g^j \right) \cdot \varphi_e^p \cdot \psi_e.$$

The last of these (involving both excited solvent and solute) leads to a dispersion term, which should be far smaller than the ion-dipole and dipole-dipole terms, and will be neglected.

The first-order correction to the ground state energy is given by,

$$\Delta E_g^{(1)} = \langle \Psi_g | V | \Psi_g \rangle = \gamma \sum_n \frac{1}{R_n^3} \langle \varphi_g^n \psi_g | \mathbf{M} \cdot \mathbf{T}_n \cdot \mathbf{M}^n | \varphi_g^n \psi_g \rangle - \gamma Q \sum_n \frac{1}{R_n^2} \langle \varphi_g^n \psi_g | \mathbf{k}_n \cdot \mathbf{M}^n | \varphi_g^n \psi_g \rangle \quad (\text{B.76})$$

Introducing $\boldsymbol{\mu}_g = \langle \psi_g | \mathbf{M} | \psi_g \rangle$, and $\boldsymbol{\mu}_g^n = \langle \varphi_g^n | \mathbf{M}^n | \varphi_g^n \rangle$, we can rewrite this as,

$$\Delta E_g^{(1)} = \gamma \sum_n \frac{1}{R_n^3} \boldsymbol{\mu}_g \cdot \mathbf{T}_n \cdot \boldsymbol{\mu}_g^n - \gamma Q \sum_n \frac{1}{R_n^2} \mathbf{k}_n \cdot \boldsymbol{\mu}_g^n \quad (\text{B.77})$$

The second order corrections are given by

$$\Delta E_g^{(2)} = - \sum_e \frac{|\langle \Psi_g | V | \Psi_e \rangle|^2}{E_e - E_g},$$

where the sum is over all the excited states above. For Ψ'_e ,

$$\begin{aligned}
\Delta E_g^{(2)} &= -\sum_e \frac{|\langle \Psi_g | V | \Psi'_e \rangle|^2}{E_e - E_g} = -\sum_e \frac{\left| \left\langle \left(\prod_i \varphi_g^i \right) \cdot \psi_g \left| \sum_j V_j \right| \left(\prod_i \varphi_g^i \right) \cdot \psi_e \right\rangle \right|^2}{\varepsilon_e - \varepsilon_g} \\
&= -\sum_e \sum_{j,k} \frac{\langle \varphi_g^j \psi_g | V_j | \varphi_g^j \psi_e \rangle \langle \varphi_g^k \psi_e | V_k | \varphi_g^k \psi_g \rangle}{\varepsilon_e - \varepsilon_g} \\
&= -\gamma^2 \sum_e \sum_{j,k} \frac{1}{R_j^3} \frac{1}{R_k^3} \frac{\langle \varphi_g^j \psi_g | \mathbf{M} \cdot \mathbf{T}_j \cdot \mathbf{M}^j - Q R_j \mathbf{k}_j \cdot \mathbf{M}^j | \varphi_g^j \psi_e \rangle \langle \varphi_g^k \psi_e | \mathbf{M} \cdot \mathbf{T}_k \cdot \mathbf{M}^k - Q R_k \mathbf{k}_k \cdot \mathbf{M}^k | \varphi_g^k \psi_g \rangle}{\varepsilon_e - \varepsilon_g} \\
&= -\gamma^2 \sum_e \sum_{j,k} \frac{1}{R_j^3} \frac{1}{R_k^3} \langle \varphi_g^j | \mathbf{M}^j | \varphi_g^j \rangle \cdot \mathbf{T}_j \cdot \frac{\langle \psi_g | \mathbf{M} | \psi_e \rangle \langle \psi_g | \mathbf{M} | \psi_e \rangle}{\varepsilon_e - \varepsilon_g} \cdot \mathbf{T}^k \cdot \langle \varphi_g^k | \mathbf{M}^k | \varphi_g^k \rangle \\
&= -\frac{1}{2} \gamma^2 \sum_e \sum_{j,k} \frac{1}{R_j^3} \frac{1}{R_k^3} \langle \varphi_g^j | \mathbf{M}^j | \varphi_g^j \rangle \cdot \mathbf{T}_j \cdot \alpha_g \cdot \mathbf{T}^k \cdot \langle \varphi_g^k | \mathbf{M}^k | \varphi_g^k \rangle,
\end{aligned} \tag{B.78}$$

where $\alpha_g = 2 \sum_e \frac{\langle \psi_g | \mathbf{M} | \psi_e \rangle \langle \psi_e | \mathbf{M} | \psi_g \rangle}{\varepsilon_e - \varepsilon_g}$. For $\Psi_e''^p$,

$$\begin{aligned}
\Delta E_g^{(2)p} &= -\sum_e \frac{|\langle \Psi_g | V | \Psi_e''^p \rangle|^2}{E_e^p - E_g^p} = -\sum_e \frac{\left| \left\langle \left(\prod_i \varphi_g^i \right) \cdot \psi_g \left| \sum_j V_j \right| \left(\prod_{i \neq p} \varphi_g^i \right) \cdot \varphi_e^p \cdot \psi_g \right\rangle \right|^2}{\varepsilon_e^p - \varepsilon_g^p} \\
&= -\sum_e \frac{\left| \left\langle \left(\prod_i \varphi_g^i \right) \cdot \psi_g \left| V_p \right| \left(\prod_{i \neq p} \varphi_g^i \right) \cdot \varphi_e^p \cdot \psi_g \right\rangle \right|^2}{\varepsilon_e^p - \varepsilon_g^p} \\
&= -\sum_e \frac{\left| \left\langle \left(\prod_i \varphi_g^i \right) \cdot \psi_g \left| \gamma \frac{1}{R_p^3} \mathbf{M} \cdot \mathbf{T}_p \cdot \mathbf{M}^p - \gamma \frac{Q}{R_p^2} \mathbf{k}_p \cdot \mathbf{M}^p \right| \left(\prod_{i \neq p} \varphi_g^i \right) \cdot \varphi_e^p \cdot \psi_g \right\rangle \right|^2}{\varepsilon_e^p - \varepsilon_g^p} \\
&= -\gamma^2 \sum_e \frac{1}{R_p^6} \frac{|\langle \varphi_e^p \cdot \psi_g | \mathbf{M} \cdot \mathbf{T}_p \cdot \mathbf{M}^p - Q R_p \mathbf{k}_p \cdot \mathbf{M}^p | \varphi_e^p \cdot \psi_g \rangle|^2}{\varepsilon_e^p - \varepsilon_g^p} \\
&= -\gamma^2 \sum_e \frac{1}{R_p^6} \frac{\langle \varphi_e^p \cdot \psi_g | \mathbf{M} \cdot \mathbf{T}_p \cdot \mathbf{M}^p - Q R_p \mathbf{k}_p \cdot \mathbf{M}^p | \varphi_e^p \cdot \psi_g \rangle \langle \varphi_e^p \cdot \psi_g | \mathbf{M}^p \cdot \mathbf{T}_p \cdot \mathbf{M} - Q R_p \mathbf{M}^p \cdot \mathbf{k}_p | \varphi_e^p \cdot \psi_g \rangle}{\varepsilon_e^p - \varepsilon_g^p} \\
&= -\gamma^2 \sum_e \frac{1}{R_p^6} \frac{\langle \varphi_e \cdot \psi_g | \mathbf{M} \cdot \mathbf{T}_p \cdot \mathbf{M}^p | \varphi_g^p \cdot \psi_g \rangle \langle \varphi_g^p \cdot \psi_g | \mathbf{M}^p \cdot \mathbf{T}_p \cdot \mathbf{M} | \varphi_e^p \cdot \psi_g \rangle}{\varepsilon_e^p - \varepsilon_g^p} \\
&\quad + \gamma^2 Q \sum_e \frac{1}{R_p^5} \frac{\langle \varphi_e^p \cdot \psi_g | \mathbf{M} \cdot \mathbf{T}_p \cdot \mathbf{M}^p | \varphi_g^p \cdot \psi_g \rangle \langle \varphi_g^p \cdot \psi_g | \mathbf{M}^p \cdot \mathbf{k}_p | \varphi_e^p \cdot \psi_g \rangle}{\varepsilon_e^p - \varepsilon_g^p} \\
&\quad + \gamma^2 Q \sum_e \frac{1}{R_p^5} \frac{\langle \varphi_e^p \cdot \psi_g | \mathbf{k}_p \cdot \mathbf{M}^p | \varphi_g^p \cdot \psi_g \rangle \langle \varphi_g^p \cdot \psi_g | \mathbf{M}^p \cdot \mathbf{T}_p \cdot \mathbf{M} | \varphi_e^p \cdot \psi_g \rangle}{\varepsilon_e^p - \varepsilon_g^p} \\
&\quad - \gamma^2 Q^2 \sum_e \frac{1}{R_p^4} \frac{\langle \varphi_e^p \cdot \psi_g | \mathbf{k}_p \cdot \mathbf{M}^p | \varphi_g^p \cdot \psi_g \rangle \langle \varphi_g^p \cdot \psi_g | \mathbf{M}^p \cdot \mathbf{k}_p | \varphi_e^p \cdot \psi_g \rangle}{\varepsilon_e^p - \varepsilon_g^p},
\end{aligned} \tag{B.79}$$

or,

$$\begin{aligned}
 \Delta E_g''(2)p &= -\gamma^2 \sum_e \frac{1}{R_j^6} \langle \psi_g | \mathbf{M} | \psi_g \rangle \cdot \mathbf{T}_p \cdot \frac{\langle \varphi_e^p | \mathbf{M}^p | \varphi_g^p \rangle \langle \varphi_g^p | \mathbf{M}^p | \varphi_e^p \rangle}{\varepsilon_e^p - \varepsilon_g^p} \cdot \mathbf{T}_p \cdot \langle \psi_g | \mathbf{M} | \psi_g \rangle \\
 &+ \gamma^2 Q \sum_e \frac{1}{R_p^5} \langle \psi_g | \mathbf{M} | \psi_g \rangle \cdot \mathbf{T}_p \cdot \frac{\langle \varphi_e^p | \mathbf{M}^p | \varphi_g^p \rangle \langle \varphi_g^p | \mathbf{M}^p | \varphi_e^p \rangle}{\varepsilon_e^p - \varepsilon_g^p} \cdot \mathbf{k}_p \\
 &+ \gamma^2 Q \sum_e \frac{1}{R_p^5} \mathbf{k}_p \cdot \frac{\langle \varphi_e^p | \mathbf{M}^p | \varphi_g^p \rangle \langle \varphi_g^p | \mathbf{M}^p | \varphi_e^p \rangle}{\varepsilon_e^p - \varepsilon_g^p} \cdot \mathbf{T}_p \cdot \langle \psi_g | \mathbf{M} | \psi_g \rangle \\
 &- \gamma^2 Q^2 \sum_e \frac{1}{R_p^4} \mathbf{k}_p \cdot \frac{\langle \varphi_e^p | \mathbf{M}^p | \varphi_g^p \rangle \langle \varphi_g^p | \mathbf{M}^p | \varphi_e^p \rangle}{\varepsilon_e^p - \varepsilon_g^p} \cdot \mathbf{k}_p \\
 &= -\gamma^2 \frac{1}{R_p^6} \boldsymbol{\mu}_g \cdot \mathbf{T}_p \cdot \alpha_g^p \cdot \mathbf{T}_p \cdot \boldsymbol{\mu}_g + \gamma^2 Q \frac{1}{R_p^5} \boldsymbol{\mu}_g \cdot \mathbf{T}_p \cdot \alpha_g^p \cdot \mathbf{k}_p + \gamma^2 Q \frac{1}{R_p^5} \mathbf{k}_p \cdot \alpha_g^p \cdot \mathbf{T}_p \cdot \boldsymbol{\mu}_g \\
 &- \gamma^2 Q^2 \frac{1}{R_p^4} \mathbf{k}_p \cdot \alpha_g^p \cdot \mathbf{k}_p,
 \end{aligned} \tag{B.80}$$

where $\alpha_g^p = 2 \sum_e \frac{\langle \varphi_e^p | \mathbf{M}^p | \varphi_g^p \rangle \langle \varphi_g^p | \mathbf{M}^k | \varphi_e^p \rangle}{\varepsilon_e^p - \varepsilon_g^p}$. Summing over all solvent molecules,

$$\begin{aligned}
 \Delta E_g''(2) &= \sum_j \Delta E_g''(2)j \\
 &= -\frac{1}{2} \gamma^2 \sum_j \frac{1}{R_j^6} \boldsymbol{\mu}_g \cdot \mathbf{T}_j \cdot \alpha_g^j \cdot \mathbf{T}_j \cdot \boldsymbol{\mu}_g + \gamma^2 Q \frac{1}{R_j^5} \boldsymbol{\mu}_g \cdot \mathbf{T}_j \cdot \alpha_g^j \cdot \mathbf{k}_j \gamma^2 Q \frac{1}{R_j^5} \mathbf{k}_j \cdot \alpha_g^j \cdot \mathbf{T}_j \cdot \boldsymbol{\mu}_g \\
 &- \gamma^2 Q^2 \frac{1}{R_j^4} \mathbf{k}_j \cdot \alpha_g^j \cdot \mathbf{k}_j.
 \end{aligned} \tag{B.81}$$

Putting together all the perturbation terms we have,

$$\begin{aligned}
 \Delta E_g &= \Delta E_g^{(1)} + \Delta E_g''(2) + \Delta E_g'''(2) \\
 &= \gamma \sum_j \frac{1}{R_j^3} \boldsymbol{\mu}_g \cdot \mathbf{T}^j \cdot \boldsymbol{\mu}_g^j - \frac{1}{2} \gamma^2 \sum_{j,k} \frac{1}{R_j^3 R_k^3} \boldsymbol{\mu}_g^j \cdot \mathbf{T}^j \cdot \alpha_g \cdot \mathbf{T}^k \cdot \boldsymbol{\mu}_g^k - \frac{1}{2} \gamma^2 \sum_j \frac{1}{R_j^6} \boldsymbol{\mu}_g \cdot \mathbf{T}^j \cdot \alpha_g^j \cdot \mathbf{T}^j \cdot \boldsymbol{\mu}_g \\
 &- \gamma Q \sum_j \frac{1}{R_j^2} \mathbf{k} \cdot \boldsymbol{\mu}_g^j + \frac{1}{2} \gamma^2 Q \sum_j \frac{1}{R_j^5} \boldsymbol{\mu}_g \cdot \mathbf{T}^j \cdot \alpha_g^j \cdot \mathbf{k} + \frac{1}{2} \gamma^2 Q \sum_j \frac{1}{R_j^5} \mathbf{k} \cdot \alpha_g^j \cdot \mathbf{T}^j \cdot \boldsymbol{\mu}_g \\
 &- \frac{1}{2} \gamma^2 Q^2 \sum_j \frac{1}{R_j^4} \mathbf{k} \cdot \alpha_g^j \cdot \mathbf{k}.
 \end{aligned} \tag{B.82}$$

For the solute excited state, we will assume that solute dipole moment changes dominate and take $\alpha_g \approx \alpha_e$. Thus, writing the difference in solvation energies of the ground and excited state $\Delta E_{e-g} \equiv \Delta E_e - \Delta E_g$, we have,

$$\Delta E_{e-g} = (\Delta E_e^{\text{d-d}} + \Delta E_e^{\text{d-id}}) - (\Delta E_g^{\text{d-d}} + \Delta E_g^{\text{d-id}}), \tag{B.83}$$

where $\Delta E_g^{\text{d-d}} = \gamma \sum_j \frac{1}{R_j^3} \boldsymbol{\mu}_g \cdot \mathbf{T}^j \cdot \boldsymbol{\mu}_g^j$ and $\Delta E_g^{\text{d-id}} = -\gamma Q \sum_j \frac{1}{R_j^2} \mathbf{k} \cdot \boldsymbol{\mu}_g^j$.

We now carry out a classical Boltzmann averaging of these terms to get the expected ensemble average $\langle \Delta E_{e-g} \rangle$. For each energy term (i.e. each solute-solvent pair), we need to evaluate the expression,

$$\left\langle (\Delta E_g^n)_j \right\rangle = \frac{1}{Z_j} \int_{\mathbf{p}_j} d\mathbf{p}_j (\Delta E_g^n)_j \exp\left(-(\Delta E_g)_j / kT\right), \tag{B.84}$$

where,

$$\int_{\mathbf{p}_j} d\mathbf{p}_j \equiv \int_{\Theta=0}^{\pi} \int_{\Phi=0}^{2\pi} \int_{\theta_j=0}^{\pi} \int_{\varphi_j=0}^{2\pi} d\Theta d\Phi d\theta_j d\varphi_j \sin \Theta \sin \theta_j, \tag{B.85}$$

and,

$$Z_j = \int_{\mathbf{p}_j} d\mathbf{p}_j \exp\left(-(\Delta E_g)_j/kT\right). \quad (\text{B.86})$$

For a charged solute, we expect that the ion-dipole interaction $\Delta E_g^{\text{i-d}}$ will be dominant, and hence use $(\Delta E_g)_j \approx (\Delta E_g^{\text{i-d}})_j$ in the Boltzmann factor. If, however, this expectation value vanishes, then we include the next most significant dipole-dipole term, $(\Delta E_g)_j \approx (\Delta E_g^{\text{i-d}})_j + (\Delta E_g^{\text{d-d}})_j$.

In terms of spherical polar coordinates, with

$$\boldsymbol{\mu}_g = [\sin \Theta \cos \Phi, \sin \Theta \sin \Phi, \cos \Theta]^T, \quad (\text{B.87})$$

we have,

$$(\Delta E_g^{\text{d-d}})_j = \frac{\gamma}{R_j^3} \boldsymbol{\mu}_g \cdot \mathbf{T}^j \cdot \boldsymbol{\mu}_g^j = \frac{\gamma}{R_j^3} \mu_g \mu_g^j (\cos \varphi_j \sin \theta_j \cos \Phi \sin \Theta + \sin \varphi_j \sin \theta_j \sin \Phi \sin \Theta - 2 \cos \theta_j \cos \Theta), \quad (\text{B.88})$$

and, $(\Delta E_g^{\text{i-d}})_j = -\gamma \frac{Q}{R_j^2} \mathbf{k} \cdot \boldsymbol{\mu}_g^j = -\gamma Q \mu_g^j \frac{1}{R_j^2} \cos \theta_j$, and the appropriate Boltzmann factor is then given by,

$$\exp\left[-\frac{1}{kT} (\Delta E_g^{\text{i-d}})_j\right] = \exp\left(\gamma \frac{Q}{kT} \mu_g^j \frac{1}{R_j^2} \cos \theta_j\right) \equiv \exp(A_j \cos \theta_j), \quad (\text{B.89})$$

with $A_j \equiv \gamma \frac{Q}{kT} \mu_g^j \frac{1}{R_j^2}$, or, if this result vanishes,

$$\begin{aligned} \exp\left[-\frac{1}{kT} \left\{(\Delta E_g^{\text{i-d}})_j + (\Delta E_g^{\text{d-d}})_j\right\}\right] &\approx \exp\left(-\frac{1}{kT} (\Delta E_g^{\text{i-d}})_j\right) \left[1 - \frac{1}{kT} (\Delta E_g^{\text{d-d}})_j\right] \\ &= \exp(A_j \cos \theta_j) \left[1 - \frac{1}{kT} \frac{\gamma}{R_j^3} \mu_g \mu_g^j (\cos \varphi_j \sin \theta_j \cos \Phi \sin \Theta + \sin \varphi_j \sin \theta_j \sin \Phi \sin \Theta - 2 \cos \theta_j \cos \Theta)\right]. \end{aligned} \quad (\text{B.90})$$

For $\langle (\Delta E_g^{\text{d-d}})_j \rangle$ the averaging with only $(\Delta E_g^{\text{i-d}})_j$ vanishes. Thus we take,

$$\begin{aligned} \langle (\Delta E_g^{\text{d-d}})_j \rangle &= \frac{1}{Z_j} \int_{\mathbf{p}_j} d\mathbf{p}_j (\Delta E_g^{\text{d-d}})_j \exp\left(\frac{1}{kT} (\Delta E_g^{\text{i-d}})_j\right) \left[1 - \frac{1}{kT} (\Delta E_g^{\text{d-d}})_j\right] \\ &= -\frac{1}{kT Z_j} \int_{\mathbf{p}_j} d\mathbf{p}_j (\Delta E_g^{\text{d-d}})_j^2 \exp(A_j \cos \theta_j) \\ &= -\frac{2}{3} \frac{\gamma^2}{kT} (\mu_g \mu_g^j)^2 \frac{1}{R_j^6} \left[2 - \frac{3}{A_j} L(A_j)\right], \end{aligned} \quad (\text{B.91})$$

where $L(A_j) \equiv \coth(A_j) - \frac{1}{A_j}$ is the Langevin function.

For $\langle (\Delta E_g^{\text{d-id}})_j \rangle$,

$$\langle (\Delta E_g^{\text{d-id}})_j \rangle = \frac{1}{Z_j} \int_{\mathbf{p}_j} d\mathbf{p}_j (\Delta E_g^{\text{d-id}})_j \exp(A_j \cos \theta_j) = \gamma^2 (\mu_g)^2 \alpha_g^j \frac{1}{R_j^6} \quad (\text{B.92})$$

For the excited state, from the Franck-Condon principle, we retain the ground state energies in the Boltzmann factors, due to the fact that the solvent cannot reorient on the time scale of the absorption process. In general, we can write the solute excited state dipole as,

$$\boldsymbol{\mu}_e = \mu_e \left\{ \frac{(\boldsymbol{\mu}_e \cdot \boldsymbol{\mu}_g) \boldsymbol{\mu}_g}{\mu_e \mu_g} + \mu_e \left[1 - \left(\frac{\boldsymbol{\mu}_e \cdot \boldsymbol{\mu}_g}{\mu_e \mu_g}\right)^2\right]^{\frac{1}{2}} (\cos \alpha \mathbf{r}_\perp + \sin \alpha \mathbf{r}'_\perp) \right\} \quad (\text{B.93})$$

where $\mathbf{r}_\perp = [\cos \Theta \cos \Phi, \cos \Theta \sin \Phi, -\sin \theta]^\top$ and $\mathbf{r}'_\perp = [-\sin \Phi, \cos \Phi, 0]^\top$.
 Hence,

$$\boldsymbol{\mu}_e = \mu_e \begin{bmatrix} \sin \Theta \cos \Phi \cos \delta + \sin \delta (\cos \Theta \cos \Phi \cos \alpha - \sin \Phi \sin \alpha) \\ \sin \Theta \sin \Phi \cos \delta + \sin \delta (\cos \Theta \sin \Phi \cos \alpha + \cos \Phi \sin \alpha) \\ \cos \Theta \cos \delta + \sin \delta (-\sin \Theta \cos \alpha) \end{bmatrix}, \quad (\text{B.94})$$

where δ is the angle between $\boldsymbol{\mu}_g$ and $\boldsymbol{\mu}_e$. Then,

$$\begin{aligned} \langle (\Delta E_e^{\text{d-d}})_j \rangle &= \frac{1}{Z_j} \int_{\mathbf{p}_j} d\mathbf{p}_j (\Delta E_e^{\text{d-d}})_j \exp\left(-\frac{1}{kT} (\Delta E_g^{\text{i-d}})_j\right) \left[1 - \frac{1}{kT} (\Delta E_g^{\text{d-d}})_j\right] \\ &= -\frac{1}{kT Z_j} \int_{\mathbf{p}_j} d\mathbf{p}_j (\Delta E_e^{\text{d-d}})_j (\Delta E_g^{\text{d-d}})_j \exp\left(-\frac{1}{kT} (\Delta E_g^{\text{i-d}})_j\right) \\ &= -\frac{2}{3} \frac{1}{kT} \frac{\gamma^2}{R_j^6} \boldsymbol{\mu}_g \cdot \boldsymbol{\mu}_e (\mu_g^j)^2 \left[2 - \frac{3}{A_j} L(A_j)\right], \end{aligned} \quad (\text{B.95})$$

and,

$$\langle (\Delta E_e^{\text{d-id}})_j \rangle = \frac{1}{Z} \int_{\mathbf{p}} d\mathbf{p} (\Delta E_e^{\text{d-id}})_j \exp(A_j \cos \Theta) = -\gamma^2 (\mu_e)^2 \alpha_g^j \frac{1}{R_j^6}. \quad (\text{B.96})$$

Combining these results, and taking identical solvent molecules, $\mu_g^j = \mu_g^s$, $\alpha_g^j = \alpha_g^s$,

$$\langle \Delta E_{e-g} \rangle = -\frac{2}{3} \frac{\gamma^2}{kT} \boldsymbol{\mu}_g \cdot (\boldsymbol{\mu}_e - \boldsymbol{\mu}_g) (\mu_g^s)^2 \sum_j \frac{1}{R_j^6} \left[2 - \frac{3}{A_j} L(A_j)\right] - \gamma^2 (\mu_e^2 - \mu_g^2) \alpha_g \sum_j \frac{1}{R_j^6}. \quad (\text{B.97})$$

Note that for $Q \rightarrow 0$, $A_j \rightarrow 0$ $\left[2 - \frac{3}{A_j} L(A_j)\right] \rightarrow 1$. We introduce the molecular density, $n_s = \frac{N_A \rho}{M}$, and take the continuum limit, i.e. $\sum_j f(R_j) \rightarrow 4\pi n \int_a^\infty dr r^2 f(r)$. Putting $A(R_j) = \gamma Q \frac{\mu_g^s}{kT} \frac{1}{R_j^2} \equiv \frac{B}{R_j^2}$, where $B \equiv \gamma Q \frac{\mu_g^s}{kT}$, we have,

$$\begin{aligned} \sum_j \frac{1}{R_j^6} \left[2 - \frac{3}{A_j} L(A_j)\right] &\rightarrow 4\pi n_s \int_a^\infty dr \frac{1}{r^4} \left[2 + \frac{3r^4}{B^2} \left(1 - \frac{B}{r^2} \coth\left(\frac{B}{r^2}\right)\right)\right] \\ &= \frac{4\pi n_s}{3} \frac{1}{a^3} \left\{ 3a^3 \int_a^\infty dr \frac{1}{r^4} \left[2 + \frac{3r^4}{B^2} \left(1 - \frac{B}{r^2} \coth\left(\frac{B}{r^2}\right)\right)\right] \right\} \\ &\equiv \frac{4\pi n_s}{3} \frac{1}{a^3} \Xi(a, B), \end{aligned} \quad (\text{B.98})$$

where we define the integral function,

$$\begin{aligned} \Xi(a, B) &= 3a^3 \int_a^\infty dr \frac{1}{r^4} \left[2 + \frac{3r^4}{B^2} \left(1 - \frac{B}{r^2} \coth\left(\frac{B}{r^2}\right)\right)\right] \\ &= 3 \left(\frac{a}{\sqrt{B}}\right)^3 \int_{a/\sqrt{B}}^\infty dx \frac{1}{x^4} \left[2 + 3x^4 \left(1 - \frac{1}{x^2} \coth\left(\frac{1}{x^2}\right)\right)\right] = \Xi\left(\frac{a}{\sqrt{B}}\right). \end{aligned} \quad (\text{B.99})$$

Moreover,

$$\sum_j \frac{1}{R_j^6} \rightarrow n \int_{r=a}^\infty \int_{\theta=0}^\pi \int_{\varphi=0}^{2\pi} dr d\theta d\varphi r^2 \sin \theta r^{-6} = n \int_{r=a}^\infty dr r^{-4} \int_{\theta=0}^\pi d\theta \sin \theta \int_{\varphi=0}^{2\pi} d\varphi = \frac{4\pi n_s}{3} \frac{1}{a^3} \quad (\text{B.100})$$

Substitution into Eq. B.97 yields,

$$\langle \Delta E_{e-g} \rangle = -\frac{2\gamma}{a^3} \Xi \left(\frac{a}{\sqrt{B}} \right) \boldsymbol{\mu}_g \cdot (\boldsymbol{\mu}_e - \boldsymbol{\mu}_g) \frac{n_s}{3\varepsilon_0} \frac{(\mu_g^s)^2}{3kT} - \frac{\gamma}{a^3} (\mu_e^2 - \mu_g^2) \frac{n_s}{3\varepsilon_0} \alpha_g^s \quad (\text{B.101})$$

Using the Clausius-Debye equation [48]

$$\frac{n_s}{3\varepsilon_0} \left(\frac{(\mu_g^s)^2}{3kT} + \alpha_s \right) = \frac{\varepsilon_s - 1}{\varepsilon_s + 2} \equiv \varphi(\varepsilon_s)$$

and the Clausius-Mossotti equation,

$$\frac{n_s}{3\varepsilon_0} \alpha_g^s = \frac{n^2 - 1}{n^2 + 2} \equiv \varphi(n^2),$$

where,

$$\varphi(x) \equiv \frac{x - 1}{x + 2}, \quad (\text{B.102})$$

then,

$$\langle \Delta E_{e-g} \rangle = -\frac{2\gamma}{a^3} \Xi \left(\frac{a}{\sqrt{B}} \right) \boldsymbol{\mu}_g \cdot (\boldsymbol{\mu}_e - \boldsymbol{\mu}_g) (\varphi(\varepsilon_s) - \varphi(n^2)) - \frac{\gamma}{a^3} (\mu_e^2 - \mu_g^2) \varphi(n^2). \quad (\text{B.103})$$

If we now assume the special case of a symmetric displacement of charge about the molecular centre, we impose an origin of coordinates such that $\boldsymbol{\mu}_e = -\boldsymbol{\mu}_g = \frac{1}{2}\Delta\boldsymbol{\mu}$, then,

$$\Delta E_{\text{solv}} \equiv \langle \Delta E_{e-g} \rangle = \frac{\gamma}{a^3} \Xi \left(\frac{a}{\sqrt{B}} \right) (\Delta\mu)^2 (\varphi(\varepsilon_s) - \varphi(n^2)). \quad (\text{B.104})$$

For the expected corresponding solvent-induced bandwidth, we need to evaluate, $\sigma_{e-g}^2 = \langle \Delta E_{e-g}^2 \rangle - \langle \Delta E_{e-g} \rangle^2$. For the first term, we perform the following expansion and carry out classical averaging as above.

$$\begin{aligned} \Delta E_{e-g}^2 &= \left[\left(\sum_j (\Delta E_e^{\text{d-d}})_j + \sum_j (\Delta E_e^{\text{d-id}})_j \right) - \left(\sum_j (\Delta E_g^{\text{d-d}})_j + \sum_j (\Delta E_g^{\text{d-id}})_j \right) \right]^2 \\ &= \left[\sum_j (\Delta E_e^{\text{d-d}})_j \right]^2 + \left[\sum_j (\Delta E_e^{\text{d-id}})_j \right]^2 + \left[\sum_j (\Delta E_g^{\text{d-d}})_j \right]^2 + \left[\sum_j (\Delta E_g^{\text{d-id}})_j \right]^2 \\ &= \left[\sum_j \sum_k (\Delta E_e^{\text{d-d}})_j (\Delta E_e^{\text{d-d}})_k \right] + \left[\sum_j \sum_k (\Delta E_e^{\text{d-id}})_j (\Delta E_e^{\text{d-id}})_k \right] \\ &\quad + \left[\sum_j \sum_k (\Delta E_g^{\text{d-d}})_j (\Delta E_g^{\text{d-d}})_k \right] + \left[\sum_j \sum_k (\Delta E_g^{\text{d-id}})_j (\Delta E_g^{\text{d-id}})_k \right] \\ &\quad + 2 \sum_j \sum_k (\Delta E_e^{\text{d-d}})_j (\Delta E_e^{\text{d-id}})_k - 2 \sum_j \sum_k (\Delta E_e^{\text{d-d}})_j (\Delta E_g^{\text{d-d}})_k - 2 \sum_j \sum_k (\Delta E_e^{\text{d-d}})_j (\Delta E_g^{\text{d-id}})_k \\ &\quad - 2 \sum_j \sum_k (\Delta E_e^{\text{d-id}})_j (\Delta E_g^{\text{d-d}})_k - 2 \sum_j \sum_k (\Delta E_e^{\text{d-id}})_j (\Delta E_g^{\text{d-id}})_k + \sum_j \sum_k (\Delta E_g^{\text{d-d}})_j (\Delta E_g^{\text{d-id}})_k. \end{aligned} \quad (\text{B.105})$$

The following dominant terms are,

$$\begin{aligned} \left\langle \sum_j \sum_k (\Delta E_e^{\text{d-d}})_j (\Delta E_e^{\text{d-d}})_k \right\rangle &= \frac{2}{3} \gamma^2 \mu_e^2 \mu_s^2 \sum_j \frac{1}{R_j^6} \left(2 - \frac{3}{A_j} L(A_j) \right), \\ \left\langle \sum_j \sum_k (\Delta E_g^{\text{d-d}})_j (\Delta E_g^{\text{d-d}})_k \right\rangle &= \frac{2}{3} \gamma^2 \mu_g^2 \mu_s^2 \sum_j \frac{1}{R_j^6} \left(2 - \frac{3}{A_j} L(A_j) \right), \end{aligned}$$

and,

$$\left\langle \sum_j \sum_k (\Delta E_e^{\text{d-d}})_j (\Delta E_g^{\text{d-d}})_k \right\rangle = \frac{2}{3} \gamma^2 (\boldsymbol{\mu}_g \cdot \boldsymbol{\mu}_e) \mu_s^2 \sum_j \frac{1}{R_j^6} \left(2 - \frac{3}{A_j} L(A_j) \right),$$

so that,

$$\begin{aligned} \langle \Delta E_{e-g}^2 \rangle &\rightarrow \frac{2}{3} \gamma^2 (\mu_g^2 + \mu_e^2 - 2\boldsymbol{\mu}_g \cdot \boldsymbol{\mu}_e) \mu_s^2 \sum_j \frac{1}{R_j^6} \left(2 - \frac{3}{A_j} L(A_j) \right) \\ &= \frac{2}{3} \gamma^2 |\boldsymbol{\mu}_g - \boldsymbol{\mu}_e|^2 \mu_s^2 \sum_j \frac{1}{R_j^6} \left(2 - \frac{3}{A_j} L(A_j) \right). \end{aligned} \quad (\text{B.106})$$

Once again, switching to a continuum, with, $A(R_j) = \gamma Q \frac{\mu_s^s}{kT} \frac{1}{R_j^2} \equiv \frac{B}{R_j^2}$, $B \equiv \gamma Q \frac{\mu_s^s}{kT}$ we have as before, $\sum_j \frac{1}{R_j^6} \left[2 - \frac{3}{A_j} L(A_j) \right] \rightarrow \frac{4\pi}{3} \frac{n_s}{a^3} \Xi(a, B)$, and,

$$\langle \Delta E_{e-g}^2 \rangle = \frac{2}{3} \frac{\gamma}{a^3} \Xi \left(\frac{a}{\sqrt{B}} \right) |\boldsymbol{\mu}_g - \boldsymbol{\mu}_e|^2 \left(\frac{n_s}{3\varepsilon_0} \right) \mu_s^2. \quad (\text{B.107})$$

Given that all terms in $\langle \Delta E_{e-g} \rangle^2$ depend on higher orders of $(1/a^3)$ we have,

$$\sigma_{e-g}^2 \approx \langle \Delta E_{e-g}^2 \rangle = \frac{2}{3} \frac{\gamma}{a^3} \Xi \left(\frac{a}{\sqrt{B}} \right) |\boldsymbol{\mu}_g - \boldsymbol{\mu}_e|^2 \left(\frac{n_s}{3\varepsilon_0} \right) \mu_s^2 = \frac{2}{3} \frac{\gamma}{a^3} \Xi \left(\frac{a}{\sqrt{B}} \right) (\Delta\mu)^2 \left(\frac{n_s}{3\varepsilon_0} \right) \mu_s^2, \quad (\text{B.108})$$

where we assume $\boldsymbol{\mu}_e \parallel \boldsymbol{\mu}_g$, so that in terms of $\langle \Delta E_{e-g} \rangle = \frac{\gamma}{a^3} \Xi \left(\frac{a}{\sqrt{B}} \right) (\Delta\mu)^2 \frac{n_s}{3\varepsilon_0} \frac{\mu_s^2}{3kT}$ we can write,

$$\sigma_{e-g}^2 = 2kT \langle \Delta E_{e-g} \rangle \equiv 2kT \Delta E_{\text{solv}}. \quad (\text{B.109})$$

C. Auxiliary results from theoretical (TD-)DFT calculations

	Crystal structure [1A]PF₆	Theoretical structure [1]⁺(H)
Bond lengths (Å)		
B-C(11)	1.592	1.573
B-N(21)	1.613	1.596
B-N(31)	1.580	1.579
N(21)-C(26)	1.360	1.351
N(31)-C(36)	1.352	1.355
C(26)-C(36)	1.457	1.459
Bond angles (°)		
N(21)-B-N(31)	94.9	95.5
B-N(21)-C(26)	112.5	112.8
B-N(31)-C(36)	113.8	113.1
N(21)-C(26)-C(36)	109.2	109.2
N(31)-C(36)-C(26)	109.4	109.3
Dihedrals (°)		
C(25)-C(26)-C(36)-C(35)	-2.2	+0.4
C(1)-B-C(11)-C(12)	39.7	34.9

Table C.1.: Comparison of selected bond lengths, angles and dihedrals from (a) X-ray diffractometry structure determination of **[1A]PF₆** and (b) theoretical structure for prototype **[1]⁺(H)** from DFT calculations.

Transition	Coeff.	HOMO	→	LUMO	λ (nm)	E (eV)	$E_{\text{HOMO-LUMO}}$	f
1	0.70	[0]	→	[0]	1058	1.17	1.66	0.0006
2	0.70	[-1]	→	[0]	1029	1.20	1.69	0.0028
3	0.70	[-2]	→	[0]	699	2.01	2.67	0.0084
4	0.68	[0]	→	[+1]	598	2.07	2.64	0.0004
	-0.13	[0]	→	[+2]				
	0.12	[-1]	→	[+1]				
5	0.68	[-1]	→	[+1]	589	2.10	2.67	0.0031
	-0.13	[-1]	→	[+2]				
	-0.12	[0]	→	[+2]				
6	0.66	[0]	→	[+2]	548	2.26	2.94	0.0013
	0.15	[0]	→	[+4]				
	-0.12	[-1]	→	[+5]				
	0.11	[0]	→	[+2]				
7	0.64	[-1]	→	[+2]	543	2.28	3.12	0.0004
	0.17	[-1]	→	[+4]				
	0.15	[0]	→	[+5]				
	-0.11	[-1]	→	[+6]				
	0.10	[-1]	→	[+1]				
8	0.41	[0]	→	[+5]	516	2.40	5.11	0.0002
	0.38	[-1]	→	[+4]				
	-0.26	[-1]	→	[+2]				
	-0.24	[-1]	→	[+6]				
	-0.19	[0]	→	[+4]				
	0.12	[-1]	→	[+5]				
9	0.51	[-3]	→	[0]	499	2.48	2.97	0.0013
	0.47	[-4]	→	[0]				
	0.11	[-5]	→	[0]				
10	0.51	[-4]	→	[0]	492	2.52	2.96	0.0003
	-0.48	[-3]	→	[0]				

Table C.2.: Calculated lowest-energy electronic transitions for $[\mathbf{1}]^+(\text{H})$ from TD-DFT calculations.

Bibliography

- [1] K. Ma, M. Scheibitz, S. Scholz, and M. Wagner. Applications of boron-nitrogen and boron-phosphorus adducts in organometallic chemistry. *J. Organomet. Chem.*, 652:11–19, 2002.
- [2] K. Ma, F. Fabrizi de Biani, M. Bolte, P. Zanello, and M. Wagner. Electronic communication in a series of novel multistep redox systems. *Organometallics*, 21:3979–3989, 2002.
- [3] L. Ding, K. Ma, F. Fabrizi de Biani, M. Bolte, P. Zanello, and M. Wagner. Electronic communication in a novel five-step redox system. *Organometallics*, 20:1041–1043, 2001.
- [4] L. Ding, K. Ma, M. Bolte, F. Fabrizi de Biani, P. Zanello, and M. Wagner. Multistep redox properties of 2,2'-bipyridylboronium substituted ferrocenes. *J. Organomet. Chem.*, 637-639:390–397, 2001.
- [5] L. Ding, F. Fabrizi de Biani, M. Bolte, P. Zanello, and M. Wagner. Reactivity of ferrocenylboranes: rearrangements versus electron transfer reactions. *Organometallics*, 19:5763–5768, 2000.
- [6] F. Jäkle, T. Priermeier, and M. Wagner. Synthesis, structure, and dynamic behaviour of ansa-ferrocenes with pyrazabole bridges. *Organometallics*, 15:2033–2040, 1996.
- [7] F. Fabrizi de Biani, T. Gmeinwieser, E. Herdtweck, F. Jäkle, F. Laschi, M. Wagner, and P. Zanello. Multistep redox processes and intramolecular charge transfer in ferrocene-based 2,2'-bipyridylboronium salts. *Organometallics*, 16:4776–4787, 1997.
- [8] M. D. Thomson, H.G. Roskos, and M. Wagner. On the way to 'optical doping' of electronically low-dimensional polymer systems with strong charge and spin correlations. *Appl. Phys. A*, 78:477–481, 2004.
- [9] L. Ding, K. Ma, G. Dürner, M. Bolte, F. Fabrizi de Biani, P. Zanello, and M. Wagner. Reactions of ferrocenylboranes with 2,5-bis(pyridyl)pyrazine and quaterpyridine: charge-transfer complexes and redox-active macrocycles. *J. Chem. Soc. Dalton Trans.*, pages 1566–1573, 2002.
- [10] S. Guo, F. Peters, F. Fabrizi de Biani, J. W. Bats, E. Herdtweck, P. Zanello, and M. Wagner. Electronic communication in oligometallic complexes with ferrocene-based tris(1-pyrazolyl)borate ligands. *Inorg. Chem.*, 40:4928–4936, 2001.
- [11] M. Grosche, E. Herdtweck, F. Peters, and M. Wagner. Boron-nitrogen coordination polymers bearing ferrocene in the main chain. *Organometallics*, 18:4669–4672, 1999.
- [12] M. Fontani, F. Peters, W. Scherer, W. Wachter, M. Wagner, and P. Zanello. Adducts of ferrocenylboranes and pyridine bases: generation of charge-transfer complexes and reversible coordination polymers. *Eur. J. Inorg. Chem.*, pages 1453–1465, 1998.

- [13] E. Herdtweck, F. Peters, W. Scherer, and M. Wagner. Sterically demanding ferrocene-based tris(1-pyrazolyl)borate ligands. *Polyhedron*, 17:1149–1157, 1998.
- [14] F. Fabrizi de Biani, F. Jäkle, M. Spiegler, M. Wagner, and P. Zanello. Ferrocene-based tris(1-pyrazolyl)borates: a new approach to heterooligometallic complexes and organometallic polymers containing transition metal atoms in the backbone. *Inorg. Chem.*, 36:2103–2111, 1997.
- [15] D. O. Cowan, C. LeVanda, J. Park, and F. Kaufman. Mixed-valence ferrocene chemistry. *Acc. Chem. Res.*, 6:1–7, 1973.
- [16] J. S. Miller and M. Drillon (Ed.s). *Magnetism: molecules to materials*. Wiley-VCH, Weinheim, 2001.
- [17] K. Itoh and M. Kinoshita (Ed.s). *Molecular magnetism, new magnetic materials*. Kodansha, Tokyo, 2000.
- [18] J. S. Miller, A. J. Epstein, and W. M. Reiff. Ferromagnetic molecular charge-transfer complexes. *Chem. Rev.*, 88:201–220, 1988.
- [19] J. S. Miller, J. C. Calabrese, H. Rommelmann, S. R. Chitipreddi, J. H. Zhang, W. M. Reiff, and A. J. Epstein. Ferromagnetic behaviour of $[\text{Fe}(\text{C}_5\text{Me}_5)_2]^+[\text{TCNE}]^-$. Structural and magnetic characterization of decamethylferrocenium tetracyanoethenide, $[\text{Fe}(\text{C}_5\text{Me}_5)_2]^+[\text{TCNE}]^+\text{MeCN}$, and decamethylferrocenium pentacyanopropenide, $[\text{Fe}(\text{C}_5\text{Me}_5)_2]^+[\text{C}_3(\text{CN})_5]^-$. *J. Am. Chem. Soc.*, 109:769–781, 1987.
- [20] J. S. Miller, J. C. Calabrese, A. J. Epstein, R. W. Bigelow, J. H. Zhang, and W. M. Reiff. Ferromagnetic properties of one-dimensional decamethylferrocenium tetracyanoethylene (1:1): $[\text{Fe}(\eta^5\text{-C}_5\text{Me}_5)_2]^+[\text{TCNE}]^-$. *J. Chem. Soc. Chem. Commun.*, pages 1026–1028, 1986.
- [21] I. Asselberghs, K. Clays, A. Persoons, A. M. McDonagh, M. D. Ward, and J. A. McCleverty. In situ reversible electrochemical switching of the molecular first hyperpolarizability. *Chem. Phys. Lett.*, 368:408–411, 2003.
- [22] K. Roque, F. Barangé, G. G. A. Balavoine, J. Daran, P. G. Lacroix, and E. Manoury. New chiral ferrocenyl-pyridinium salts for non-linear optics. *J. Organomet. Chem.*, 637-639:531–537, 2001.
- [23] M. Malaun, Z. R. Reeves, R. L. Paul, J. C. Jeffrey, J. A. McCleverty, M. D. Ward, I. Asselberghs, K. Clays, and A. Persoons. Reversible switching of the first hyperpolarizability of an NLO-active donor-acceptor molecule based on redox interconversion of the octamethylferrocene donor unit. *Chem. Commun.*, pages 49–50, 2001.
- [24] S. Barlow, H. E. Bunting, C. Ringham, J. C. Green, G. U. Bublitz, S. G. Boxer, J. W. Perry, and S. R. Marder. Studies of the electronic structure of metallocene-based second-order nonlinear optical dyes. *J. Am. Chem. Soc.*, 121:3715–3723, 1999.

- [25] V. Alain, A. Fort, M. Barzoukas, C. Chen, M. Blanchard-Desce, S. R. Marder, and J. W. Perry. The linear and non-linear optical properties of some conjugated ferrocene compounds with potent heterocyclic acceptors. *Inorg. Chim. Acta*, 242:43–49, 1996.
- [26] M. Blanchard-Desce, C. Runser, A. Fort, M. Barzoukas, J. Lehn, V. Bloy, and V. Alain. Large quadratic hyperpolarizabilities with donor-acceptor polyenes functionalized with strong donors. Comparison with donor-acceptor diphenylpolyenes. *Chem. Phys.*, 199:253–261, 1995.
- [27] B. J. Coe, C. J. Jones, J. A. McCleverty, D. Bloor, and G. Cross. An assessment of second harmonic generation by donor acceptor molecules containing stilbenyl or diarylazo bridges between ferrocenyl donor and nitro acceptor groups. *J. Organomet. Chem.*, 464:225–232, 1994.
- [28] R. Loucif-Saïbi, J. A. Delaire, L. Bonazzola, G. Doisneau, G. Balavoine, T. Fillebeen-Khan, I. Ledoux, and G. Puccetti. Molecular hyperpolarizabilities of new bimetallic ferrocenyl derivatives. *Chem. Phys.*, 167:369–375, 1992.
- [29] J. C. Calabrese, L. Cheng, J. C. Green, S. R. Marder, and W. Tam. Molecular second-order optical nonlinearities of metallocenes. *J. Am. Chem. Soc.*, 113:7227–7232, 1991.
- [30] M. L. H. Green, S. R. Marder, M. E. Thompson, J. A. Bandy, D. Bloor, P. V. Kolinsky, and R. J. Jones. Synthesis and structure of (cis)-[1-ferrocenyl-2-(4-nitrophenyl)ethylene], and organotransition metal compound with a large second-order optical nonlinearity. *Nature*, 330:360–362, 1987.
- [31] E. Baigar, P. Gilch, W. Zinth, M. Stöckl, P. Härter, T. von Felitzsch, and M. E. Michel-Beyerle. Ultrafast intramolecular electron transfer from a ferrocene donor moiety to a Nile blue acceptor. *Chem. Phys. Lett.*, 352:176–184, 2002.
- [32] M. Fujitsuka, N. Tsuboya, R. Hamasaki, M. Ito, S. Onodera, O. Ito, and Y. Yamamoto. Solvent polarity dependence of photoinduced charge separation and recombination processes of ferrocene- C_{60} dyads. *J. Phys. Chem. A*, 107:1452–1458, 2003.
- [33] D. M. Guldi, M. Maggini, G. Scorrano, and M. Prato. Intramolecular electron transfer in fullerene/ferrocene based donor-bridge-acceptor dyads. *J. Am. Chem. Soc.*, 119:974–980, 1997.
- [34] H. Fukutome, A. Takahashi, and M. Ozaki. Design of conjugated polymers with polaronic ferromagnetism. *Chem. Phys. Lett.*, 133:34–38, 1987.
- [35] M. M. Murray, P. Kaszynski, D. S. Kaisaki, W. Chang, and D. A. Dougherty. Prototypes for the polaronic ferromagnet. Synthesis and characterization of high-spin organic polymers. *J. Am. Chem. Soc.*, 116:8152–8161, 1994.
- [36] K. K. Anderson and D. A. Dougherty. An improved model for one-dimensional polaronic ferromagnetism: electrochemically doped poly(m-phenylene-fuchsome). *Adv. Mater.*, 10:688–692, 1998.
- [37] M. Klessinger and J. Michl. *Excited states and photochemistry of organic molecules*. VCH Publishers Inc., New York, 1995.

- [38] V. May and O. Kühn. *Charge and energy transfer dynamics in molecular systems*. Wiley-VCH, Berlin, 1st edition, 2000.
- [39] B. Balzer, S. Hahn, and G. Stock. Mechanism of a photochemical funnel: a dissipative wave-packet dynamics study. *Chem. Phys. Lett.*, 379:351–358, 2003.
- [40] D. G. Truhlar and C. A. Mead. Relative likelihood of encountering conical intersections and avoided intersections on the potential energy surfaces of polyatomic molecules. *Phys. Rev. A*, 68:032501–032502, 2003.
- [41] A. Dreuw and M. Head-Gordon. Failure of the time-dependent density functional theory for long-range charge-transfer excited states: the zincbacteriochlorin-bacteriochlorin and bacteriochlorophyll-spherodiene complexes. *J. Am. Chem. Soc.*, 126:4007–4016, 2004.
- [42] R. S. Mulliken. Molecular compounds and their spectra. II. *J. Am. Chem. Soc.*, 74:811–824, 1952.
- [43] J. N. Murrell. The theory of charge-transfer spectra. *Chem. Rev. Quart. Rev.*, 15:191–206, 1961.
- [44] T. Förster. Delocalized excitation and excitation transfer. In O. Sinanoğlu, editor, *Modern quantum chemistry. Istanbul lectures. Part III*, pages 93–137. Academic Press, New York, 1965.
- [45] M. Kasha, H. R. Rawls, and M. Ashraf el Bayoumi. The exciton model in molecular spectroscopy. *Pure Appl. Chem.*, 11:371–392, 1965.
- [46] E. R. Brown, J. Sandifer, B. W. Rossiter (Ed.), and J. F. Hamilton (Ed.). *Physical methods in chemistry. Electrochemical methods*. Wiley, New York, 1986.
- [47] S. I. Gorelsky, V. Y. Kotov, and A. B. P. Lever. Vertical ionization energies and electron affinities of ions in solution from outer-sphere charge transfer transition energies. *Inorg. Chem.*, 37:4584–4588, 1998.
- [48] A. T. Amos and B. L. Burrows. Solvent-shift effects on electronic spectra and excited-state dipole moments and polarizabilities. *Adv. Quant. Chem.*, 7:289–313, 1973.
- [49] P. Suppan. Solvatochromic shifts: the influence of the medium on the energy of electronic states. *J. Photochem. Photobiol. A*, 50:293–330, 1990.
- [50] C. Reichardt. *Solvents and solvent effects in organic chemistry*. VCH Verlagsgesellschaft, Weinheim, 1988.
- [51] P. Fromherz. Monopole-dipole model for symmetrical solvatochromism of hemicyanine dyes. *J. Phys. Chem.*, 99:7188–7192, 1995.
- [52] J. D. Jackson. *Classical electrodynamics*. Wiley, New York, 2nd edition, 1975.
- [53] T. J. Kealy and P. L. Pauson. A new type of organo-iron compound. *Nature (London)*, 168:1039–1040, 1951.
- [54] S. A. Miller, J. A. Tebboth, and J. F. Tremaine. Dicyclopentadienyliron. *J. Chem. Soc.*, pages 632–635, 1952.

- [55] R. B. Woodward, M. Rosenblum, and M. C. Whiting. A new aromatic system. *J. Amer. Chem. Soc.*, 74:3458–3459, 1952.
- [56] K. R. Gordon and K. D. Warren. Spectroscopic and magnetic studies of the 3d metallocenes. *Inorg. Chem.*, 17:987–994, 1978.
- [57] Y. S. Sohn, D. N. Hendrickson, and H. B. Gray. Electronic structure of metallocenes. *J. Am. Chem. Soc.*, 93:3603–3612, 1971. Testing the note feature.
- [58] A. T. Armstrong, E. Elder F. Smith, and S. P. McGlynn. Electronic absorption spectrum of ferrocene. *J. Chem. Phys.*, 46:4321–4328, 1967.
- [59] D. R. Scott and R. S. Becker. Comprehensive investigation of the electronic spectroscopy and theoretical treatments of ferrocene and nickelocene. *J. Chem. Phys.*, 35:516–531, 1961.
- [60] D. R. Scott and R. S. Becker. Ligand field absorption bands and d-orbital splitting in ferrocene. *J. Organomet. Chem.*, 4:409–411, 1965.
- [61] S. Yamada, A. Nakahara, and R. Tsuchida. Dichroism of the crystal of dicyclopentadienyl-iron. *J. Chem. Phys.*, 22:1620–1621, 1954.
- [62] M. Rosenblum, J. O. Santer, and W. G. Howells. The chemistry and structure of ferrocene. VIII. Interannular resonance and the mechanism of electrophilic substitution. *J. Am. Chem. Soc.*, 85:1450–1458, 1963.
- [63] D. N. Hendrickson. Electronic structure of ferrocene. *Inorg. Chem.*, 11:1161–1162, 1972.
- [64] H. H. Jaffé. The electronic structure of ferrocene. *J. Chem. Phys.*, 21:156–157, 1953.
- [65] K. Warren. Ligand field theory of metal sandwich complexes. *Struct. Bonding*, 27:45–159, 1976.
- [66] G. Wilkinson and F. A. Cotton. Cyclopentadienyl and arene metal complexes. *Prog. Inorg. Chem.*, 1:1–124, 1959.
- [67] A. T. Armstrong, D. G. Carroll, and S. P. McGlynn. Semiempirical molecular-orbital calculations. IV. Some metallocenes. *J. Chem. Phys.*, 47:1104–1111, 1967.
- [68] M. C. Zerner, G. H. Loew, R. F. Kirchner, and U. T. Mueller-Westerhoff. An intermediate neglect of differential overlap technique for spectroscopy of transition-metal complexes. Ferrocene. *J. Am. Chem. Soc.*, 102:589–599, 1980.
- [69] N. Roesch and K. H. Johnson. An SCG $X\alpha$ scattered-wave calculation for ferrocene. *Chem. Phys. Lett.*, 24:179–184, 1974.
- [70] N. Rösch and H. Jörg. A linear combination of Gaussian-type orbitals (LCGTO) $X\alpha$ study of ferrocene: The metal-to-ring distance and ionization potentials. *J. Chem. Phys.*, 84:5967–5968, 1986.
- [71] M. Rohmer, A. Veillard, and M. H. Wood. Excited states and electronic spectrum of ferrocene. *Chem. Phys. Lett.*, 29:466–468, 1974.

- [72] P. S. Bagus, U. I. Walgren, and J. Almlöf. A theoretical study of the electronic structure of ferrocene and ferricinium: Application to Mössbauer isomer shifts, ionization potentials, and conformation. *J. Chem. Phys.*, 64:2324–2334, 1976.
- [73] H. P. Lüthi, J. H. Ammeter, J. Almlöf, and K. Faegri Jr.. How well does the Hartree-Fock model predict equilibrium geometries of transition metal complexes? Large-scale LCAO-SCF studies on ferrocene and decamethylferrocene. *J. Chem. Phys.*, 77:2002–2009, 1982.
- [74] C. Park and J. Almlöf. The electronic and molecular structure of ferrocene. *J. Chem. Phys.*, 95:1829–1833, 1991.
- [75] K. Pierloot, B. Joakim Persson, and B. O. Roos. Theoretical study of the chemical bonding in Ni(C₂H₄) and ferrocene. *J. Phys. Chem.*, 99:3465–3472, 1995.
- [76] H. Koch, P. Jørgensen, and T. Helgaker. The molecular structure of ferrocene. *J. Chem. Phys.*, 104:9528–9530, 1996.
- [77] K. Ishimura, M. Hada, and H. Nakatsuji. Ionized and excited states of ferrocene: symmetry adapted cluster-configuration-interaction study. *J. Chem. Phys.*, 117:6533–6537, 2002.
- [78] L. Fan and T. Ziegler. Optimization of molecular structures by self-consistent and non-local density-functional theory. *J. Chem. Phys.*, 95:7401–7408, 1991.
- [79] A. Bérces, T. Ziegler, and L. Fan. Density functional study of the harmonic force fields of Cp⁻, LiCp, and ferrocene. *J. Phys. Chem.*, 98:1584–1595, 1994.
- [80] N. Matsuzawa, J. Seto, and D. A. Dixon. Density functional theory predictions of second-order hyperpolarizabilities of metallocenes. *J. Phys. Chem. A*, 101:9391–9398, 1997.
- [81] M. J. Mayor-López and J. Weber. DFT calculations of the binding energies of metallocenes. *Chem. Phys. Lett.*, 281:226–232, 1997.
- [82] G. Schreckenbach. The ⁵⁷Fe nuclear magnetic resonance shielding in ferrocene revisited. A density-functional study of orbital energies, shielding mechanisms, and the influence of the exchange-correlation functional. *J. Chem. Phys.*, 110:11936–11949, 1999.
- [83] G. Frenking. Understanding the nature of the bonding in transition metal complexes: from Dewar’s molecular orbital model to an energy partitioning analysis of the metal-ligand bond. *J. Organomet. Chem.*, 635:9–23, 2001.
- [84] M. Lein, J. Frunzke, A. Timoshkin, and G. Frenking. Iron bis(pentazole) Fe(η⁻n₅)₂, a theoretically predicted high-energy compound: Structure, bonding analysis, metal-ligand bond strength and a comparison with the isoelectronic ferrocene. *Chem. Eur. J.*, 7:4155–4163, 2001.
- [85] Z. Xu, Y. Xie, W. Feng, and H. F. Schaefer III. Systematic investigation of electronic and molecular structures for the first transition metal series metallocenes M(C₅H₅)₂ (M = V, Cr, Mn, Fe, Co and Ni). *J. Phys. Chem. A*, 107:2716–2729, 2003.

- [86] P. Boulet, H. Chermette, C. Daul, F. Gilardoni, F. Rogemond, J. Weber, and G. Zuber. Absorption spectra of several metal complexes revisited by the time-dependent density-functional theory-response theory formalism. *J. Phys. Chem. A*, 105:885–894, 2001.
- [87] C. Daul, H. Güdel, and J. Weber. A density functional investigation of the ground- and excited-state properties of ruthenocene. *J. Chem. Phys.*, 98:4023–4029, 1993.
- [88] R. K. Bohn and A. Haaland. On the molecular structure of ferrocene, $\text{Fe}(\text{C}_5\text{H}_5)_2$. *J. Organomet. Chem.*, 5:470–476, 1966.
- [89] J. D. Dunitz, L. E. Orgel, and A. Rich. The crystal structure of ferrocene. *Acta Crystallogr.*, 9:373–375, 1956.
- [90] A. Haaland. Molecular structure and bonding in the 3d metallocenes. *Acc. Chem. Res.*, 12:415–422, 1979.
- [91] J. A. Page and G. Wilkinson. The polarographic chemistry of ferrocene, ruthenocene and the metal hydrocarbon ions. *J. Amer. Chem. Soc.*, 74:6149–6150, 1952.
- [92] M. M. Sabbatini and E. Cessarotti. The additivity of the substituents effects on the polarographic potentials of ferrocene derivatives. *Inorg. Chim. Acta*, 24:L9–L10, 1977.
- [93] S. Evans, M. L. H. Green, B. Jewitt, A. F. Orchard, and C. F. Pygall. Electronic structure of metal complexes containing π -cyclopentadienyl and related ligands. *J. Chem. Soc. Faraday Trans. II*, 68:1847–1865, 1972.
- [94] M. L. Ceccarani, P. Sassi, and R. S. Cataliotti. Electronic transitions in metallocenes by resonance Raman scattering. *J. Chem. Soc. Faraday Trans.*, 90:1397–1403, 1994.
- [95] D. Nielson, D. Boone, and H. Eyring. Magnetic circular dichroism of ferrocene and substituted ferrocenes: the d-d transitions. *J. Phys. Chem.*, 76:511–515, 1972.
- [96] D. Nielson, M. Farmer, and H. Eyring. Electronic absorption and magnetic circular dichroism spectra of ferrocene. *J. Phys. Chem.*, 80:717–721, 1976.
- [97] J. L. Robbins, N. Edelstein, B. Spencer, and J. C. Smart. Syntheses and electronic structures of decamethylmetallocenes. *J. Am. Chem. Soc.*, 104:1882–1893, 1982.
- [98] P. W. Atkins. *Physical chemistry*. Oxford university press, Oxford, 4th edition, 1990.
- [99] E. A. Kassab, M. I. Marzouk, and M. el Hashash. Substituted ferrocenes: synthesis and correlation of their electronic spectra with structure (LFER). *J. Serb. Chem. Soc.*, 67:593–603, 2002.
- [100] R. E. Bozak. Photochemistry in the metallocenes. *Adv. Photochem.*, 8:227–244, 1972.
- [101] H. Sponer and E. Teller. Electronic spectra of polyatomic molecules. *Rev. Mod. Phys.*, 13:76–182, 1941.

- [102] E. Kraus and J. Ferguson. The spectroscopy of the $[\text{Ru}(\text{bpy})_3]^{2+}$ system. *Prog. Inorg. Chem.*, 37:293–391, 1989.
- [103] A. Togni and T. Hayashi (ed.s). *Ferrocenes*. VCH Verlagsgesellschaft, Weinheim, 1995.
- [104] U. Siemeling, J. von der Brüggen, U. Vorfeld, B. Neumann, A. Stammeler, H. Stammeler, A. Brockhinke, R. Plessow, P. Zanello, F. Laschi, F. Fabrizi de Biani, M. Fontani, S. Steenken, M. Stapper, and G. Gurzadyan. Ferrocenyl-functionalised terpyridines and their transition-metal complexes: syntheses, structures and spectroscopic and electrochemical properties. *Chem. Eur. J.*, 9:2819–2833, 2003.
- [105] M. Hobi, O. Ruppert, V. Gramlich, and A. Togni. Stepwise synthesis of octamethylferrocene-1,1'-dicarbaldehyde. Preparation of new electron donors for charge-transfer complexes. *Organomet.*, 16:1384–1391, 1997.
- [106] A. C. Albrecht. "forbidden" character in allowed electronic transitions. *J. Chem. Phys.*, 33:156–169, 1960.
- [107] M. Rosenblum, A. K. Banerjee, N. Danieli, R. W. Fish, and V. Schlatter. The structure and chemistry of ferrocene. VII bridged ferrocenes. *J. Am. Chem. Soc.*, 85:316–324, 1963.
- [108] Jr. K. L. Rinehart, D. E. Bublitz, and D. H. Gustafson. Organic chemistry of ferrocene. VI. Acetylation of mono-, di- and tri-bridged ferrocenes. *J. Am. Chem. Soc.*, 85:970–982, 1963.
- [109] A. Nakamura, P. Kim, and N. Hagihara. Interaction of cumulene systems with organometallic π -complexes: II. Ferrocenylbutatrienes and related compounds. *J. Organomet. Chem.*, 3:355–363, 1965.
- [110] K. Schlögl and W. Steyrer. VI. Synthese und Lichtabsorption von Ferrocenyl-Polyinen. *J. Organomet. Chem.*, 6:399–411, 1966.
- [111] H. Hennig and O. Gürtler. Beziehung zwischen polarographischem und spektralem Verhalten einiger substituierter Ferrocene. *J. Organomet. Chem.*, 11:307–316, 1968.
- [112] T. H. Barr and W. E. Watts. Bridged ferrocenes III. The visible and near ultraviolet absorption spectra of [m]ferrocenophanes and related compounds. *J. Organomet. Chem.*, 15:177–185, 1968.
- [113] A. M. Tarr and D. M. Wiles. Electronic absorption spectra and photodecomposition of some substituted ferrocenes. *Can. J. Chem.*, 46:2725–2731, 1968.
- [114] Š. Toma, A. Gáplovský, and P. Elečko. Synthesis and electronic spectra of 1-aryl-2-ferrocenylethylenes. *Chem. Pap.*, 39:115–124, 1985.
- [115] A. Berenbaum, H. Braunschweig, R. Dirk, U. Englert, J. C. Green, F. Jäkle, A. J. Lough, and I. Manners. Synthesis, electronic structure, and novel reactivity of strained boron-bridged [1]ferrocenophanes. *J. Am. Chem. Soc.*, 122:5765–5774, 2000.
- [116] A. Krishnan, S. K. Pal, P. Nandakumar, A. G. Samuelson, and P. K. Das. Ferrocenyl donor-organic acceptor complexes for second order nonlinear optics. *Chem. Phys.*, 265:313–322, 2001.

- [117] S. K. Pal, A. Krishnan, P. K. Das, and A. G. Samuelson. Schiff base linked ferrocenyl complexes for second-order nonlinear optics. *J. Organomet. Chem.*, 604:248–259, 2000.
- [118] Y. Zhu and M. O. Wolf. Charge transfer and delocalization in conjugated (ferrocenylethynyl)oligothiophene complexes. *J. Am. Chem. Soc.*, 122:10121–10125, 2000.
- [119] A. Green, M. R. Bryce, A. S. Batsanov, and J. A. K. Howard. A novel π -donor- π -acceptor system: 1-(4,5-dimethyl-1,3-dithiol-2-ylidene)-1-ferrocenyl-3,3-dicyanopropene. *J. Organomet. Chem.*, 590:180–183, 1999.
- [120] C. Lambert, W. Gaschler, M. Zabel, R. Matschiner, and R. Wortmann. Linear and non-linear optical properties of arene-Fe-Cp complexes. *J. Organomet. Chem.*, 592:109–114, 1999.
- [121] W. R. Thiel, T. Priermeier, D. A. Fiedler, A. M. Bond, and M. R. Mattner. Synthesis, redox chemistry and solid state structure of di- and trinuclear ferrocenyl substituted n-alkylpyrazolyl pyridine complexes. *J. Organomet. Chem.*, 514:137–147, 1996.
- [122] D. R. Kanis, M. A. Ratner, and T. J. Marks. Description of quadratic optical nonlinearities for transition-metal organometallic chromophores using SCF-LCAO MECI formalism. *J. Am. Chem. Soc.*, 112:8203–8204, 1990.
- [123] D. R. Kanis, M. A. Ratner, and T. J. Marks. Calculation and electronic description of quadratic hyperpolarizabilities. Toward a molecular understanding of NLO responses in organotransition metal chromophores. *J. Am. Chem. Soc.*, 114:10338–10357, 1992.
- [124] D. R. Kanis, M. A. Ratner, and T. J. Marks. Design and construction of molecular assemblies with large second-order optical nonlinearities. Quantum chemical aspects. *Chem. Rev.*, 94:195–242, 1994.
- [125] P. G. Gassman, D. W. Macomber, and J. W. Hershberger. Evaluation by ESCA of the electronic effect of methyl substitution on the cyclopentadienyl ligand. A study of titanocenes, zirconocenes, hafnocenes, and ferrocenes. *Organometallics*, 2:1470–1472, 1983.
- [126] L. Karki, H. P. Lu, and J. T. Hupp. Electroabsorption studies of intervalence charge transfer in $(\text{NC})_5\text{FeCNOs}(\text{NH}_3)_5^-$: experimental assessment of charge-transfer distance, solvent reorganization, and electronic coupling parameters. *J. Phys. Chem.*, 100:15637–15639, 1996.
- [127] D. H. Oh, M. Sano, and S. G. Boxer. Electroabsorption (Stark effect) spectroscopy of mono- and biruthenium charge-transfer complexes: Measurements of changes in dipole moments and other electrooptic properties. *J. Am. Chem. Soc.*, 113:6880–6890, 1991.
- [128] D. H. Oh and S. G. Boxer. Electrochromism in the near-infrared absorption spectra of bridged ruthenium mixed-valence complexes. *J. Am. Chem. Soc.*, 112:8161–8162, 1990.
- [129] G. U. Bublitz, R. Ortiz, S. R. Marder, and S. G. Boxer. Stark spectroscopy of donor/acceptor substituted polyenes. *J. Am. Chem. Soc.*, 119:3365–3376, 1997.

- [130] T. Abe and I. Iwebo. Comparison of the excited-state dipole moments and polarizabilities estimated from solvent spectral shifts with those from electrooptical measurements. *Bull. Chem. Soc. Jpn.*, 58:3415–3422, 1985.
- [131] M. Marcaccio, F. Paolucci, C. Paradisi, M. Carano, S. Roffia, C. Fontanesi, L. J. Yellowlees, S. Serroni, S. Campagna, and V. Balzani. Electrochemistry and spectroelectrochemistry of ruthenium(II)-bipyridine building blocks. Different behaviour of the 2,3- and 2,5-bis(2-pyridyl)pyrazine bridging ligands. *J. Electroanal. Chem.*, 532:99–112, 2002.
- [132] S. Campagna, G. Denti, De Rosa G., L. Sabatino, M. Ciano, and V. Balzani. Syntheses, absorption spectra, luminescence properties, and electrochemical behaviour of mono- and binuclear ruthenium(II) complexes of isomeric bis(2-pyridyl)pyrazines. *Inorg. Chem.*, 28:2565–2570, 1989.
- [133] S. Roffia, M. Marcaccio, C. Paradisi, F. Paolucci, V. Balzani, G. Denti, S. Serroni, and S. Campagna. Electrochemical reduction of (2,2'-bipyridine)- and bis((2-pyridyl)pyrazine)ruthenium(II) complexes used as building blocks for supramolecular species. Redox series made of 8, 10, and 12 redox steps. *Inorg. Chem.*, 32:3003–3009, 1993.
- [134] S. Hünig and I. Wehner. Two step redox systems LII. 2,2'-bipyridylboronium salts. *Heterocycles*, 28:359–363, 1989.
- [135] Y. R. Shen. *The principles of nonlinear optics*. 1984.
- [136] A. Brodeur and S. L. Chin. Ultrafast white-light continuum generation and self-focusing in transparent condensed media. *J. Opt. Soc. Am. B*, 16:637–650, 1999.
- [137] R. L. Fork, C. V. Shank, C. Hirilman, R. Yen, and W. J. Tomlinson. Femtosecond white-light continuum pulses. *Opt. Lett.*, 8:1–3, 1983.
- [138] J. Diels and W. Rudolph. *Ultrashort laser pulse phenomena: fundamentals, techniques, and applications on a femtosecond time scale*. Academic Press, San Diego, 1996.
- [139] A. Yariv. *Optical electronics in modern communications*. Oxford University Press, New York, 1997.
- [140] O. E. Martinez, J. P. Gordon, and R. L. Fork. Negative group-velocity dispersion using refraction. *J. Opt. Soc. Am. A*, 1:1003–1006, 1984.
- [141] R. E. Sherriff. Analytic expressions for group-delay dispersion and cubic dispersion in arbitrary prism sequences. *J. Opt. Soc. Am. B*, 15:1224–1230, 1998.
- [142] R. Trebino, K. W. DeLong, D. N. Fittinghoff, J. N. Sweetster, M. A. Krumbügel, B. A. Richman, and D. J. Kane. Measuring ultrashort laser pulses in the time-frequency domain using frequency-resolved optical gating. *Rev. Sci. Instrum.*, 68:3277–3295, 1997.
- [143] L. Gallmann, D. H. Sutter, N. Matsuchek, G. Steinmeyer, and U. Keller. Characterization of sub-6-fs optical pulses with spectral phase interferometry for direct electric-field reconstruction. *Opt. Lett.*, 24:1314–1316, 1999.

- [144] T. Feurer, A. Glass, and R. Sauerbrey. Two-photon photoconductivity in SiC photodiodes and its application to autocorrelation measurements of femtosecond optical pulses. *Appl. Phys. B*, 65:295–297, 1997.
- [145] G. Cerullo and S. De Silvestri. Ultrafast optical parametric amplifiers. *Rev. Sci. Instrum.*, 74:1–18, 2003.
- [146] E. Riedle, M. Beutler, S. Lochbrunner, J. Piel, S. Schenkl, S. Spörlein, and W. Zinth. Generation of 10 to 50 fs pulses tunable through all of the visible and the nir. *Appl. Phys. B*, 71:457–465, 2000.
- [147] K. Ekvall, P. van der Meulen, C. Dhollande, L. E. Berg, S. Pommeret, R. Naskercki, and J. C. Mialocq. Cross phase modulation artifact in liquid phase transient absorption spectroscopy. *J. Appl. Phys.*, 87:2340–2352, 2000.
- [148] S. A. Kovalenko, A. L. Dobryakov, J. Ruthmann, and N. P. Ernsting. Femtosecond spectroscopy of condensed phases with chirped supercontinuum probing. *Phys. Rev. A*, 59:2369–2384, 1999.
- [149] G. P. Agrawal. *Nonlinear fiber optics*. Academic Press, San Diego, 2nd edition, 1995.
- [150] G. R. Fleming. *Chemical applications of ultrafast spectroscopy*. Oxford University Press, Oxford, 1986.
- [151] R. Huber, J. E. Moser, M. Grätzel, and J. Wachtveitl. Photoinduced electron transfer in dye/semiconductor systems on a sub-10-fs time scale. In R. D. Miller, M. M. Murnane, F. F. Scherer, and A. M. Weiner, editors, *Ultrafast Phenomena XIII*, pages 316–318, Berlin, 2003. Springer.
- [152] E. Herdtweck, J. Jäkle, G. Opramolla, M. Spiegler, M. Wagner, and P. Zanello. Structural features and electrochemical properties of ansa-ferrocenes with pyrazabole bridges. *Organometallics*, 15:5524–5535, 1996.
- [153] L. Banford and G. E. Coates. Colored boronium salts. *J. Chem. Soc.*, 102:3564–3568, 1964.
- [154] F. W. Vance, L. Karki, J. K. Riegler, J. T. Hupp, and M. A. Ratner. Aspects of intervalence charge transfer in cyanide-bridged systems: modulated electric field assessment of distances, polarizability changes, and anticipated first hyperpolarizability characteristics. *J. Phys. Chem. A*, 102:8320–8324, 1998.
- [155] P. Suppan. Excited-state dipole moments from absorption/fluorescence solvatochromic ratios. *Chem. Phys. Lett.*, 94:272–275, 1983.
- [156] D. Noukakis and P. Suppan. Excited state dipole moments of fluoroanilines from solvatochromic shift measurements. *Spectrochimica Acta*, 43A:1317–1322, 1987.
- [157] E. Lippert. Dipolmoment und elektronstruktur von angeregten molekülen. *Z. Naturforsch. A*, 10:541–545, 1955.
- [158] E. M. Kober, B. P. Sullivan, and T. J. Meyer. Solvent dependence of metal-to-ligand charge-transfer transitions. Evidence of initial electron localisation in MLCT excited states of 2,2'-bipyridine complexes of ruthenium(II) and osmium(II). *Inorg. Chem.*, 23:2098–2104, 1984.

- [159] C. A. van Walree, M. R. Roest, W. Schuddeboom, L. W. Jenneskens, J. W. Verhoeven, J. W. Warman, H. Kooijman, and A. L. Spek. Comparison between SiMe₂ and CMe₂ spacers as σ -bridges for photoinduced charge transfer. *J. Am. Chem. Soc.*, 118:8395–8407, 1996.
- [160] R. W. Callahan and T. J. Meyer. Intervalence transfer in the mixed-valence ion (bipy)₂ClRu(py₂)RuCl(bipy)₂³⁺. *Chem. Phys. Lett.*, 39:82–84, 1976.
- [161] E. M. Voigt. Charge-transfer spectra in non-polar solvents. *J. Phys. Chem.*, 70:598–600, 1966.
- [162] A. Kawski. On the estimation of excited-state dipole moments from solvatochromic shifts of absorption and fluorescence spectra. *Z. Naturforsch.*, 57a:255–262, 2002.
- [163] K. Wynne, C. Galli, and R. M. Hochstrasser. Ultrafast charge transfer in an electron donor-acceptor complex. *J. Chem. Phys.*, 100:4797–4810, 1993.
- [164] C. J. Timpson, C. A. Biggnozzi, B. P. Sullivan, E. M. Kober, and T. J. Meyer. Influence of the solvent on the spectroscopic properties of cyano complexes of ruthenium(II). *J. Phys. Chem.*, 100:2915–2925, 1996.
- [165] I. Cacelli and A. Ferretti. Solvent effect on the optical properties of [(NH₃)₅Ru-pyrazine]^{+m} ($m = 2, 3$) complexes by ab initio calculations. *J. Chem. Phys.*, 109:8583–8590, 1998.
- [166] C. J. Cramer and D. G. Truhlar. Implicit solvation models: equilibria, structure, spectra and dynamics. *Chem. Rev.*, 99:2161–2200, 1999.
- [167] W. Kaim, S. Kohlmann, S. Ernst, B. Olbrich-Deussner, C. Bessenbacher, and A. Schulz. What determines the solvatochromism of metal-to-ligand charge transfer transitions? A demonstration involving 17 tungsten carbonyl complexes. *J. Organomet. Chem.*, 321:215–226, 1987.
- [168] P. E. Smith and B. M. Pettitt. Modeling solvent in biomolecular systems. *J. Phys. Chem.*, 98:9700–9711, 1994.
- [169] E. G. McRae. Theory of solvent effects on molecular electronic spectra. Frequency shifts. *J. Phys. Chem.*, 61:562–572, 1957.
- [170] M. M. Karelson and M. C. Zerner. Theoretical treatment of solvent effects on electronic spectroscopy. *J. Phys. Chem.*, 96:6949–6957, 1992.
- [171] L. Onsager. Electric moments of molecules in liquids. *J. Am. Chem. Soc.*, 58:1486–1493, 1936.
- [172] J. E. Brady and P. W. Carr. An analysis of dielectric models of solvatochromism. *J. Phys. Chem.*, 89:5759–5766, 1985.
- [173] B. S. Brunschwig, S. Ehrenson, and N. Sutin. Solvent reorganization in optical and thermal electron-transfer processes: solvatochromism and intramolecular electron-transfer barriers in spheroidal molecules. *J. Phys. Chem.*, 91:4714–4723, 1987.
- [174] A. H. Reddoch and S. Konoshi. The solvent effect on di-tert-butyl nitroxide. A dipole-dipole model for polar solutes in polar solvents. *J. Chem. Phys.*, 70:2121–2130, 1979.

- [175] J. R. Lombardi. Solvatochromic shifts reconsidered: field-induced mixing in the non-linear region and application to indole. *J. Phys. Chem. A*, 103:6335–6338, 1999.
- [176] J. R. Lombardi. Solvatochromic shifts: a reconsideration. *J. Phys. Chem. A*, 102:2817–2823, 1998.
- [177] S. Fantacci, F. de Angelis, and A. Selloni. Absorption spectrum and solvatochromism of the $[\text{Ru}(4,4'\text{-COOH-2,2'}\text{-bpy})_2(\text{NCS})_2]$ molecular dye by time dependent density functional theory. *J. Am. Chem. Soc.*, 125:4381–4387, 2003.
- [178] V. Barone, F. Fabrizi de Biani, E. Ruiz, and B. Sieklucka. Electron transfer in the $[\text{Pt}(\text{NH}_3)_4]^{2+} + [\text{W}(\text{CN})_8]^{3-}$ donor-acceptor system. The environment effect: a time-dependent density functional study. *J. Am. Chem. Soc.*, 123:10742–10743, 2001.
- [179] M. S. Gudipati. Exciton, exchange, and through-bond interaction in multichromophoric molecules: an analysis of the electronic excited states. *J. Phys. Chem.*, 98:9750–9763, 1994.
- [180] E. G. McRae and M. Kasha. *The molecular exciton model*, pages 23–42. Academic Press, New York, 1964.
- [181] G. S. Levinson, W. T. Simpson, and W. Curtis. Electronic spectra of pyridocyanine dyes with assignments of transitions. *J. Am. Chem. Soc.*, 79:4314–4320, 1957.
- [182] H. Neugebauer, C. Kvarnström, C. Brabec, and N. S. Sariciftci. Infrared spectroelectrochemical investigations on the doping of soluble poly(isothianaphthene methine) (PIM). *J. Chem. Phys.*, 110:12108–12115, 1999.
- [183] S. H. Pullen and M. D. Edington and S. L. Studer-Martinez, J. D. Simon, and H. A. Staab. Experimental verification of the through-bond mechanisms of electron transfer in bridged donor-acceptor complexes. *J. Phys. Chem. A*, 103:2740–2743, 1999.
- [184] S. H. Pullen, S. L. Studer-Martinez, M. D. Edington, A. L. Harris, A. Long, S. W. Baldwin, H. A. Staab, and J. D. Simon. Comparison of the photoinduced electron transfer reaction in a rigid cyclophane and its corresponding bimolecular donor/acceptor complex. *J. Phys. Chem. A*, 103:10220–10225, 1999.
- [185] H. Oevering, J. W. Verhoeven, M. N. Padden-Row, and J. M. Warman. Charge-transfer absorption and emission resulting from long-range through-bond interaction: exploring the relation between the electronic coupling and electron-transfer in bridged donor-acceptor systems. *Tetrahedron*, 45:4751–4766, 1989.
- [186] M. Pope and C. E. Swenberg. *Electronic processes in organic crystals and polymers*. Oxford University Press, Oxford, 2nd edition, 1999.
- [187] W. L. Parker and G. A. Crosby. Charge-transfer intensity in complexes with symmetrically equivalent acceptors. *Int. J. Quant. Chem.*, 39:299–308, 1991.

- [188] D. O. Cowan, P. Shu, F. L. Hedberg, M. Rossi, and T. J. Kistenmacher. Ferrocenyl(III)tris(ferrocenyl(II))borate. Synthesis, electrochemistry, and molecular structure of an unusual mixed-valence zwitterion. *J. Am. Chem. Soc.*, 101:1304–1306, 1979.
- [189] C. LeVanda, D. O. Cowan, C. Leitch, and K. Bechgaard. Mixed-valence differocenylylacetylene cation. *J. Am. Chem. Soc.*, 96:6788–6789, 1974.
- [190] P. Shu, K. Bechgaard, and D. O. Cowan. Studies of mixed-valence diferrocenyl selenide and differrocenyl diselenide. *J. Org. Chem.*, 41:1849–1852, 1976.
- [191] C. Le Vanda, D. O. Cowan, and K. Bechgaard. Electronic and stereoelectronic effects on the intervalence transfer transition in biferrocene cations. *J. Am. Chem. Soc.*, 97:1980–1981, 1975.
- [192] D. O. Cowan and C. Le Vanda. 1,1'-biferrocenylene[Fe(II)Fe(III)] salts. *J. Am. Chem. Soc.*, 94:9271–9272, 1972.
- [193] M. B. Robin and P. Day. Mixed valence chemistry - a survey and classification. *Advan. Inorg. Chem. Radiochem.*, 10:247, 1967.
- [194] A. B. P. Lever, S. R. Pickens, P. C. Minor, S. Licoccia, B. S. Ramaswamy, and K. Magnell. Charge-transfer spectra of metallophthalocyanines: correlation with electrode potentials. *J. Am. Chem. Soc.*, 103:6800–6806, 1981.
- [195] J. E. Monat and J. K. McCusker. Femtosecond excited-state dynamics of an iron(II) polypyridyl solar cell sensitizer model. *J. Am. Chem. Soc.*, 122:4092–4097, 2000.
- [196] E. S. Dodsworth and A. B. P. Lever. Correlation of electronic charge transfer transitions and electrochemical potentials. The bipyrazine(tetracarbonyl)molebdenum(0) system in various solvents. *Chem. Phys. Lett.*, 112:567–570, 1984.
- [197] T. Matsubara and P. C. Ford. Some applications of cyclic voltammetry to the reactions and properties of ruthenium ammine complexes. Reduction potentials and rate studies. *Inorg. Chem.*, 15:1107–1110, 1976.
- [198] D. F. Shriver and J. Posner. Bridge addition compounds. III. The influence of boron-containing Lewis acids on electronic spectra, vibrational spectra, and oxidation potentials of some iron-cyanide complexes. *J. Am. Chem. Soc.*, 88:1672–1677, 1966.
- [199] D. P. Rillema and K. B. Mack. The low-lying excited state in ligand π -acceptor complexes of ruthenium(II): mononuclear and binuclear species. *Inorg. Chem.*, 21:3849–3854, 1982.
- [200] P. Ford, De F. P. Rudd, R. Gaunder, and H. Taube. Synthesis and properties of pentaamminepyridineruthenium(II) and related pentaammineruthenium complexes of aromatic nitrogen heterocycles. *J. Am. Chem. Soc.*, 90:1187–1194, 1968.
- [201] S. Goswami, A. R. Chakravarty, and A. Chakravorty. Chemistry of ruthenium. 5 reaction of trans-dihalobis[2-(arylo)pyridine]ruthenium(II) with tertiary phosphines: chemical, spectroelectrochemical, and mechanistic characterization of geometrically isomerized substitution products. *Inorg. Chem.*, 21:2737–2742, 1982.

- [202] S. E. Dodsworth and A. B. P. Lever. Relationships between electronic spectroscopy and electrochemistry. A probe of reorganisation energies. *Chem. Phys. Lett.*, 119:61–66, 1985.
- [203] J. V. Caspar, B. P. Sullivan, E. M. Kober, and T. J. Meyer. Application of the energy gap law to the decay of charge transfer excited states. Solvent effects. *Chem. Phys. Lett.*, 91:91–95, 1982.
- [204] C. Creutz and M. H. Chou. Solvent dependences of spectral and redox properties of pyrazine (pz) complexes of ruthenium and osmium pentaammines: $\text{Ru}(\text{NH}_3)_5\text{pzCH}_3^{3+}$, $\text{Os}(\text{NH}_3)_5\text{pzCH}_3^{3+}$, and $[\text{Ru}(\text{NH}_3)_5]_2^{5+}$. *Inorg. Chem.*, 26:2995–3000, 1987.
- [205] E. S. Dodsworth and A. B. P. Lever. Correlations between electrochemical potentials and optical charge transfer energies in ruthenium bipyridine derivatives. *Chem. Phys. Lett.*, 124:152–166, 1986.
- [206] M. D. Thomson, M. Novosel, H. G. Roskos, T. Müller, M. Scheibitz, M. Wagner, F. Fabrizi de Biani, and P. Zanello. Electronic structure, photophysics, and relaxation dynamics of charge transfer excited states in boron-nitrogen bridged ferrocene-donor organic-acceptor compounds. *J. Phys. Chem. A*, 108:3281–3291, 2004.
- [207] J. K. McCusker. Femtosecond absorption spectroscopy of transition metal charge-transfer complexes. *Acc. Chem. Res.*, 36:876–887, 2003.
- [208] W. Koch and M. C. Holthausen. *A chemist's guide to density functional theory*. Wiley VCH, Weinheim, 2nd edition, 2001.
- [209] M. E. Casida, K. C. Casida, and D. R. Salahub. Excited-state potential energy curves from time-dependent density-functional theory: a cross section of formaldehyde's 1A_1 manifold. *Int. J. Quant. Chem.*, 70:933–941, 1998.
- [210] T. M. Halasinski, J. L. Weisman, R. Ruitenkamp, T. J. Lee, F. Salama, and M. Head-Gordon. Electronic absorption spectra of neutral perylene ($\text{C}_{20}\text{H}_{12}$), terrylene ($\text{C}_{30}\text{H}_{16}$), and quaterrylene ($\text{C}_{40}\text{H}_{20}$) and their positive and negative ions: Ne matrix-isolation spectroscopy and time-dependent density functional theory calculations. *J. Phys. Chem. A*, 107:3660–3669, 2003.
- [211] D. J. Tozer, R. D. Amos, N. C. Handy, B. O. Roos, and L. Serrano-Andrés. Does density functional theory contribute to the understanding of excited states of unsaturated organic compounds. *Mol. Phys.*, 97:859–868, 1999.
- [212] S. J. A. van Gisbergen, J. A. Groeneveld, A. Rosa, J. G. Snijders, and E. J. Baerends. Excitation energies for transition metal compounds from time-dependent density functional theory. Applications to MnO_4^- , $\text{Ni}(\text{CO})_4$, and $\text{Mn}_2(\text{CO})_{10}$. *J. Phys. Chem. A*, 103:6835–6844, 1999.
- [213] G. Ricciardi, A. Rosa, S. J. A. van Gisbergen, and E. J. Baerends. A density functional study of the optical spectra and non-linear optical properties of heteroleptic tetrapyrrole sandwich complexes: the porphyrinato-porphyrinato-zirconium(IV) complex as a case study. *J. Phys. Chem. A*, 104:635–643, 2000.
- [214] S. I. Gorelsky, S. C. da Silva, A. B. P. Lever, and D. W. Franco. Electronic spectra of trans- $[\text{Ru}(\text{NH}_3)_4(\text{L})\text{NO}]^{3+/2+}$ complexes. *Inorg. Chim.*, 300:302:698–708, 2000.

- [215] C. Daul, E. J. Baerends, and P. Vernooijs. A density functional study of the MLCT states of $[\text{Ru}(\text{bpy})_3]^{2+}$ in D_3 symmetry. *Inorg. Chem.*, 33:3538–3543, 1994.
- [216] C. Adamo and V. Barone. Inexpensive and accurate predictions of optical excitations in transition-metal complexes: the TDDFT/PBE0 route. *Theor. Chem. Acc.*, 105:169–172, 2000.
- [217] G. Ricciardi, A. Rosa, and E. J. Baerends. Ground and excited states of zinc phthalocyanine studied by density functional methods. *J. Phys. Chem. A*, 105:5242–5254, 2001.
- [218] A. Rosa, E. J. Baerends, S. J. A. van Gisbergen, E. van Lenthe, J. A. Gronveld, and J. G. Snijders. Electronic spectra of $\text{M}(\text{CO})_6$ $\text{M}=\text{Cr}, \text{Mo}, \text{W}$ revisited by a relativistic TDDFT approach. *J. Am. Chem. Soc.*, 121:10356–10365, 1999.
- [219] A. Rosa, G. Ricciardi, E. J. Baerends, and S. J. A. van Gisbergen. The optical spectra of NiP, NiPz, NiTBP, and NiPc: electronic effects of meso-tetraaza substitution and tetrabenzo annulation. *J. Phys. Chem. A*, 105:3311–3327, 2001.
- [220] X. Wang, L. Chen, A. Endou, M. Kubo, and A. Miyamoto. A study of the excitations of ligand-to-metal charge transfer in complexes Cp_2MCl_2 ($\text{Cp}=\pi\text{-C}_5\text{H}_5$, $\text{M}=\text{Ti}, \text{Zr}, \text{Hf}$) by density functional theory. *J. Organomet. Chem.*, 678:156–165, 2003.
- [221] Dr. A. Dreuw. J. W. Goethe Universität, Frankfurt, Germany, personal communication.
- [222] A. D. Becke. Density-functional thermochemistry. III. The role of exact exchange. *J. Chem. Phys.*, 98:5648–5652, 1992.
- [223] J. P. Perdew. Density-functional approximation for the correlation energy of the inhomogeneous electron gas. *Phys. Rev. B*, 33:8822–8824, 1986.
- [224] P. Fuentealba, L. von Szentpály, H. Preuss, and H. Stoll. Pseudopotential calculations for alkaline-earth atoms. *J. Phys. B*, 18:1287–1296, 1985.
- [225] T. Müller. J. W. Goethe Universität, Personal communication.
- [226] B. J. Berne and M. Borkovec. Classical theories of reaction dynamics: transition state theory, spatial diffusion controlled reactions, and the energy diffusion limit. *J. Chem. Soc. Faraday Trans.*, 94:2717–2723, 1998.
- [227] W. H. Press, B. P. Flannery, S. A. Teukolsky, and W. T. Vetterling. *Numerical recipes in C: the art of scientific computing*. Cambridge University Press, Cambridge, 2nd edition, 1992.
- [228] G. Fleming and M. Cho. Chromophore-solvent dynamics. *Annu. Rev. Phys. Chem.*, 47:109–134, 1996.
- [229] M. A. Kahlow, W. Jarzeba, T. J. Kand, and P. F. Barbara. Femtosecond resolved solvation dynamics in polar solvents. *J. Chem. Phys.*, 90:151–158, 1989.
- [230] S. J. Strickler and R. A. Berg. Relationship between absorption intensity and fluorescence lifetime of molecules. *J. Chem. Phys.*, 37:814–822, 1963.

-
- [231] Prof. J. Wachtveitl. J. W. Goethe Universität, Frankfurt, Germany, personal communication.
- [232] Prof. G. Stock. J. W. Goethe Universität, Frankfurt, Germany, personal communication.
- [233] A. T. Yeh, C. V. Shank, and J. K. McCusker. Ultrafast electron localization dynamics following photo-induced charge transfer. *Science*, 289:935–938, 2000.
- [234] N. Matsumi, K. Naka, and Y. Chujo. Extension of the π -conjugation length via the vacant p-orbital of the boron atom. Synthesis of novel electron deficient π -conjugated systems by hydroboration polymerization and their blue light emission. *J. Am. Chem. Soc.*, 120:5112–5113, 1998.
- [235] H. Margenau and G. M. Murphy. *The mathematics of physics and chemistry*. Van Nostrand Co., Inc., New York, 1943.

Curriculum Vitae

Mark David Thomson, born 27. August 1974 in Palmerston North, New Zealand



Marital status: Single

Pre-university Education:

1979 - 1987: Primary schooling, Palmerston North and Auckland, New Zealand
1988 - 1992: Secondary schooling, Rangitoto College, Auckland, New Zealand
11.1992: University entrance exams (Aggregate: 426)

University education:

1993 - 1996: Bachelor of Technology (Optoelectronics),
Department of Physics, University of Auckland, New Zealand
Grade: First class honours
1997 - 1998: Master of Science (Physics), under Professor J. D.
Harvey, Department of Physics, University of Auckland, New Zealand
Masters degree topic: 'Complete characterisation of ultra-short
pulses using cross-phase modulation in optical fibres'
Grade: A+, completed with distinction

Doctoral studies:

15.05.1998- 'Wissenschaftlicher Mitarbeiter' in the research group
'Ultrakurzzeitspektroskopie' under Prof. Dr. H. G. Roskos,
working on photophysical investigation of organosilicon and
organometallic molecular systems, including fabrication of
thin film polymer light-emitting diodes, photoluminescence and
photochemistry of organosilicon compounds (in collaboration with
AG Auner, Anorganische Chemie, J. W. Goethe-Universität,
Frankfurt am Main), spectroscopic characterisation of
organometallic charge-transfer compounds (in collaboration
with AG Wagner, Anorganische Chemie, J. W. Goethe-Universität,
Frankfurt am Main), femtosecond molecular spectroscopy,
theoretical work on terahertz-radiation generation and detection.

Acknowledgments

I would like to thank Prof. Hartmut Roskos for providing an extremely interesting research programme, and for always being there to offer excellent advice. Many thanks to Prof. Matthias Wagner and his group (including Kuangbiao Ma, Ding Li, Matthias Scheibitz) for their careful preparation of the organometallic compounds and their help with the characterisation. Dr. Thomas Müller deserves special mention for performing numerous theoretical calculations and providing many hours of helpful discussions over the years. Moreover, I am grateful for the kind help from Prof. Roser Valenti (who also kindly agreed to be the second referee of this work), Dr. Andreas Dreuw (who does ace quantum chemistry on the fly), Prof. Josef Wachtveitl, Prof. Gerhard Stock and Prof. Eberhard Riedle (Munich), and the members of their groups. Many thanks to the diplomand students who worked with me, Mimoun Bohajra, Lothar Neumann, and especially Miljenko Novosel for all their hard work. Moreover, it was a great experience, including many fruitful discussions, to work with my colleagues, in particular Karsten Siebert, Kai Rönnerberg, Johanna Kolb, Anne Beate Hummel, Torsten Löffler, Frank Jacob, Robert Sachs, Tobias Bauer, Markus Krefß, and Gabriel Loata. I cannot thank Marion Jordan enough for taking care of so many practical issues over the years, and Hannah Döring for administrating the Forschergruppe project. I also express thanks to Herbert Hassenpflug and the great guys in the mechanical workshop of the Physikalisches Institut for producing so many valuable components for the experiments, as well as the electronic workshop for all the useful devices. I am grateful for all the help from the other research groups in the Physikalisches Institut, especially the group of Prof. Wolf Assmus. Many thanks to Dr. Fabrizia Fabrizi de Biani and Prof. Zanello (University of Siena) for the electrochemistry measurements, and Dr. Heidi Höfer and Jan Heliosch (Institut für Mineralogie, J. W. Goethe-Universität) for helping with the crystal preparation.

For everything besides physics, I wish to thank my wonderful companion, Al-muth, for her patience and caring nature, and my mother, Rosemary. Many friends and families (especially the Meyers and the Sieberts) have made my time here in Germany a truly enriching experience.